

Czech Technical University in Prague
Faculty of Nuclear Sciences and Physical
Engineering

Department of Physics
Specialization: Nuclear and Particle Physics



D^0 meson production in p+Au and
p+p collisions in the STAR
experiment

MASTER'S THESIS

Author: Bc. Michal Svoboda
Supervisor: doc. Mgr. Jaroslav Bielčík, Ph.D.
Year: 2023

České vysoké učení technické v Praze
Fakulta jaderná a fyzikálně inženýrská

Katedra fyziky

Program: Jaderná a částicová fyzika



Produkce mezonu D^0 v $p+Au$ a $p+p$ srážkách na experimentu STAR

DIPLOMOVÁ PRÁCE

Vypracoval: Bc. Michal Svoboda

Vedoucí práce: doc. Mgr. Jaroslav Bielčík, Ph.D.

Rok: 2023



Katedra: fyziky

Akademický rok: 2021/2022

ZADÁNÍ DIPLOMOVÉ PRÁCE

Student: Bc. Michal Svoboda

Studijní program: Jaderná a částicová fyzika

Název práce: Produkce mezonu D_0 v p+Au a p+p srážkách na experimentu STAR
(česky)

Název práce: D_0 meson production in p+Au and p+p collisions in the STAR
(anglicky) experiment

Pokyny pro vypracování:

- 1) Produkce půvabných mezonů
- 2) Přehled aktuálních výsledů produkce půvabných mezonů
- 3) Experiment STAR
- 4) Rekonstrukce mezonu D_0 v srážkách p+Au při energii 200 GeV
- 5) Rekonstrukce mezonu D_0 v srážkách p+p při energii 500 GeV
- 6) Aplikace metod strojového učení
- 7) Výhled a závěr



Doporučená literatura:

- [1] S.Sarkar, H. Satz and B. Sinha: The Physics of the Quark-Gluon Plasma, Lecture Notes in Physics, Springer, 2010
- [2] F.Prino and R. Rapp: Open Heavy Flavor in QCD Matter and in Nuclear Collisions, J.Phys.G 43 (2016) 9, 093002
- [3] Z.-B. Tang, et al.: An experimental review of open heavy flavor and quarkonium production at RHIC, Nucl.Sci.Tech. 31 (2020)
- [4] P. B. Gossiax: Open Heavy Flavors in Nuclear Collisions: Theory Overview, Nucl.Phys.A 982 (2019)
- [5] I. Schmidt and M.Siddikov: Production mechanisms of open-heavy flavor mesons, Phys.Rev.D 101 (2020) 9, 094020

Jméno a pracoviště vedoucího diplomové práce:

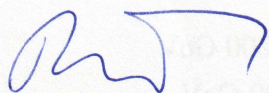
doc. Mgr. Jaroslav Bielčík, Ph.D., Katedra fyziky, Fakulta jaderná a fyzikálně inženýrská ČVUT v Praze

Ing. Jan Vaněk - konzultant, Katedra fyziky, Fakulta jaderná a fyzikálně inženýrská ČVUT v Praze

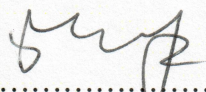
Datum zadání diplomové práce: 01.03.2022

Termín odevzdání diplomové práce: 05.01.2023

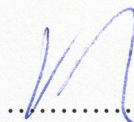
Doba platnosti zadání je dva roky od data zadání.



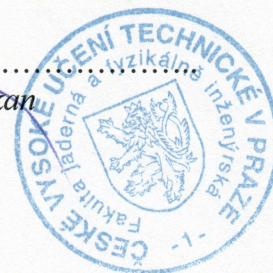
.....
garant studijního programu



.....
vedoucí katedry



.....
děkan



V Praze dne 01.03.2022

ČESKÉ VYSOKÉ UČENÍ TECHNICKÉ V PRAZE

Fakulta jaderná a fyzikálně inženýrská

Břehová 7
115 19 Praha 1



PROHLÁŠENÍ

Já, níže podepsaný

Jméno a příjmení studenta: Bc. Michal Svoboda
Osobní číslo: 473945
Název studijního programu (oboru): Jaderná a částicová fyzika

prohlašuji, že jsem diplomovou práci s názvem:

Produkce mezonu D_0 v $p+Au$ a $p+p$ srážkách na experimentu STAR

vypracoval samostatně a uvedl veškeré použité informační zdroje v souladu s Metodickým pokynem o dodržování etických principů při přípravě vysokoškolských závěrečných prací.

V Praze dne 4. 1. 2023

.....
podpis

Acknowledgments

In the first place I would like to express my gratitude to my supervisor doc. Jaroslav Bielčík for his guidance in the past three years, for his time and endless patience and for bringing me into the STAR group at the CTU.

Very special thanks belong to my consultant Dr. Jan Vaněk for the past two years. His advice were one of the building blocks which helped to create this thesis despite of my stupid questions and ways of finding problems that no one encountered before.

My thanks also go to my classmates and friends from our group for such a great environment and for all the tips and pieces of advice which I collected during the time spent at our faculty.

And at last I would like to thank my family and my girlfriend for all the support they provided me along this journey.

Thank you all!

Bc. Michal Svoboda

Název práce:

Produkce mezonu D^0 v p+Au a p+p srážkách na experimentu STAR

Autor: Bc. Michal Svoboda

Studijní program: Jaderná a částicová fyzika

Druh práce: Diplomová práce

Vedoucí práce: doc. Mgr. Jaroslav Bielčík, Ph.D.

Katedra fyziky, Fakulta jaderná a fyzikálně inženýrská, České vysoké učení technické v Praze

Konzultant: Ing. Jan Vaněk, Ph.D.

Brookhavenská národní laboratoř

Abstrakt: Velké urychlovače částic stojí v současné době na hranici poznání fyziky základních částic a interakcí. Mohou sloužit k široké škále měření od studia vnitřní struktury protonu až po studium kvark-gluonového plazmatu, což je stav hmoty přítomný ve Vesmíru krátce po Velkém třesku. Aby bylo možné správně popsat srážky těžkých jader, je nutné pochopit i vlastnosti srážek protonů a asymetrických srážek, které pomáhají pochopit fenomény způsobené pouhou přítomností jádra ve srážce. Dobrou sondou do všech těchto srážek jsou D mezony obsahující půvabný kvark, jelikož vznikají v raných fázích srážky. Tato práce ukazuje výsledky analýzy mezonů D^0 a D^* v p+Au a p+p srážkách změřených detektorem STAR.

Klíčová slova: kvark-gluonové plazma, efekty studené jaderné hmoty, D mezony, experiment STAR, RHIC

Title:

D^0 meson production in p+Au and p+p collisions in the STAR experiment

Author: Bc. Michal Svoboda

Abstract: Large particle colliders stand at the edge of the understanding of the physics of elementary particles and forces. They can serve as a tool to study wide scale of measurements from the inner structure of proton up to the study of the Quark-Gluon Plasma which is a state of matter present in the Universe shortly after the Big Bang. To fully describe the collisions of heavy ions, it is also necessary to understand properties of the collisions of protons and asymmetric collisions which help to understand phenomenons caused by a bare presence of a nucleus in a collision. A good probe to study all these systems are D mesons containing charm quark which are created in the early phases of a collision. This thesis shows results of the D^0 and D^* mesons in p+Au and p+p collisions measured by the STAR detector.

Key words: Quark-Gluon Plasma, Cold Nuclear Matter Effects, D Mesons, STAR, RHIC

Contents

Introduction	1
1 Physics Introduction	3
1.1 History of Particle Physics	3
1.2 The Standard Model	4
1.3 Quantum Chromodynamics	6
1.3.1 QCD Phase Diagram	7
1.3.2 Quark-Gluon Plasma	8
1.3.3 Time Evolution of Heavy-Ion Collisions	9
1.4 Variables in High Energy Physics	10
1.5 Signatures of the QGP	13
1.5.1 Nuclear Modification Factor	13
1.5.2 Jet Quenching	16
1.5.3 Quarkonia Suppression	19
1.5.4 Baryon to Meson Ratios	20
1.5.5 Hydrodynamic Flow	22
2 STAR Experiment at RHIC	27
2.1 Brookhaven National Laboratory	27
2.2 The Relativistic Heavy Ion Collider	29
2.3 The Solenoidal Tracker at RHIC	32
2.3.1 Time Projection Chamber	32
2.3.2 Time-Of-Flight detector	35
2.3.3 Heavy Flavor Tracker	36
2.3.4 Barrel Electromagnetic Calorimeter	38
2.3.5 Trigger systems	38
2.3.6 Other STAR Detectors	40
2.3.7 Forward Upgrade	40
2.4 Electron-Ion Collider	42
3 Cold Nuclear Matter Effects	45

3.1	Cold Nuclear Matter Effects	45
3.1.1	Parton Distribution Function Modification	46
3.1.2	Parton Saturation	47
3.1.3	Multiple Parton Scattering	49
3.1.4	Quarkonia Absorption	50
3.2	D^0 in p+Pb collisions	50
3.3	Asymmetric Collisions at PHENIX	55
4	Open Charm Hadrons Production	57
4.1	Properties of Charm Hadrons	57
4.2	Open-charm Hadrons in p+p Collisions	60
4.3	Open-charm Hadrons in Heavy-Ion Collisions	64
4.3.1	Open-charm Hadrons Measured by STAR	64
4.3.2	Open-charm Hadrons Measured by ALICE	72
5	Analysis of Experimental Data	77
5.1	Analysis of p+Au Collisions	78
5.1.1	Dataset and Event Selection	78
5.1.2	Particle Identification	79
5.1.3	D^0 Invariant Mass Spectra	84
5.1.4	D^* Invariant Mass Spectra	93
5.2	Analysis of p+p Collisions	98
5.2.1	Dataset and Event Selection	98
5.2.2	Particle Identification	98
5.2.3	D^0 Invariant Mass Spectra	102
5.2.4	D^* Invariant Mass Spectra	110
	Summary and Discussion	119
	References	I

List of Figures

1.1	Summary of elementary particles	6
1.2	An illustration of QCD phase diagram	7
1.3	Schematic view of a color confinement	9
1.4	Illustration of the time evolution of the Quark-Gluon Plasma	10
1.5	Schematic view of a collision of two heavy nuclei before and after the collision	11
1.6	A cartoon showing the centrality definition at the LHC energies from the final-state particle multiplicity and its correlation with the impact parameter b and the number of participating nucleons $\langle N_{\text{part}} \rangle$ in the collision	12
1.7	Comparison of R_{AA} of various particles measured by various experiments at different collision energies	14
1.8	Nuclear modification factors measured by ALICE in central (0–5 %) and peripheral (70–80 %) Pb+Pb collisions and in p+Pb collisions at $\sqrt{s_{\text{NN}}} = 5.02$ TeV	15
1.9	R_{CP} of charged hadrons as a function of p_{T} measured by STAR at various RHIC BES energies	16
1.10	Two particle azimuthal distribution of charged hadrons measured in p+p and d+Au collisions and central Au+Au collisions measured by STAR detector	17
1.11	Both panels: R_{AA} as a function of p_{T} in different centrality classes for jets with $ y < 2.8$ measured by ATLAS detector in Pb+Pb collisions at $\sqrt{s_{\text{NN}}} = 5.02$ TeV	18
1.12	Illustration of charm quarkonia used as a thermometer	19

1.13	Dimuon invariant mass distributions in p+p (left) and Pb+Pb (right) collisions at $\sqrt{s} = 2.76$ TeV and $\sqrt{s_{NN}} = 2.76$ TeV, respectively, measured by the CMS collaboration. The requirement for individual muons was $p_T > 4$ GeV/c	20
1.14	Inclusive J/ ψ R_{AA} measured by ALICE collaboration in Au+Au collisions at $\sqrt{s_{NN}} = 2.76$ TeV and $\sqrt{s_{NN}} = 5.02$ TeV and PHENIX collaboration at $\sqrt{s_{NN}} = 200$ GeV	21
1.15	The p/ π^+ (a) and \bar{p}/π^- (b) yield ratios measured by STAR in Au+Au and d+Au collisions at $\sqrt{s_{NN}} = 200$ GeV	22
1.16	Schematic view of a collision of two nuclei	23
1.17	The p_T dependent v_2 of various hadrons measured in Pb+Pb collisions at $\sqrt{s_{NN}} = 5.02$ TeV by ALICE detector	24
1.18	Elliptic flow v_2 (top) and triangular flow v_3 (bottom) as a function of collision multiplicity $N_{\text{trk}^{\text{offline}}}$ measured by CMS in Pb+Pb collisions at $\sqrt{s_{NN}} = 2.76$ TeV, p+Pb collisions at $\sqrt{s_{NN}} = 5.02$ TeV and p+p collisions at various energies	25
2.1	Schematic view of RHIC	29
2.2	Cartoon of the process of the accelerating of ions at RHIC	31
2.3	STAR detector and its sub-detectors	33
2.4	Schematic view of the STAR Time Projection Chamber	34
2.5	dE/dx of TPC (left) and $1/\beta$ of TOF (right) from Au+Au collisions	35
2.6	Illustration of the endcap-Time-Of-Flight detector	36
2.7	Cartoon of the subdetectors of the Heavy Flavor Tracker	37
2.8	The HFT pointing resolution in the transverse plane σ_{xy} as a function of momentum for pions, kaons and protons	38
2.9	A cartoon of subdetectors on STAR	39
2.10	STAR detector with the forward upgrade	41
2.11	A cartoon of Electron-Ion Collider	43
3.1	Visualization of the shadowing factor R_i^A depending on the Bjorken x	46

3.2	The nuclear modification factor R_{pPb} for J/ψ (left) and Υ (right) calculated using the EPS09 modification in p+Pb collisions at $\sqrt{s_{\text{NN}}} = 5.02$ TeV	47
3.3	Hadron structure in $1/x$ and Q^2 plane. Each circle is a parton with a fraction of momentum x . The saturation line separates the dilute (DGLAP) regime from the saturation regime. Different evolution regimes and saturation area are shown.	48
3.4	Nuclear modification factor $R_{\text{pA}}(y)$ for D and J/ψ in the CGC approach in p+Pb collisions at $\sqrt{s_{\text{NN}}} = 5.02$ TeV	49
3.5	Theoretical calculations for R_{pPb} of J/ψ and Υ as a function of p_{T} in minimum bias collisions with a small (red curve) and large (blue curve) energy loss effect at RHIC (left) and LHC (right)	50
3.6	Nuclear modification factor R_{pPb} of prompt D mesons in p+Pb collisions at $\sqrt{s_{\text{NN}}} = 5.02$ TeV measured by ALICE. Left: results for D^0 , D^+ and D^{+*} . Right: Average of non strange D mesons in $1 < p_{\text{T}} < 36$ GeV/ c , D^0 in $0 < p_{\text{T}} < 1$ GeV/ c and strange D meson in $2 < p_{\text{T}} < 24$ GeV/ c	51
3.7	Nuclear modification factor R_{pPb} of prompt D mesons in p+Pb collisions at $\sqrt{s_{\text{NN}}} = 5.02$ TeV measured by ALICE. Left: Comparison with models that include only CNM effects. Right: Comparison with transport models	52
3.8	Nuclear modification factor of prompt D mesons in p+Pb collisions at $\sqrt{s_{\text{NN}}} = 5.02$ TeV measured by ALICE in different centrality classes compared with charged particles	53
3.9	p_{T} -differential cross sections for various D meson kinds with $-0.96 < y_{\text{cms}} < 0.04$ in p+Pb collisions at $\sqrt{s_{\text{NN}}} = 5.02$ TeV measured by ALICE compared with the p+p cross sections scaled by Pb mass number	54
3.10	The nuclear modification factor R_{dAu} as a function of transverse momentum p_{T} in 0–20 % and 60–88 % centrality classes in d+Au collisions at $\sqrt{s_{\text{NN}}} = 200$ GeV measured by PHENIX. Data are compared to a PYTHIA calculation considering EPS09 LO and a calculation by Vitev et al. considering nPDFs, k_{T} broadening and CNM energy loss	56

3.11	Flow coefficients v_n of charged particles as a function of p_T in three collisions systems p+Au, d+Au and $^3\text{He}+\text{Au}$ measured by PHENIX detector at $\sqrt{s_{\text{NN}}} = 200$ GeV. The data are compared to SONIC iEBE-VISHNU and MSTV theoretical calculations	56
4.1	The ratios of the splitting-angle probability distributions $R(\theta)$ for D^0 -meson tagged jets to inclusive jets measured in p+p collisions at $\sqrt{s} = 13$ TeV, are shown for $5 < E_{\text{Radiator}} < 10$ GeV (left panel), $10 < E_{\text{Radiator}} < 20$ GeV (middle panel) and $20 < E_{\text{Radiator}} < 35$ GeV (right panel). The data are compared to PYTHIA v.8 and SHERPA simulations including the no dead-cone limit given by the ratio of the angular distributions for light-quark jets (LQ) to inclusive jets. The pink shaded areas correspond to the angles within which emissions are suppressed by the dead-cone effect, assuming a charm-quark mass of $1.275 \text{ GeV}/c^2$	59
4.2	Production p_T differential cross section of prompt D^0 , D^+ and D^{*+} measured by ALICE experiment in p+p collisions at $\sqrt{s} = 7$ TeV. The data are compared to FONLL and GM-VFNS theoretical calculations	61
4.3	Production p_T differential cross section of D^\pm and $D^{*\pm}$ measured by ATLAS experiment in p+p collisions at $\sqrt{s} = 7$ TeV. The data are compared to NLO QCD calculations of FONLL, POWHEG+PYTHIA, POWHEG+HERWIG, MC@NLO and GM-VFNS	62
4.4	$c\bar{c}$ production cross section inferred from D^0 and D^* production in p+p collisions at $\sqrt{s} = 200$ GeV compared to FONLL calculations (left) and PYTHIA calculations (right)	63
4.5	Ratios of p_T -integrated yields of Λ_c^+ and D^0 hadrons measured by ALICE in p+p collisions at $\sqrt{s} = 13$ TeV. Results from p+p and p+Pb collisions at $\sqrt{s} = 5.02$ TeV are also shown together with the corresponding PYTHIA predictions	63
4.6	The p_T dependence of $D^0 R_{\text{AA}}$ in 0-10 % central Au+Au collisions measured by STAR at $\sqrt{s_{\text{NN}}} = 200$ GeV. The data are compared to measurement of charged pions by STAR at the same collision energy and to ALICE experiment results for D mesons and charged hadrons in Pb+Pb collisions at $\sqrt{s_{\text{NN}}} = 2.76$ TeV	65
4.7	The centrality dependence of $D^0 R_{\text{AA}}$ in Au+Au collisions measured by STAR at $\sqrt{s_{\text{NN}}} = 200$ GeV with the HFT from 2014 and without in from 2010/11	66

4.8	R_{AA} as a function of p_T of D^0 and D^\pm mesons measured by STAR in Au+Au collisions at $\sqrt{s_{NN}} = 200$ GeV in 0-10 %, 10-40 % and 40-80 % centrality classes. Data are compared to ALICE measurement of D^\pm mesons in Pb+Pb collisions at $\sqrt{s_{NN}} = 5.02$ TeV	68
4.9	(a) v_2 as a function of p_T and (b) v_2/n_q as a function of $(m_T - m_0/n_q)$ where n_q is the number of constituent quarks for D^0 in the 10-40 % centrality class in Au+Au collisions and comparison with K_S^0 , Λ and Ξ^- measured by STAR	69
4.10	Λ_c/D^0 ratio as a function of p_T at midrapidity for Au+Au collisions at $\sqrt{s_{NN}} = 200$ GeV in 10-80 % centrality compared to light quarks (top) and theoretical calculations (bottom)	70
4.11	Directed flow of D^0 and $\overline{D^0}$ mesons as a function of rapidity y in 10-80 % central Au+Au collisions at $\sqrt{s_{NN}} = 200$ GeV measured by STAR. Panel (a) shows the average of D^0 and $\overline{D^0}$ v_1 and panel (b) shows the difference between v_1 of D^0 and $\overline{D^0}$. The data are compared to multiple theoretical calculations and to the measurement of charged kaons	71
4.12	R_{AA} of averaged D mesons (D^0 , D^+ and D^{*+}) measured by ALICE and D^0 mesons measured by CMS in 0-10 % Pb+Pb collisions at $\sqrt{s_{NN}} = 5.02$ TeV. ALICE results from Pb+Pb collisions at $\sqrt{s_{NN}} = 2.76$ TeV are also shown. The data are compared to Djordjevic model predictions	72
4.13	Average R_{AA} of prompt D mesons (D^0 , D^+ and D^{*+}) mesons in the 0 – 10 % (left), 30–50 % (middle) and 60–80 % (right) centrality classes measured by ALICE at $\sqrt{s_{NN}} = 5.02$ TeV compared to the R_{AA} of charged particles in the same centrality classes. The ratios of the R_{AA} are shown in the bottom panels	73
4.14	Average R_{AA} of prompt D mesons (D^0 , D^+ and D^{*+}) mesons in the 0–10 % (left) and their average elliptic flow v_2 in the 30-50 % centrality class (right) measured by ALICE at $\sqrt{s_{NN}} = 5.02$ TeV	74
4.15	Λ_c^+/D^0 ratio as a function of p_T measured by ALICE in the 0–80 % central Pb+Pb collisions at $\sqrt{s_{NN}} = 5.02$ TeV compared to p+Pb collisions at $\sqrt{s_{NN}} = 5.02$ TeV and p+p collisions at $\sqrt{s_{NN}} = 7$ TeV (left). The right panel shows comparison to various model predictions	75
5.1	Cartoon of decay of the charm quark c and subsequently D^0	78

5.2	Number of events that passed individual event selection criteria . . .	79
5.3	Difference of measured and theoretical value of $1/\beta$ of kaon candidates as a function of momentum p . The blue lines represent the cuts for which the following results are shown and the black lines represents simple rectangular cuts used in the first iteration	81
5.4	Points represent sigmas of gaussian fits of the slices in Fig 5.3 and are fitted by a power law function (5.1)	82
5.5	Points represent means of gaussian fits of the slices in Fig 5.3 and are fitted by a power law function (5.1)	82
5.6	Difference of measured and theoretical value of $1/\beta$ of pion candidates as a function of momentum p . The blue lines represent the cuts for which the following results are shown and the black lines represents simple rectangular cuts used in the first iteration	83
5.7	Invariant mass distribution of opposite charge kaon and pion pairs ($K\pi$) with the combinatorial background estimated by like-sign method and the difference of unlike-sign and like-sign distributions for all p_T bins in the p+Au collisions at $\sqrt{s_{NN}} = 200$ GeV	85
5.8	Invariant mass distribution of opposite charge kaon and pion pairs ($K\pi$) with the combinatorial background estimated by like-sign method and the difference of unlike-sign and like-sign distributions for $1 < p_T < 2$ GeV/ c bin in the p+Au collisions at $\sqrt{s_{NN}} = 200$ GeV	86
5.9	Invariant mass distribution of opposite charge kaon and pion pairs ($K\pi$) with the combinatorial background estimated by like-sign method and the difference of unlike-sign and like-sign distributions for $2 < p_T < 3$ GeV/ c bin in the p+Au collisions at $\sqrt{s_{NN}} = 200$ GeV	86
5.10	Invariant mass distribution of opposite charge kaon and pion pairs ($K\pi$) with the combinatorial background estimated by like-sign method and the difference of unlike-sign and like-sign distributions for $3 < p_T < 4$ GeV/ c bin in the p+Au collisions at $\sqrt{s_{NN}} = 200$ GeV	87
5.11	Invariant mass distribution of opposite charge kaon and pion pairs ($K\pi$) with the combinatorial background estimated by like-sign method and the difference of unlike-sign and like-sign distributions for $p_T > 4$ GeV/ c bin in the p+Au collisions at $\sqrt{s_{NN}} = 200$ GeV	87

- 5.12 Invariant mass distribution of opposite charge kaon and pion pairs ($K\pi$) with the combinatorial background estimated by like-sign method and the difference of unlike-sign and like-sign distributions (multiplied by 10 for visibility) for all p_T bins in the window around expected D^0 peak in the p+Au collisions at $\sqrt{s_{NN}} = 200$ GeV 88
- 5.13 Invariant mass distribution of opposite charge kaon and pion pairs ($K\pi$) with the combinatorial background estimated by like-sign method and the difference of unlike-sign and like-sign distributions (multiplied by 10 for visibility) for $1 < p_T < 2$ GeV/ c bin in the window around expected D^0 peak in the p+Au collisions at $\sqrt{s_{NN}} = 200$ GeV 88
- 5.14 Opposite charge kaon and pion pairs with the combinatorial background estimated by like-sign method and the difference of unlike-sign and like-sign distributions (multiplied by 10 for visibility) for $2 < p_T < 3$ GeV/ c bin in the window around expected D^0 peak in the p+Au collisions at $\sqrt{s_{NN}} = 200$ GeV 89
- 5.15 Invariant mass distribution of opposite charge kaon and pion pairs ($K\pi$) with the combinatorial background estimated by like-sign method and the difference of unlike-sign and like-sign distributions (multiplied by 10 for visibility) for $3 < p_T < 4$ GeV/ c bin in the window around expected D^0 peak in the p+Au collisions at $\sqrt{s_{NN}} = 200$ GeV 89
- 5.16 Invariant mass distribution of opposite charge kaon and pion pairs ($K\pi$) with the combinatorial background estimated by like-sign method and the difference of unlike-sign and like-sign distributions (multiplied by 5 for visibility) for $p_T > 4$ GeV/ c bin in the window around expected D^0 peak in the p+Au collisions at $\sqrt{s_{NN}} = 200$ GeV 90
- 5.17 Third order polynomial fit of the unlike-sign pairs in the shown area 91
- 5.18 Unlike-sign spectrum ($k\pi$ pairs) of the invariant mass with subtracted polynomial fit of the background obtained from the side-band method for all p_T bins in the p+Au collisions at $\sqrt{s_{NN}} = 200$ GeV 91
- 5.19 Upper panel: Invariant mass spectrum of $K\pi$ pairs with background reconstructed by Like-Sign and Rotated Momentum techniques for $1 < p_T < 2$ GeV/ c . Lower panel: Invariant mass spectrum after subtraction of background for both methods 92
- 5.20 Distribution of $\cos(\theta^*)$ in the CMS frame of $K\pi$ pair in the p+Au collisions at $\sqrt{s_{NN}} = 200$ GeV. The red line represents the used cut 93

5.21	The $M_{K^\mp\pi^\pm\pi^\pm} - M_{K^\mp\pi^\pm}$ spectrum with combinatorial background estimated by wrong-sign method and the subtracted wrong-sign background and correct-sign signal for all D^* candidate p_T bins in the p+Au collisions at $\sqrt{s_{NN}} = 200$ GeV	94
5.22	The $M_{K^\mp\pi^\pm\pi^\pm} - M_{K^\mp\pi^\pm}$ spectrum with combinatorial background estimated by wrong-sign method and the subtracted wrong-sign background and correct-sign signal for D^* candidate $2 < p_T < 3$ GeV/ c bin in the p+Au collisions at $\sqrt{s_{NN}} = 200$ GeV	95
5.23	The $M_{K^\mp\pi^\pm\pi^\pm} - M_{K^\mp\pi^\pm}$ spectrum with combinatorial background estimated by wrong-sign method and the subtracted wrong-sign background and correct-sign signal for D^* candidate $3 < p_T < 4$ GeV/ c bin in the p+Au collisions at $\sqrt{s_{NN}} = 200$ GeV	95
5.24	The $M_{K^\mp\pi^\pm\pi^\pm} - M_{K^\mp\pi^\pm}$ spectrum with combinatorial background estimated by wrong-sign method and the subtracted wrong-sign background and correct-sign signal for D^* candidate $p_T > 4$ GeV/ c bin in the p+Au collisions at $\sqrt{s_{NN}} = 200$ GeV	96
5.25	Upper panel: $M_{K^\mp\pi^\pm\pi^\pm} - M_{K^\mp\pi^\pm}$ spectrum with background reconstructed by Side-band and Wrong-sign techniques. Lower panel: $M_{K^\mp\pi^\pm\pi^\pm} - M_{K^\mp\pi^\pm}$ spectrum after subtraction of Wrong-sign background and the gaussian fit	97
5.26	Number of events that passed individual event selection criteria	99
5.27	Points represent sigmas of gaussian fits of the slices of $\Delta 1/\beta$ distribution and are fitted by a power law function (5.1)	100
5.28	Points represent means of gaussian fits of the slices of $\Delta 1/\beta$ distribution and are fitted by a power law function (5.1)	100
5.29	Invariant mass distribution of opposite charge kaon and pion pairs ($K\pi$) with the combinatorial background estimated by like-sign method and the difference of unlike-sign and like-sign distributions for all p_T bins in the p+p collisions at $\sqrt{s} = 510$ GeV	102
5.30	Invariant mass distribution of opposite charge kaon and pion pairs ($K\pi$) with the combinatorial background estimated by like-sign method and the difference of unlike-sign and like-sign distributions for $1 < p_T < 2$ GeV/ c bin in the p+p collisions at $\sqrt{s} = 510$ GeV	103

-
- 5.31 Invariant mass distribution of opposite charge kaon and pion pairs ($K\pi$) with the combinatorial background estimated by like-sign method and the difference of unlike-sign and like-sign distributions for $2 < p_T < 3$ GeV/ c bin in the p+p collisions at $\sqrt{s} = 510$ GeV 103
- 5.32 Invariant mass distribution of opposite charge kaon and pion pairs ($K\pi$) with the combinatorial background estimated by like-sign method and the difference of unlike-sign and like-sign distributions for $3 < p_T < 4$ GeV/ c bin in the p+p collisions at $\sqrt{s} = 510$ GeV 104
- 5.33 Invariant mass distribution of opposite charge kaon and pion pairs ($K\pi$) with the combinatorial background estimated by like-sign method and the difference of unlike-sign and like-sign distributions for $p_T > 4$ GeV/ c bin in the p+p collisions at $\sqrt{s} = 510$ GeV 104
- 5.34 Invariant mass distribution of opposite charge kaon and pion pairs ($K\pi$) with the combinatorial background estimated by like-sign method and the difference of unlike-sign and like-sign distributions (multiplied by 10 for visibility) for all p_T bins in the window around expected D^0 peak in the p+p collisions at $\sqrt{s} = 510$ GeV 105
- 5.35 Invariant mass distribution of opposite charge kaon and pion pairs ($K\pi$) with the combinatorial background estimated by like-sign method and the difference of unlike-sign and like-sign distributions (multiplied by 10 for visibility) for $1 < p_T < 2$ GeV/ c bin in the window around expected D^0 peak in the p+p collisions at $\sqrt{s} = 510$ GeV 105
- 5.36 Invariant mass distribution of opposite charge kaon and pion pairs ($K\pi$) with the combinatorial background estimated by like-sign method and the difference of unlike-sign and like-sign distributions (multiplied by 10 for visibility) for $2 < p_T < 3$ GeV/ c bin in the window around expected D^0 peak in the p+p collisions at $\sqrt{s} = 510$ GeV 106
- 5.37 Invariant mass distribution of opposite charge kaon and pion pairs ($K\pi$) with the combinatorial background estimated by like-sign method and the difference of unlike-sign and like-sign distributions (multiplied by 10 for visibility) for $3 < p_T < 4$ GeV/ c bin in the window around expected D^0 peak in the p+p collisions at $\sqrt{s} = 510$ GeV 106

5.38	Invariant mass distribution of opposite charge kaon and pion pairs ($K\pi$) with the combinatorial background estimated by like-sign method and the difference of unlike-sign and like-sign distributions (multiplied by 5 for visibility) for $p_T > 4$ GeV/ c bin in the window around expected D^0 peak in the p+p collisions at $\sqrt{s} = 510$ GeV	107
5.39	Third order polynomial fit of the unlike-sign pairs in the shown area .	108
5.40	Unlike-sign spectrum ($k\pi$ pairs) of the invariant mass with subtracted polynomial fit of the background obtained from the side-band method for all p_T bins in the p+p collisions at $\sqrt{s} = 510$ GeV	108
5.41	Comparison of like-sign background (red triangles), event-mixing background (green line) and unlike-sign (blue triangles) distributions for all p_T bins in the p+p collisions at $\sqrt{s} = 510$ GeV	109
5.42	Comparison of like-sign background (red triangles), event-mixing background (green line) and unlike-sign (blue triangles) distributions for all p_T bins in the p+p collisions at $\sqrt{s} = 510$ GeV	109
5.43	Unlike-sign (signal) distribution (blue triangles) and scaled background estimated by event mixing method (red triangles) and its subtraction scaled by 10 (black diamonds) for all p_T bins in the p+p collisions at $\sqrt{s} = 510$ GeV	110
5.44	Unlike-sign (signal) distribution (blue triangles) and scaled background estimated by event mixing method (red triangles) and its subtraction scaled by 10 (black diamonds) for $1 < p_T < 2$ bin in the p+p collisions at $\sqrt{s} = 510$ GeV	111
5.45	Unlike-sign (signal) distribution (blue triangles) and scaled background estimated by event mixing method (red triangles) and its subtraction scaled by 10 (black diamonds) for $2 < p_T < 3$ bin in the p+p collisions at $\sqrt{s} = 510$ GeV	111
5.46	Unlike-sign (signal) distribution (blue triangles) and scaled background estimated by event mixing method (red triangles) and its subtraction scaled by 10 (black diamonds) for $3 < p_T < 4$ bin in the p+p collisions at $\sqrt{s} = 510$ GeV	112
5.47	Unlike-sign (signal) distribution (blue triangles) and scaled background estimated by event mixing method (red triangles) and its subtraction scaled by 10 (black diamonds) for $p_T > 4$ bin in the p+p collisions at $\sqrt{s} = 510$ GeV	112

-
- 5.48 The $M_{K^{\mp}\pi^{\pm}\pi^{\pm}} - M_{K^{\mp}\pi^{\pm}}$ spectrum with combinatorial background estimated by wrong-sign method and the subtracted wrong-sign background and correct-sign signal for all D^* candidate p_T bins in the p+p collisions at $\sqrt{s} = 510$ GeV 113
- 5.49 The $M_{K^{\mp}\pi^{\pm}\pi^{\pm}} - M_{K^{\mp}\pi^{\pm}}$ spectrum with combinatorial background estimated by wrong-sign method and the subtracted wrong-sign background and correct-sign signal for D^* candidate $2 < p_T < 3$ GeV/ c bin in the p+p collisions at $\sqrt{s} = 510$ GeV 113
- 5.50 The $M_{K^{\mp}\pi^{\pm}\pi^{\pm}} - M_{K^{\mp}\pi^{\pm}}$ spectrum with combinatorial background estimated by wrong-sign method and the subtracted wrong-sign background and correct-sign signal for D^* candidate $3 < p_T < 4$ GeV/ c bin in the p+p collisions at $\sqrt{s} = 510$ GeV 114
- 5.51 The $M_{K^{\mp}\pi^{\pm}\pi^{\pm}} - M_{K^{\mp}\pi^{\pm}}$ spectrum with combinatorial background estimated by wrong-sign method and the subtracted wrong-sign background and correct-sign signal for D^* candidate $p_T > 4$ GeV/ c bin in the p+p collisions at $\sqrt{s} = 510$ GeV 114
- 5.52 The $M_{K^{\mp}\pi^{\pm}\pi^{\pm}} - M_{K^{\mp}\pi^{\pm}}$ spectrum with combinatorial background estimated by wrong-sign method and the subtracted wrong-sign background and correct-sign signal for all D^* candidate p_T bins in the p+p collisions at $\sqrt{s} = 510$ GeV 115
- 5.53 The $M_{K^{\mp}\pi^{\pm}\pi^{\pm}} - M_{K^{\mp}\pi^{\pm}}$ spectrum with combinatorial background estimated by wrong-sign method and the subtracted wrong-sign background and correct-sign signal for D^* candidate $2 < p_T < 3$ GeV/ c bin in the p+p collisions at $\sqrt{s} = 510$ GeV 116
- 5.54 The $M_{K^{\mp}\pi^{\pm}\pi^{\pm}} - M_{K^{\mp}\pi^{\pm}}$ spectrum with combinatorial background estimated by wrong-sign method and the subtracted wrong-sign background and correct-sign signal for D^* candidate $3 < p_T < 4$ GeV/ c bin in the p+p collisions at $\sqrt{s} = 510$ GeV 116
- 5.55 The $M_{K^{\mp}\pi^{\pm}\pi^{\pm}} - M_{K^{\mp}\pi^{\pm}}$ spectrum with combinatorial background estimated by wrong-sign method and the subtracted wrong-sign background and correct-sign signal for D^* candidate $p_T > 4$ GeV/ c bin in the p+p collisions at $\sqrt{s} = 510$ GeV 117

Introduction

Since the times of ancient civilizations, philosophers and scientists were trying to understand the basic principles of the Universe around us. The understanding of physics of the elementary forces and particles made huge leap in the previous century. One of the tools which we use today to study the smallest elements of the matter around us are collisions of particles done at the large particle colliders such as Relativistic Heavy-Ion Collider (RHIC) located at Brookhaven National Laboratory (BNL) and the Large Hadron Collider (LHC) at the European Organization for Nuclear Research (CERN from French *Conseil Européen pour la Recherche Nucléaire*). These facilities can reach the center of mass energies of hundreds GeV or even TeV per nucleon-nucleon collision. Colliders are used to study large variety of properties - from the inner structure of the proton up to the hot and dense state of matter called Quark-Gluon Plasma (QGP) which was present in the universe shortly after the Big Bang [1].

Hundreds of new particles can be created in the heavy-ion collisions. However heavy particles containing the charm (or c) quark serve as a perfect probe of the properties of the collisions. At RHIC energies charm quarks can only be created in the early stages of a collision also called hard partonic scattering and thus are created before the hot QGP is formed. Particles containing charm quarks are heavy and short-lived and so their reconstruction is a challenging task. For this reason, very precise devices have to be built to reach maximal understanding of the collisions. One of these devices is the Solenoidal Tracker At RHIC (STAR).

The first chapter serves as an introduction to various basic concepts used in the particle physics and variables used to describe the particle collisions.

The Solenoidal Tracker at RHIC is introduced in the second chapter with its subdetectors. Future project which is about to be built in the Brookhaven National Laboratory called Electron-Ion Collider (EIC) is also introduced.

The third chapter provides a short overview of so called Cold Nuclear Matter (CNM) effects which are effects playing role in the collisions and are caused by a

bare presence of the nucleus in the collision. For this reason the asymmetric collisions (such as p+Au, p+Pb or d+Au) are studied.

The next chapter summarizes various results from the measurement of charm hadrons at different experiments (mainly STAR and ALICE) and in different collision systems and collision energies.

The last chapter provides an analysis of D^0 and D^* mesons in p+Au collisions measured by STAR detector at $\sqrt{s_{NN}} = 200$ GeV in 2015 and in p+p collisions measured by STAR detector at $\sqrt{s} = 510$ GeV in 2017. Analysis of both datasets follow the analysis of d+Au collisions done [2] and p+p collisions [3]. The goal of the analysis in both datasets is to estimate p_T D^0 yield.

Chapter 1

Physics Introduction

1.1 History of Particle Physics

The desire to understand the fundamental laws of the matter and world around us dates as far as the ancient civilizations such as Babylonia, India or Greece. In the latter one, a philosopher named Democritus came with the idea that there has to exist a fundamental component of matter which he named atom from Greek word *Atomos* which means indivisible.

The idea of atom became largely accepted in the nineteenth century as a result of chemistry experiments and discoveries such as Brownian motion in 1827. However atom did not live up to its name when J. J. Thomson conducted series of experiments with cathode rays and concluded that atoms are further divisible and discovered a negatively charged particle which got name electron in 1897 [4].

Another groundbreaking discovery was made by Ernest Rutherford in 1911 in his scattering experiments of helium nuclei on a gold foil [5]. He realized that a positive charge is gathered in the centre of atom and this positive charge has a small radius compared to the radius of whole atom. His results led to a discovery of a positive nucleus of atoms and realization that nucleus consist of positive particles which were named protons. In the following years multiple models of atom, general relativity and quantum mechanics were introduced. However the model of atom was still missing an important piece called neutron which was discovered in 1932 by James Chadwick [6].

The three aforementioned particles were considered as elementary for another three decades. During that time were discovered muons, neutrinos or pions followed by many others. This was possible thanks to the discovery of a bubble chamber and the development of particle accelerators. As more and more particles were being

discovered, theoretical physicists realized that all these new particles cannot be elementary and have to consist of something else.

1.2 The Standard Model

In 1964 Murray Gell-Mann and George Zweig independently of each other proposed the idea of quarks (back then also called aces). It was not clear whether quarks are real particles or just a theoretical concept. This led to the experimental hunt for quarks. In 1968 were experimentally confirmed quarks u (up), d (down) and s (strange) in deep inelastic experiments [7], [8]. In 1974 c (charm) quark was discovered on the Alternating-Gradient Synchrotron (AGS) at BNL [9] and experiment SPEAR at Stanford Linear Accelerator Center (SLAC) at Stanford Linear Accelerator Laboratory [10]. In 1976 directors of both experiments received the Nobel prize for physics [11], for the discovery. Quark b (bottom, beauty) was measured in 1977 at the E288 experiment on the Bevalac accelerator at Fermilab when the Υ was discovered [12] and the last one of the quark family t (top, truth) was also discovered at Fermilab at D0 experiment in 1995 [13].

Soon after the discovery of the first quarks, physicist started to wonder why there were not observed any free quarks or gluons. This led to development of theoretical description of hadronic matter and its conditions, i. e. when the quarks are confined in hadrons and under which conditions the quarks can deconfine and become free. These calculations further formed the theory describing the strong interaction which is called Quantum Chromodynamics (QCD).

In recent days the complex theory describing elementary particles and their interactions through electromagnetic, weak and strong force is called The Standard Model. Particles are sorted into two groups depending whether they follow the Pauli exclusion principle or not.

Half-integer spin particles are known as fermions and follow the Pauli exclusion principle. Fermions are classified by their interaction. Those interacting weakly and if charged, electromagnetically, but not strongly are leptons (electron, muon, tauon, their according neutrinos and antiparticles). Electrons were known from its discovery by J. J. Thomson in 1897. Muons were discovered in cosmic ray showers in 1936 by C. D. Anderson [14] and the same person previously discovered electron's antiparticle positron in 1932 [15]. Neutrinos were predicted in the early '30s by Wolfgang Pauli and then by Enrico Fermi in a theory of beta-decay and experimentally observed in 1956 [16]. Last member of the lepton family tauon was discovered in the '70s at SLAC [17]. Fermions interacting strongly (apart from weak and electromagnetic

interaction) are quarks which are similarly as leptons divided into three generations and carry color charge (R - red, G - green, B - blue) and also non-integer electric charge (u, c and $t +2/3$; $d, s, b -1/3$).

Integer spin particles are called bosons. They mediate the interactions and are force carriers. The massless and chargeless mediator of electromagnetic interaction is called photon γ and is described by Quantum Electrodynamics (QED). In 1968 Sheldon Lee Glashow, Steven Weinberg and Mohammad Abdus Salam predicted that intermediate vector bosons W^+ , W^- and Z^0 are responsible for the weak interaction. These bosons were observed at UA1 and UA2 experiments at SPS¹ collider at CERN in 1983 (W^+ , W^- [18], [19] and Z^0 [20],[21]). Together with quarks, the gluons were predicted as mediators of the strong force. There are eight types of gauge gluons. They were experimentally discovered at PETRA accelerator at DESY² in 1976 [22]. The last discovered elementary particle was the Higgs boson at experiments ATLAS³ [23] and CMS⁴ [24] at CERN in 2012. Peter Higgs, François Englert and Robert Brout (together with their teams) predicted the existence of the Higgs boson in 1964 [25], [26], [27] but had to wait almost 50 years for the confirmation of his theory. Peter Higgs and François Englert received Nobel Prize for physics in 2013 "for the theoretical discovery of a mechanism that contributes to our understanding of the origin of mass of subatomic particles, and which recently was confirmed through the discovery of the predicted fundamental particle, by the ATLAS and CMS experiments at CERN's Large Hadron Collider" [11].

The summary of all the aforementioned particles can be seen in Fig. 1.1. The values shown in Figure are not fully up to date as the figure is from 2018. This can be shown on an example of neutrinos. In 2022 the KATRIN Collaboration measured new maximal limit of neutrino mass to $m_\nu < 0.8 \text{ eV}/c^2$ [28]. The current values of particle masses can be found in [29].

Even though the Standard model manages to describe large variety of properties and phenomenons, it has its limitations. First of those is the neutrino mass. Standard model predicts that neutrinos are massless which was disproved at the Super-KAMIOKANDE⁵ experiment in Japan [30] and for this discovery was awarded Nobel Prize for physics in 2015 [11]. Another challenge that the Standard model faces is gravity. Theoretical calculations managed to incorporate only three elementary interactions into the Standard model theory (strong, weak and electromagnetic). Nevertheless currently gravity is not included in the Standard model. The theory also

¹Super Proton-antiproton Synchrotron

²German Electron Synchrotron from German *Deutsches Elektronen-Synchrotron*

³A Toroidal LHC ApparatuS (LHC)

⁴The Compact Muon Solenoid (LHC)

⁵Super-Kamioka Neutrino Detection Experiment

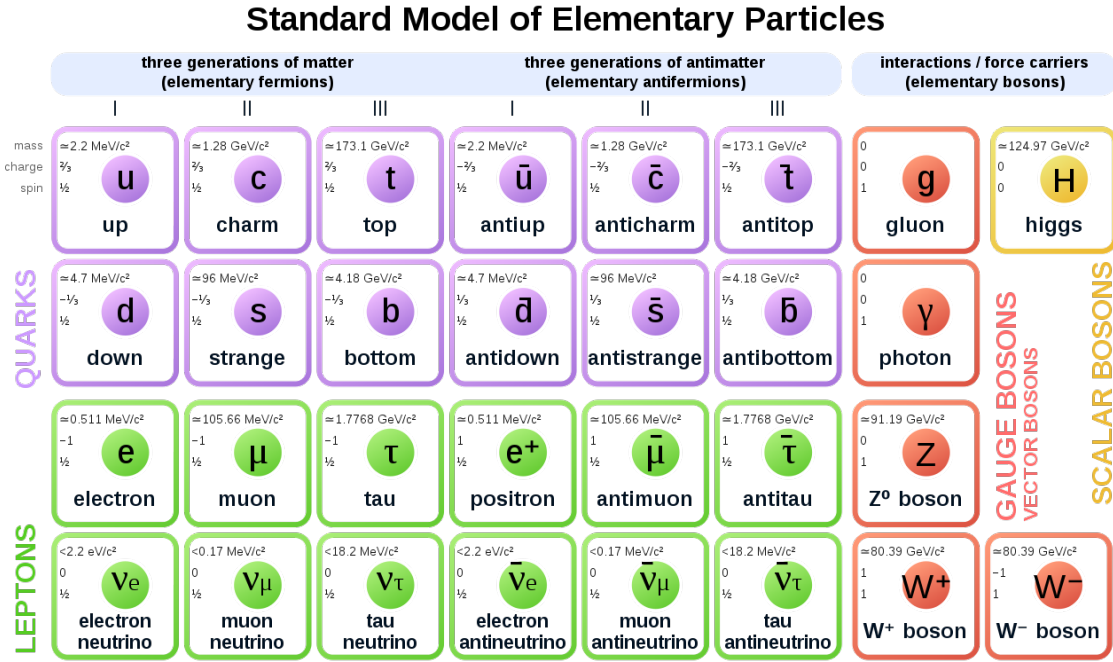


Figure 1.1: Summary of elementary particles. Values are from 2018 and are not up to date. Taken from Ref. [31].

fails to describe the disproportion between matter and antimatter in the Universe. Current assumption is that the conditions in the early Universe should produce matter and antimatter in the same amounts however that is not what is observed. The Standard model also is not able to describe so called Dark Matter and Dark Energy. Our classical matter mass takes up only five percent of the Universe and the rest should be Dark Matter and Dark Energy.

1.3 Quantum Chromodynamics

The strong interaction of particles with color charge is described by a gauge theory called Quantum Chromodynamics. Gluons in this theory work similarly as photons in Quantum Electrodynamics with the difference that gluons carry color charge and thus can interact among themselves. This property has two implications. Colored system is very strongly coupled at low energy densities and low temperatures (equivalent to large distances \sim above tens of fermis) which is called confinement (this is equivalent to hadronic matter at low temperatures) and weakly coupled at high energy densities and high temperatures (equivalent to short distances) and this property is called asymptotic freedom (equivalent to high temperatures such as those in the Quark-Gluon Plasma).

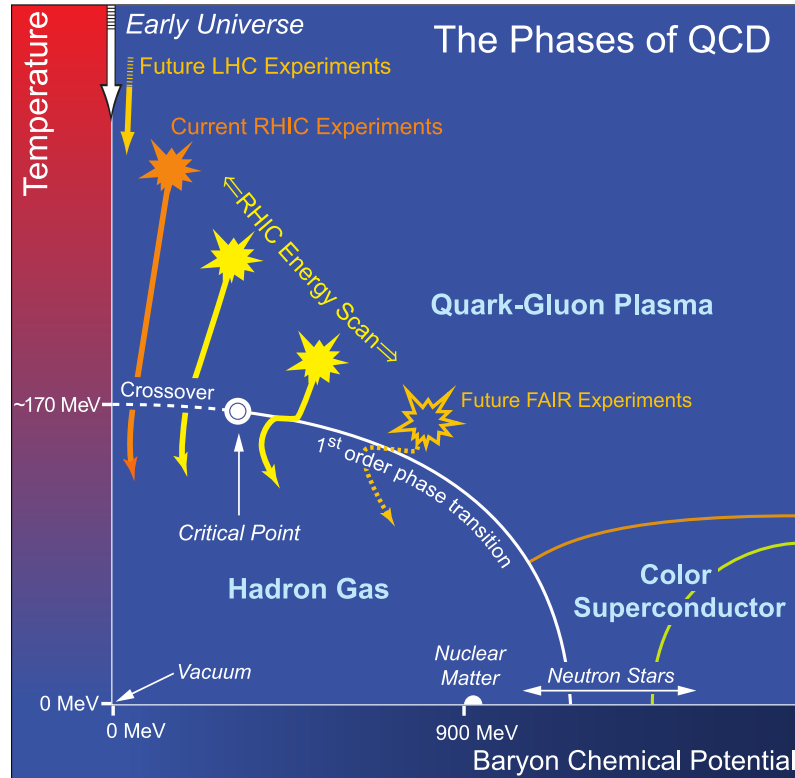


Figure 1.2: An illustration of QCD phase diagram. Taken from Ref. [32].

1.3.1 QCD Phase Diagram

Similarly as for example for the water a phase diagram can be drawn for the QCD matter. Its completion is goal of multiple experiments including STAR at RHIC and program Beam Energy Scan II. Example of a QCD phase diagram can be seen in Fig. 1.2. It is drawn in terms of temperature T and baryon chemical potential μ_B . This variable quantifies the difference between the number of baryons and anti-baryons in the system. The situation $\mu_B = 0$ is equivalent to the same number of baryons and anti-baryons present in the system which is approximately the situation observed in heavy-ion collisions at the LHC and RHIC.

At low μ_B and T the quarks and gluons are bound inside hadrons and this phase is called hadronic gas. With rising temperature the system undergoes the transition into QGP. For low μ_B a crossover phase transition is expected (dashed line in Fig. 1.2) and this is consistent with the data measured both at RHIC and LHC. At higher μ_B the calculations predict first order phase transition. The point where the first order transition switches into cross-over transition is called critical point. The first calculations and estimations were made in the 70's after the first phase diagram were suggested. Those calculations lead to estimate the critical point to critical temperature of $T_c \sim 170$ MeV [1] and that the transition is not likely of

the first order or second order. Its exact location is not known and finding it is one of the goals of current high energy physics.

At the low temperature and high baryon chemical potential is the area of properties of neutron stars. At even higher μ_B is expected exotic phase called color superconductor which is expected to have analogous properties as classical superconductors.

Program Beam Energy Scan I at RHIC made several improvements in our understanding of properties of the QCD phase diagram. Currently second program called BES II is in progress which aims to find the critical point or point of chiral symmetry restoration [33].

1.3.2 Quark-Gluon Plasma

Only fraction of a second ($\sim 10^{-6}$) [34] after the Big Bang quarks and gluons weren't bound in hadrons as they are today. They were in a hot and dense state of matter which is called Quark-Gluon Plasma (QGP). As far as we know, QGP is not present anywhere in the present Universe except maybe for the centres of neutron stars and brief moments during collisions of heavy ions at the particle colliders where is achieved sufficient temperature (~ 150 MeV) and energy density (~ 2 GeV/fm³) [35].

In 1975 John Collins and Malcolm Perry came up with the idea that the superdense matter present in the neutron stars, exploding black holes or that was present shortly after the Big Bang is composed of quarks and not of hadrons. In the same year Giorgio Parisi and Nicola Cabibbo identified the limiting Hagedorn temperature of the hadronic mass and sketched the first phase diagram of strongly interacting matter. This strongly interacting matter was named Quark-Gluon Plasma by Edward Shuryak in 1978 from the analogy with classical plasma where ions and electrons are dissociated similarly as quarks and gluons in the QGP.

The first experimental confirmation of QGP was done in 2000 at Super Proton Synchrotron in CERN. This result was later finally confirmed at RHIC.

Creation of the QGP is a consequence of properties of the strong force which is described by a widespread QCD. Quarks possess the strong charge which can be viewed similarly as an electric charge connected with the electromagnetic interaction. But whereas electric charge can be only positive or negative, strong color charge can be red, green or blue and corresponding anti-colors anti-red, anti-green, anti-blue. Each quark carries one color charge and gluons carry a combination of two color charges (one color and one anti-color). A particle that consists of quarks has to have

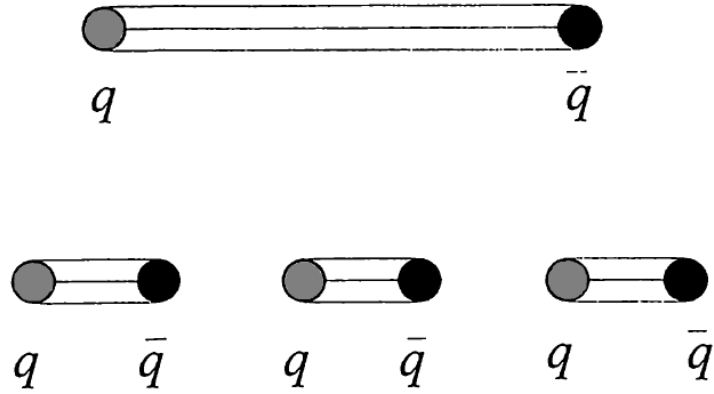


Figure 1.3: Schematic view of a color confinement. Taken from Ref. [36].

neutral color. That means that hadron which consists of three quarks must contain all three colors (antiquarks contain all three anti-colors) and meson consisting of two quarks must contain a color and the respective anti-color. Another difference between electromagnetic and strong force is that the carriers of the force gluons can interact with each other but photons can not.

One of the properties that strong interaction (and consequently quarks) has is so called quark confinement. This can be illustrated on a pair of quark and antiquark. Those are connected with an imaginary string. When the quarks were pulled apart, the string would stretch. At some point the string would break and at each loose end another quark would appear to reduce the tension. Illustration of this effect can be seen in Fig. 1.3. Because of this effect single quarks can not be observed. But in QGP quarks and gluons are instead of pulling apart pushed together and have quasi-free behavior. Color confinement is caused due to the form of the strong interaction coupling constant.

1.3.3 Time Evolution of Heavy-Ion Collisions

During the heavy-ion collision nucleons of both nuclei interact among themselves. If the energy density is large enough new particles and antiparticles can be created out of the vacuum. This early period of the collision is called the hard scattering and all the heavy quarks (c , b) originate in this stage. The system is not in equilibrium during the hard scattering. If the temperature rises above a certain point called the critical temperature T_c quarks and gluons are no longer bound in nucleons and QGP sets in. The medium of the participants is called a fireball. It lasts until the thermal equilibrium is reached and the systems starts to cool down according to the laws of hydrodynamics. This new stage is called hadronization and can be further

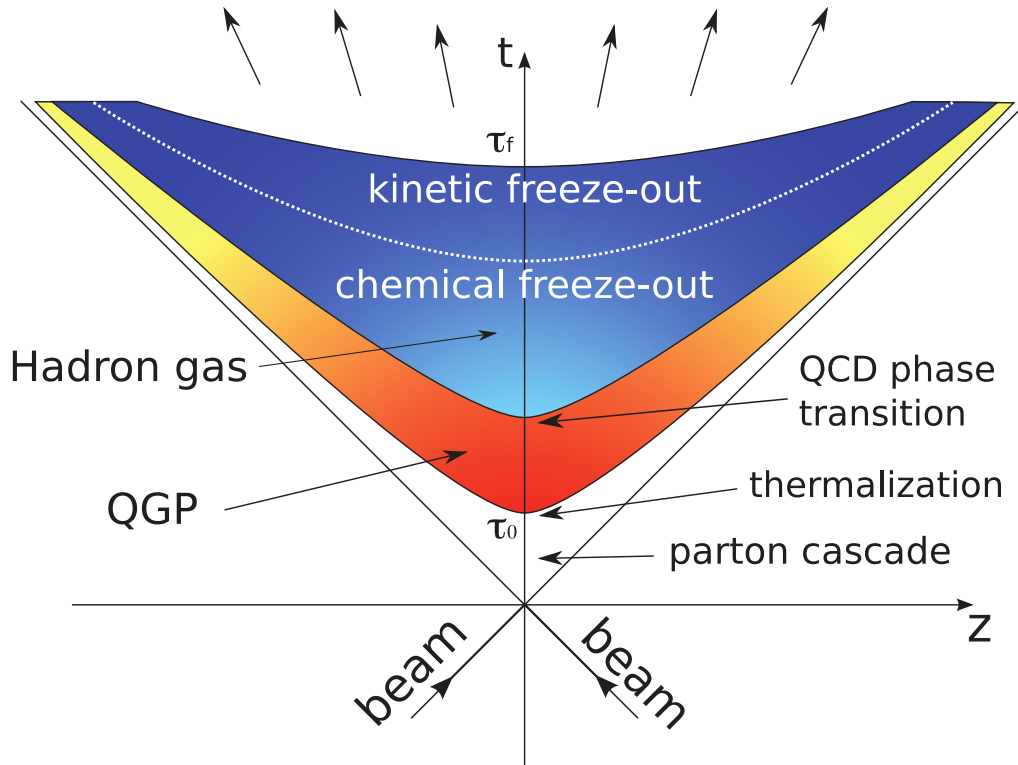


Figure 1.4: Illustration of the time evolution of the Quark-Gluon Plasma, where t -axis represents evolution in time and z -axis represents evolution in one spacial coordinate. Taken from Ref. [37].

split into two stages. During the first new particles can still be created (can interact inelastically) until the threshold is reached and the chemical freeze-out occurs. In the second stage particles can still kinetically interact (elastically) until the threshold for the kinetic freeze-out is reached. The resulting hadronic gas is detected by the detector. Stages of the creation and cooling down of the QGP are illustrated in Fig. 1.4.

1.4 Variables in High Energy Physics

Although collisions of heavy ions is a difficult concept for the understanding, quite simple geometrical descriptions are being used. Assuming rectilinear motion of all the nucleons in the nucleus, nucleons participating in the collision are called participants and those not participating in a collision are called spectators.

Very important variable used for the description of heavy-ion collisions is a **multiplicity**. It describes number of particles produced in a collision.

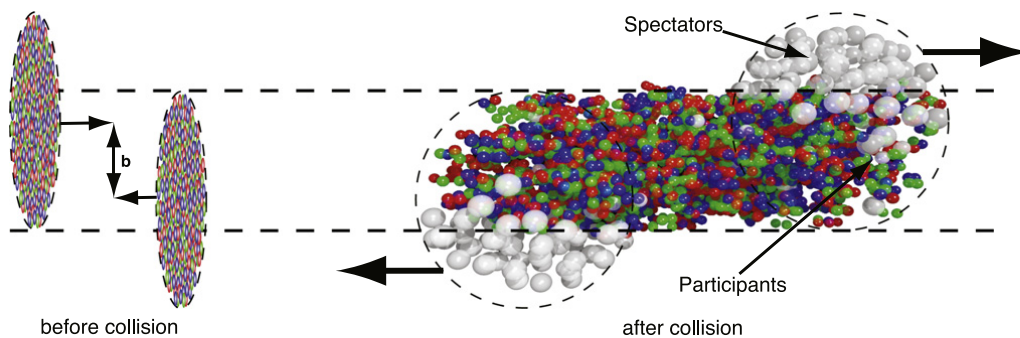


Figure 1.5: Schematic view of a collision of two heavy nuclei before and after the collision. Taken from Ref. [38].

As is shown in Fig. 1.5 the two dimensional vector that connects centres of the colliding nuclei is called impact vector and its length is **impact parameter** b . It can not be measured directly but is closely connected with the number of spectators and participants as the figure shows. To describe a collision, it is necessary to describe the system with a coordinate system. Collider experiments nowadays usually use a laboratory system where point $(0,0,0)$ is the center of the detector, z axis is parallel to the particle beam, x -axis is horizontal and perpendicular to z and y is the vertical axis. So called **reaction plane** is given by the angle from the x -axis.

The impact parameter determines the **centrality** of a collision. Central collisions are collisions where the impact parameter is small. Centrality classes can be defined using the multiplicity. Central collisions are in the area 0-10 %, then follow semi-central collisions and the class with lowest multiplicity (higher than 70 %) are peripheral collisions. Centrality classes are shown in Fig. 1.6.

Another commonly used variable is the **cross-section** σ . It is used to express the probability of a interaction under given conditions. In the quantum mechanics the cross-section is a probability of a transition of one quantum state into another.

For the description of heavy-ion collisions it is also used momentum \mathbf{p} . However classical momentum is not Lorentz-invariant and so is defined the **transverse momentum** p_T . Its size is

$$p_T = \sqrt{p_x^2 + p_y^2}, \quad (1.1)$$

where p_x and p_y are first and second component of the momentum. Transverse momentum is Lorentz-invariant.

In a collision where the speed is almost equal to the speed of light it is useful to use Lorentz invariant variables or Lorentz additive ones. Analogy of the classical velocity is a **rapidity** y defined for the accelerator experiments as

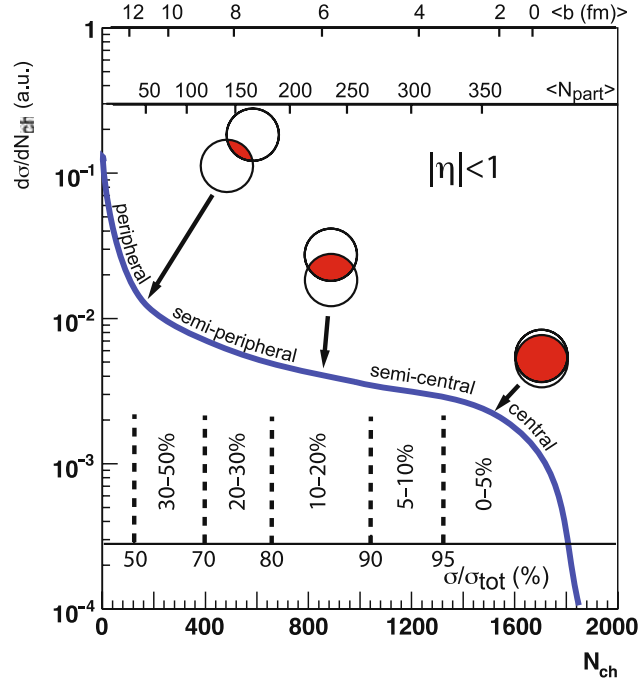


Figure 1.6: A cartoon showing the centrality definition at the LHC energies from the final-state particle multiplicity and its correlation with the impact parameter b and the number of participating nucleons $\langle N_{part} \rangle$ in the collisions. Taken from Ref. [1].

$$y = \frac{1}{2} \ln \left(\frac{E + p_z c}{E - p_z c} \right), \quad (1.2)$$

where E is particle energy, p_z is longitudinal momentum and c is the velocity of light in a vacuum. Rapidity is additive under Lorentz transformation.

Rather than rapidity, it is simpler to measure variable η called **pseudorapidity** which is defined as

$$\eta = - \ln \left[\tan \left(\frac{\theta}{2} \right) \right], \quad (1.3)$$

where θ is the angle of the original direction of the particle and the new direction, also called scattering angle. With high enough energy pseudorapidity converges to rapidity and can be derived from

$$\eta = \frac{1}{2} \ln \left(\frac{|\mathbf{p}| + p_z}{|\mathbf{p}| - p_z} \right). \quad (1.4)$$

By the **collision energy** \sqrt{s} is understood total energy in the center of mass frame. In the case of colliding nuclei, collision energy is usually expressed as a energy per one nucleon-nucleon pair $\sqrt{s_{NN}}$.

To compare particle productions in the collisions of nuclei (AA) and protons (pp), resp. proton+nuclei or deuteron+nuclei (pA, resp. dA), the **nuclear modification factor** R_{AA} is used which is defined as

$$R_{AA} = \frac{1}{\langle N_{\text{bin}} \rangle} \frac{\frac{dN}{dp_T}|_{AA}}{\frac{dN}{dp_T}|_{pp}}, \quad (1.5)$$

where $\langle N_{\text{bin}} \rangle$ is the mean number of individual binary collisions of nucleons calculated from the Glauber model, $\frac{dN}{dp_T}|_{AA}$ and $\frac{dN}{dp_T}|_{pp}$ is a invariant **yield** p_T spectrum of particles of interest in a nucleus+nucleus collision and proton+proton collision, respectively. To compare p+p collisions to asymmetric collisions, the AA yield has to be replaced by pA or dA yield.

In high energy physics natural units system is often used which means that three elementary constants (speed of light c , Planck constant \hbar , Boltzmann constant k_B) are equal to 1.

1.5 Signatures of the QGP

Quark-Gluon Plasma created in heavy-ion collision is studied via several properties. Some of the below mentioned processes were also proves of the bare existence of QGP in the collisions.

1.5.1 Nuclear Modification Factor

Measurement of above mentioned variable R_{AA} is used as a signature of QGP. If heavy-ion collisions were just superposition of binary p+p collisions scaled by the number of binary collision in the heavy-ion event, the nuclear modification factor would be $R_{AA} = 1$. Partons (quarks and gluons) loose energy in the medium and other effects, such as cold nuclear matter effects, shadowing and others also contribute to the modification of the particle yields measured in A+A collisions with respect to the scaled yields measured in p+p collisions.

As can be seen in Fig. 1.7, the nuclear modification factor depends on both collision energy and p_T . Data from RHIC and LHC fall from unity in the whole p_T range which means that particle production is suppressed in central heavy-ion collisions compared to p+p collisions. High transverse momentum hadrons probably originate from hadronization of partons in the hard scattering and their suppression is probably caused by the energy loss in the QGP. The LHC data suggest that for high- p_T particles the medium is more transparent which can be seen in the slow rise of R_{AA} .

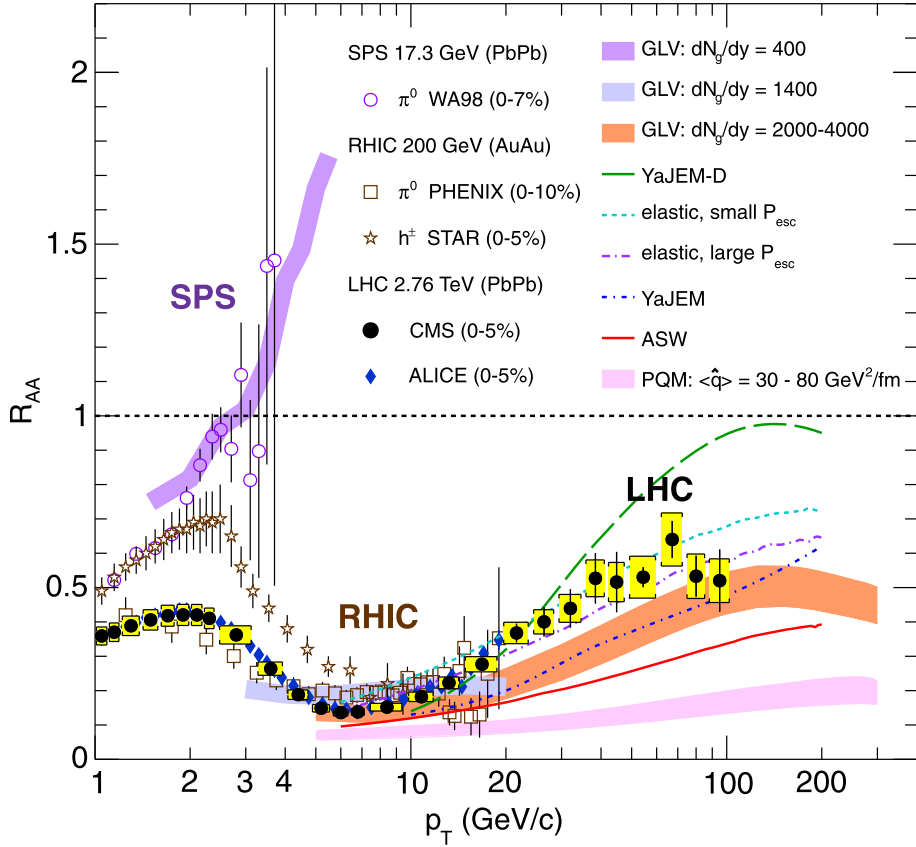


Figure 1.7: Comparison of R_{AA} of various particles measured by various experiments at different collision energies. Shown results are for π^0 from WA98 at SPS [39],[40] and from PHENIX at RHIC [41], charged hadrons measured by STAR at RHIC [42] and charged particles from ALICE [43] and CMS [44] at the LHC. The data are compared to various theoretical models [45]-[50]. Taken from Ref. [44].

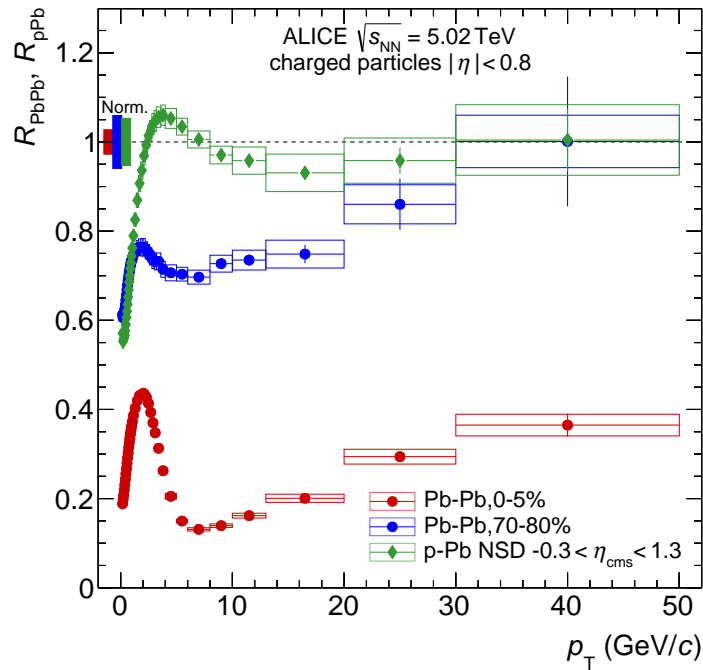


Figure 1.8: Nuclear modification factors measured by ALICE in central (0–5 %) and peripheral (70–80 %) Pb+Pb collisions and in p+Pb collisions at $\sqrt{s_{\text{NN}}} = 5.02$ TeV. Taken from Ref. [51].

Apart from nuclear modification factor R_{AA} , the R_{pA} or R_{dA} are also being measured to separate the effects of the medium and the effects of the nuclear matter.

A measurement done by ALICE⁶ collaboration is shown in Fig. 1.8. The figure shows the R_{pPb} factor compared to R_{AA} measured in the 0-5 % and 70-80 % centrality classes for Pb+Pb collisions at $\sqrt{s_{\text{NN}}} = 5.02$ GeV. The maximum of R_{pPb} is at intermediate p_{T} range $2 < p_{\text{T}} < 6$ GeV/ c and this behavior is known as the Cronin effect. The R_{pPb} is consistent with unity for $p_{\text{T}} > 8$ GeV/ c which demonstrates that the strong suppression observed in the heavy-ion collisions is not related to the initial state effects but rather to the formation of the QGP.

Another way of comparing the effects of the hot medium is to calculate the central-to-peripheral modification factor R_{CP} , which compares yields in two different centrality bins and is scaled by the corresponding mean number of binary collisions. Such measurement done by STAR detector at various collision energies is shown in Fig. 1.9. The R_{CP} was constructed as a function of p_{T} with data from (0–5) % and (60–80) % centralities. The R_{CP} is lowest at the highest collision energy and increases with the energy up to the enhancement at the lowest energies. This enhancement

⁶A Large Ion Collider Experiment (LHC)

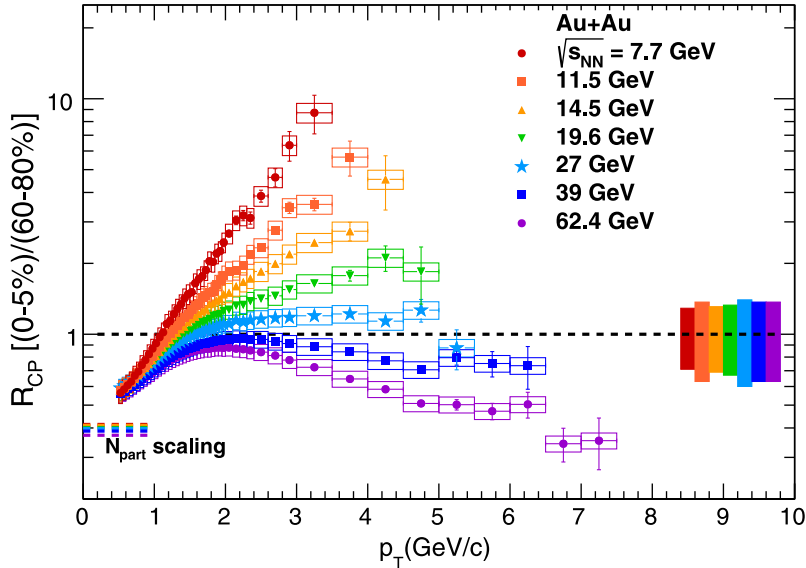


Figure 1.9: R_{CP} of charged hadrons as a function of p_T measured by STAR at various RHIC BES energies. Taken from Ref. [52].

may have contributions from Cronin-type interactions, radial flow or the relative dominance of coalescence versus fragmentation for hadronization. The goal of the Beam Energy Scan was to locate the critical point and identify at which energy the QGP is formed. However the more sensitive observables are required and hopefully will be provided by results from BES II.

1.5.2 Jet Quenching

Jets are collimated sprays of particles that originate from one highly energetic quark or gluon which comes from the hard hard scattering appearing in the early stage of a collision and usually has high transverse momentum.

In p+p collisions the highly energetic partons propagate through vacuum where they radiate gluons and create even more partons.

Momentum and energy conservation laws require that jets are produced as dijets in back to back directions. The case of dijets is the simplest one however there are also processes where three or more jets are created. The most interesting dijets are those created at the borders or close to the borders of the fireball. One of the jets fly away just through the vacuum and is very similar to jets originating from p+p collisions but the second jet has to go through the medium. It interacts in the medium and loses some portion of its energy. This jet is suppressed or may be fully quenched - no jet will be visible in this direction.

Measurement of this phenomena can be seen in Fig. 1.10 where are results

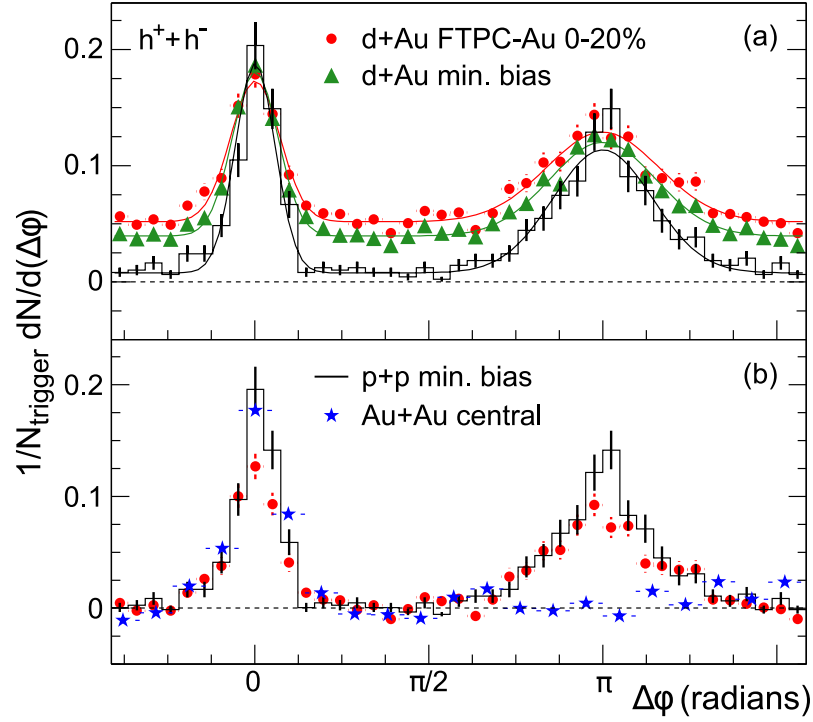


Figure 1.10: Two particle azimuthal distribution of charged hadrons measured in p+p and d+Au collisions and central Au+Au collisions measured by STAR detector. Taken from Ref. [53].

for the measurement of angular correlations of charged hadrons done by STAR collaboration. In the upper panel can be seen a comparison of minimum bias p+p and d+Au collisions and d+Au collisions with centrality 0-20 %. N_{trigger} is number of particles with transverse momenta $4 < p_T < 6$ GeV/c. Particles with such high transverse momentum are typical for jets. The near-side peak corresponds to two particles coming from the same jet. d+Au collisions show same trend as the p+p collisions which is expected because no QGP is present in these types of collisions. In the lower panel is comparison of p+p and central Au+Au collisions and d+Au collisions. All three measurements show same peak in the near-side area ($\Delta\phi = 0$) but in the away-side area ($\Delta\phi = \pi$) Au+Au peak is completely suppressed. This suppression is caused by the interaction (both radiative and collision) in the volume of the QGP. The distribution shows associated particles with $p_T > 2$ GeV/c to a trigger particle with $p_T > 4$ GeV/c. The associated particles in the away-side jet lost energy in the QGP and thus have $p_T < 2$ GeV/c in the Au+Au collisions.

In recent days jets can be studied and reconstructed with many different tools and algorithms. One of such tools is already mentioned nuclear modification factor related to particles within a jet. Example of measurement of jet R_{AA} measured by ATLAS detector in Pb+Pb collisions at $\sqrt{s_{NN}} = 5.02$ TeV [54] can be seen in Fig.

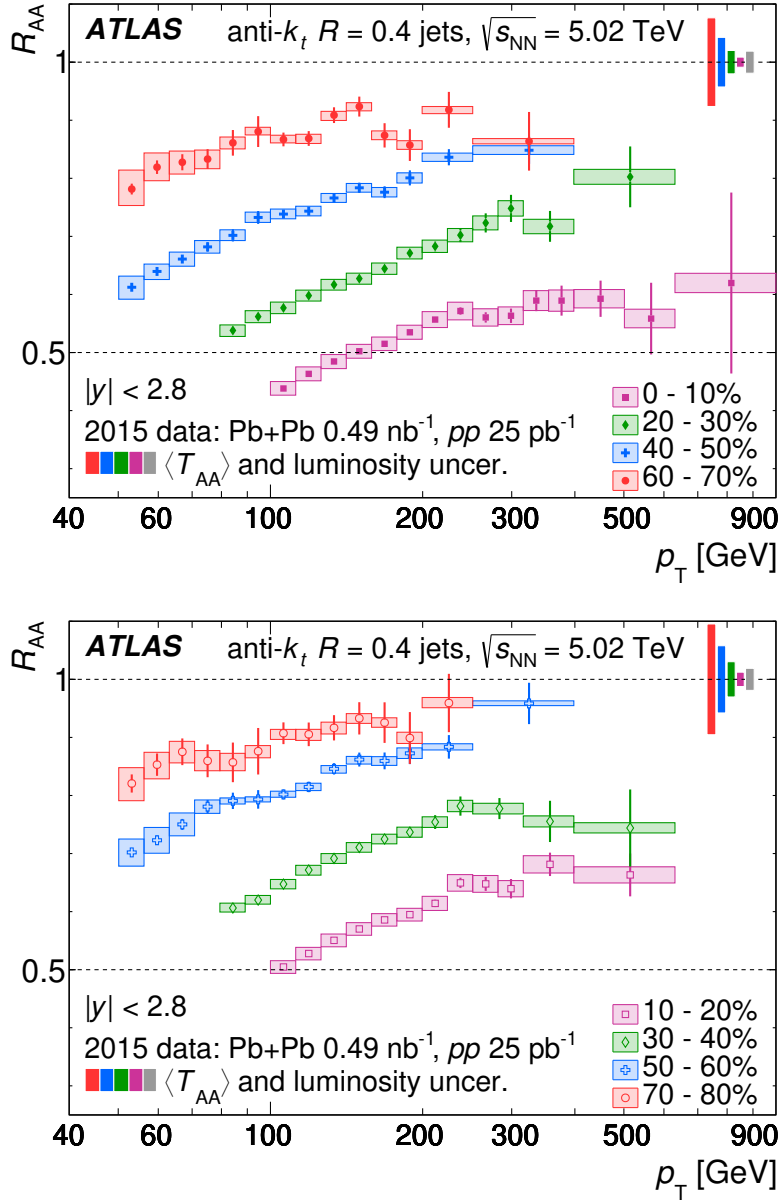


Figure 1.11: Both panels: R_{AA} as a function of p_{T} in different centrality classes for jets with $|y| < 2.8$ measured by ATLAS detector in Pb+Pb collisions at $\sqrt{s_{\text{NN}}} = 5.02$ TeV. Taken from Ref. [54].

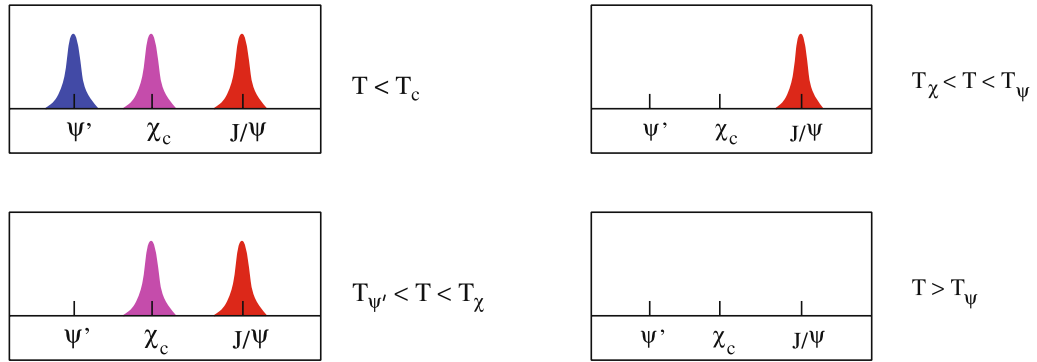


Figure 1.12: Illustration of charm quarkonia used as a thermometer. Taken from Ref. [1].

1.11. The nuclear modification factor is shown as a function of p_T and centrality. A clear suppression of jet production in central Pb+Pb collisions relative to pp collisions is observed.

1.5.3 Quarkonia Suppression

Quarkonia are heavy-flavor mesons consisting of a heavy quark and respective antiquark, J/ψ ($c\bar{c}$) and Υ ($b\bar{b}$). Quarkonia consist of heavy quarks which are produced in the hard partonic scattering, before creation of the QGP, and thus can serve as a useful outside probe. Its binding energy is large (0.6 GeV for J/ψ and 1.2 GeV for Υ) compared to typical hadronic scale ~ 0.2 GeV. Quarkonia thus have small radius (0.1 and 0.2 fm) which allows some of them to survive above the critical temperature T_c in the QGP [1]. The higher the quarkonium state, the easier it is for them to dissolve since their relative binding energy is lower (they are more tightly bound however have larger radii). Phenomenon causing melting of the bond in quarkonium is called Debye screening. The Debye radius describes the distance at which the quark can still "feel" the presence of the other one. In the QGP, free color charges are present which cause the decrease of the Debye radius under the actual radius of the quarkonium causing it to dissolve. Different types of quarkonia have different value of Debye radius which means that quarkonia can be used to determine the temperature of the medium. The radius of $J/\psi(1S)$ is about 2 fm, that of $\chi_c(1P)$ is about 0.3 fm and that of $\psi'(2S)$ is 0.4 fm. This situation is illustrated in Fig. 1.12.

Clear experimental example of this phenomenon can be seen in Fig. 1.13 where measurement of dimuon invariant mass measured by CMS collaboration [55] in p+p (left) and Pb+Pb (right) at $\sqrt{s} = 2.76$ TeV and $\sqrt{s_{NN}} = 2.76$ TeV, respectively is shown. The three peaks correspond to three states of Υ . In p+p collisions all

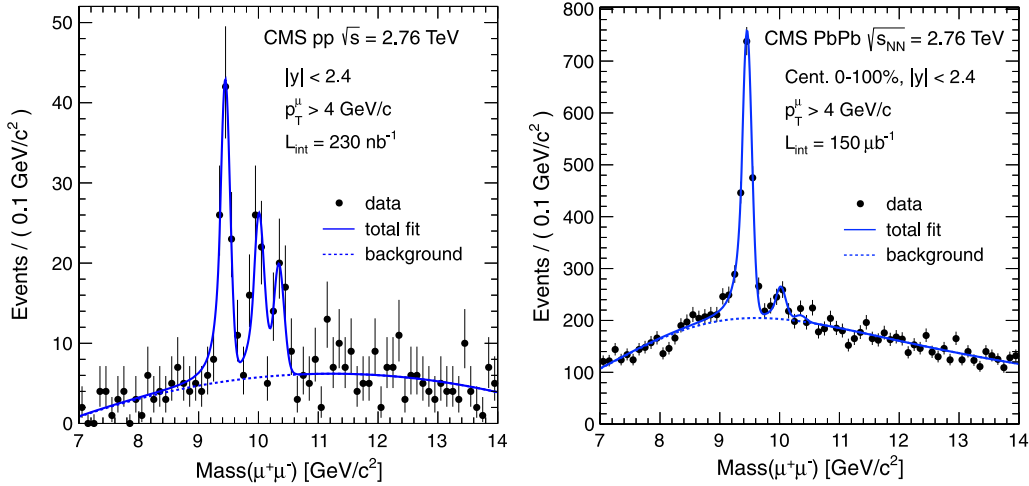


Figure 1.13: Dimuon invariant mass distributions in p+p (left) and Pb+Pb (right) collisions at $\sqrt{s} = 2.76$ TeV and $\sqrt{s_{NN}} = 2.76$ TeV, respectively, measured by the CMS collaboration. The requirement for individual muons was $p_T > 4$ GeV/c. Taken from Ref. [55].

three peaks are clearly visible whereas in Pb+Pb collision the two higher states are highly suppressed. $\Upsilon(2S)$ and $\Upsilon(3S)$ have less energetic bound between quarks so they dissolve earlier than $\Upsilon(1S)$ [1]. The state of dissolution of the quarkonia serves as a thermometer.

However, the situation with quarkonia is much more difficult. Larger or the same suppression would be expected at LHC compared to RHIC collision as the energy density is much larger at LHC. Fig. 1.14 shows a comparison of a J/ψ nuclear modification factor R_{AA} as a function of centrality measured by ALICE collaboration in Au+Au collisions at $\sqrt{s_{NN}} = 2.76$ TeV [56] and $\sqrt{s_{NN}} = 5.02$ TeV [57] and PHENIX collaboration at $\sqrt{s_{NN}} = 200$ GeV [58]. The suppression is much lower for the ALICE results compared to PHENIX results. The effect called recombination is responsible for this phenomenon. When the quarkonia are dissolved in the QGP, there is a probability for the c quark to recombine with its antiquark and form a quarkonium again. At LHC, about 10 times more quarkonia are created than at RHIC, so the larger suppression is counter-weighted. The stronger suppression in the PHENIX data clearly shows that recombination does not play an important role at lower energies.

1.5.4 Baryon to Meson Ratios

Another tool which can be used to study properties of the QGP is measuring the baryon/meson yield ratio. These measurements can also be done in the small

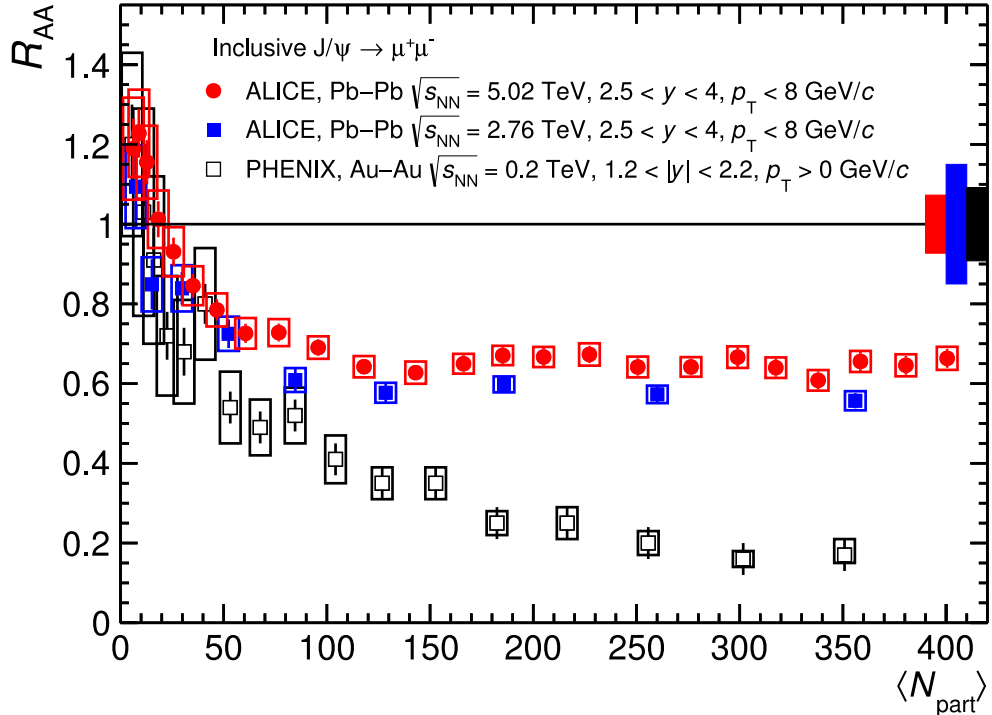


Figure 1.14: Inclusive J/ψ R_{AA} measured by ALICE collaboration in Au+Au collisions at $\sqrt{s_{NN}} = 2.76$ TeV [56] and $\sqrt{s_{NN}} = 5.02$ TeV [57] and PHENIX collaboration at $\sqrt{s_{NN}} = 200$ GeV [58]. Taken from Ref. [59].

systems and provide information about hadronization process in the collisions.

Example of such measurement can be seen in Fig. 1.15 where the ratios of p/π^+ and π^- measured by STAR experiment can be seen. The ratio is enhanced in the central Au+Au collisions compared to peripheral Au+Au collisions and d+Au collisions for $1 < p_T < 4$ GeV/ c .

The dominant hadronization process in the peripheral heavy-ion collisions and in the small systems is the fragmentation. The particles (hadrons such as pions or protons) originate from the hard scattering processes. This mechanism is also present in the central heavy-ion collisions but as can be seen in Fig. 1.15 there is an additional process which is explained by the presence of the QGP. This process is usually called a coalescence hadronization. The partons from the hard scattering and those present in the medium can hadronize with each other provided that they are closed with each other in space and have similar momenta. The abundance of partons with low momenta is larger than those with higher transverse momenta because the spectra of partons in the QGP are steeply falling with the growing p_T . This means that there is a larger probability of creating a baryon than meson with the same p_T in the coalescence hadronization and this explains the shown baryon/meson enhancement in the central heavy-ion collisions compared to small

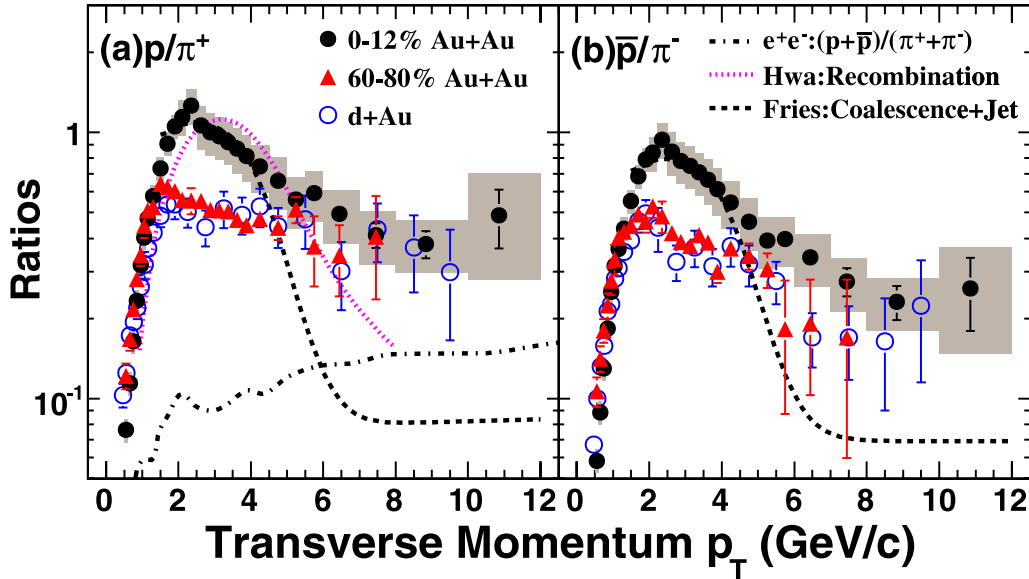


Figure 1.15: The p/π^+ (a) and \bar{p}/π^- (b) yield ratios measured by STAR in Au+Au and d+Au collisions at $\sqrt{s_{NN}} = 200$ GeV [60], [61]. The data are compared to $(p+\bar{p})/(\pi^++\pi^-)$ yield ratio measured by DELPHI Collaboration in e^++e^- collisions at $\sqrt{s} = 91.2$ GeV [62] and theoretical calculations [63] and [64]. Taken from Ref. [65].

systems or peripheral collisions.

1.5.5 Hydrodynamic Flow

If the collision of the nuclei is not central the overlap area has a shape of an almond. This situation is visualized in Fig. 1.16. The plane connecting the centers of the nuclei is the reaction plane. Under these conditions the distribution of pressure and participants is not uniform and the system is anisotropic - some properties depend on the direction. The mentioned pressure gradient leads to a collective motion of the particles inside the medium. The observed overlap of the particles has approximately shape of an ellipsoid and the observed symmetry is thus called elliptic flow.

This property is being described by the laws of hydrodynamics. To observe this asymmetry in azimuthal distribution of particles is being used. This asymmetry is described using so called flow coefficients v_n which are present in the Fourier expansion of the particle momentum distribution function

$$\frac{dN}{dyd^2p_T} = \frac{dN}{2\pi p_T dy dp_T} \left[1 + \sum_{n=1}^{\infty} 2v_n \cos(n(\psi_p - \Psi_{RP})) \right], \quad (1.6)$$

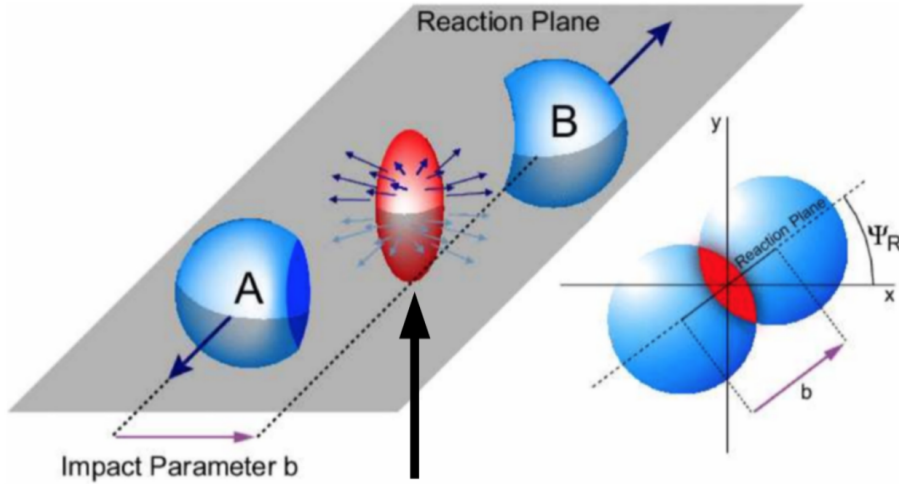


Figure 1.16: Schematic view of a collision of two nuclei with impact parameter b . Taken from Ref. [66].

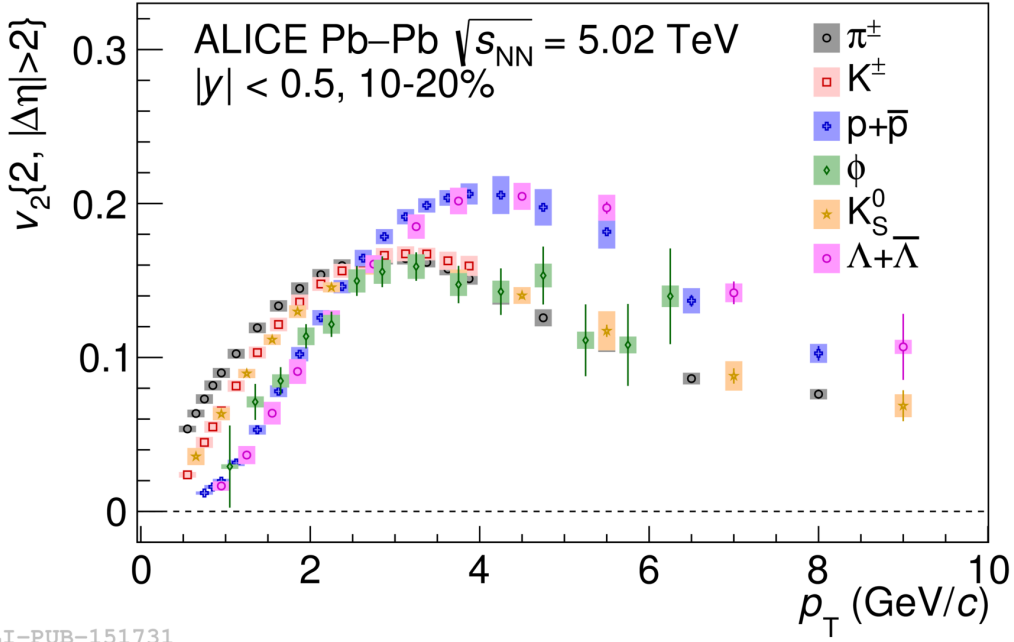
where Ψ_{RP} is the angle of reaction plane and the direction of a particle and ψ_p is the azimuthal angle of the transverse momenta of the particle. Coefficients v_n describe the momentum anisotropy and rapidity and transverse momentum dependent $v_n = v_n(y, p_T)$. The first Fourier coefficient v_1 is directed flow, v_2 elliptic flow and v_3 triangular flow.

However the situation is not usually that straightforward as described in Fig. 1.16. The nuclei are not perfectly spherical and consist of protons and neutrons which have their own distribution in the volume. In reality the reaction plane can be "tilted". Even further the shape of the overlap is not usually in the shape of perfect ellipsoid and so coefficients v_n for n larger than 2 are non-zero. For these reasons the measurement of anisotropic flow is a challenging task.

The directed flow mainly originates from the rotation of the QGP in the reaction plane. The elliptic flow has been used as a proof of a QGP formation. It arises from the initial anisotropy. The triangular flow also originates from the initial anisotropy but its origin is fluctuation of shape of the overlap of colliding nuclei.

An example of a measurement of the elliptic flow done by ALICE experiment in Pb+Pb collisions at $\sqrt{s_{NN}} = 5.02$ TeV is in Fig. 1.17. For low p_T can be seen clear mass ordering which comes from the collective expansion of the medium and incorporates the effects of radial flow. At intermediate p_T is visible clear baryon-meson grouping which shows that partons are those who flow and are grouped together at freeze-out.

Even though it was assumed that hydrodynamic flow is produced purely by the volume of the QGP in the ultra-relativistic heavy-ion collisions, quite recently



ALI-PUB-151731

Figure 1.17: The p_T dependent v_2 of various hadrons measured in Pb+Pb collisions at $\sqrt{s_{\text{NN}}} = 5.02$ TeV by ALICE detector. Taken from Ref. [67].

the hydrodynamic flow was also measured in the small systems (p+Pb or p+p) at sufficiently large energies (such as at the LHC) as well. Such measurement done by CMS [68] can be seen in Fig. 1.18. In the top panel is elliptic flow v_2 and in the bottom triangular v_3 as a function of collision multiplicity $N_{\text{trk}}^{\text{offline}}$ in Pb+Pb collisions at $\sqrt{s_{\text{NN}}} = 2.76$ TeV, p+Pb collisions at $\sqrt{s_{\text{NN}}} = 5.02$ TeV and p+p collisions at various energies. A clear ordering of collision systems is visible for the elliptic flow. The v_2 is largest for the heavy-ion collisions, for the asymmetric collisions is lower and the lowest is for the collisions of protons. The triangular flow is similar for all the systems which might be caused by initial shape fluctuations to which the v_3 is sensitive (in A+A collisions). Also different method has to be used to obtain the flow, because the event plane method does not work in the small systems as there is no well defined geometrical overlap.

Discovery of the collective flow in the small systems requires new model which describes flow in all the collision systems. One that is successful in describing the experimental data is the superSONIC model [69] which uses viscous hydrodynamics to describe v_2 , v_3 and v_4 . The viscosity in this model is very low compared to common liquids like water or liquid helium. According to this model the QGP would behave as almost perfect fluid and flow in small systems could be described with the same set of parameters.

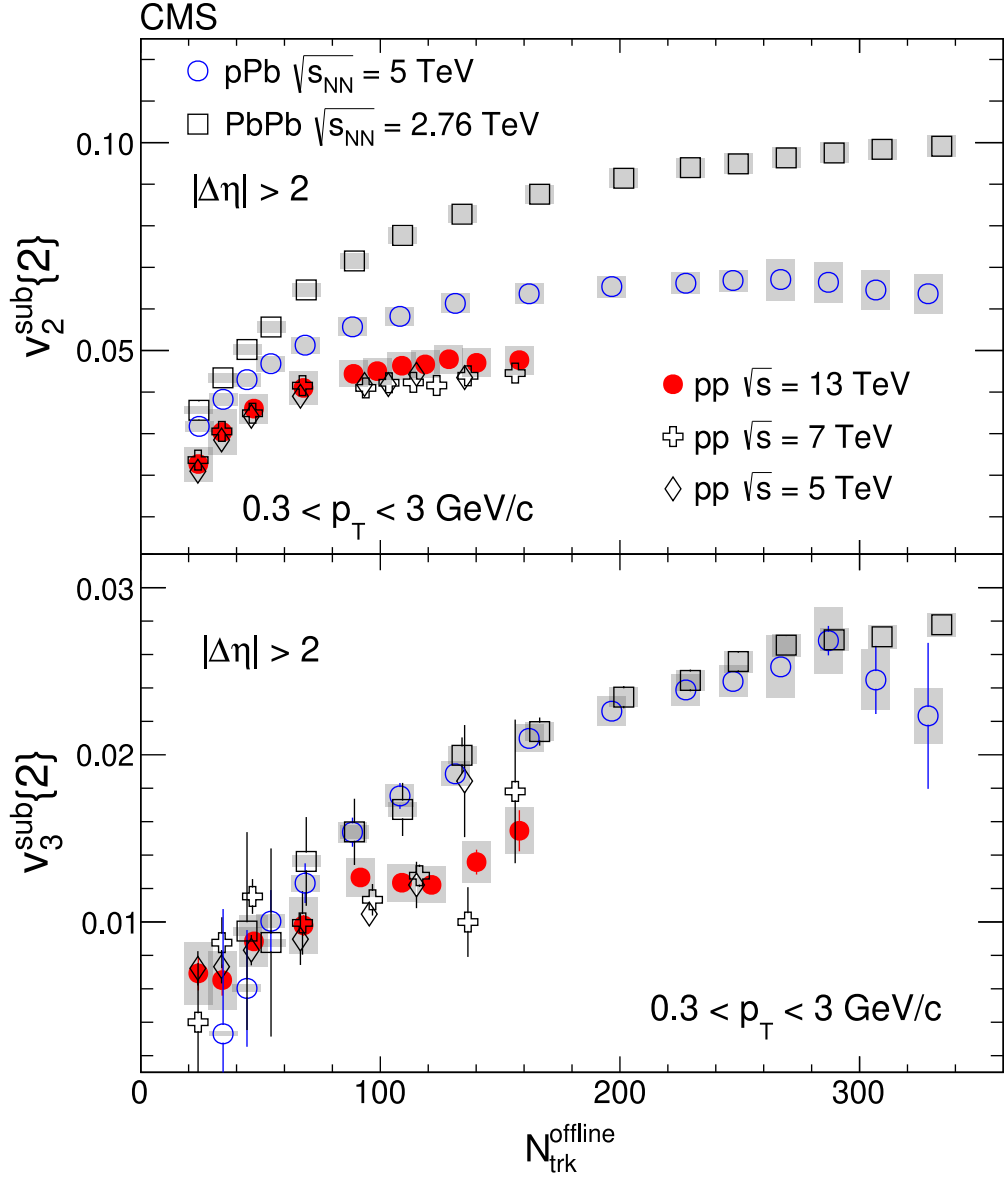


Figure 1.18: Elliptic flow v_2 (top) and triangular flow v_3 (bottom) as a function of collision multiplicity $N_{\text{trk}}^{\text{offline}}$ measured by CMS in Pb+Pb collisions at $\sqrt{s_{\text{NN}}} = 2.76$ TeV, p+Pb collisions at $\sqrt{s_{\text{NN}}} = 5.02$ TeV and p+p collisions at various energies. Taken from Ref. [68].

Chapter 2

STAR Experiment at RHIC

In the present universe it is possible to observe QGP only for a fraction of second at large particle colliders such as LHC and RHIC in the collisions of heavy ions. These collisions produce hundreds of particles and antiparticles in each collision so really precise complex detectors with large acceptance are needed to detect particles, trace them back to their parent particles and measure desired properties of QGP. Such detector is STAR at RHIC accelerator in the Brookhaven National Laboratory.

2.1 Brookhaven National Laboratory

BNL was founded in 1947 from a former military facility U. S. Army's Camp Upton where American soldiers were trained in both World War 1 and World War 2. It is located on the eastern part of Long Island in Upton in New York state. The original goal was to search for nonmilitary use of nuclear energy but these days the scientific spectrum is much wider.

The first nuclear reactor build after the war was Brookhaven Graphite Research Reactor which operated until 1969. High Flux Beam Reactor was being used between years 1965 and 1999. Simultaneously operated the first nuclear reactor for medical research in the United States called Brookhaven Medical Research Reactor which was in use from 1959 to 2000 [70].

The first particle accelerator Cosmotron was opened in 1952 and was used up to 1966 when it was replaced by the Alternating Gradient Synchrotron (AGS). Research on AGS led to the obtaining of three Nobel prizes. Nowadays AGS serves as a preaccelerator for RHIC.

Seven Nobel prizes were awarded to scientists participating in BNL out of which

five were in the field of physics

- 1957 – Chen Ning Yang a Tsung-Dao (T.D.) Lee – *for their penetrating investigation of the so-called parity laws which has led to important discoveries regarding the elementary particles* [11],
- 1976 – Samuel Chao Chung Ting – *for their pioneering work in the discovery of a heavy elementary particle of a new kind* [11],
- 1980 – James Watson Cronin a Val Logsdon Fitch – *for the discovery of violations of fundamental symmetry principles in the decay of neutral K-mesons* [11],
- 1988 – Leon M. Lederman, Melvin Schwartz a Jack Steinberger – *for the neutrino beam method and the demonstration of the doublet structure of the leptons through the discovery of the muon neutrino* [11],
- 2002 – Raymond Davis Jr. – *for pioneering contributions to astrophysics, in particular for the detection of cosmic neutrinos* [11].

and two in the field of chemistry

- 2003 – Roderick MacKinnon – *for structural and mechanistic studies of ion channels* [11],
- 2009 – Venkatraman Ramakrishnan a Thomas A. Steitz – *for studies of the structure and function of the ribosome* [11].

From 1982 to 2014 operated the National Synchrotron Light Source which used to accelerate electrons the speed close to the speed of light and thus produced synchrotron radiation of various wavelengths. This radiation was being used to study materials in the nanoscale. NSLS was replaced by National Synchrotron Light Source II.

Construction of the Relativistic Heavy Ion Collider began in 1991 in the tunnel which was originally dug for the ISABELLE project which was never finished and cancelled in 1983. RHIC was put into service in 2000.

Other facilities in the BNL are Brookhaven Linac Isotope Producer which is high energy particle accelerator used for the production of radioisotopes which are used to diagnose and cure cancer; Center of Functional Nanomaterials which studies and develops nanoelectric components, nanophotonics or medical devices; and Space Radiation Laboratory which falls under the National Aeronautic and Space Administration and studies effects of space radiation on the cells and tissues.

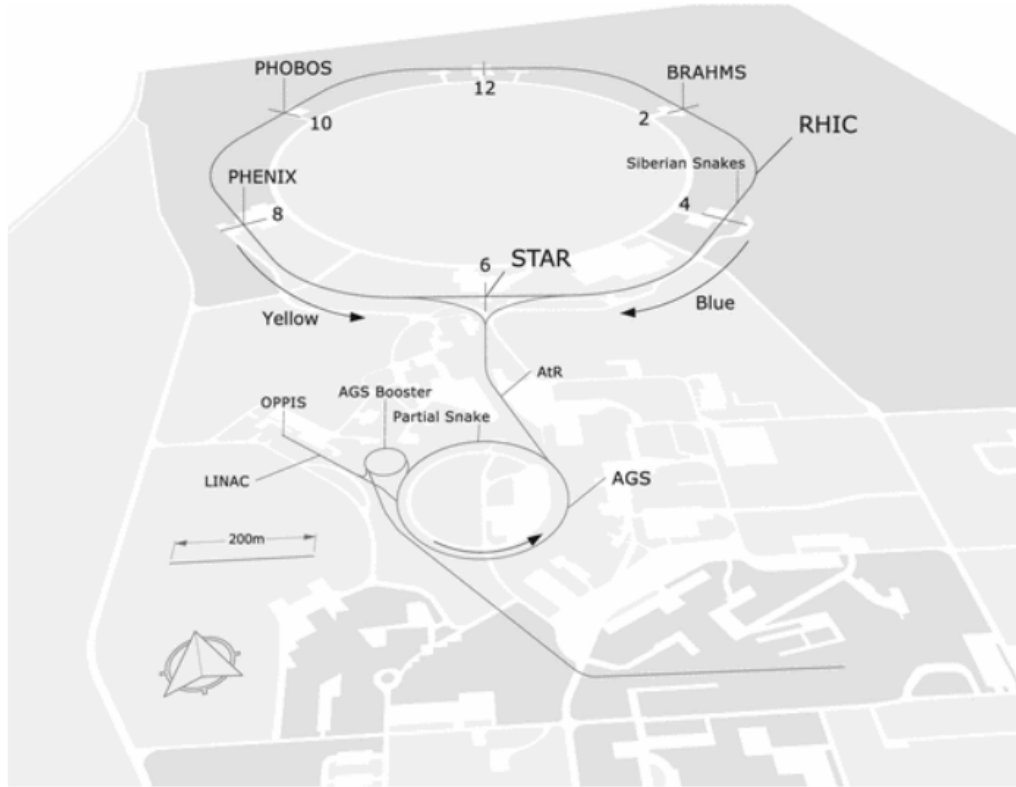


Figure 2.1: Schematic view of RHIC. Taken from Ref. [71].

2.2 The Relativistic Heavy Ion Collider

RHIC is the second largest collider in the world (following Large Hadron Collider in Switzerland) and is capable of colliding various atomic nuclei, ranging from protons up to uranium. It is the first and only device that is capable of colliding polarized protons. This is essential for the understanding the structure of spin of a proton. RHIC is capable of colliding multiple different nuclei at various energies which allows to study QCD phase diagram. Cartoon of RHIC and a cascade of its preaccelerators can be seen in a Fig. 2.1. The circumference of RHIC is 3 834 meters (2.4 mile) [72]. For a comparison the circumference of LHC is 26 659 meters [73].

RHIC was launched in 2000 and aimed to study the Quark-Gluon Plasma via the collisions of heavy nuclei (mainly gold nuclei). These ions are collided at energy of $\sqrt{s_{NN}} = 200$ GeV. Apart from gold protons, proton+gold or deuteron+gold are also collided but much more nuclei were used in the past, such as uranium, aluminium or helium.

The accelerator consists of two rings in which the particles circulate in the opposite directions. The first one is blue (clockwise) and the second one is yellow (counterclockwise). These rings intercept at six points which are called interaction

points. They are called by the numbers on the clock. In these points are placed the experiments.

As a source of ions for RHIC serves the Electron Beam Ion Source (EBIS) with Laser ion source (LION) which consists of high-energy pulse laser with a fixed target. Following the EBIS lies Radio Frequency Quadrupole (RFQ) and a short linear accelerator Linac. In the past was being used Hollow Cathode Ion Source and two Van de Graaf generators as a source. Compared to them LION and EBIS can switch between different kinds of ions very quickly and EBIS is placed much closer to the following accelerator stages so the intensity of ions is higher.

Ions are produced in LION and have a positive charge $+1$. Gold ions are produced by a laser pulse which hits a golden foil and then continue to EBIS where their charge is multiplied by an electron beam and leave with energy of 16.24 keV/u . In RFQ is energy raised up to 314.72 keV/u . Another part of the process continues in the Linac where the ions get the energy of 2 MeV/u . This energy is sufficient for the Booster which is a circular accelerator with a circumference of 201.78 m [74]. Particles obtain energy of 70 MeV/u and their speed is 0.37 of speed of light. Leaving Booster ions loose electrons and get charge $+77$ (in a case of Au). This process is done by stripping foils. Ions continue their journey to AGS which has circumference of 807.12 m and get energy of 10 MeV/u . When leaving AGS ions have speed equal to 0.997 of the speed of light. The next step is RHIC. Before the ions enter the collider, another two electrons are stripped by another stripping foil. The final charge is then $+79$ and final energy is 100 GeV/u . Usually 112 bunches are filled into each of two RHIC rings. Schematic view of the whole process is in Fig. 2.2.

Accelerating of protons is the same process with the difference that protons begin their journey in optically pumped H^- ion source OPPIS instead of EBIS.

Four superconducting radiofrequency cavities are used for the acceleration and ten storage cavities are installed to maintain the beam at the maximum energy. Superconductive dipole magnets curve the track of a beam. Superconductive quadrupole magnets are used to focus the beam with the goal to achieve maximum luminosity.

The beams circulate for multiple hours colliding again and again in the interaction points (nowadays only at 6 o'clock where STAR is located). The quality of a beam decreases with time so one the beam reaches a threshold quality, it is dumped by a kicker magnet and RHIC has to be filled again.

Four experiments were operated at RHIC - PHOBOS, BRAHMS, PHENIX and STAR, out of which STAR is the only one currently running. Broad Range Hadron Magnetic Spectrometer (BRAHMS) aimed to measure charged hadrons to study highly excited matter created in the collisions of heavy ions and ended its operations

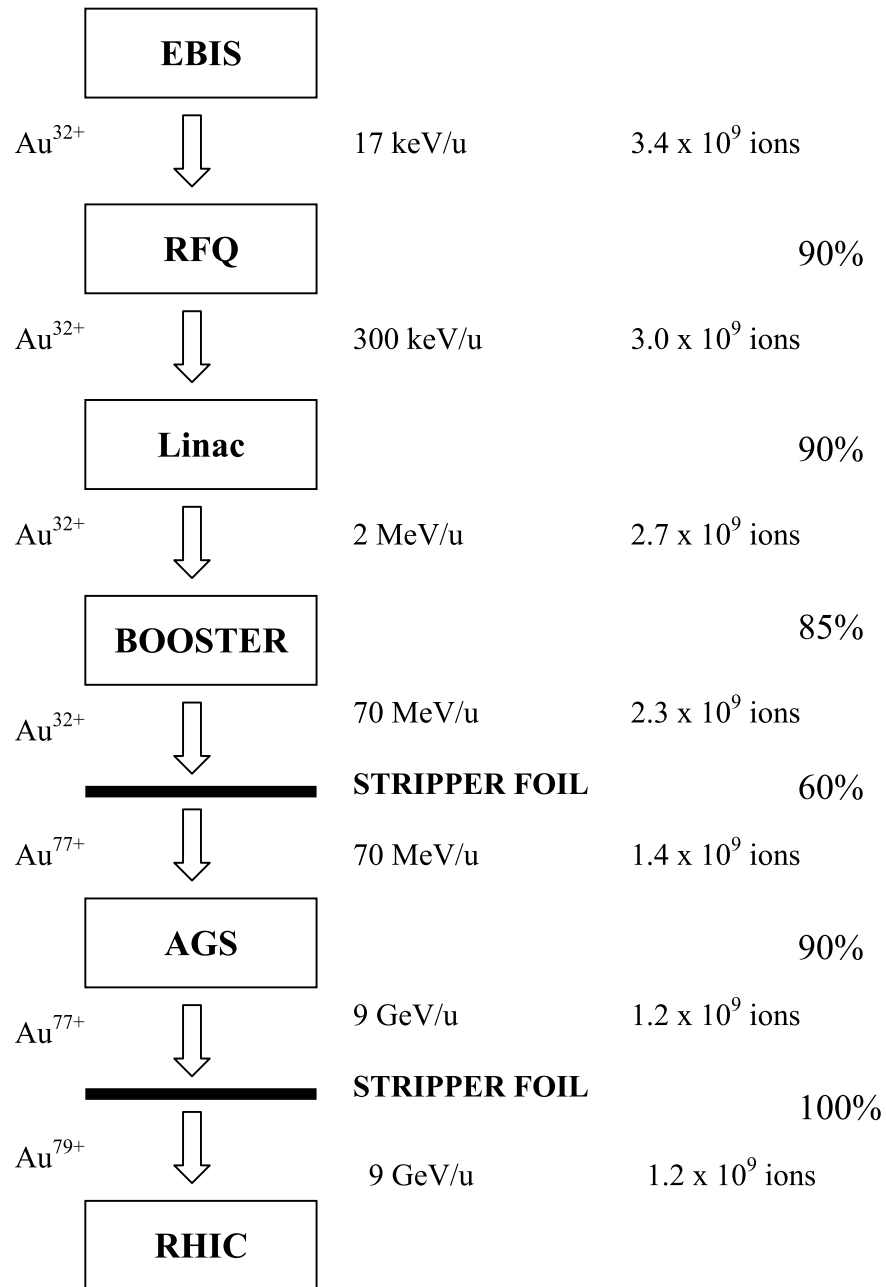


Figure 2.2: Cartoon of the process of the accelerating of ions at RHIC. Taken from Ref. [75].

in 2005. PHOBOS aimed to measure new physics and was studying QGP as well and ended in 2006. Pioneering High Energy Nuclear Interaction Experiment (PHENIX) was operated to measure direct probes in the collisions of heavy ions such as electrons, muons or photons. PHENIX ended in 2016 and these days is being upgraded to sPHENIX which was being implemented in 2022 and data taking should begin in the first half of 2023. Aim of this experiment will be study of jets and heavy quarkonia.

RHIC is expected to end its program in 2025. After that should begin the transformation to the Electron-Ion Collider. It is expected that two detectors will be constructed at EIC, but for the first runs there will be only one. Proposals for three detectors have been made ATHENA, ECCE and CORE. In 2022 ECCE was selected to be the core design for the first detectors but ATHENA and ECCE projects are supposed to be merged into one detector called EPIC (Electron/Proton-Ion Collider Experiment).

2.3 The Solenoidal Tracker at RHIC

STAR (Solenoidal Tracker at RHIC) is a multipurpose detector with full azimuthal coverage. Its aim is to study polarized p+p collisions and ultra-relativistic heavy-ion collisions. STAR is located at the 6 o'clock interaction point and was named after the solenoid magnet operated at a room temperature. The barrel magnet surrounds almost all STAR sub-detectors. At full strength the magnet has magnetic field 0.5 T. STAR consists of multiple sub-detectors as shown in Fig. 2.3 and thus serves as a multipurpose detector. The subsystems used for particle identification are Time Projection Chamber (TPC), Time of Flight Detector (TOF), Heavy Flavor Tracker (HFT), Barrel Electromagnetic Calorimeter (BEMC) and Muon Telescope Detector (MTD), and trigger systems are Vertex Position Detector (VPD), Beam-beam Counter (BBC) and Zero Degree Calorimeter (ZDC). After 2016 HFT was removed and in the following years the Forward Upgrade was installed. The weight of whole STAR is approximately 1200 tons [76].

2.3.1 Time Projection Chamber

Time Projection Chamber is the most important detector present at STAR. Aim of this cylindrical gaseous detector is to measure tracks of charged particles passing through the detector. With the measured track curvature in the magnetic field and energy loss in the TPC gas, it is possible to determine charged particle's momentum

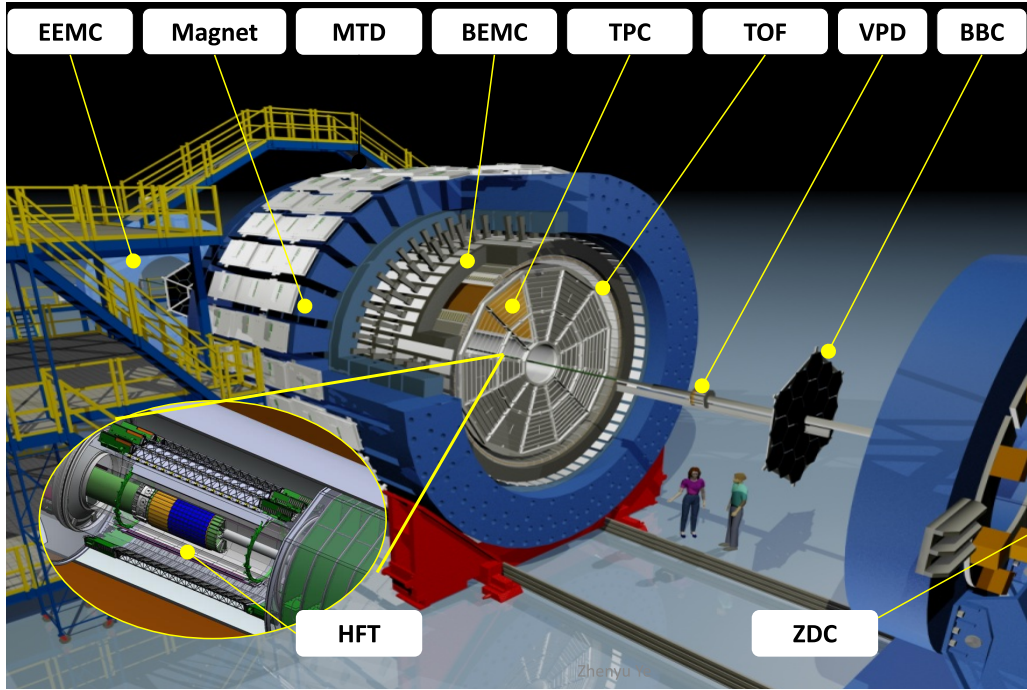


Figure 2.3: STAR detector and its sub-detectors. Taken from Ref. [77].

and determine species of the particle.

Schematic cartoon of the Time Projection Chamber can be seen in Fig. 2.4. TPC is a 4.2 meter long cylinder with inner radius 0.5 m and outer radius 2 m filled with a mixture of argon (90 %) and methane (10 %). It covers whole azimuthal angle of $0 < \phi < 2\pi$ and pseudorapidity $|\eta| \leq 1, 5$. The pressure of the gas is 2 mbar above the atmospheric pressure. Minimum of the measured transverse momentum p_T is 150 MeV/ c .

In the middle of the TPC is a cathode operated at -28 kV and this provides electric field of 140 V·cm⁻¹. The uniformity of the electric field ensures the field cage surrounding the whole surface of the detector.

Particles created in the collision drift through TPC and ionize molecules of the gas and thus loose portion of their energy. Secondary electrons originating from the ionization drift to the endcap parts which are grounded multi-wire proportional chambers (MWPC). Total number of these read-out modules is 24 at each side. Ions drift to the cathode. The drift time of electrons in TPC is approximately 40 μ s. If the event is evaluated as good by the trigger system, the gated grid lets pass the electrons from the main volume into MWPCs. The electrons are accelerated during their drift to the anode wires and they produce avalanches of more electrons. The signal is afterwards readout. Signal read out by the modules is proportional to the number of electrons which entered the readout electronics. MWPCs are divided into

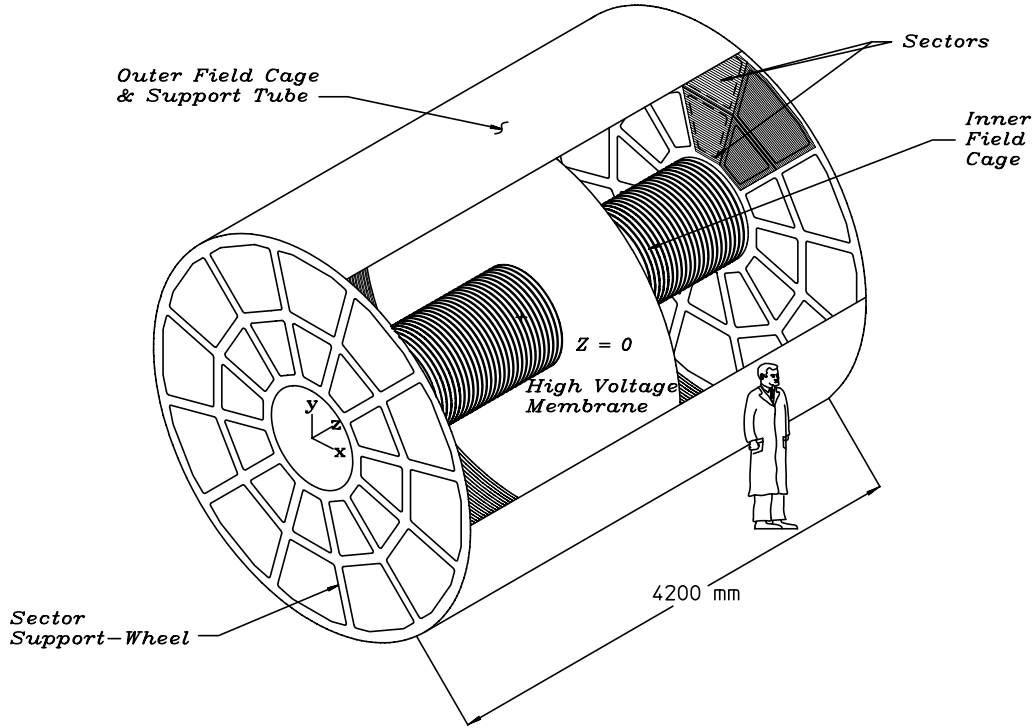


Figure 2.4: Schematic view of the STAR Time Projection Chamber. Taken from Ref. [78].

12 sectors out of which every has 45 pad rows. This means that every measured particle can have maximum of 45 hits in TPC.

From the sectors is obtained position in x and y . Sectors are organized into 45 rows and have 5962 readout pads. Position in z is determined from the drift time, so the TPC provides precise information about all 3 dimensions of the tracks. The nominal drift velocity is $5.45 \text{ cm}/\mu\text{s}$ but the currently measured drift velocity is being used. This velocity is measured by TPC laser system. This is important for the reconstruction of both primary and secondary vertices of the particles that originated in the collision. Energy loss per unit length dE/dx is obtained from the number of ionized electrons. Particle identification is done using Bichsel formula which were developed for STAR TPC. The resolution normalized energy loss dE/dx is defined as

$$n\sigma_X = \frac{1}{R} \ln \left(\frac{\langle \frac{dE}{dx} \rangle_n}{\langle \frac{dE}{dx} \rangle_X} \right), \quad (2.1)$$

where $\langle \frac{dE}{dx} \rangle_n$ is the measured ionization energy loss, $\langle \frac{dE}{dx} \rangle_X$ is the mean value of ionization loss in TPC given by the Bichsel function, X is species of a calculated particle, in further text pion or kaon, R is corresponding resolution ($\sim 8 \%$).

Furthermore, multiplicity measured by TPC serves to determine centrality in the heavy-ion collisions.

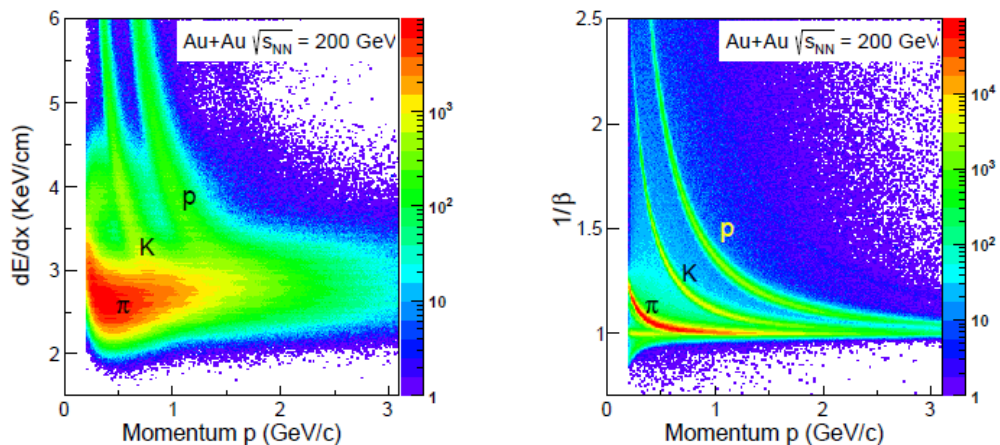


Figure 2.5: dE/dx of TPC (left) and $1/\beta$ of TOF (right) from Au+Au collisions. Taken from Ref. [79].

In 2018 the TPC was upgraded into so called iTPC or inner TPC. Even though TPC had very good performance for the high energy measurements, the planned Beam Energy Scan program required to improve resolution at lower energies as well. After this upgrade particles can have up to 60 hits in the TPC and the pseudorapidity acceptance was extended from $|\eta| < 1$ to $|\eta| < 1.5$.

2.3.2 Time-Of-Flight detector

TOF was installed to improve the particle identification at STAR done by TPC. At $p_T < 1$ GeV/ c it has better resolution than TPC as can be seen in Fig. 2.5. TOF covers whole azimuthal angle 2π , pseudorapidity $|\eta| \leq 1$ and measures time of flight of the particles. Start time is determined by the moment of the collision measured by VPD and TOF barrel determines the stop time. The velocity of a particle is determined from the path length and the time it takes the particle to reach TOF modules placed just outside of the TPC.

TOF consist of 120 trays where each contains 32 Multi-gap Resistive Plate Chambers (MRPC) modules. Those are made of 7 glass plates and the gaps between them are filled with gas. This construction is placed between two graphite electrodes which provide the high-voltage electric field. Information is read by readout pads.

The charged particles leave trays in the gas gaps and thus are detected by MRPCs. Similarly as in the TPC the ionization electrons are accelerated cause avalanches in the strong electric field. Readout pads then read clouds of electrons. This whole process is very fast and TOF has time resolution of ≈ 100 ps. TOF works well in the low momentum region but for $p_T > 1.5$ GeV/ c^2 it is difficult to

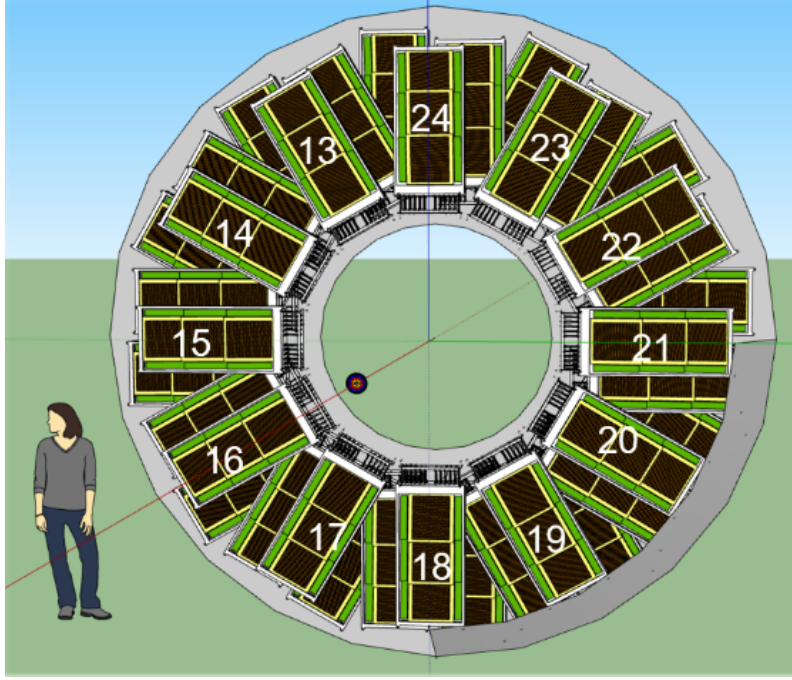


Figure 2.6: Illustration of the endcap-Time-Of-Flight detector. Taken from Ref. [80].

distinguish between particles since all particle species become relativistic and their relative momentum is close to one for all of them.

Particle identification is done by comparing measured value of inverse velocity $1/\beta_{\text{TOF}}$ with an expected theoretical value $1/\beta_{\text{th}}$

$$\Delta \left| \frac{1}{\beta_{\text{th}}} - \frac{1}{\beta_{\text{TOF}}} \right|, \quad (2.2)$$

where β_{th} is calculated using the particle momentum p measured by TPC and expected rest mass m from the formula $\beta_{\text{th}} = p/\sqrt{p^2 + m^2}$.

In 2019 the TOF coverage was improved by a new upgrade which is called the endcap-Time-Of-Flight (eTOF). This detector was developed together with the Compressed Baryonic Matter (CBM) experiment and this detector is tested at STAR. eTOF is mounted to the endcap of the TOF. It consists of trays similar design as TOF. Illustration of eTOF can be seen in Fig. 2.6.

2.3.3 Heavy Flavor Tracker

Heavy Flavor Tracker was installed on STAR from 2014 to 2016. It was placed closest to the beam axis. HFT was a high-resolution silicon detector consisting of

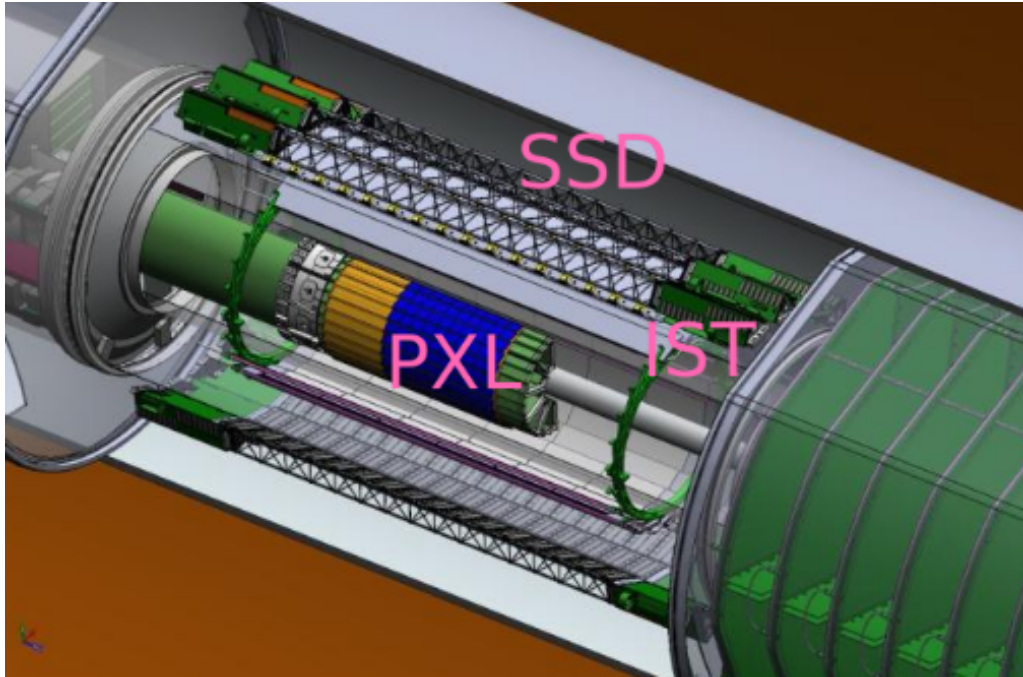


Figure 2.7: Cartoon of the subdetectors of the Heavy Flavor Tracker. Taken from Ref. [81].

three parts - Silicon Strip Detector, Intermediate Silicon Tracker and 2 Pixel Detector layers. Aim of HFT was to measure and reconstruct secondary vertices of heavy flavor particles which decay very quickly due to their large masses. HFT surrounded whole beam axis and thus covered whole azimuthal angle 2π and pseudorapidity $|\eta| \leq 1$. A render of the HFT can be seen in Fig. 2.7.

Position close to beam pipe had a consequence of a need to have high radiation resistance. The first layer of PXL was 2.8 cm away from the beam axis and the second one was in distance of 8 cm and the Pixel detector was the most important part of the HFT. It was composed of 40 ladders of which each contained 10 monolithic CMOS (Complementary Metal-Oxide Semiconductor) chips and together it added up to 400 MAPS (Monolithic Active Pixel Sensor). The pixel sensors are very thin which is useful because it does not produce unnecessary background as would other commonly used sensors do. IST was placed 14 cm from the axis and was made of silicon pad sensors. It aimed to support the tracking done by TPC and PXL. SSD was positioned 22 cm from the center of STAR and helped to improve momentum resolution and tracking efficiency of TPC.

HFT allowed to precisely measure topological variables and thus to massively improve pointing resolution (about $46 \mu\text{m}$ for $750 \text{ MeV}/c$ kaon) and signal to background ratio of the heavy flavor particles compared to STAR without HFT. The HFT pointing resolutions for pions, kaons and protons is shown in Fig. 2.8.

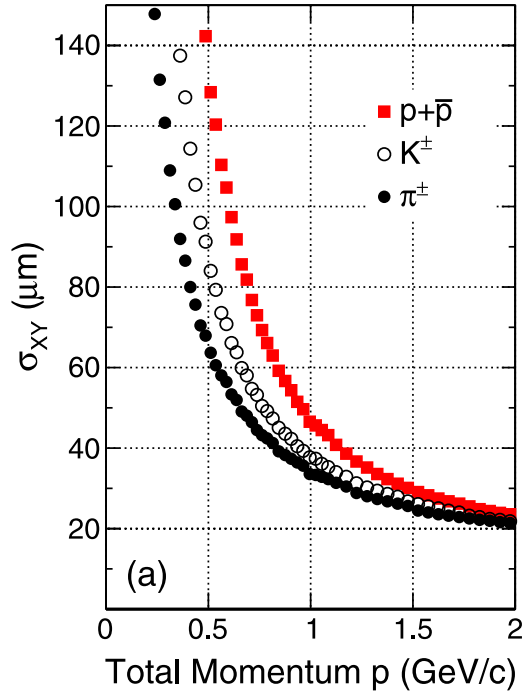


Figure 2.8: The HFT pointing resolution in the transverse plane σ_{xy} as a function of momentum for pions, kaons and protons. Taken from Ref. [82].

2.3.4 Barrel Electromagnetic Calorimeter

STAR has two main calorimetric systems Endcap Electromagnetic Calorimeter (EEMC) and Barrel Electromagnetic Calorimeter (BEMC). Since the detector is a barrel, it covers full azimuthal angle and pseudorapidity $|\eta| < 1$. The inner radius of the BEMC is 223.5 cm and outer radius is 263 cm. Totally 120 modules make up BEMC each segmented into 40 towers. BEMC is a sampling calorimeter which means it consist of two materials. Those are 20 layers of thick lead absorber plates sandwiched with 21 scintillator plates. Position of BEMC can be seen in Fig. 2.9.

2.3.5 Trigger systems

Vertex Position Detector

VPD is also a part of TOF and consists of two identical parts, east and west VPD, each placed in distance 5.7 m from the interaction point, on both sides of the STAR detector. Each of the parts has 19 sub-detectors which consist of of a lead converter, followed by a fast plastic scintillator which is readout by a photomultiplier tube. The pseudorapidity coverage is $4, 24 \leq |\eta| \leq 5, 1$. This detector is a very fast trigger detector and the aim of it is to localize the primary vertex and provide start

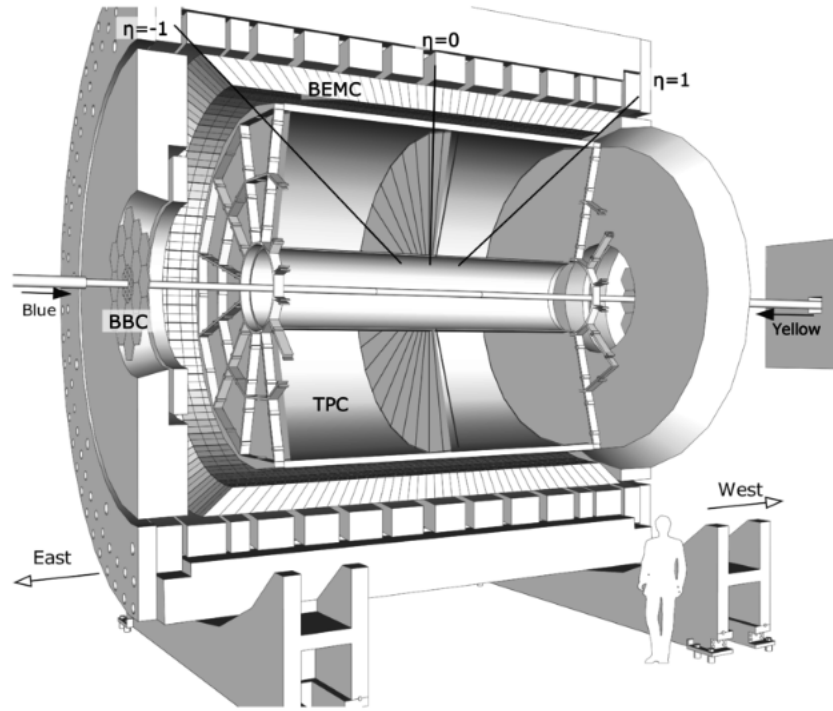


Figure 2.9: A cartoon of subdetectors on STAR. Taken from Ref. [76].

time for TOF using photons.

The start time used by other detectors is calculated as

$$T_0 = (T_{\text{west}} + T_{\text{east}})/2 - L/c, \quad (2.3)$$

where T_{west} and T_{east} are times from each of the VPD parts and L is a distance from the center of STAR. The resolution of start time is in the order of 0.1 ps. The position of a primary vertex with a resolution of 1 cm can be calculated as

$$z_{\text{PV}} = c(T_{\text{west}} + T_{\text{east}})/2. \quad (2.4)$$

Zero Degree Calorimeter

Similarly as VPD, ZDC also consist of two parts, one at each side of STAR located 18 m from the center. ZDC is used primarily for the heavy-ion collisions and apart from that it also helps with monitoring RHIC luminosity during data-taking. Each ZDC module consists of three individual towers, and each of them contains a sandwich of tungsten plates and plastic optical fibres. In each tower there is one photomultiplier which reads out signal from all the connected fibres.

The ZDC detects neutrons which are spectators in the heavy-ion collision. Those convert in the tungsten plates and produce sprays of charged particles. These par-

icles cross the speed of light in the fibres and thus produce Cherenkov radiation which is detected by the photomultipliers.

Beam Beam Counter

Since the ZDC is designed for the heavy-ion collisions, it is not very efficient for the proton+proton collisions. For this reason BBC was installed at STAR. Beam Beam Counter again consists of two parts one at each side of STAR 3.75 m from the center. Apart from triggering p+p collisions, BBC also helps to measure polarization in the polarized p+p collisions

2.3.6 Other STAR Detectors

STAR is also equipped with other detectors which are not important for the following text but are important for different physics goals in different analyses.

One of those detectors is the Event Plane Detector (EPD) which was installed on STAR in 2018. As its name indicates, this detectors aims to determine the event plane in the heavy-ion collisions and is also part of the trigger system. In consist of the parts which are located approximately in the position of former BBC detectors.

The Endcap Electromagnetic Calorimeter (EEMC) serves as an extension of BEMC in the pseudorapidity region of $1.086 \leq \eta \leq 2.00$.

The Muon Telescope Detector (MTD) is mainly designed to identify muons, which are further used to reconstruct quarkonia in dimuon events.

2.3.7 Forward Upgrade

Between 2018 and 2020 so called Forward Rapidity Upgrade was being installed at STAR. The new detectors are placed in the forward rapidity region ($2.5 < \eta < 4$). This upgrade allows novel measurements in all the collision systems and will be installed until the expected end of the RHIC program. This extension in kinematic reach allows to measure new detailed studies of cold QCD physic sat both very high and very low partonic momentum fraction. The detectors are capable of measuring neutral pions, hadrons, photons, electrons, jets and add charged-particle tracking, electromagnetic and hadronic calorimetry to STAR capabilities at high pseudorapidity. A render of STAR Forward Upgrade can be seen in Fig. 2.10.

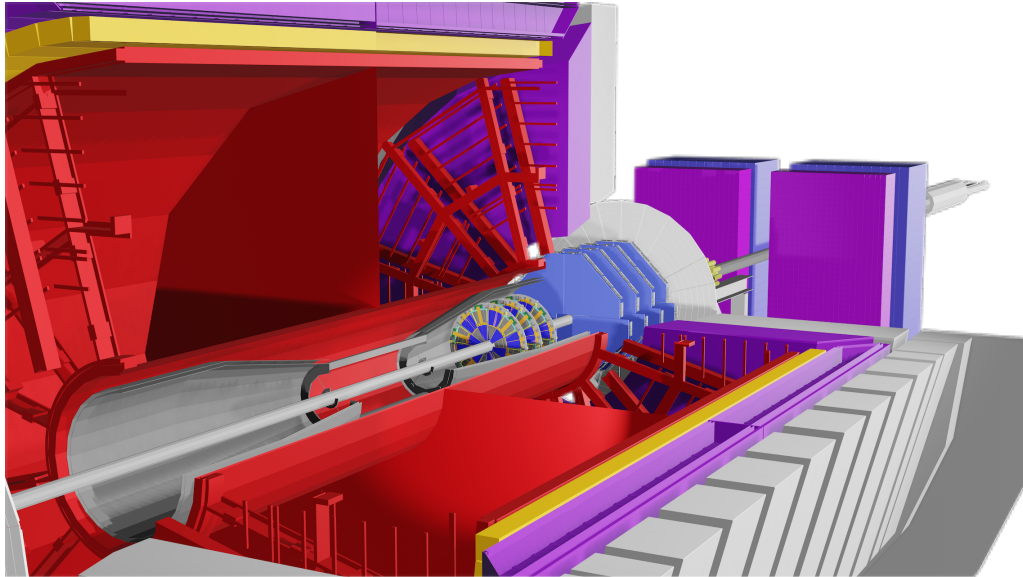


Figure 2.10: A render of STAR detector, including the forward tracking system and the forward calorimeter. The silicon mini-strip detectors are shown closest to the center of STAR, followed by pentagonal sTGC detector. The event plane detector (grey disk) is used as a preshower detector for the forward calorimeter system (purple and blue). Taken from Ref. [83].

Forward Tracking System

The FTS combines two technologies - three stations of silicon mini-strip detectors and four stations small-strip thin gap chambers (sTGCs). The silicon detectors are 140 to 200 cm from the interaction point whereas the sTGCs are placed 300 to 360 cm. The silicon sensors are still in the homogenous 0.5 T magnetic field, but the sTGCs are in the region where the field is changing gradually.

For the silicon mini-strip detectors was used the knowledge obtained from the use of intermediate silicon tracker (part of HFT). Each silicon disk is made up of 12 modules and each is segmented into 128 strips. The DAQ and cooling systems also use the ones previously used for IST.

Four quadrants made of two double sized chambers each make up every of the sTGC detectors. Each detector includes X, Y and one layer of diagonal strips to measure hit location. The mixture in the detector is 55 % n-pentane and 45 % CO₂. The readout electronics follows the ATLAS design since similar detectors were used in the ATLAS small wheel upgrade.

Forward Calorimeter System

The FCS is located 7 m from the center of STAR. For the electromagnetic calorimeter (ECAL) was used lead-scintillator (PbSc) from PHENIX equipped with new readout electronics. Each PbSc tower consists of sampling cells of 1.5 mm lead, 4 mm scintillator and wavelength shifting fibres. In total ECAL has 1496 readout channels. The hadronic calorimeter (HCAL) is also sampling detector (FeSc). Each of the sandwiches consists of 20 mm iron plates and 3 mm scintillators. The HCAL uses the same readout SiPM electronics as ECAL, but total number is 520. The Event Plane detector (EPD) is used as preshower system for the calorimeters. The FCS provides triggering capability for the entire forward system of detectors.

2.4 Electron-Ion Collider

On January 9 2020 Department of Energy of the USA announced BNL as a place for the construction of Electron-Ion collider (EIC). It is expected that the EIC could begin its mission shortly after 2030. Cartoon of this future collider can be found in Fig. 2.11.

EIC aims to understand the inner structure of protons and nuclei. Electrons passing through the bigger particle can interact with the inner structure of it and thus provide valuable information from the inside of a nuclei.

Present experiment suggest that gluons play an important role in determining key properties of a nuclear matter and protons. EIC should be able to take "pictures" at different energies and thus show gluons and quarks originating from gluon-gluon interaction.

EIC is going to be the first accelerator where both protons and electrons are going to have their spin oriented. This will allow to measure how quarks and gluons and their interactions contribute to the inner angular momentum or the spin of a proton. There are hints that gluons might contribute even more than quarks. Another of the goals will be to measure gluon saturation, strength of the gluon field which will hint more about interactions of gluons and how gluons contribute to the matter around us.

It has been discovered that distribution of quarks is different in a nuclei and in a proton. This effect is called a nuclear shadowing. It is not known whether gluons undergo similar process. Electron-ion collisions will also be a good tool for the measurement of energy loss of light and heavy quarks in nuclear matter.

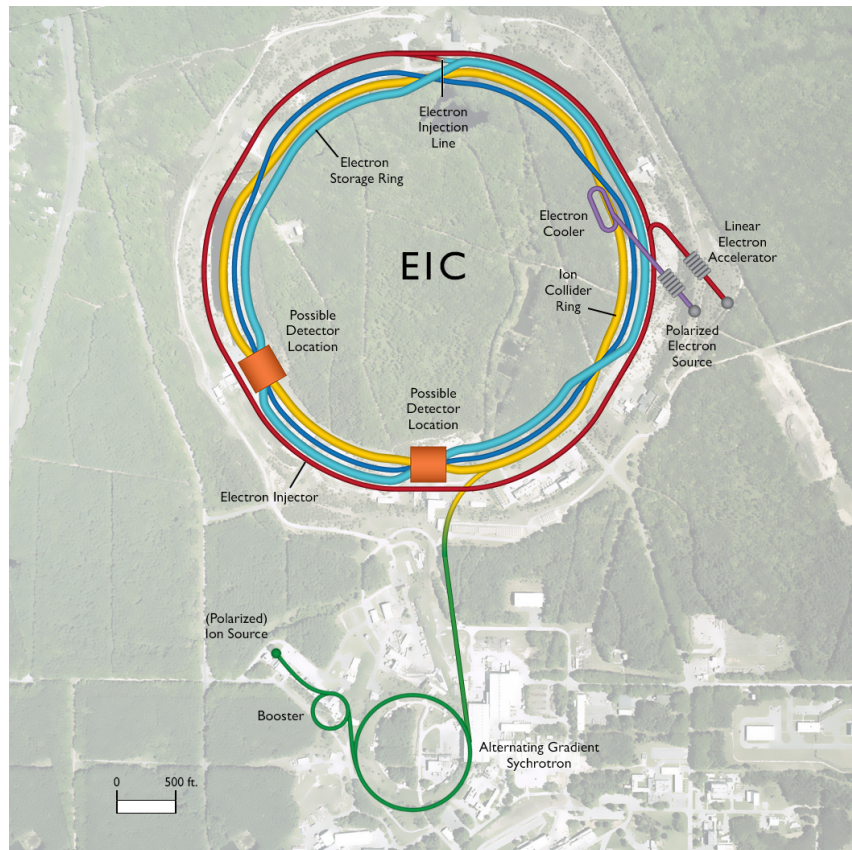


Figure 2.11: A cartoon of Electron-Ion Collider. Taken from Ref. [70].

Highly energetic electron beams are able to kick out the quarks and gluons from their original particle. These free partons quickly acquire color charge from the vacuum so they become colorless. Observing of this effect might contribute to understanding of a quantum vacuum and mechanism of confinement.

The Electron-Ion collider has many possibilities where to move frontiers of our current knowledge. More about its goals can be found in the white papers [84] or [85].

Chapter 3

Cold Nuclear Matter Effects

There are many competing processes that occur in a relativistic heavy-ion collision. To study the QGP it is necessary to separate effects originating from the interactions with the medium. Collisions of the protons serve as a baseline for the collisions of heavy ions. Apart from these properties it is needed to estimate effects caused by simple presence of the nuclei. This can be done by colliding protons (deuterons) with a nuclei. Effects contributing in this initial state are called Cold Nuclear Matter (CNM) Effects. In QGP are present all the aforementioned effects and so we need to study all systems (p+p, p+A, A+A).

CNM effects are studied via p+Pb collisions at the LHC and p+Au, d+Au collisions at RHIC. It is often assumed that no Quark-Gluon Plasma is being created in these collisions. However it is necessary to explain collective flow which was recently discovered in the small systems. Nuclear modification factor in p+A collisions (R_{pA}) serves as an indicator of the CNM effects. As was already mentioned, QGP is studied via collisions of heavy nuclei. If the R_{pA} would be approximately one, it could be expected that no effects are present.

3.1 Cold Nuclear Matter Effects

Production of both hidden and open charm heavy flavor particles is a very sensitive probe for studying QGP because their origin is in the pre-medium phase during the hard processes. Heavy flavor particles are influenced by the QGP medium, however multiple Cold Nuclear Matter effects or initial state effects might also influence production of both hidden and open heavy flavor. Separating initial/CNM effects and effects of the hot and dense medium is a challenging task, nevertheless it is necessary to understand increment from all the sources to fully understand both

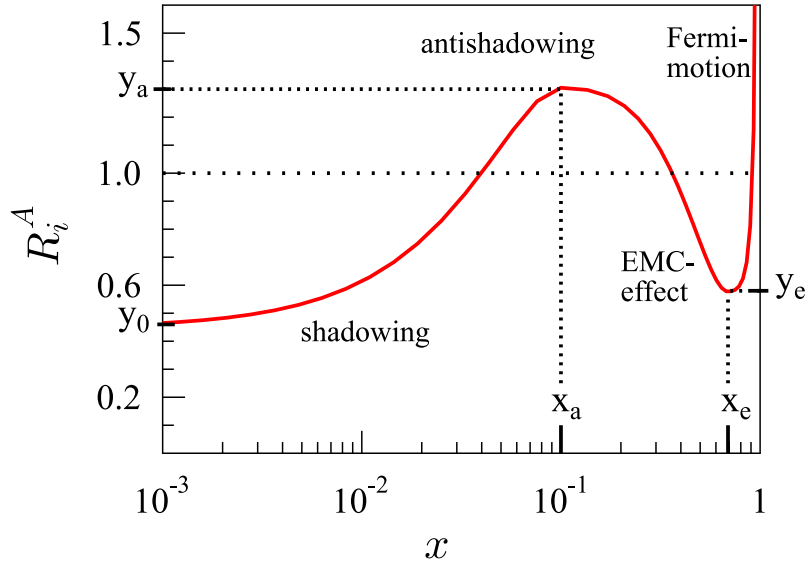


Figure 3.1: Visualization of the shadowing factor R_i^A depending on the Bjorken x . Taken from Ref. [86].

QGP and collisions of small systems.

3.1.1 Parton Distribution Function Modification

Parton distribution function (PDF) $f(x, Q^2)$ is dependent on a Bjorken x and scale of the process Q^2 (transferred squared four-momentum) and describes the probability of finding the parton with a momentum fraction x at a scale Q^2 and effectively describes the distribution of partons inside a nucleon. Partons described by PDF can be gluons, quarks or antiquarks. Parton distribution function that was modified by a nuclei is denoted nPDF.

Modification of PDF in the colliding nuclei with respect to colliding protons is caused mainly by different behavior of partons in a free proton and that bound in a nuclei. Different parton density is responsible for this effect. To quantify the modification the shadowing factor R_i^A can be used

$$R_i^A(x, Q^2) = \frac{f_i^A(x, Q^2)}{f_i^{\text{nucleon}}(x, Q^2)}, \quad (3.1)$$

where f_i^A is the PDF of a bound nucleon (nPDF) of flavor i and f_i^{nucleon} is the PDF of free nucleon. Values of R_i^A for different x are in Fig. 3.1 where multiple regimes can be seen depending on the values of x : a shadowing ($R_i < 1$) which is related to phase-space saturation at $x < 10^{-2}$, anti-shadowing ($R_i > 1$) at $10^{-2} < x < 10^{-1}$, and the EMC effect at large $x > 10^{-1}$.

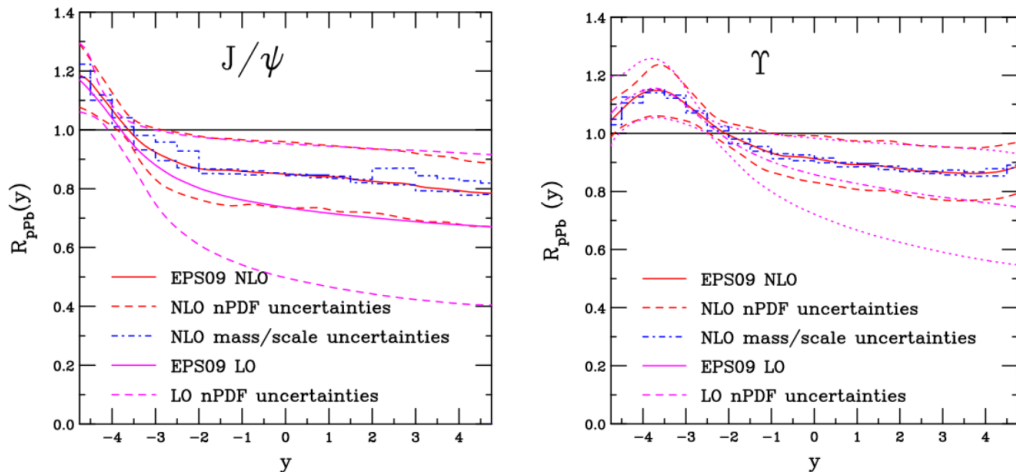


Figure 3.2: The nuclear modification factor R_{pPb} for J/ψ (left) and Υ (right) calculated using the EPS09 [86] modification in p+Pb collisions at $\sqrt{s_{NN}} = 5.02$ TeV. Taken from Ref. [87].

A result of rapidity dependence of nPDF effects on J/ψ and Υ production are shown in Fig. 3.2 at $\sqrt{s_{NN}} = 5.02$ TeV (LHC energy). Other CNM effects are neglected. Color evaporation model (CEM) [88] had been used to obtain these results at next-to-leading order in the total cross-section. In Figure LO results exhibit larger shadowing effect than NLO calculations. The calculations were taken from [89], where a comparison with experimental data from ALICE and LHCb¹ can be found as well. The right panel shows the same calculations for Υ and the difference between LO and NLO results is reduced because the mass scale and thus the factorization scale is larger.

3.1.2 Parton Saturation

The QCD description of hadrons in terms of quarks and gluons consists of several components depending on their transverse momentum k_T and longitudinal momentum fraction x . The partons behave differently which reflects the different regimes of hadronic/nuclear wave function. At very low x the QCD evolution is non-linear because of the growth of parton densities. At some point arises the saturation and the gluons recombine instead of creating more partons ($gg \rightarrow g$, $gg \rightarrow q$) In this non-linear regime QCD stays weakly coupled.

For larger momentum k_T the x needs to be lower in order to reach the saturation regime. This is illustrated in Fig. 3.3. The separation between the dilute and dense regimes is characterized by a momentum scale $Q_s(x)$ also called saturation scale

¹Large Hadron Collider beauty (LHC)

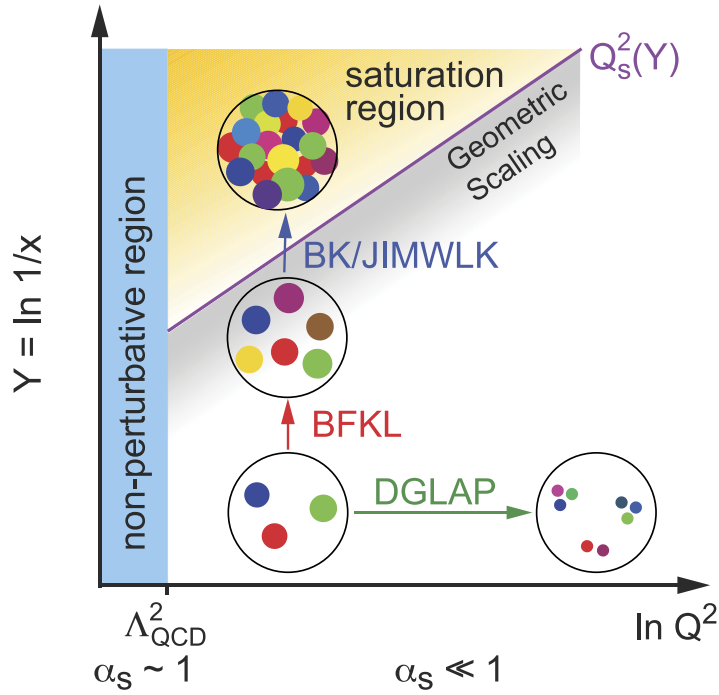


Figure 3.3: Hadron structure in $1/x$ and Q^2 plane. Each circle is a parton with a fraction of momentum x . The saturation line separates the dilute (DGLAP) regime from the saturation regime. Different evolution regimes and saturation area are shown. Taken from Ref. [90].

which increases as x decreases. The non-linearity is also responsible for different regimes of particle scattering. Dilute partons scatter incoherently but for large partons densities partons scatter collectively and the particle production also becomes non-linear.

Saturation can be well described in a theory of color glass condensate (CGC) [91], [92] both in terms of practical applicability and phenomenological success. It is unlike of nPDF approach (based on DGLAP evolution) described by Balitsky-Kovchegov or JIMWLK non-linear evolution equations. The CGC approach has its limitations depending on the level of accuracy of the calculations (LO vs. NLO) and on the amount of non-perturbative inputs (initial conditions to the small- x evolution, impact parameter dependence) [90]. These uncertainties could be reduced by results from electron-ion collisions.

One of the important observables used to investigate saturation is the rapidity dependence of nuclear modification factor and CGC based models. Extrapolation of RHIC data to LHC energies can be seen in Fig. 3.4.

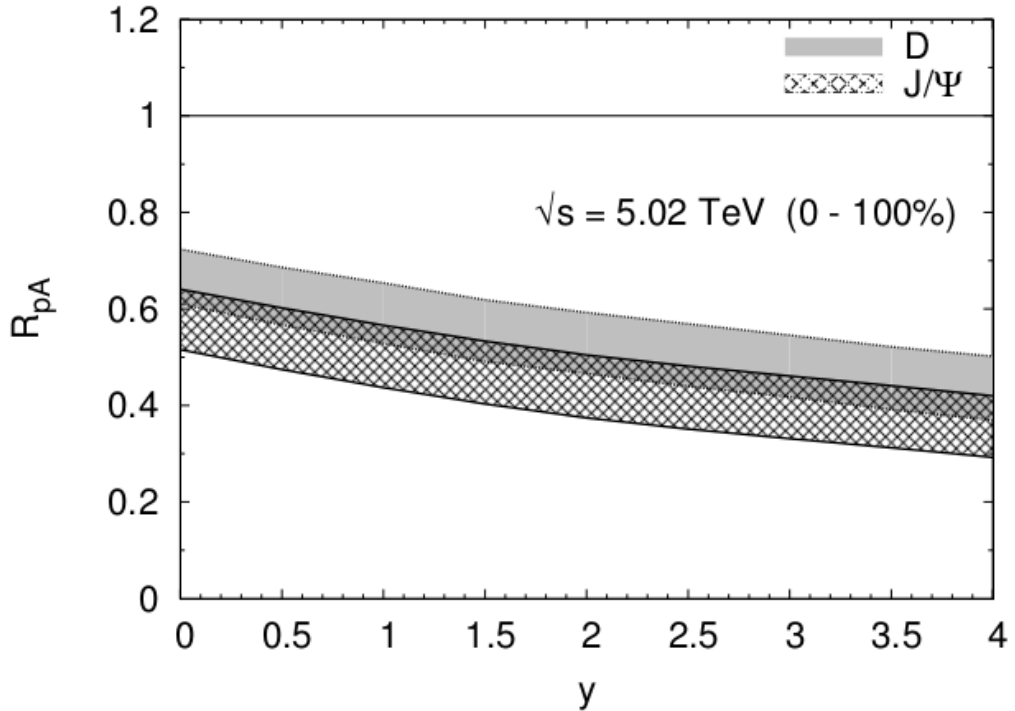


Figure 3.4: Nuclear modification factor $R_{pA}(y)$ for D and J/ψ in the CGC [91], [92] approach in p+Pb collisions at $\sqrt{s_{NN}} = 5.02$ TeV. Taken from Ref. [87].

3.1.3 Multiple Parton Scattering

Multiple parton scattering can arise in a nuclei before or after the hard scattering or in the both cases. Multiple scattering means that partons of the colliding objects (for example proton and nucleus) exchange gluons among those objects. This leads to the loss of the parton energy (both radiation and collision) and broadening of the p_T spectrum. This effect which is a consequence of multiple parton scattering is called Cronin effect or Cronin-like enhancement. In most approaches it is characterized by a transport coefficient of the cold nuclear matter \hat{q} .

Various approaches of multiple parton scattering can be used, describing various effects such as $q\bar{q}$ propagation and attenuation in nuclei [93], [94], initial and final state energy loss [95], [96] and coherent energy loss [97]-[101].

When the scattering from the medium is largely incoherent the parton modification is dominated by a broadening of the transverse momentum. At few GeV/ c we can talk about Cronin-like enhancement. When the longitudinal momentum transfer is small, the scattering becomes coherent and we can talk about shadowing. Multiple scattering also leads to radiative energy loss.

Theoretical predictions [102] for Υ R_{dAu} and J/ψ R_{pPb} (quarkonium modifica-

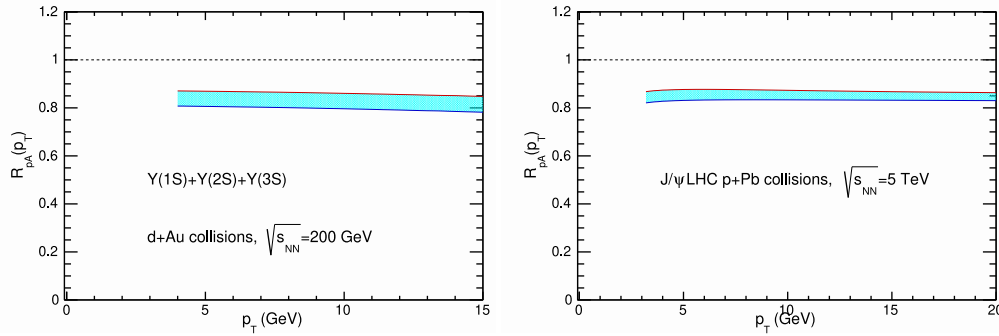


Figure 3.5: Theoretical calculations [102] for R_{pPb} of J/ψ and Υ as a function of p_T in minimum bias collisions with a small (red curve) and large (blue curve) energy loss effect at RHIC (left) and LHC (right). Taken from Ref. [87].

tion) incorporating the above mentioned processes are shown as bands in Fig. 3.5 for STAR (left panel) and LHC (right panel).

3.1.4 Quarkonia Absorption

When the created quarkonium travel through the nucleus, it can interact inelastically and thus be absorbed. In the yield suppression of production is then observed. Important parameter is the absorption cross-section (inelastic cross-section of an interaction of heavy quarkonia with a nucleus.)

The J/ψ absorption cross section was assumed to be independent of the production kinematics however dependencies of the nuclear effects on p_T and Feynman variable x_F were measured. J/ψ production is further sensitive to the gluon distribution in the nucleus. Nuclear absorption effects are negligible at the LHC energy since the quarkonium production time is larger than the nucleus size, however at lower energies this effect might be more significant.

3.2 D^0 in p+Pb collisions

This section is based on the article [103] which refers to the measurement of p_T -differential production cross sections and nuclear modification factors of various D mesons in p+Pb collisions at $\sqrt{s_{NN}} = 5.02$ TeV measured by ALICE in 2016 with the integrated luminosity $L = 292 \pm 11 \mu\text{b}^{-1}$.

The results for the measurement of the nuclear modification factor of various D mesons are shown in Fig. 3.6. The R_{pPb} is compatible with unity in the whole range of p_T within two standard deviations. Because of the size of uncertainties it is not

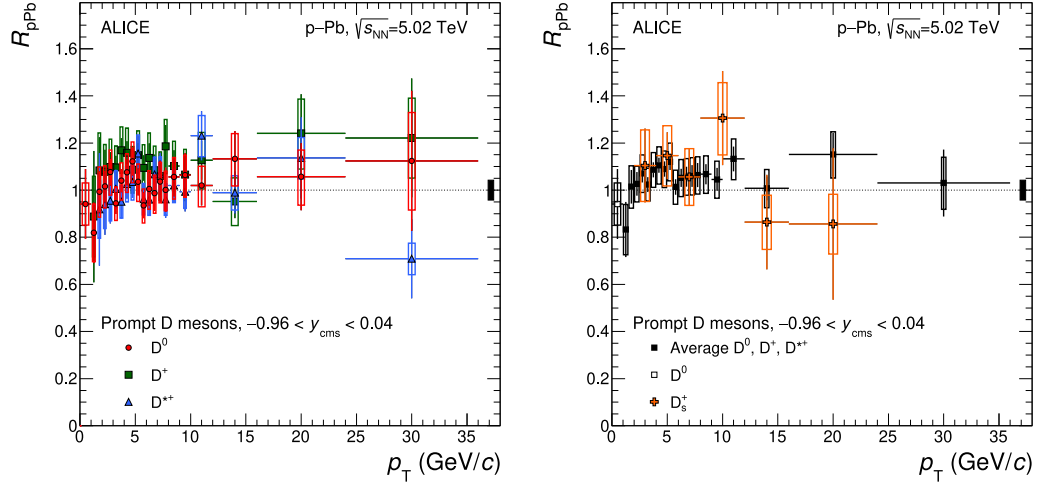


Figure 3.6: Nuclear modification factor R_{pPb} of prompt D mesons in p+Pb collisions at $\sqrt{s_{NN}} = 5.02$ TeV measured by ALICE. Left: results for D^0 , D^+ and D^{*+} . Right: Average of non strange D mesons in $1 < p_T < 36$ GeV/c, D^0 in $0 < p_T < 1$ GeV/c and strange D meson in $2 < p_T < 24$ GeV/c. Taken from Ref. [103].

possible to discuss possible mass dependence that would originate from the collective expansion. This would modify the spectrum of strange D meson with respect to non strange ones. The average of non strange D mesons was calculated using the inverse of the relative statistical uncertainties as weights.

Comparison of the measured data with various models can be seen in Fig. 3.7. In the left panel four models that include only cold nuclear matter effects are shown. A model based on the Color Glass Condensate [104] describes the data within two standard deviations but the model underestimates the data at low p_T . FONLL [105] calculation which is based on perturbative calculations at next-to-leading order describes the data within uncertainties. A model from Vitev et al. [106] based on a LO pQCD calculations with intrinsic k_T broadening, nuclear shadowing and quark charms energy loss in CNM also describes the data. A model from Kang et al. [107] shows different trend and does not describe the data at low p_T . In the right panel is a comparison to models which assume creation of QGP in p+Pb collisions. The Duke model [108] includes both collision and radiative energy losses, whereas the POWLANG [109] takes into account only collision processes. Neither of these models describes the data, but both show a similar trend as the data with a peak at low p_T .

The centrality dependence of the nuclear modification factor of prompt D mesons and charged particles is shown in Fig. 3.8. The data show a hint of suppression at $p_T < 2$ GeV/c which is strongest in the most central collisions. A hint of enhancement can also be seen at $2 < p_T < 6$ GeV/c which is also strongest for the most central

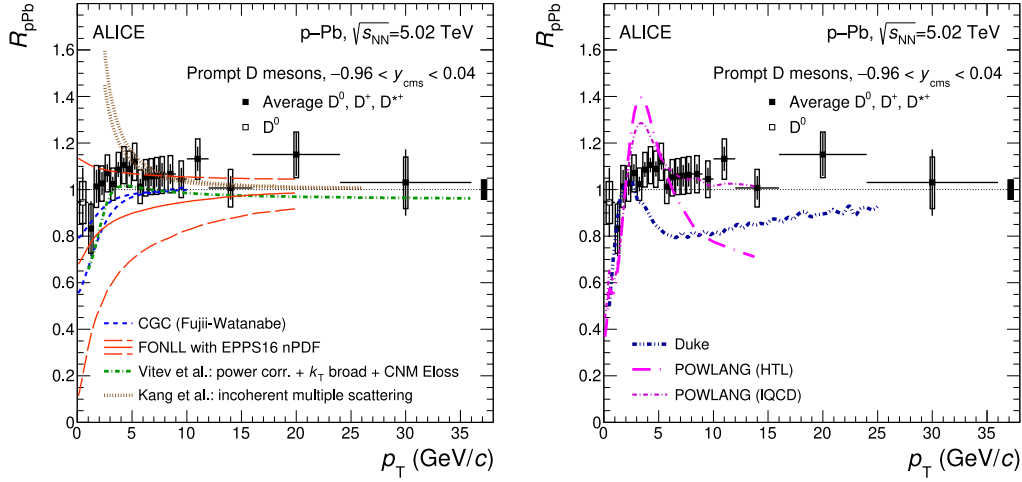


Figure 3.7: Nuclear modification factor R_{pPb} of prompt D mesons in p+Pb collisions at $\sqrt{s_{NN}} = 5.02$ TeV measured by ALICE. Left: Comparison with models that include only CNM effects: CGC [104], FONLL [124] with EPPS16 nPDFs [105], LO pQCD calculation (Vitev et al.) [106] and a calculation based on incoherent multiple scatterings (Kang et al.) [107]. Right: Comparison with transport models: Duke [108] and POWLANG [109]. Taken from Ref. [103].

collisions. The charged particles show similar trend as prompt D mesons in each centrality bin.

Measured p_T differential cross sections of various D mesons are shown in Fig. 3.9. These results significantly differ from the measurements done by LEP so more precise measurements of charm-particle cross sections have to be made for an accurate calculations. The total cross section of D^0 meson per unit rapidity in $-0.96 < y_{cms} < 0.04$ was calculated by integrating the p_T differential cross section from top left panel. The value is

$$d\sigma_{p+Pb, 5.02 \text{ TeV}}^{\text{prompt } D^0}/dy = 88.5 \pm 2.7(\text{stat.})_{-6.1}^{+5.3}(\text{syst.}) \pm 3.3(\text{lumi.}) \pm 0.9(\text{BR}) \text{ mb.} \quad (3.2)$$

The measurements of other D mesons are compatible with the 2013 measurements and are compared with p+p reference [103].

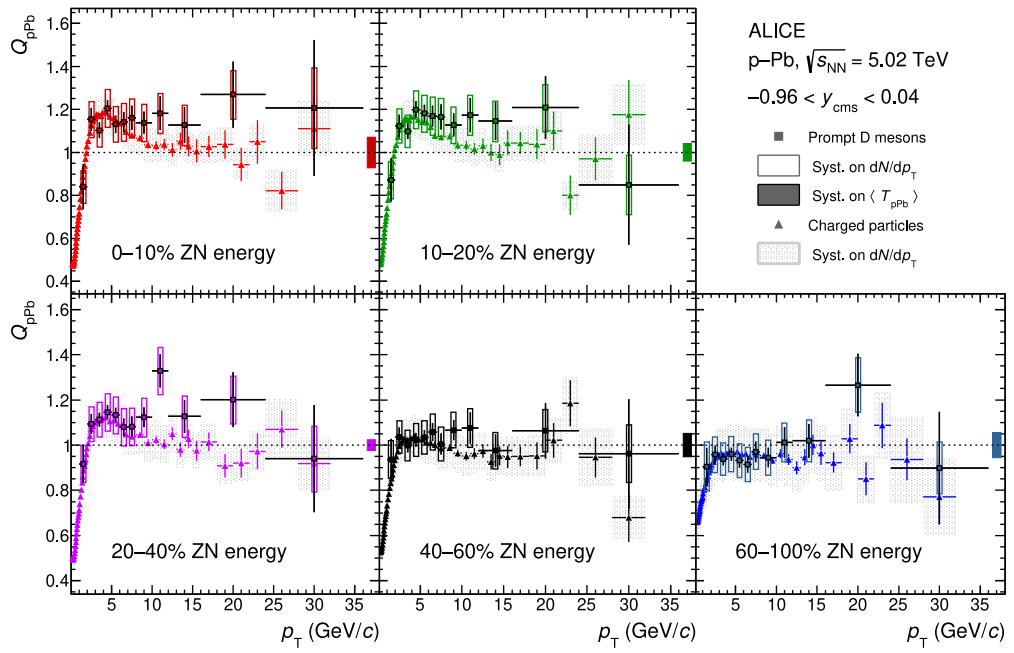


Figure 3.8: Nuclear modification factor of prompt D mesons in p+Pb collisions at $\sqrt{s_{NN}} = 5.02$ TeV measured by ALICE in different centrality classes compared with charged particles. Taken from Ref. [103].

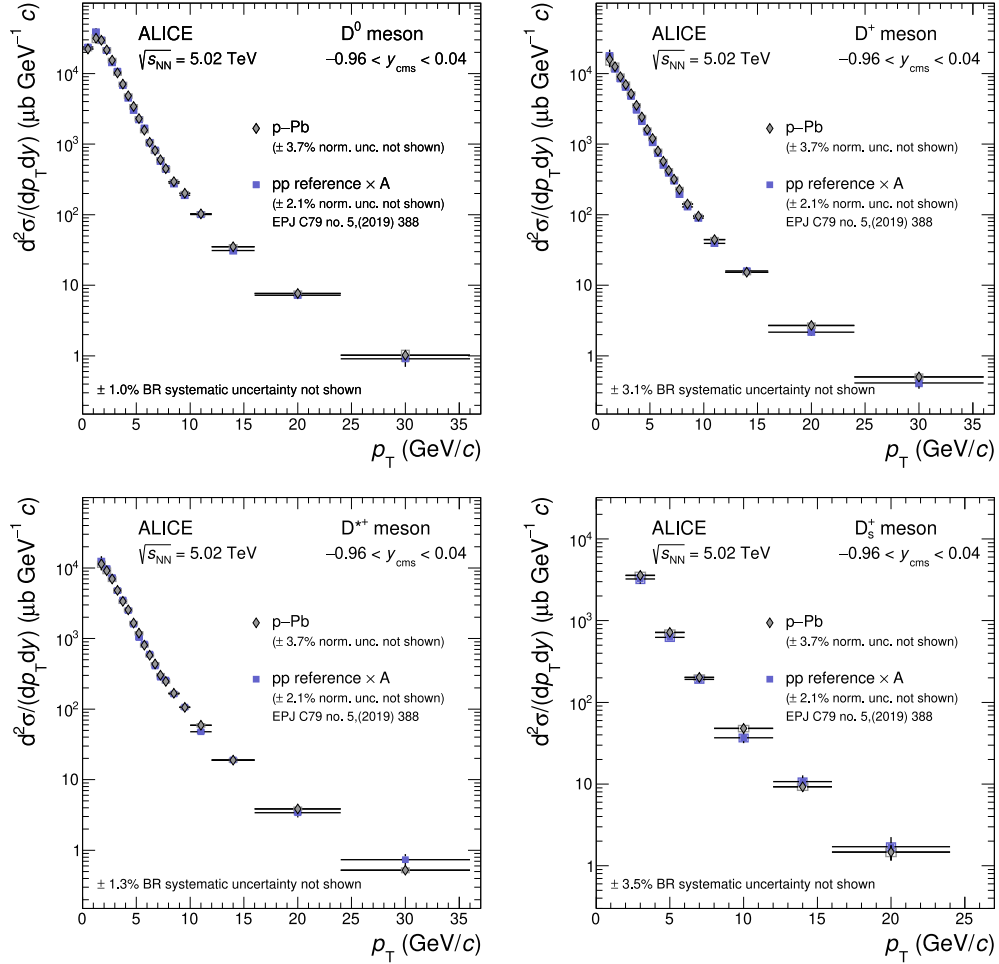


Figure 3.9: p_T -differential cross sections for various D meson kinds with $-0.96 < y_{\text{cms}} < 0.04$ in p+Pb collisions at $\sqrt{s_{\text{NN}}} = 5.02$ TeV measured by ALICE compared with the p+p cross sections scaled by Pb mass number. Taken from Ref. [103].

3.3 Asymmetric Collisions at PHENIX

PHENIX detector was operating at RHIC until 2017 and it has published several results for the asymmetric collisions (p+Au, d+Au...) as well. First of these results is the nuclear modification factor R_{dAu} of prompt D mesons as a function of p_T in Fig. 3.10 in 0–20 % and 60–88 % centrality classes in d+Au collisions at $\sqrt{s_{NN}} = 200$ GeV. The data show a mild dependence with the multiplicity at mid-rapidity. The results at forward and backward rapidities are similar for peripheral collisions, but evidence a strong deviation for the most central events. Data at forward rapidities are described by both theoretical calculation whereas the data at backward rapidity cannot be described using only the nPDFs. This means that other mechanisms not included in the models also play role.

A measurement of v_2 and v_3 of charged particles in three collisions systems p+Au, d+Au and $^3\text{He}+\text{Au}$ measured by PHENIX detector at $\sqrt{s_{NN}} = 200$ GeV [110] are shown in Fig. 3.11. These results were published in Nature Physics and later were largely discussed. The data show non-zero flow coefficients described by models which include hydrodynamic flow (SONIC [111], iEBE-VISHNU [112]) in all three small systems which indicates that hydrodynamic flow is also present in collisions that are not ultra-relativistic heavy-ion. This contradicts the assumption that flow is purely caused by the bulk of the QGP. Authors suggested that there might be droplets of QGP in the small systems but this idea was not largely accepted and is a bit abbreviated. Both above-mentioned models have similar core structure. The initial conditions are evolved using viscous hydrodynamics, the fluid hadronizes, hadron scattering occurs and the flow coefficients are determined using the two-particle correlation method. The model calculations are consistent with the data in all three systems. Both models describe the difference between v_2 and v_3 , collision system dependence and general p_T dependence. However for larger p_T models tend to diverge from the data which might be caused by the hadronic rescattering. Other experiments also measured non-zero flow in the small systems which leads to idea that hydrodynamic flow is not fully understood.

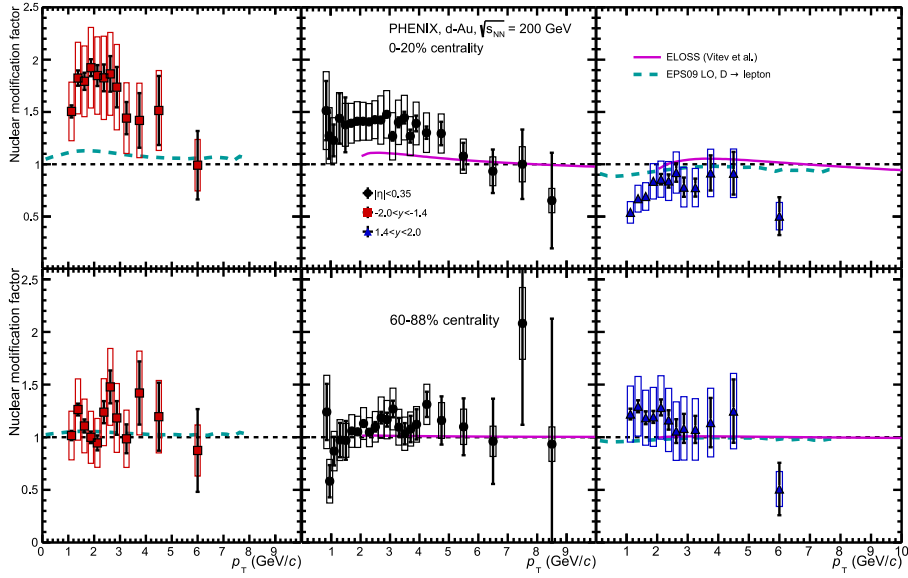


Figure 3.10: The nuclear modification factor R_{dAu} as a function of transverse momentum p_T in 0–20 % and 60–88 % centrality classes in d+Au collisions at $\sqrt{s_{NN}} = 200$ GeV measured by PHENIX. Data are compared to a PYTHIA calculation considering EPS09 LO and a calculation by Vitev et al. considering nPDFs, k_T broadening and CNM energy loss. Taken from Ref. [87].

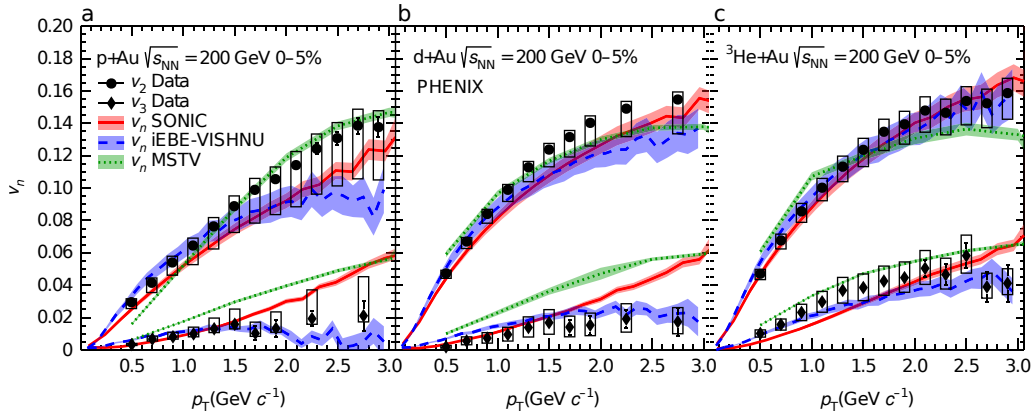


Figure 3.11: Flow coefficients v_n of charged particles as a function of p_T in three collisions systems p+Au, d+Au and ${}^3\text{He}+\text{Au}$ measured by PHENIX detector at $\sqrt{s_{NN}} = 200$ GeV. The data are compared to SONIC [111], iEBE-VISHNU [112] and MSTV [113], [114] theoretical calculations. Taken from Ref. [110].

Chapter 4

Open Charm Hadrons Production

4.1 Properties of Charm Hadrons

Apart from carrying electromagnetic charge or isospin, charmed quarks carry another quantum number which is called charm $C = 1$ (similarly beauty quarks carry beauty $B = -1$ or strange quarks strangeness $S = -1$). The corresponding antiquarks carry quantum number with the opposite sign. Hadrons which have non-zero charm are called open-charm hadrons. On the other hand are hadrons with zero charm and are called hidden charm or quarkonia (or any other heavy-flavor).

In this thesis we focus on the D mesons which are open charm mesons. A summary of elementary properties of various charm particles mentioned in this thesis are in Tab. 4.1. If we compared charmed hadrons to strange particles, charmed particles are heavier and have shorter lifetime. Those properties make the reconstruction of charm hadrons challenging.

Hadron	Quark composition	m [MeV/ c^2]	$c\tau$ [μm]
D^0	$c\bar{u}$	1864.84 ± 0.05	122.9 ± 0.5
D^+	$c\bar{d}$	1869.66 ± 0.05	311.8 ± 2.1
D^{*+}	$c\bar{u}$	2010.26 ± 0.05	—
D_s^+	$c\bar{s}$	1968.35 ± 0.07	151.2 ± 1.2
Λ_c^+	cud	2286.46 ± 0.14	60.7 ± 0.9

Table 4.1: Elementary properties of the open-charm hadrons. Shown properties are quark composition, rest mass m and the mean lifetime $c\tau$. Values taken from Ref. [29].

Charm quarks were theoretically predicted in the '60s when the three quark model was not sufficient to describe all the experimental phenomena. First mea-

surement of charm particles was done simultaneously by two experimental groups in 1974 at BNL and SLAC. The new particle which is a bound state of charm quark and charm antiquark with mass around $3.1 \text{ GeV}/c^2$ was named J/ψ .

The first open-charm hadron was discovered at SLAC-LBL and it was the D^0 meson in the two decay channels $D^0 \rightarrow K^\pm \pi^\mp$ and $D^0 \rightarrow K^\pm \pi^\mp \pi^\pm \pi^\mp$ [115]. The D^\pm meson was firstly observed at the same facility in the $D^\pm \rightarrow K^\mp \pi^\pm \pi^\pm$ decay channel [116].

D mesons are the lightest particles containing a charm quark. It has a consequence that they have to change flavor during their process of decaying and so the weak force is responsible for the decay. This is due to fact that only during the weak interaction can change quark flavor.

Measurement of open-heavy flavor hadrons can provide access to multiple properties of both Quark-Gluon Plasma and high energy collisions in general. The nuclear modification factor R_{AA} can be used to study the energy loss in the hot and dense QCD medium. Production of light-flavor hadrons is suppressed in the central heavy-ion collisions compared to the vacuum collisions of protons. Therefore it is important to measure nuclear modification factor of open-charm hadron for the understanding of particle modification in heavy-ion collisions. The advantage of measuring R_{AA} of open-charm hadrons compared to that of light hadrons is that the heavy quarks contained in the heavy hadrons are produced from the hadronization processes of those quarks whereas light quarks can originate from different processes as well (can be induced from QGP, fragmentation of jets...). The thermal energy of the system (at RHIC energies) is too low to create the heavy quarks after the hard partonic scattering and as a result they originate only from these processes.

The advantage of the origin of heavy quarks mentioned in the previous paragraph can be also used during the measurement of hydrodynamic flow. Since heavy quarks are created in the collision before the QGP, they do not have any original geometry dependence and the only non zero flow contribution can be caused by an interaction with the medium.

Open charm mesons can be also used to test the initial conditions of heavy-ion collisions. This can be accessed by the measurement of the directed flow v_1 . Charm quarks are expected to have every flow coefficient equal to zero in the moment of their creation and two effects can afterwards contribute to their non-zero v_1 . First one is the tilt of the QGP in the reaction plane which would lead to negative slope of v_1 for both D^0 and \overline{D}^0 as a function of rapidity. The second contributing effect might be the electromagnetic field induced by spectator nucleons in the collisions which would lead to negative slope for D^0 and positive for \overline{D}^0 . Probable is that both

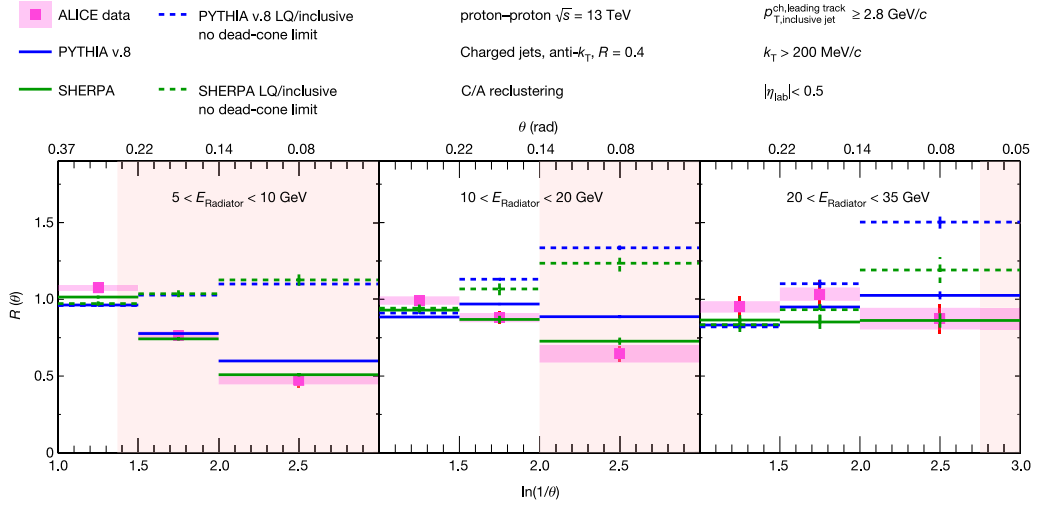


Figure 4.1: The ratios of the splitting-angle probability distributions $R(\theta)$ for D^0 -meson tagged jets to inclusive jets measured in p+p collisions at $\sqrt{s} = 13$ TeV, are shown for $5 < E_{\text{Radiator}} < 10$ GeV (left panel), $10 < E_{\text{Radiator}} < 20$ GeV (middle panel) and $20 < E_{\text{Radiator}} < 35$ GeV (right panel). The data are compared to PYTHIA v.8 [117] and SHERPA [118] simulations including the no dead-cone limit given by the ratio of the angular distributions for light-quark jets (LQ) to inclusive jets. The pink shaded areas correspond to the angles within which emissions are suppressed by the dead-cone effect, assuming a charm-quark mass of $1.275 \text{ GeV}/c^2$. Taken from Ref. [119].

effects contribute to the final v_1 .

Partons originating from the hard scattering usually have large transverse momentum and can thus produce jets. Heavy-flavor induced jets can be used to study the flavor dependence of quark interaction with the QGP. Nuclear modification factor of jets can be measured to study flavor dependence.

Another attribute of heavy quarks is so called dead-cone effect. Apart from collision losses, partons also lose energy by radiating gluons. However from QCD there is an angle below which the gluon radiation is suppressed. This angle depends on the mass of the quark and with higher mass the angle is larger. This means that heavy quarks have larger radiation angle, radiate less gluons than lighter quarks and the observer energy-loss should be lower. First direct observation of this phenomenon was done by ALICE Collaboration in p+p collisions at $\sqrt{s} = 13$ TeV [119] and was possible thanks to the development of reconstruction of cascading quarks and gluons. The jets from D^0 mesons were reconstructed using the Cambridge-Aachen (C/A) algorithm [120]. For the measurement of the dead-cone splitting a new variable called the ratio of the splitting angle $R(\theta)$ was introduced. More details are available in [119]. Results for the measurement of this variable are in Fig. 4.1 compared to

PYTHIA v.8 [117] and SHERPA [118] simulations including the no dead-cone limit given by the ratio of the angular distributions for light-quark jets (LQ) to inclusive jets. As can be seen the models including the dead-cone limit describe the data. As a next step it is necessary to study dead-cone effect in heavy-ion collisions in which the partons interact strongly in the QGP medium and undergo medium-induced energy losses.

Open-charm hadrons can provide access to various properties of hadronization mechanisms, conditions in the hard scattering or those of Quark-Gluon Plasma. Their reconstruction is challenging due to their short lifetime.

4.2 Open-charm Hadrons in p+p Collisions

One of the main motivations for the measurement of open-charm hadrons in the heavy-ion collisions is that their production and properties in the p+p collisions is quite well understood. Another reason is of course that charm quarks are too heavy to originate from the hot and dense medium and come from the hard scattering processes in the early phases of a collision. This means that they have to pass through the QGP medium and are affected by it (lose energy and momentum).

An example of measured production cross section of prompt D^0 , D^+ and D^{*+} done by ALICE at $\sqrt{s} = 7$ TeV [121] can be seen in Fig. 4.2. The data are compared to FONLL [122], [123], [124] and GM-VFNS [125], [126] theoretical models. The data are reproduced within uncertainties by both models. The data however tend to be higher than the central value of the FONLL predictions.

Another example of measurement of the production cross-section measured by ATLAS at $\sqrt{s} = 7$ TeV [127] can be seen in Fig. 4.2. The data are compared to various models which describe the measurement within uncertainties. The GM-VFSN [128], [125], [129] predictions agree with the data in both shape and normalisation, however the FONLL [122], [130], [131], [124], MC@NLO [132], [133] and POWHEG [134], [135] prediction central values lie beneath the measurement even though the prediction reproduce the shapes.

STAR collaboration also measured charm quark production cross-section as can be seen in Fig. 4.4. This measurement was done in p+p collisions at $\sqrt{s} = 200$ GeV [136]. The data are compared to FONLL calculation [137] which describes the data and to various PYTHIA tunes where only the tune used in [136] describes the data even for low p_T .

An interesting result has been published by ALICE collaboration and can be

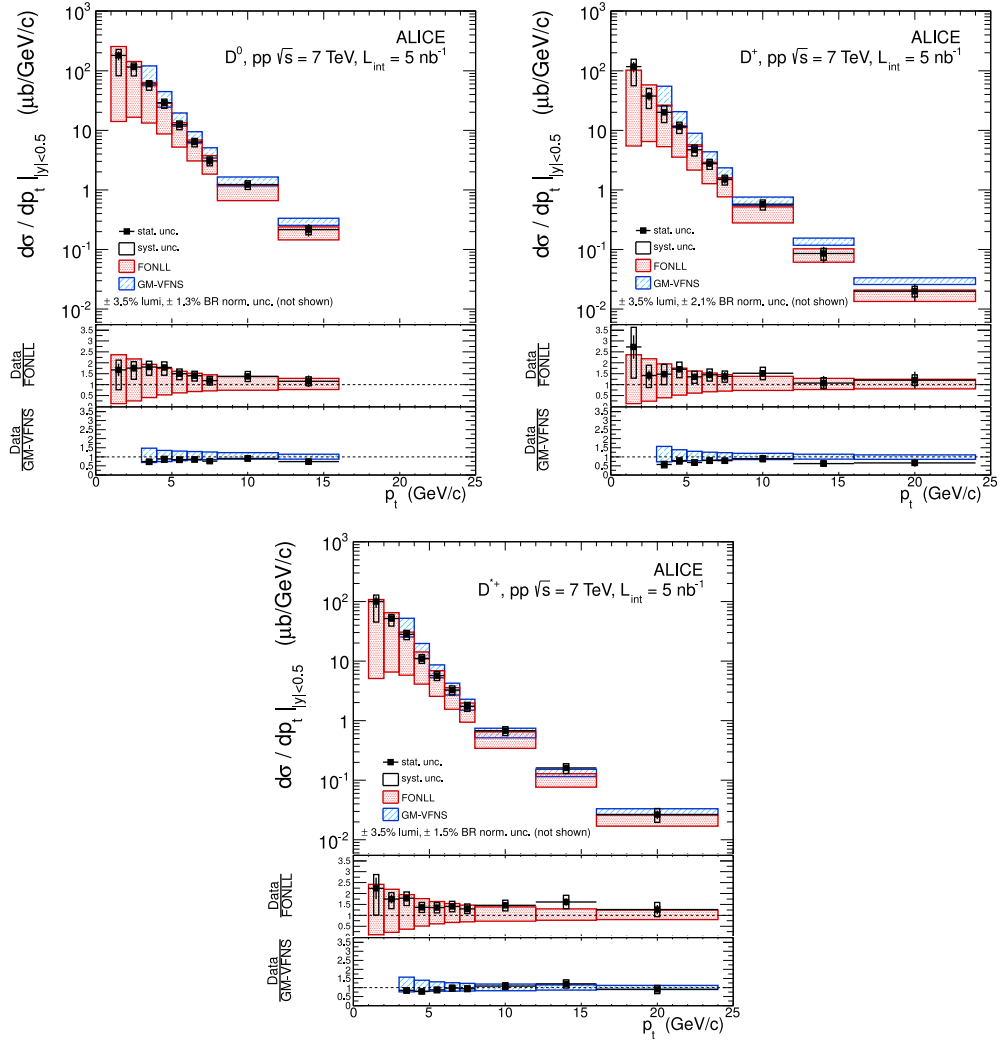


Figure 4.2: Production p_T differential cross section of prompt D^0 , D^+ and D^{*+} measured by ALICE experiment in p+p collisions at $\sqrt{s} = 7$ TeV. The data are compared to FONLL [122], [123], [124] and GM-VFNS [125], [126] theoretical calculations. Taken from Ref. [121].

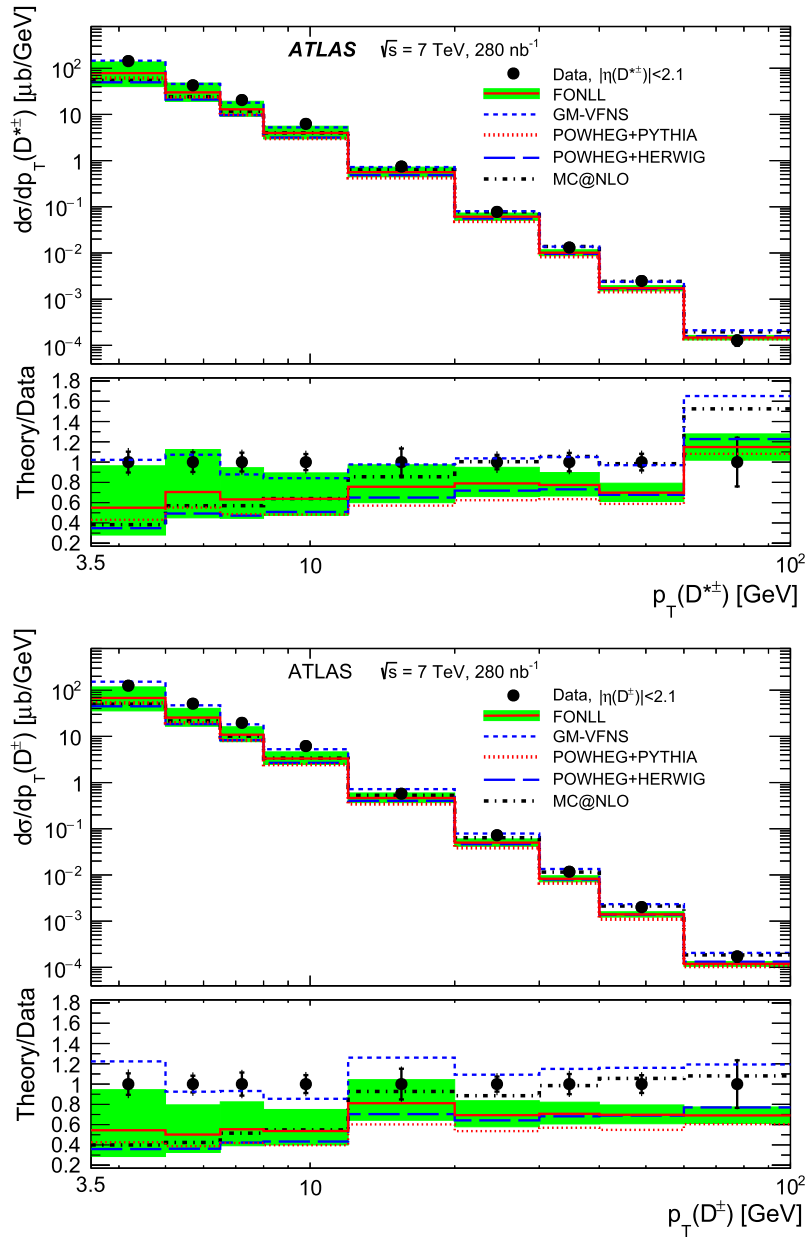


Figure 4.3: Production p_T differential cross section of D^\pm and $D^{*\pm}$ measured by ATLAS experiment in $p+p$ collisions at $\sqrt{s} = 7$ TeV. The data are compared to NLO QCD calculations of FONLL [122], [130], [131], [124], POWHEG+PYTHIA [134], POWHEG+HERWIG [135], MC@NLO [132], [133] and GM-VFNS [128], [125], [129]. Taken from Ref. [127].

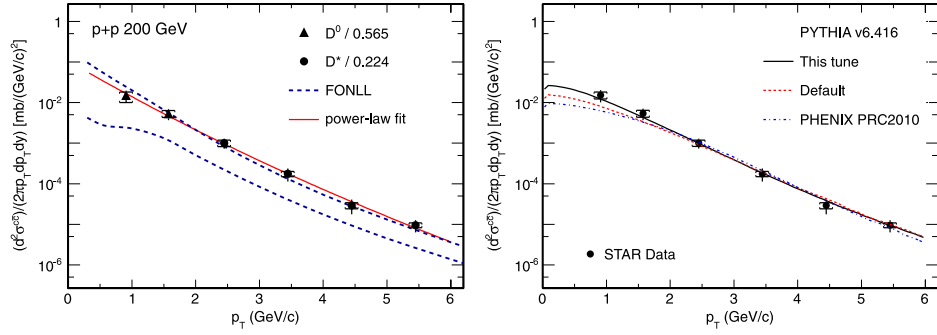


Figure 4.4: $c\bar{c}$ production cross section inferred from D^0 and D^* production in p+p collisions at $\sqrt{s} = 200$ GeV compared to FONLL [137] calculations (left) and PYTHIA calculations (right). Taken from Ref. [136].

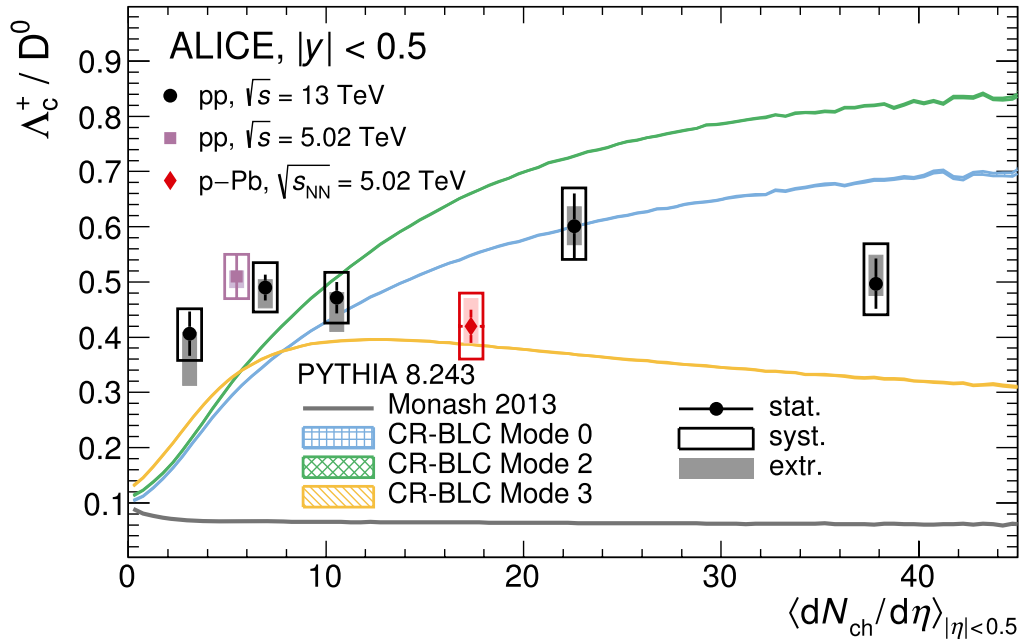


Figure 4.5: Ratios of p_T integrated yields of Λ_c^+ and D^0 hadrons measured by ALICE in p+p collisions at $\sqrt{s} = 13$ TeV. Results from p+p and p+Pb collisions at $\sqrt{s} = 5.02$ TeV [138] are also shown together with the corresponding PYTHIA predictions [139], [140]. Taken from Ref. [141].

seen in Fig. 4.5 where the ratios of p_T integrated yields of Λ_c^+ and D^0 are shown. This measurement shows clear enhancement of baryon-meson ratio in p+p collisions compared to theoretical predictions from PYTHIA. This would suggest that charm hadronization in p+p is not fully understood. The fragmentation ratios are usually taken from electron+positron collisions which is a clean environment however the behavior might be different than in the collisions of protons

4.3 Open-charm Hadrons in Heavy-Ion Collisions

4.3.1 Open-charm Hadrons Measured by STAR

The best qualitative measurements of heavy-flavor particles were done at STAR between 2014 and 2016. It is due to the Heavy Flavor Tracker which was installed at STAR in those years. The shown results from heavy-ion collisions are from 2014 and 2016 runs at $\sqrt{s_{NN}} = 200$ GeV.

One of the first measurements with the HFT was the R_{AA} of D^0 mesons [79]. The p_T dependence of R_{AA} in central collisions (0-10 %) can be seen in Fig. 4.6. It is clear that D^0 mesons are significantly suppressed in the heavy-ion collisions and the suppression is larger for larger p_T . This is caused by the energy loss of charm quarks in the volume of the QGP. The figure shows similar suppression for D mesons and charged mesons measured by ALICE in Pb+Pb collisions at $\sqrt{s_{NN}} = 2.76$ TeV [143], [144] and also for π^\pm mesons measured by STAR [142]. The suppression is similar for open-charm mesons and light quarks in the measurement of both experiments. The data are reasonably well described by theoretical calculations which contain hydrodynamic flow and energy loss of charm quarks in the QGP.

The centrality dependence of D^0 R_{AA} are in Fig. 4.7. The shown data are from the measurement with the HFT (2014) [79] and without it (2010/11) [145], [146]. The suppression for low $p_T < 1$ GeV/c is independent of centrality of the collision. However the situation is different for large $p_T > 3$ GeV/c where the suppression decreases going from central to peripheral collision. This supports the ideas of it being caused by energy loss in the QGP.

Another, yet unpublished result, of nuclear modification factor from STAR is shown in Fig. 4.8. It shows R_{AA} as a function of p_T of mesons D^\pm [147] measured by STAR in Au+Au collisions at $\sqrt{s_{NN}} = 200$ GeV in 0-10 %, 10-40 % and 40-80 % centrality classes compared to D^0 mesons [79] measured in the same system and to ALICE measurement of D^\pm mesons in Pb+Pb collisions at $\sqrt{s_{NN}} = 5.02$ TeV [148]. All the shown data are in good agreement and indicate same suppression of D

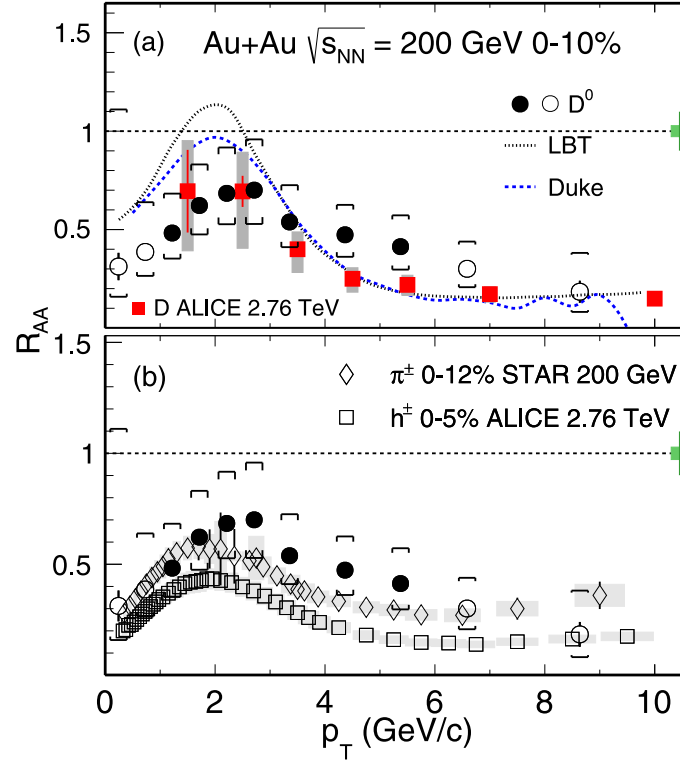


Figure 4.6: The p_T dependence of D^0 R_{AA} in 0-10 % central Au+Au collisions measured by STAR at $\sqrt{s_{NN}} = 200$ GeV. The data are compared to measurement of charged pions by STAR at the same collision energy [142] and to ALICE experiment results for D mesons and charged hadrons in Pb+Pb collisions at $\sqrt{s_{NN}} = 2.76$ TeV [143], [144]. Taken from Ref. [79].

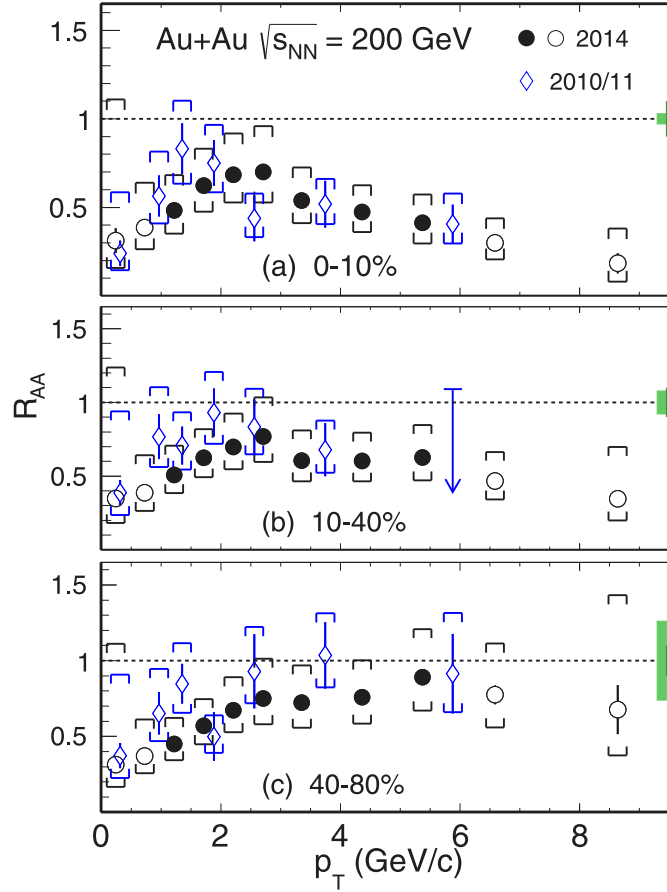


Figure 4.7: The centrality dependence of $D^0 R_{AA}$ in Au+Au collisions measured by STAR at $\sqrt{s_{NN}} = 200$ GeV with the HFT from 2014 and without in from 2010/11 [145], [146]. Taken from Ref. [79].

mesons. The centrality dependence of D^\pm is also consistent with the one previously measured for D^0 mesons. The suppression is largest at high transverse momenta in the most central collisions and gets weaker going to mid-central and peripheral collisions.

This result allowed to compute the total open charm hadron production cross section per nucleon pair in 0-40 % central Au+Au collisions at $\sqrt{s_{\text{NN}}} = 200$ GeV in the p_{T} interval $0 < p_{\text{T}} < 8$ GeV/ c . The result for total cross section and also for individual open charm hadrons is shown in Tab. 4.2. The invariant spectra D^0 [79], D^\pm [147] and D_s^\pm [149] mesons and Λ_c^\pm [150] baryons measured in Au+Au collisions at $\sqrt{s_{\text{NN}}} = 200$ GeV have been used. Also the p+p reference is shown and was calculated using the $c\bar{c}$ cross section from [136]. The cross sections in Au+Au and p+p collisions are consistent within uncertainties. This result suggests that charm quark production cross section per nucleon pair follows the scaling of total number of binary collisions. However the cross sections of individual hadrons are largely modified due to the interaction within the medium (coalescence hadronization) and this leads to redistribution of charm quarks among the open-charm species.

Collision system	Hadron	$d\sigma/dy$ [μb]
Au+Au at 200 GeV Centrality: 10-40 %	D^0	39.0 ± 0.6 (stat) ± 1.1 (syst)
	D^\pm	19.2 ± 0.9 (stat) ± 3.1 (syst)
	D_s	15.4 ± 1.7 (stat) ± 3.6 (syst)
	Λ_c	39.7 ± 5.8 (stat) ± 26.7 (syst)
	Total:	113.3 ± 6.2 (stat) ± 27.2 (syst)
p+p at 200 GeV	Total:	130 ± 30 (stat) ± 26 (syst)

Table 4.2: Total open charm hadron production cross section per binary collision as measured in 10-40 % central Au+Au collisions at $\sqrt{s_{\text{NN}}} = 200$ GeV and p+p collisions at $\sqrt{s} = 200$ GeV. The invariant spectra of D^0 [79], D^\pm [147] and D_s^\pm [149] mesons and Λ_c^\pm [150] baryons measured in Au+Au collisions at $\sqrt{s_{\text{NN}}} = 200$ GeV have been used. The p+p reference was calculated using $c\bar{c}$ cross section [136]. Taken from [147].

The elliptic flow v_2 of open-charm mesons was measured [82] to either confirm or disprove whether the quarks flow similarly as the light quarks. The results can be seen in Fig. 4.9 where the v_2 is shown as a function of p_{T} . In the upper panel there is a hint of mass ordering for $p_{\text{T}} < 2$ GeV/ c . For $p_{\text{T}} > \text{GeV}/c$ the v_2 of D^0 mesons is comparable to that of light flavor hadrons [151]. In the lower panel is the v_2 scaled by the number of constituent quarks n_q (2 for mesons and 3 for baryons) plotted as a function of $(m_{\text{T}} - m_0)/n_q$ where m_{T} is the transverse mass and m_0 rest mass of given hadron. All the shown hadrons, including D^0 , follow the scaling with

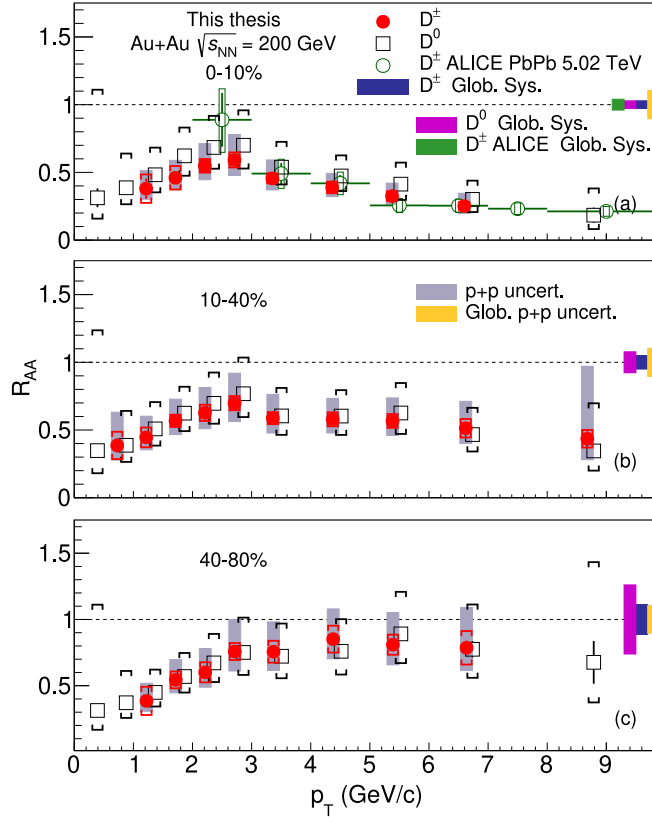


Figure 4.8: R_{AA} as a function of p_T of D^0 [79] and D^\pm [147] mesons measured by STAR in Au+Au collisions at $\sqrt{s_{NN}} = 200$ GeV in 0-10 %, 10-40 % and 40-80 % centrality classes. Data are compared to ALICE measurement of D^\pm mesons in Pb+Pb collisions at $\sqrt{s_{NN}} = 5.02$ TeV [148]. Taken from Ref. [147].

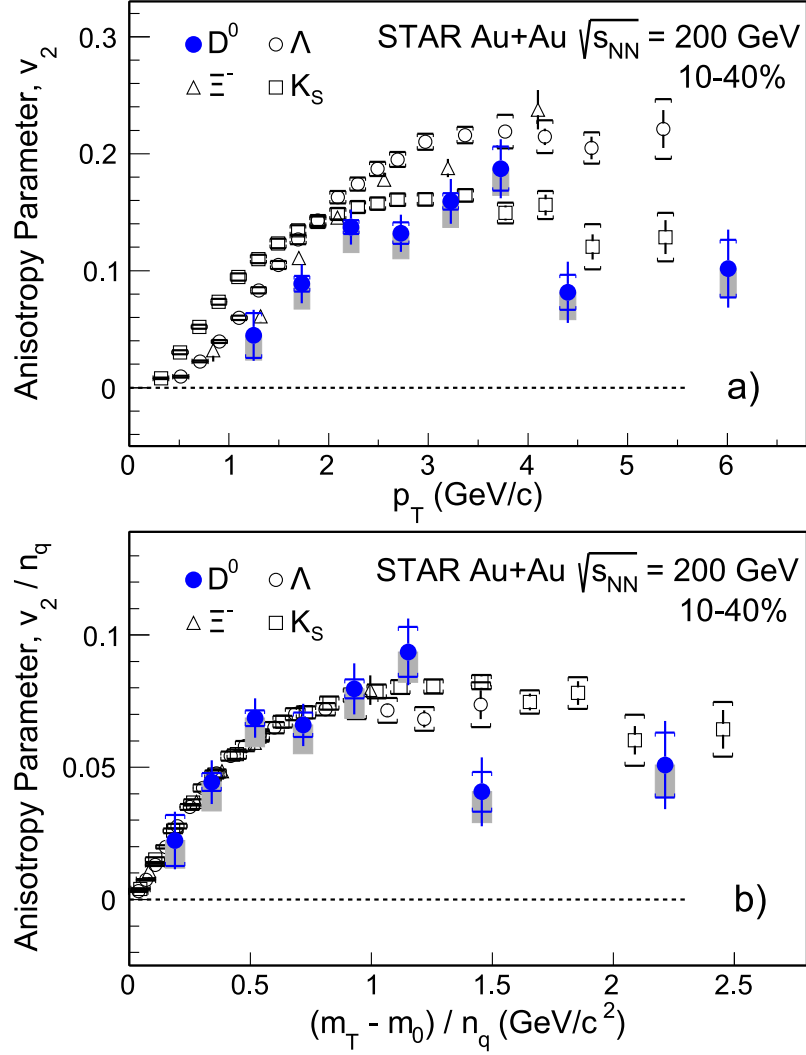


Figure 4.9: (a) v_2 as a function of p_T and (b) v_2/n_q as a function of $(m_T - m_0)/n_q$ where n_q is the number of constituent quarks for D^0 in the 10-40 % centrality class in Au+Au collisions and comparison with K_S^0, Λ and Ξ^- [151] measured by STAR. Taken from Ref. [82].

the number of constituent quarks. These results indicate that charm quarks get very close to thermal equilibrium within the QGP.

Baryon to meson ratio of open-charm mesons measured by STAR [150] is in Fig. 4.10. The Λ_c/D^0 ratio is comparable in magnitude to the light quark ratios p/π and Λ/K_S^0 [65], [65] and shows similar p_T dependence as the ratios of light quarks. In the lower panel the data are compared to various theoretical calculations. A significant enhancement with comparison to the calculation from PYTHIA (MONASH tune[139] without CR [152]) can be seen. This suggests significant modification of D_s^\pm mesons in Au+Au collisions compared to p+p collisions. The modification with CR [152] enhances the baryon production with the comparison to mesons and gives

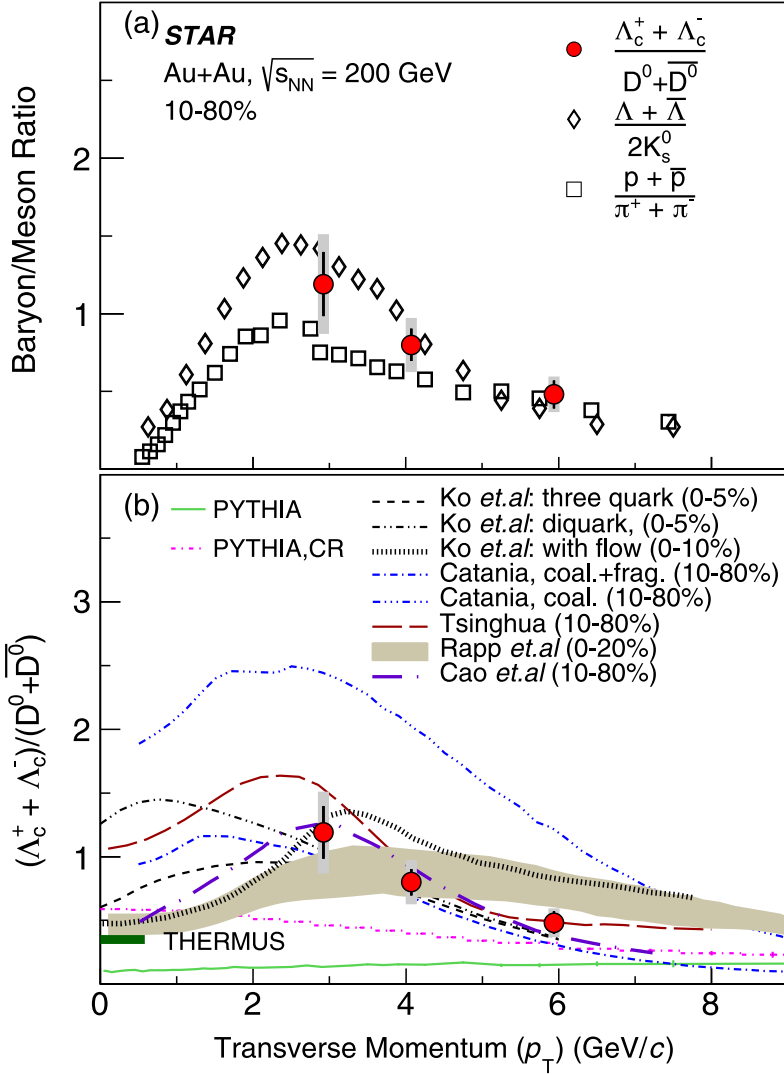


Figure 4.10: Λ_c/D^0 ratio as a function of p_T at midrapidity for Au+Au collisions at $\sqrt{s_{NN}} = 200$ GeV in 10-80 % centrality compared to light quarks (top) [65], [153] and theoretical calculations [154]-[159] (bottom). Taken from Ref. [150].

a Λ_c/D^0 ratio consistent with those measured in p+p and p+Pb collisions measured at the LHC [160], [161]. PYTHIA fails to describe the Au+Au data completely. Several models predict coalescence hadronization [154]-[159] however none of them is able to describe the data in full p_T range.

The measurement of the D^0 directed flow v_1 as a function of rapidity y in 10-80 % central Au+Au collisions measured by STAR at $\sqrt{s_{NN}} = 200$ GeV [162] can be seen in Fig. 4.11. The comparison with the measurement of charged kaons indicates that the slope of v_1 is negative and larger than that of kaons [163] which is in agreement with both theoretical predictions [164],[165],[166]. However the precision of this measurement is not sufficient to claim that the slope is caused by the electromagnetic field produced by spectators in the Au+Au collision and further measurements need

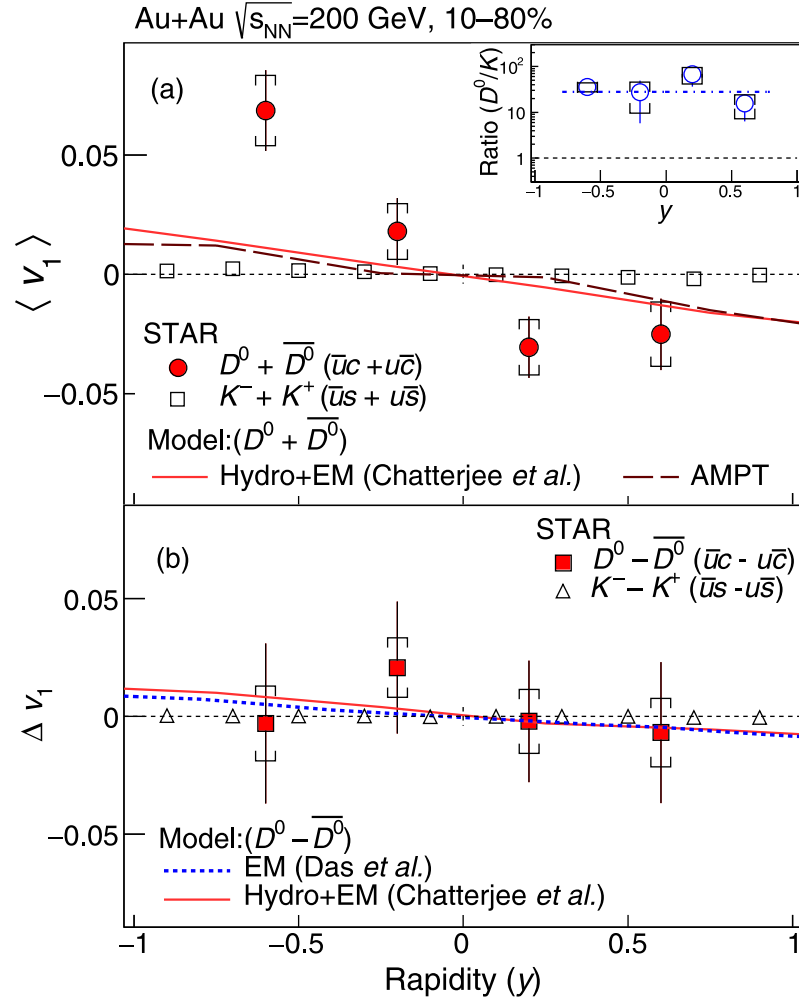


Figure 4.11: Directed flow of D^0 and \bar{D}^0 mesons as a function of rapidity y in 10–80 % central Au+Au collisions at $\sqrt{s_{NN}} = 200$ GeV measured by STAR. Panel (a) shows the average of D^0 and \bar{D}^0 v_1 and panel (b) shows the difference between v_1 of D^0 and \bar{D}^0 . The data are compared to multiple theoretical calculations [164],[165],[166] and to the measurement of charged kaons at the same energy in the same system [163]. Taken from Ref. [162].

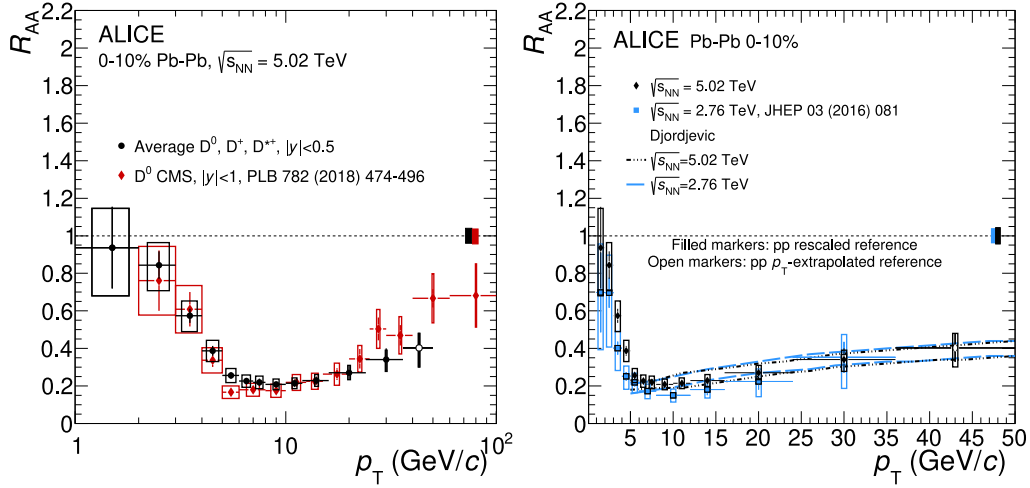


Figure 4.12: R_{AA} of averaged D mesons (D^0 , D^+ and D^{*+}) measured by ALICE and D^0 mesons measured by CMS [167] in 0-10 % Pb+Pb collisions at $\sqrt{s_{NN}} = 5.02$ TeV. ALICE results from Pb+Pb collisions at $\sqrt{s_{NN}} = 2.76$ TeV are also shown. The data are compared to Djordjevic [168] model predictions. Taken from Ref. [148].

to be conducted.

4.3.2 Open-charm Hadrons Measured by ALICE

From the four large experiments at the LHC, ALICE focuses on the heavy-ion program the most. Similarly as STAR with the HFT, ALICE is capable of great reconstruction of open-charm hadronic decays.

Measurement of R_{AA} of D mesons (D^0 , D^+ and D^{*+} average) measured by ALICE at $\sqrt{s_{NN}} = 5.02$ TeV [148] can be seen in Fig. 4.12. The left panel shows comparison with the CMS measurement at the same collision energy [167]. The data from both experiments are in a good agreement. Both show highest suppression for p_T around 10 GeV/c. The right panel compares the measurement to the older one conducted by ALICE at $\sqrt{s_{NN}} = 2.76$ TeV and to the Djordjevic model [168]. The data from both collision energies show similar suppression and are consistent within uncertainties. The model calculations are also in a good agreement with the data.

Fig. 4.13 shows a comparison of the R_{AA} in three centrality classes measured by ALICE at $\sqrt{s_{NN}} = 5.02$ TeV [148]. The suppression is decreasing when coming from the central to peripheral collisions. The R_{AA} of charmed mesons is lower than that of the charged particles [51]. The nuclear modification factors differ by more than 3σ in all the centrality classes for $p_T < 8$ GeV/c. Explanation of this phenomenon is not straightforward because multiple contributions might be responsible for the

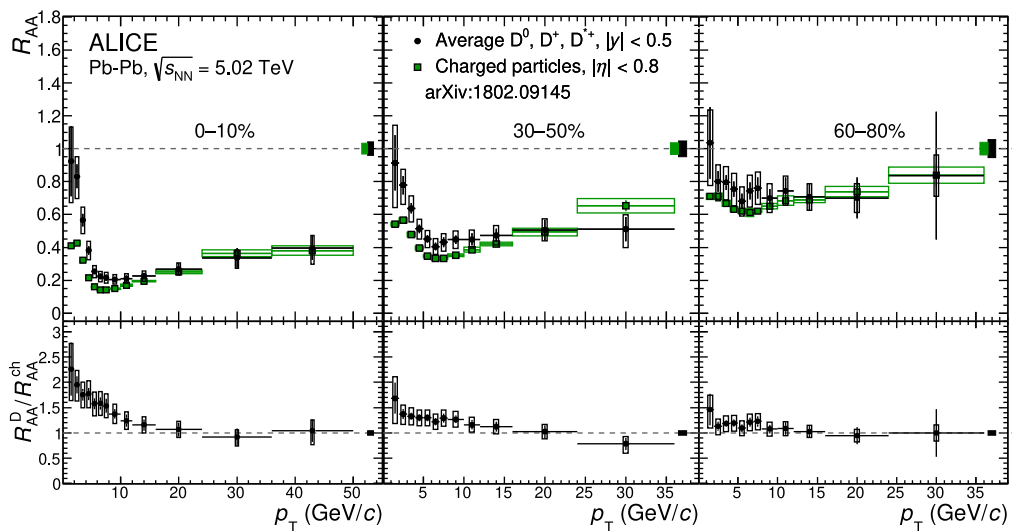


Figure 4.13: Average R_{AA} of prompt D mesons (D^0 , D^+ and D^{*+}) mesons in the 0–10 % (left), 30–50 % (middle) and 60–80 % (right) centrality classes measured by ALICE at $\sqrt{s_{NN}} = 5.02$ TeV compared to the R_{AA} of charged particles [51] in the same centrality classes. The ratios of the R_{AA} are shown in the bottom panels. Taken from Ref. [148].

difference such as the yield of light hadrons should have contribution from soft processes at low p_T , or the effects of radial flow and hadronization via recombination. These results show that charm quarks lose a significant portion of their energy also at the LHC energies.

A comparison of the D meson average to various models [169]–[174] can be seen in Fig. 4.14 in the left panel. The requirement is that the models should describe both elliptic flow and the nuclear modification factor. A significant v_2 can be observed in the right panel for $2 < p_T < 10$ GeV/c in 30–50 % central collisions. The v_2 is compared to the same theoretical models as the R_{AA} .

ALICE has also measured baryon to meson ratio of D^0 meson [175] and the result can be seen in Fig. 4.15. The left panel shows the Λ_c^+/D^0 ratio as a function of transverse momentum measured in 0–80 % central Pb+Pb collisions at $\sqrt{s_{NN}} = 5.02$ TeV compared to p+Pb collisions at $\sqrt{s_{NN}} = 5.02$ TeV and p+p collisions at $\sqrt{s_{NN}} = 7$ TeV. The Pb+Pb data are clearly enhanced compared to small system collisions. This shows Λ_c^+ modification similar to that measured at STAR which is caused by coalescence hadronization of charm quarks. In the right panel is comparison to various theoretical models [156], [176], [177]. However there is a difference between STAR and ALICE results. The STAR results were compatible with the Catania model calculation [156] which incorporates both coalescence and fragmentation whereas the ALICE result is consistent with Catania model with coalescence

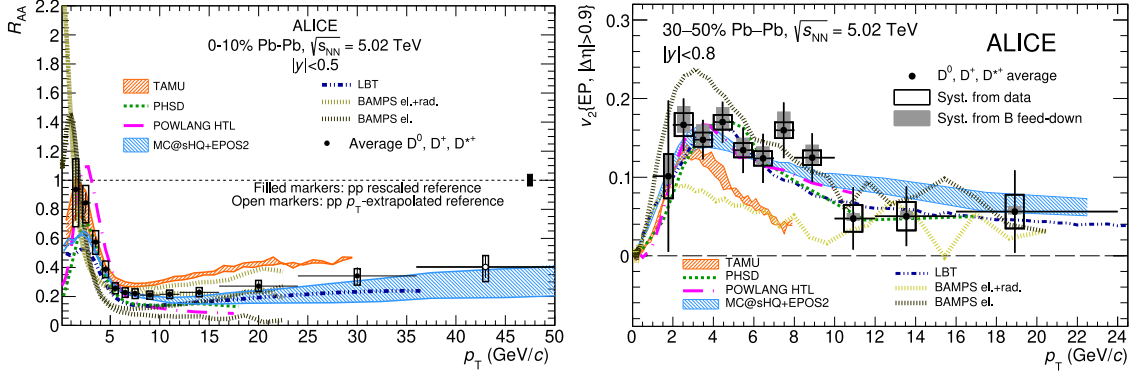


Figure 4.14: Average R_{AA} of prompt D mesons (D^0 , D^+ and D^{*+}) mesons in the 0–10% (left) and their average elliptic flow v_2 in the 30–50% centrality class [178] (right) measured by ALICE at $\sqrt{s_{NN}} = 5.02$ TeV. Data are compared to models [169]–[174] that have predictions for both observables at low p_T . Taken from Ref. [148].

only. This implies that hadronization mechanisms of charm quarks are different at LHC and RHIC energies.

However as has been previously shown in Fig. 4.5, Λ_c^+ production at LHC energies is not trivial and fully understood, because enhancement of yield has also been observed in p+p collisions where QGP is not present.

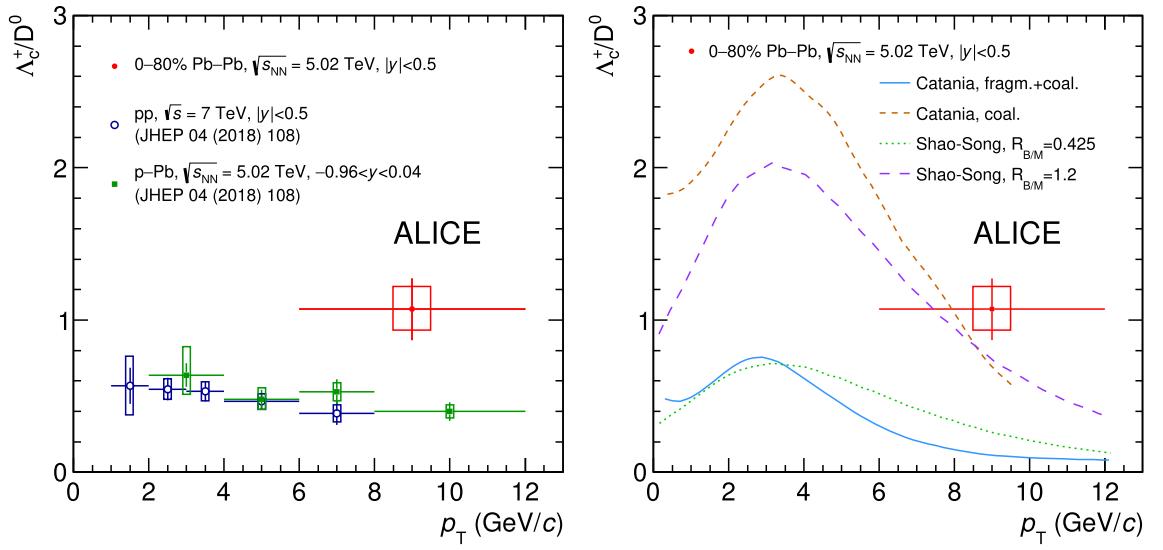


Figure 4.15: Λ_c^+/D^0 ratio as a function of p_T measured by ALICE in the 0–80 % central Pb+Pb collisions at $\sqrt{s_{NN}} = 5.02$ TeV compared to p+Pb collisions at $\sqrt{s_{NN}} = 5.02$ TeV and p+p collisions at $\sqrt{s_{NN}} = 7$ TeV (left). The right panel shows comparison to various model predictions [156], [176], [177]. Taken from Ref. [175].

Chapter 5

Analysis of Experimental Data

The aim of this thesis was preview of the future analysis in order to determine potential problems and to give an outlook for future work on this topic.

This chapter gives details of the analysis of D^0 meson in the decay channel $D^0 \rightarrow K^- \pi^+$ (branching ratio $(3.89 \pm 0.04) \%$ [29]) and D^* meson in the decay channel $D^* \rightarrow K^- \pi^+ \pi^+$. A cartoon of charm quark fragmentation is in Fig. 5.1.

Typical analysis of full data sample lasts several years and requires very careful quality assurance (QA) of data and detailed study of analysis steps is needed. This was not possible in the scope of this Master's thesis.

At STAR the collision data are saved into DAQ files. After the offline reconstruction the data are saved into MuDst files which contain full information about collisions. Unfortunately these files are quite large, so they are further reduced into PicoDst which were used as an entry for this analysis. PicoDst contain information about events, tracks, triggers or particle identification (PID) information from detectors.

The first code working on the same principle as [2] was developed and constantly improved. This code applied event cuts, PID cuts and selected candidates for D mesons. Output was a .root file containing branches for signal and background candidates. These branches were further analyzed by another macro which could implement additional cuts and create histograms of results.

The data were analyzed on RCF (RHIC Computing Facility) which is computing farm used also by STAR users. The full statistics of p+Au analysis usually was about 5000 jobs and the p+p analysis over 20 000 jobs.

The process of analyzing the dataset with given cuts took several days, usually 5-6 if there was not any problem with the RCF.

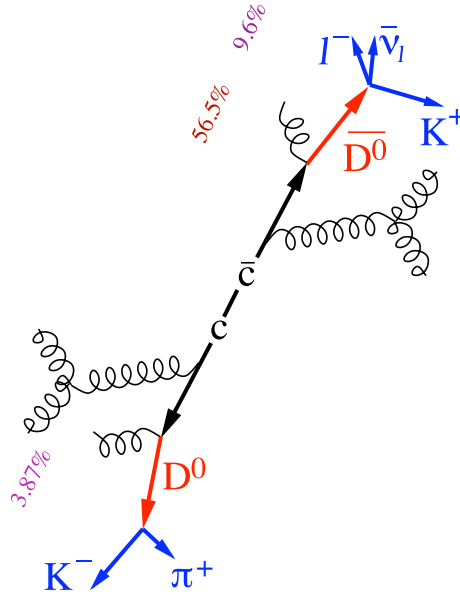


Figure 5.1: Cartoon of decay of the charm quark c and subsequently D^0 . Taken from Ref. [3].

5.1 Analysis of p+Au Collisions

5.1.1 Dataset and Event Selection

Data for this analysis were taken in the p+Au collisions in year 2015 by STAR detector at energy $\sqrt{s_{NN}} = 200$ GeV. Total number of collisions was $9 \cdot 10^8$.

The main challenge of this analysis is that in 2015 the HFT was not working properly and so the information measured by this detector are unusable for further analysis. This has a consequence that this analysis cannot rely on topological variables that were used for example in the measurement of D^0 meson in Au+Au collisions in Ref. [79] from 2014 and 2016 when the HFT performance was brilliant.

The used trigger was the minimum bias trigger. The total of $3.5 \cdot 10^8$ of events passed this trigger.

Another event selection cut is $|V_{z[\text{VPD}]} - V_{z[\text{TPC}]}|$ where $V_{z[\text{VPD}]}$ is the z-position of the vertex calculated using Eq. (2.4) from the VPD detector and $V_{z[\text{TPC}]}$ is the z-position measured by TPC. This cut is derived from the VPD resolution and value of this cut used in this analysis is 6 cm. This was used in order to reduce pile-up events.

If event is to be accepted for further analysis, it has to pass the following criteria

- pass the minimum bias trigger

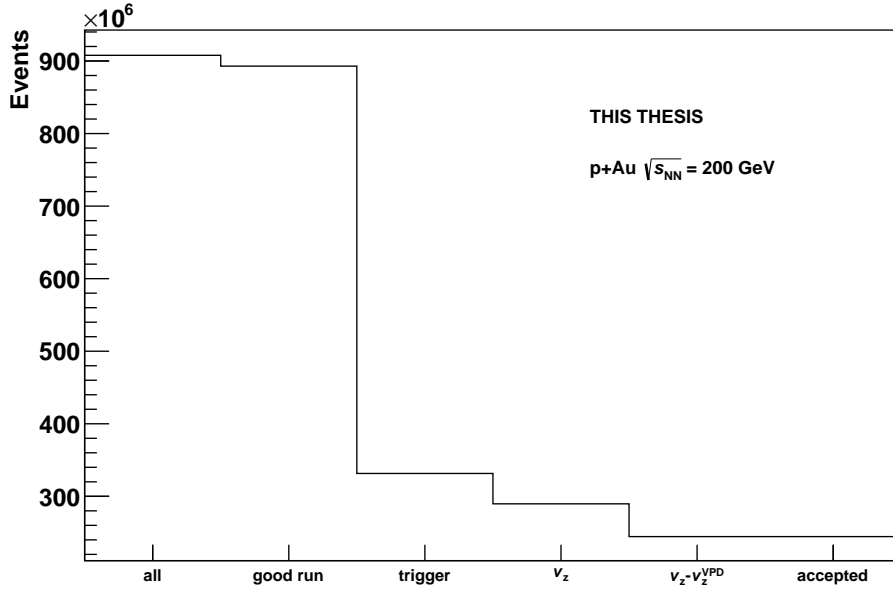


Figure 5.2: Number of events that passed individual event selection criteria.

- $|V_{z[\text{VPD}]} - V_{z[\text{TPC}]}| < 6 \text{ cm}$
- $|V_{z[\text{TPC}]}| < 30 \text{ cm}$

Histogram of the event statistics is shown in Fig. 5.2. In Figure can be seen that the biggest cut is the trigger which causes significant decrease of the number of accepted events.

5.1.2 Particle Identification

Several track quality cuts were used to improve track selection for the further analysis, which are listed below:

- number of TPC hits > 20
- $\frac{\text{number of TPC hits}}{\text{maximal possible number of TPC hits}} > 0.52$
- $p_T > 0.15 \text{ GeV}/c$
- global DCA $< 2 \text{ cm}$
- $|\eta| < 1$

where number of TPC hits denotes the number of spatial hit points used for the reconstruction of a track, $\frac{\text{number of TPC hits}}{\text{maximal possible number of TPC hits}}$ is used to prevent tracks which

split into two tracks, global DCA is the distance of the closest approach of a track to primary vertex, the minimum transverse momentum p_T and pseudorapidity η are set for the track to be able to reach TOF.

So called hybrid TOF particle identification was used in this analysis. This means that TOF matching was not strictly required for the accepting of the track. If the track was matched in TOF, cuts for $1/\beta$ were applied. If the track was not TOF matched, it could still be accepted if it passed TPC PID cuts. When the TOF matching was strictly required the resulting statistics of the tracks was too low for a reasonable analysis.

The next step was to optimize the pion and kaon selection for the reconstruction of meson D^0 . In the first iteration, the same cuts as in Ref. [79] were used for the $n\sigma$ and $1/\beta$ cuts. The TPC $n\sigma$ cut was $n\sigma < 3$ for pions and $n\sigma_K < 2$ for kaons and the TOF $|1/\beta - 1/\beta_{\text{TOF}}| < 0.03$ for both pions and kaons.

The $1/\beta$ resolution for the lower momentum (approximately < 0.4 GeV/ c) is not so precise which is caused by multiple rescattering in the TPC volume. The aforementioned cuts do not work precisely in this low p_T range. This can be solved by using momentum dependent PID cuts as was done in [3]. $1/\beta$ distribution was split into fifty slices and each slice from the Fig. 5.3 was fitted with a gaussian function. Means and sigmas were plotted and fitted by a power-law function

$$f = p0 + \frac{p1}{(p + p2)^{p3}}, \quad (5.1)$$

where p is the momentum of a kaon candidate. Fits can be seen in Fig. 5.4 and Fig. 5.5. These points were obtained from a configuration with a requirement for a strict TOF matching for both kaons and pions. The values of parameters for the functions for sigmas and means, respectively are

$$f_{\text{res}} = 0.92910 + \frac{0.77954}{(p - 0.11363)^{1.62916}}, f_{\text{pos}} = -0.05384 + \frac{0.04937}{(p - 0.06512)^{2.27704}}. \quad (5.2)$$

The candidates which were supposed to pass this stage of analysis had to fall within the band ranged by functions

$$(3 \cdot f_{\text{res}} + f_{\text{pos}}) > \frac{\Delta 1/\beta}{0.012} > (-2 \cdot f_{\text{res}} + f_{\text{pos}}) \quad (5.3)$$

These cuts can be seen in Fig. 5.3.

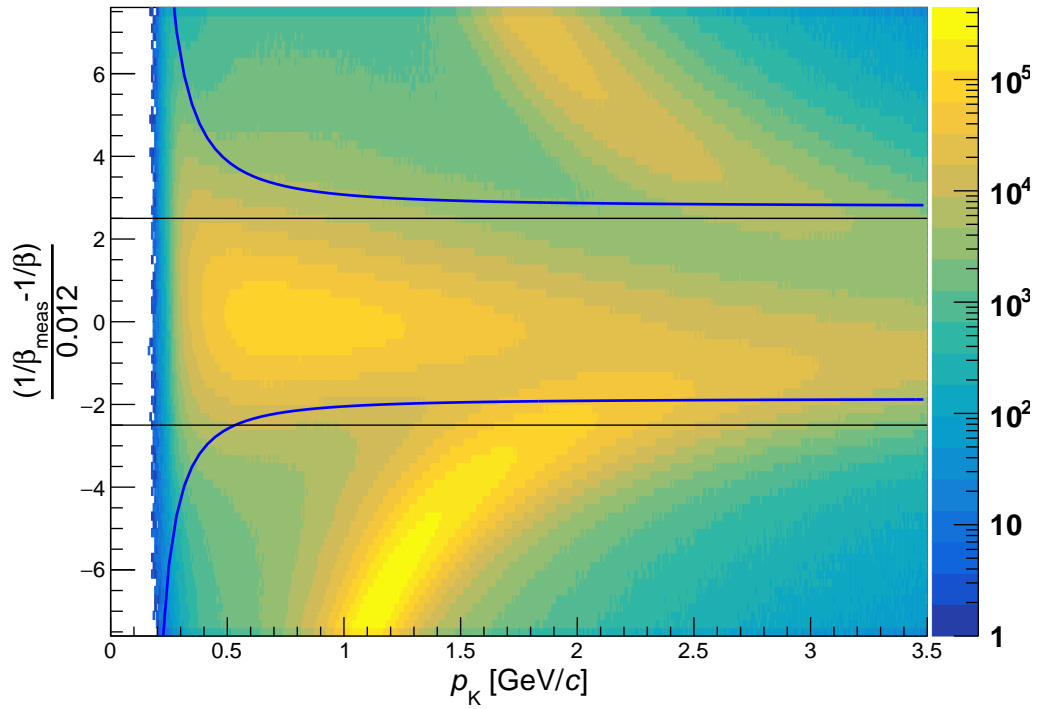


Figure 5.3: Difference of measured and theoretical value of $1/\beta$ of kaon candidates as a function of momentum p . The blue lines represent the cuts for which the following results are shown and the black lines represents simple rectangular cuts used in the first iteration.

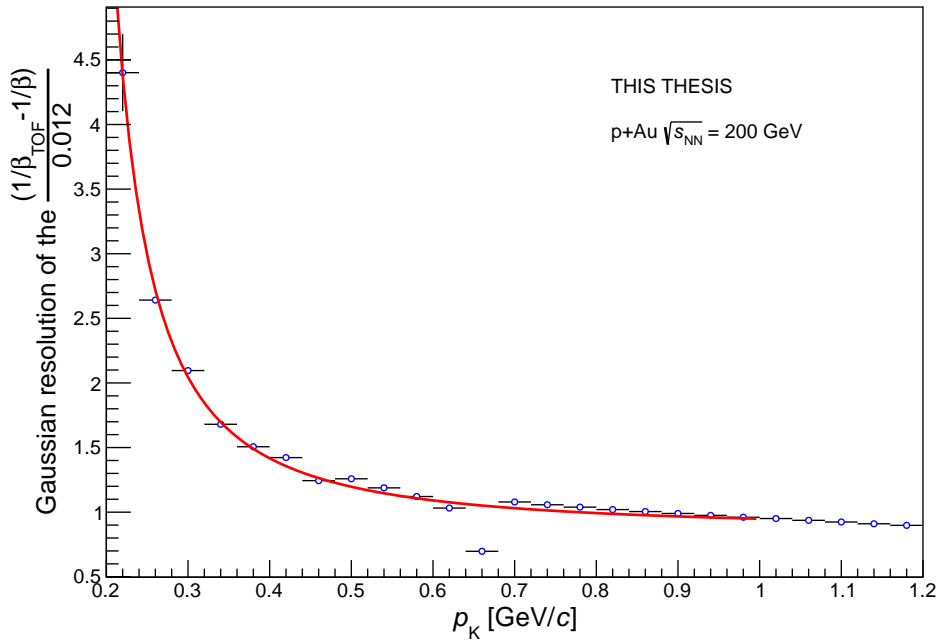


Figure 5.4: Points represent sigmas of gaussian fits of the slices in Fig 5.3 and are fitted by a power law function (5.1).

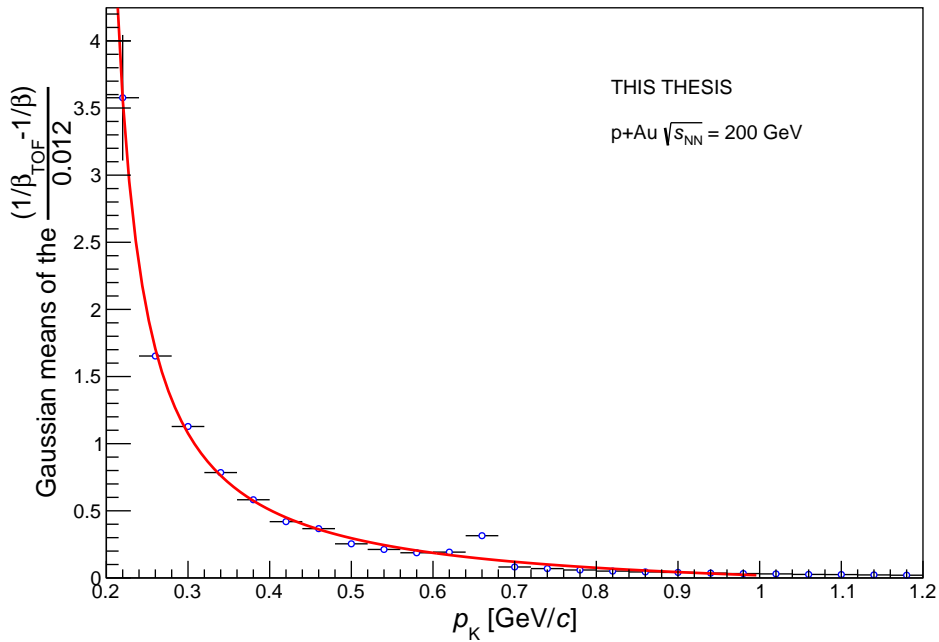


Figure 5.5: Points represent means of gaussian fits of the slices in Fig 5.3 and are fitted by a power law function (5.1).

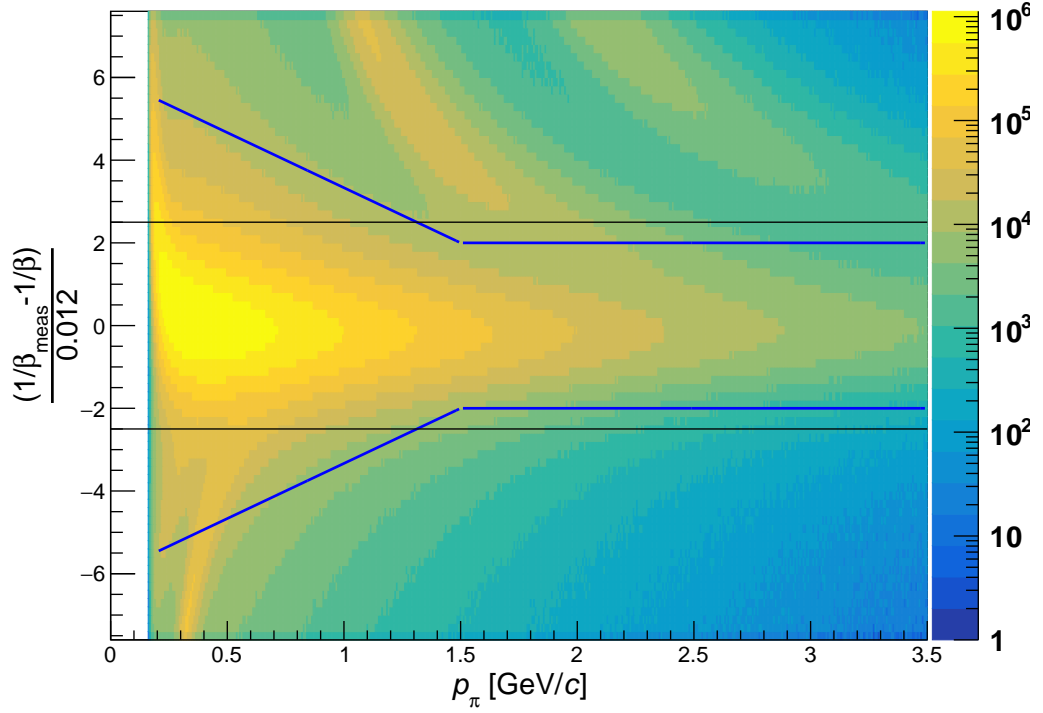


Figure 5.6: Difference of measured and theoretical value of $1/\beta$ of pion candidates as a function of momentum p . The blue lines represent the cuts for which the following results are shown and the black lines represents simple rectangular cuts used in the first iteration.

Results using these cuts were not improving the signal obtained from the data so the similar cuts were used for the $1/\beta$ of pions. In the momentum $p < 1.5$ GeV/ c were used functions

$$\left(6 - \frac{8}{3} \cdot p\right) > \frac{\Delta 1/\beta}{0.012} > \left(-6 + \frac{8}{3} \cdot p\right), \quad (5.4)$$

and for $p > 1.5$ GeV/ c was used

$$2 > \frac{\Delta 1/\beta}{0.012} > -2. \quad (5.5)$$

All of these cuts can be seen in Fig 5.6. Many choices of cuts for these cuts were used for both particles however none of those attempts was successful to obtain any visible signal in the next steps.

A summary of all the cuts used for the reconstruction is in Tab. 5.1.

	p+Au $\sqrt{s_{\text{NN}}} = 200$ GeV	p+p $\sqrt{s} = 510$ GeV
$ V_z[\text{VPD}] - V_z[\text{TPC}] $	< 6 cm	< 100 cm
$ V_z[\text{TPC}] $	< 30 cm	< 30 cm
number of TPC hits	> 20	> 20
$\frac{\text{number of TPC hits}}{\text{maximal possible number of TPC hits}}$	> 0.52	> 0.52
p_T	> 0.15 GeV/ c	> 0.15 GeV/ c
global DCA	< 2 cm	< 2 cm
$ \eta $	< 1	< 1
hybrid TOF	yes	yes
$ \text{n}\sigma_{\text{K}}^{\text{dE/dx}} $	< 2	< 2
$ \text{n}\sigma_{\pi}^{\text{dE/dx}} $	< 3	< 3
$\Delta 1/\beta_{\text{K}}$	eq. 5.3	eq. 5.8
$\Delta 1/\beta_{\pi}$	eq. 5.4 and 5.5	eq. 5.9 and 5.10
strict TOF pion matching	no	yes

Table 5.1: Comparison of cuts used in the shown results for the p+Au at $\sqrt{s_{\text{NN}}} = 200$ GeV and p+p $\sqrt{s} = 510$ GeV datasets

5.1.3 D^0 Invariant Mass Spectra

D^0 and \overline{D}^0 were analyzed together to enhance the observed signal. Multiple methods of description of the background were used in order to obtain clear signal in the distributions of invariant mass. All errors for the shown results are statistical.

The invariant mass M_{inv} is calculated as

$$M_{\text{inv}} = \sqrt{(\sum E)^2 + (\sum p)^2} \quad (5.6)$$

where $\sum E$ and $\sum p$ are summed energies, resp. momenta of the daughter particles.

Like-Sign Method

Since the D^0 is studied in the two body decay in this analysis, simple combinatorics can be used to estimate yield from the invariant mass of $K\pi$ pairs. Each kaon candidate was combined with each pion candidate of opposite charge. The invariant mass distribution of these pairs is then calculated and further called the Unlike-sign. In the distribution the D^0 and \overline{D}^0 signal (peak) should be visible around mass of these mesons (around 1.865 GeV/ c^2), however other peak is visible which is $K^{*0}(892)$ and the rest in the distribution is the combinatorial background.

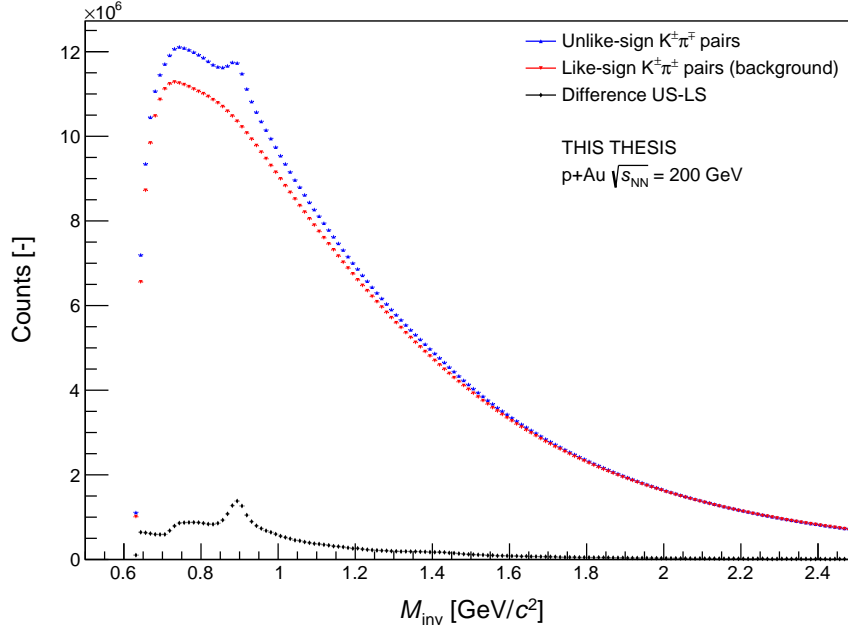


Figure 5.7: Invariant mass distribution of opposite charge kaon and pion pairs ($K\pi$) with the combinatorial background estimated by like-sign method and the difference of unlike-sign and like-sign distributions for all p_T bins in the p+Au collisions at $\sqrt{s_{NN}} = 200$ GeV.

The combinatorial background was estimated using the Like-sign invariant mass spectrum. In this case each kaon candidate was paired with each pion candidate of the same charge.

Distributions of both Unlike-sign and Like-sign spectra together with the subtraction of US-LS in the wide invariant mass range in different pair p_T bins can be seen in Figs. 5.7-5.11.

At a first sight there is not visible any peak around the expected D^0 in any of the p_T bins. Only peak that is clear in all the bins is the $K^{*0}(892)$. Another dependence can be seen from the previous figures - with increasing momentum of the D^0 candidate the description of background at lower invariant mass spectra end is worsening. In the Figs. 5.12-5.16 are zooms into the narrow windows where the expected peaks should be for the same p_T bins as the previous figures.

Unfortunately there is not visible any sign of peak in any of the p_T bins. Many choices of the above-mentioned cuts were used (TPC hits, $1/\beta$, $n\sigma$...), however none of them improved the signal so it could be translated as significant and the showed results are results of these iteration attempts.

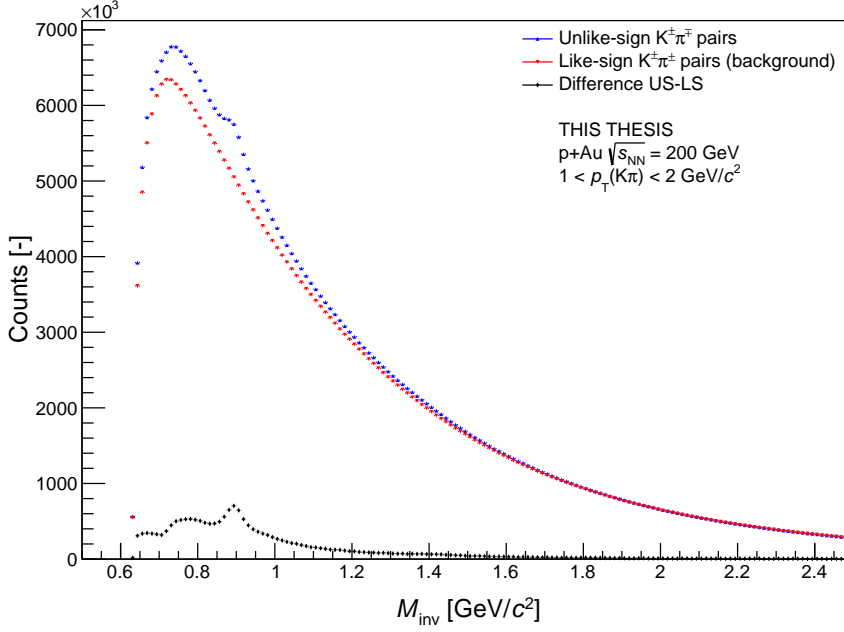


Figure 5.8: Invariant mass distribution of opposite charge kaon and pion pairs ($K\pi$) with the combinatorial background estimated by like-sign method and the difference of unlike-sign and like-sign distributions for $1 < p_T < 2$ GeV/c bin in the p+Au collisions at $\sqrt{s_{\text{NN}}} = 200$ GeV .

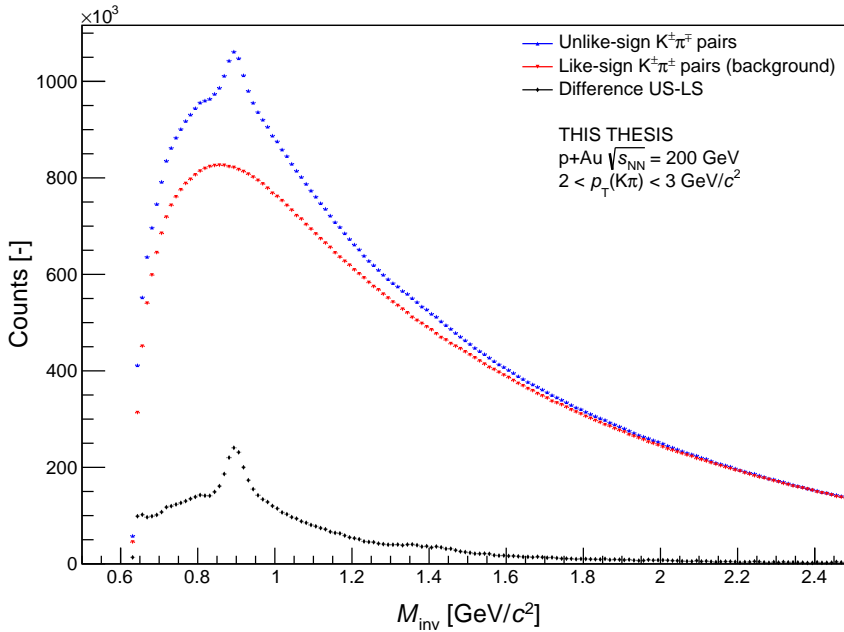


Figure 5.9: Invariant mass distribution of opposite charge kaon and pion pairs ($K\pi$) with the combinatorial background estimated by like-sign method and the difference of unlike-sign and like-sign distributions for $2 < p_T < 3$ GeV/c bin in the p+Au collisions at $\sqrt{s_{\text{NN}}} = 200$ GeV .

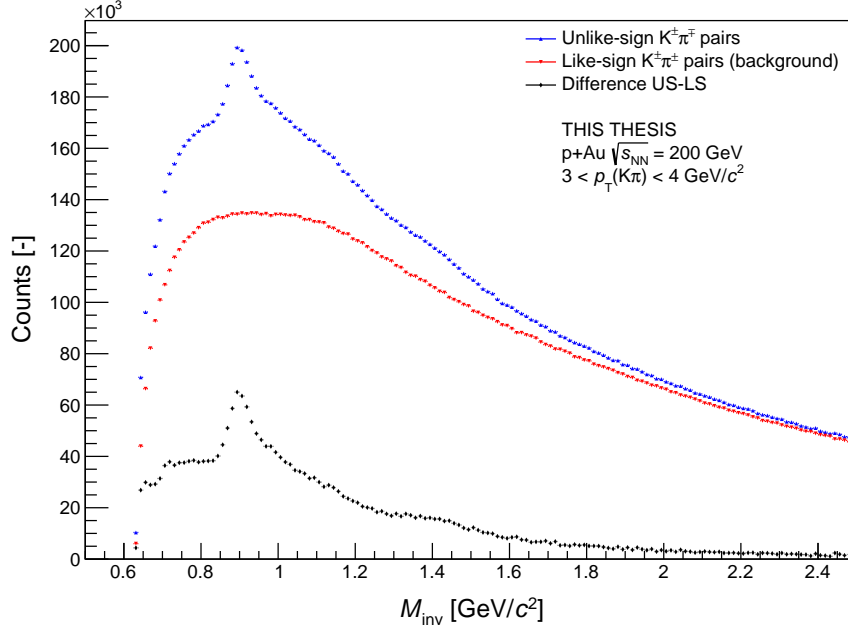


Figure 5.10: Invariant mass distribution of opposite charge kaon and pion pairs ($K\pi$) with the combinatorial background estimated by like-sign method and the difference of unlike-sign and like-sign distributions for $3 < p_T < 4$ GeV/c bin in the p+Au collisions at $\sqrt{s_{\text{NN}}} = 200$ GeV .

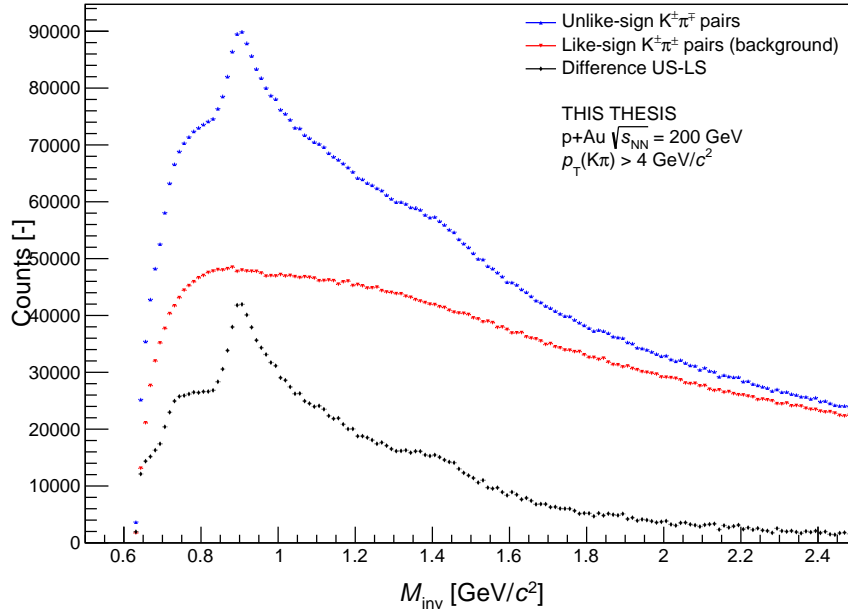


Figure 5.11: Invariant mass distribution of opposite charge kaon and pion pairs ($K\pi$) with the combinatorial background estimated by like-sign method and the difference of unlike-sign and like-sign distributions for $p_T > 4$ GeV/c bin in the p+Au collisions at $\sqrt{s_{\text{NN}}} = 200$ GeV .

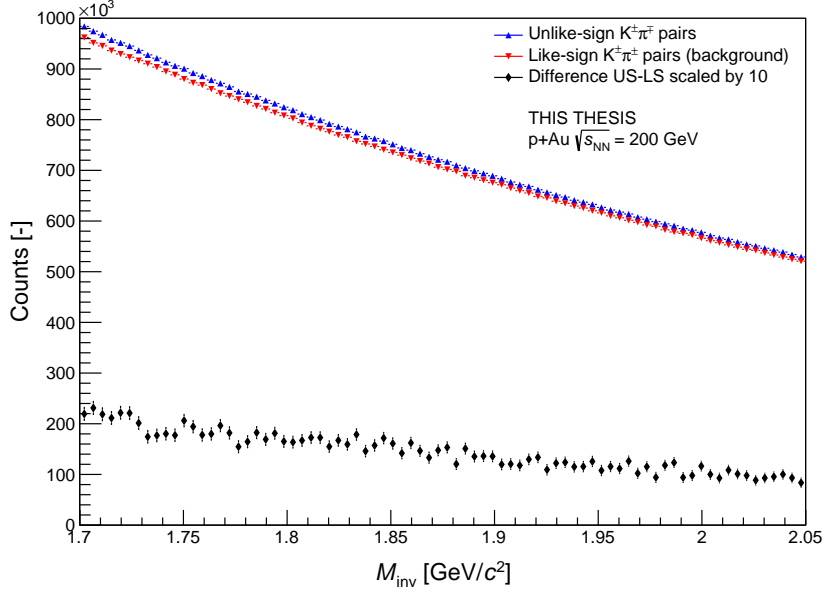


Figure 5.12: Invariant mass distribution of opposite charge kaon and pion pairs ($K\pi$) with the combinatorial background estimated by like-sign method and the difference of unlike-sign and like-sign distributions (multiplied by 10 for visibility) for all p_T bins in the window around expected D^0 peak in the p+Au collisions at $\sqrt{s_{NN}} = 200 \text{ GeV}$.

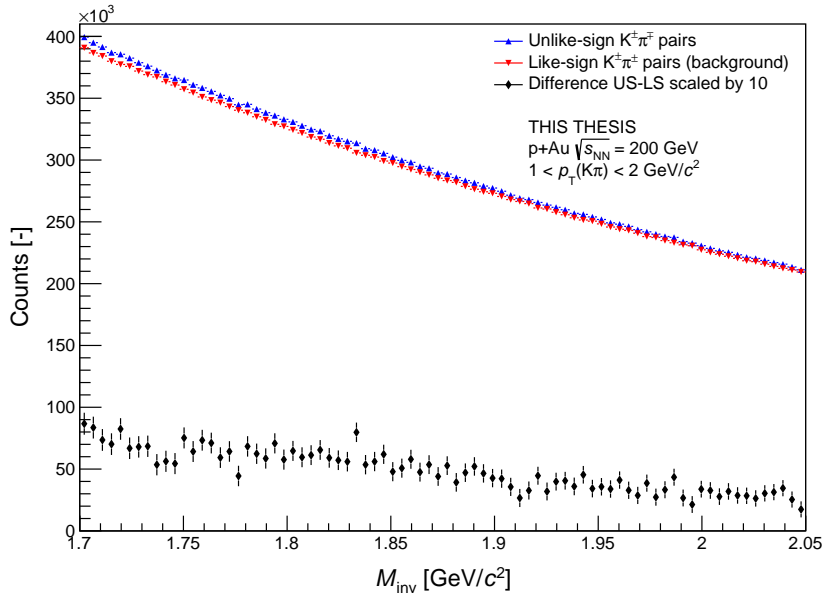


Figure 5.13: Invariant mass distribution of opposite charge kaon and pion pairs ($K\pi$) with the combinatorial background estimated by like-sign method and the difference of unlike-sign and like-sign distributions (multiplied by 10 for visibility) for $1 < p_T < 2 \text{ GeV}/c$ bin in the window around expected D^0 peak in the p+Au collisions at $\sqrt{s_{NN}} = 200 \text{ GeV}$.

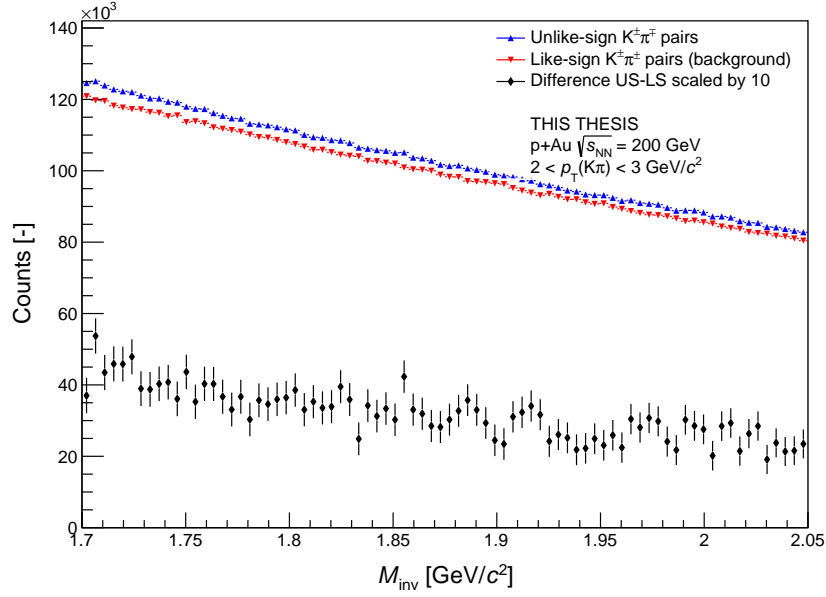


Figure 5.14: Opposite charge kaon and pion pairs with the combinatorial background estimated by like-sign method and the difference of unlike-sign and like-sign distributions (multiplied by 10 for visibility) for $2 < p_T < 3$ GeV/c bin in the window around expected D^0 peak in the p+Au collisions at $\sqrt{s_{NN}} = 200$ GeV.

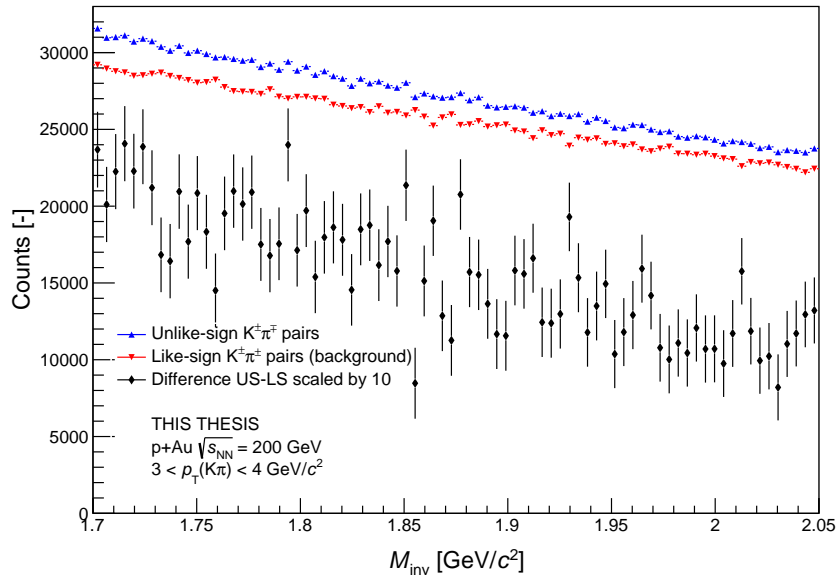


Figure 5.15: Invariant mass distribution of opposite charge kaon and pion pairs ($K\pi$) with the combinatorial background estimated by like-sign method and the difference of unlike-sign and like-sign distributions (multiplied by 10 for visibility) for $3 < p_T < 4$ GeV/c bin in the window around expected D^0 peak in the p+Au collisions at $\sqrt{s_{NN}} = 200$ GeV.

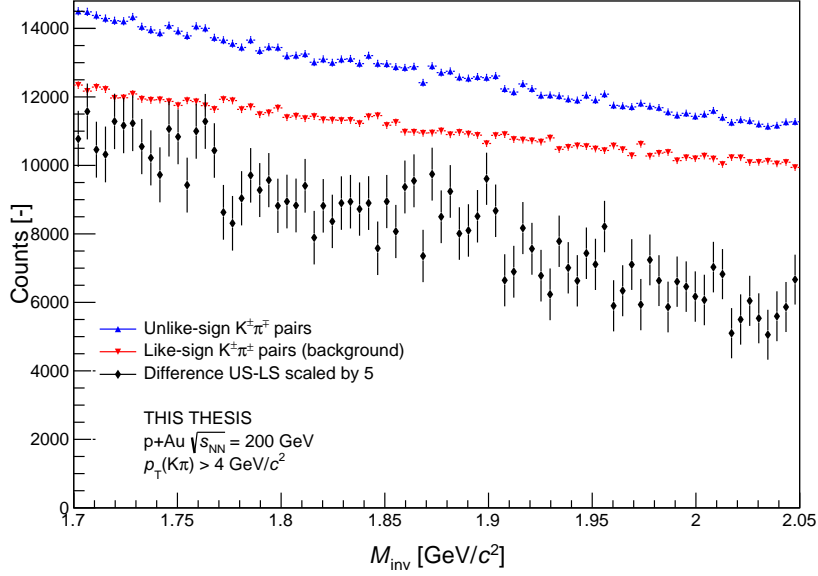


Figure 5.16: Invariant mass distribution of opposite charge kaon and pion pairs ($K\pi$) with the combinatorial background estimated by like-sign method and the difference of unlike-sign and like-sign distributions (multiplied by 5 for visibility) for $p_T > 4$ GeV/c bin in the window around expected D^0 peak in the p+Au collisions at $\sqrt{s_{\text{NN}}} = 200$ GeV .

Side-Band Method

Another option of describing the background is so called side-band method. The Unlike-sign invariant mass spectra were fitted by a 3rd order polynomial, using only points outside $\pm 3\sigma$ (taken from Ref. [3]) band around the expected D^0 signal peak. Polynomials from the order 1 were used to describe the invariant mass distribution and the third order polynomial described the background the best as can be seen in Fig. 5.17. The linear fit nor the second order polynomial described the background correctly. The obtained function is then subtracted from the like-sign distribution and in the omitted are should appear the expected D^0 peak.

Many choices of the width of the omitted area were used nevertheless none of these choices lead to the result that could be interpreted as a significant result. Result for all p_T bins can be seen in Fig. 5.18.

An example of the expected signal can be seen in Fig. 5.19. The figure represents invariant mass spectra from p+p collisions measured by STAR in 2009 and 2011. Techniques used for the reconstruction are similar as those in this thesis. However the signal of D^0 mesons is better than that done in this thesis.

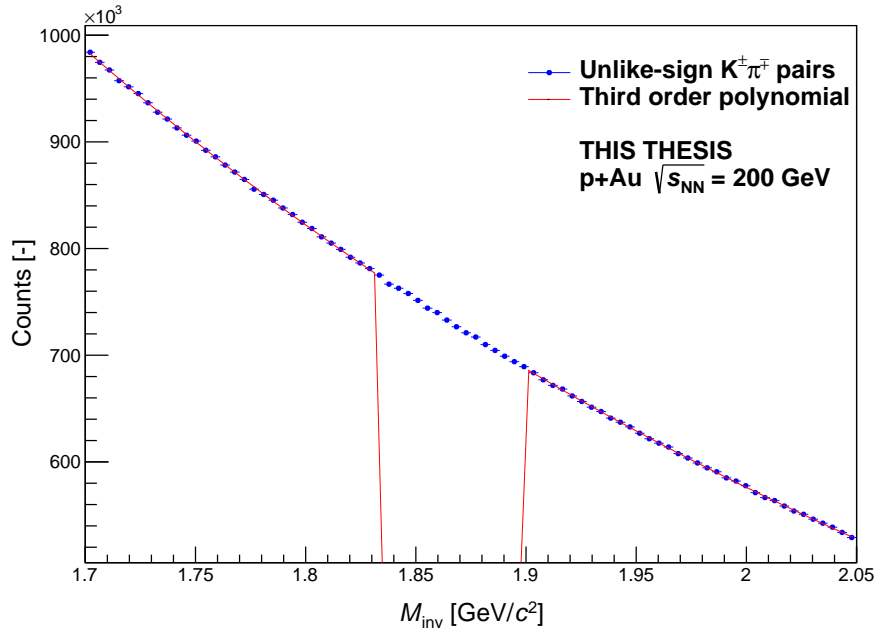


Figure 5.17: Third order polynomial fit of the unlike-sign pairs in the shown area.

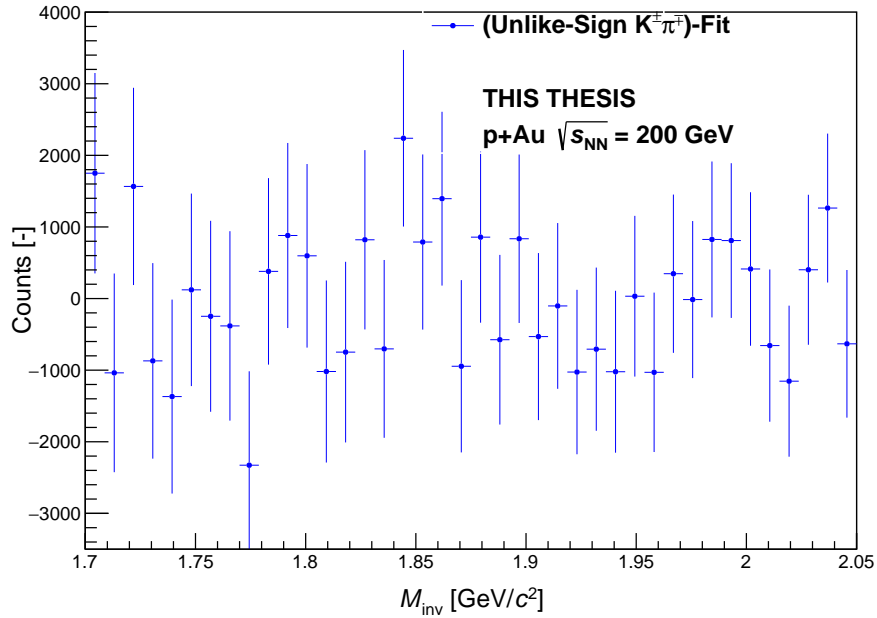


Figure 5.18: Unlike-sign spectrum ($k\pi$ pairs) of the invariant mass with subtracted polynomial fit of the background obtained from the side-band method for all p_T bins in the p+Au collisions at $\sqrt{s_{NN}} = 200$ GeV.

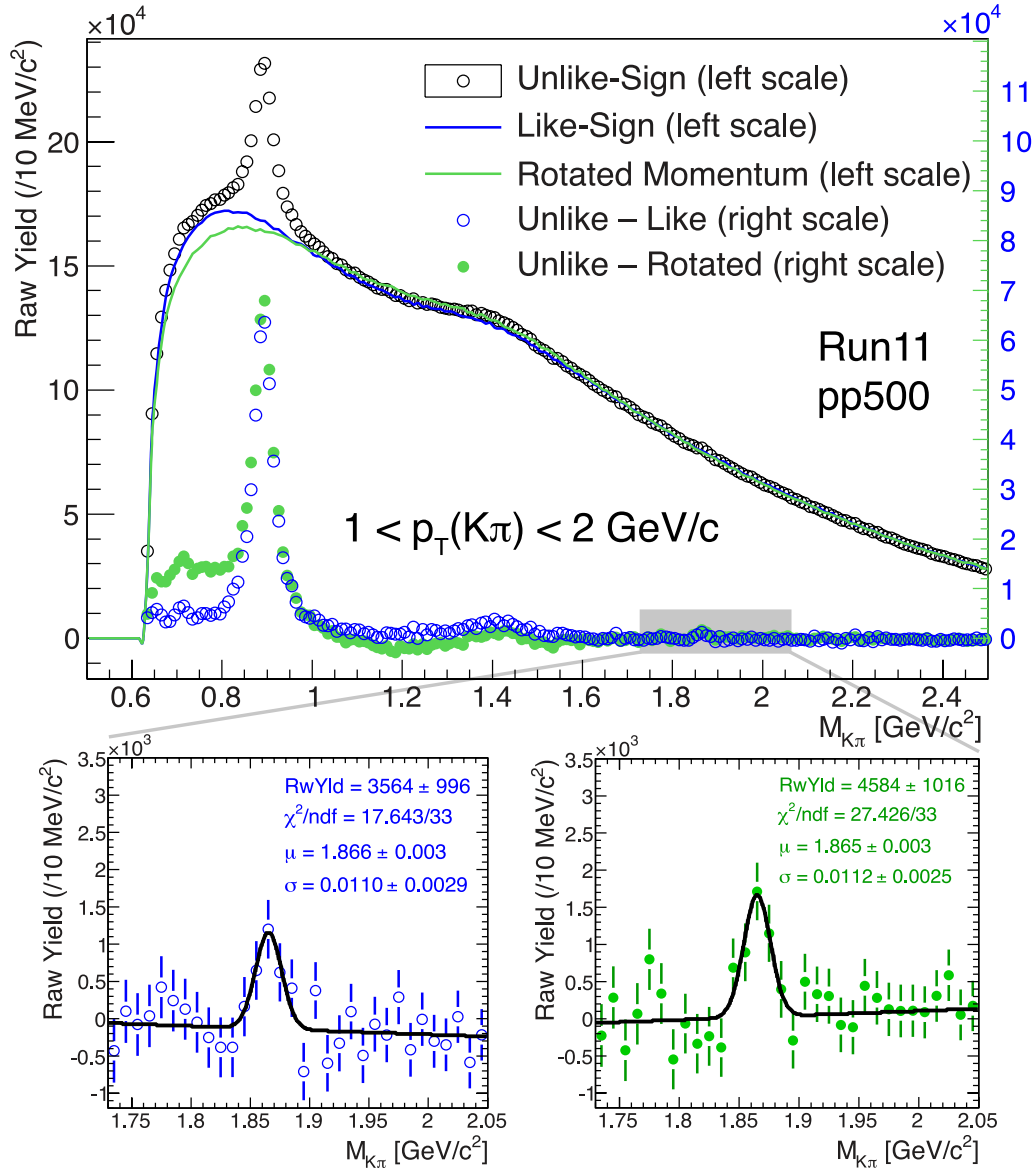


Figure 5.19: Upper panel: Invariant mass spectrum of $K\pi$ pairs with background reconstructed by Like-Sign and Rotated Momentum techniques for $1 < p_T < 2$ GeV/c. Lower panel: Invariant mass spectrum after subtraction of background for both methods. Taken from ref. [3].

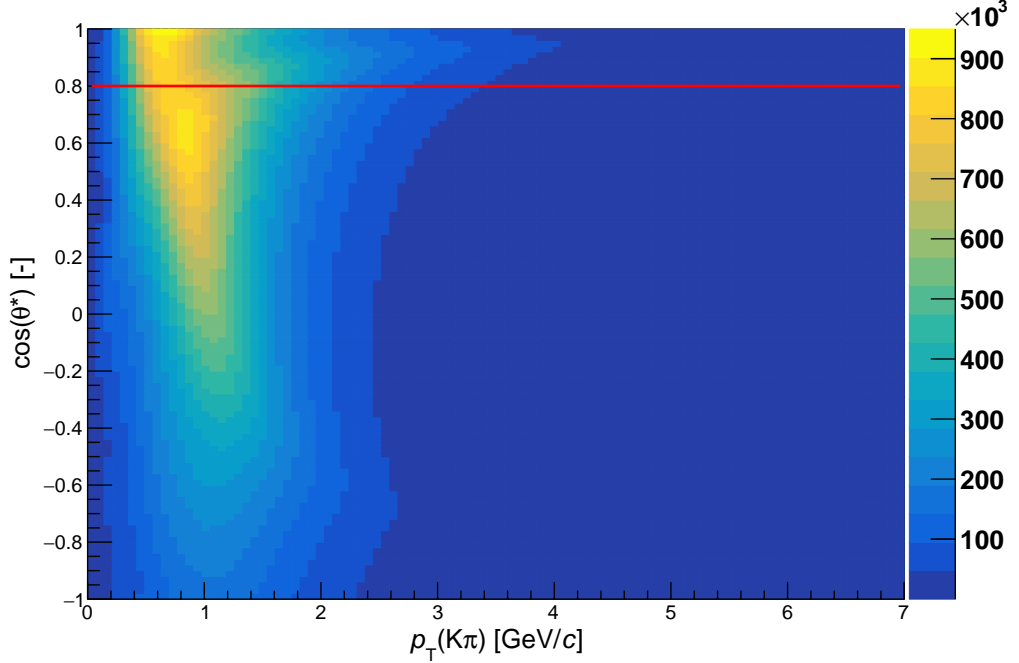


Figure 5.20: Distribution of $\cos(\theta^*)$ in the CMS frame of $K\pi$ pair in the p+Au collisions at $\sqrt{s_{NN}} = 200$ GeV. The red line represents the used cut.

5.1.4 D^* Invariant Mass Spectra

Another attempt was done with the excited $D^{*+}(2010)^\pm$ state, further denoted D^* . This meson undergoes a cascade decay $D^{*\pm} \rightarrow D^0\pi^\pm \rightarrow K^\mp\pi^\pm\pi^\pm$ (branching ratio $(67.7 \pm 0.5)\%$ [29]). The difference of masses of D^* and D^0 meson is slightly above the pion mass $M_{D^*} - M_{D^0} = (145.4258 \pm 0.0017)$ MeV/ c^2 [29]. This means that the raw yield of D^* meson could be calculated as an area of peak around $M_{K^\mp\pi^\pm\pi^\pm} - M_{K^\mp\pi^\pm} = 145.4$ MeV/ c^2 .

For the reconstruction were taken D^0 candidates with cuts and tools from the previous section. To select only relevant candidates the requirement was $1.84 < M_{K^\mp\pi^\pm} < 1.89$ GeV/ c^2 . Since D^* mesons with $p_T < 1.6$ GeV/ c are not detectable by TOF [3], the calculations started at D^* $p_T = 2$ GeV/ c . To reduce background coming from jets, another variable $\cos(\theta^*)$ is introduced. θ^* is defined as an angle of momentum of reconstructed D^0 and momentum of a kaon in the CMS system. This variable was required to be $\cos(\theta^*) < 0.8$. Distribution of $\cos(\theta^*)$ can be seen in Fig. 5.20.

In the next step the D^0 candidate was combined with another pion. Background was once again estimated by wrong-sign method, however this time the background had to be scaled by $1/3$ because in the three-body decay there exist six wrong-sign

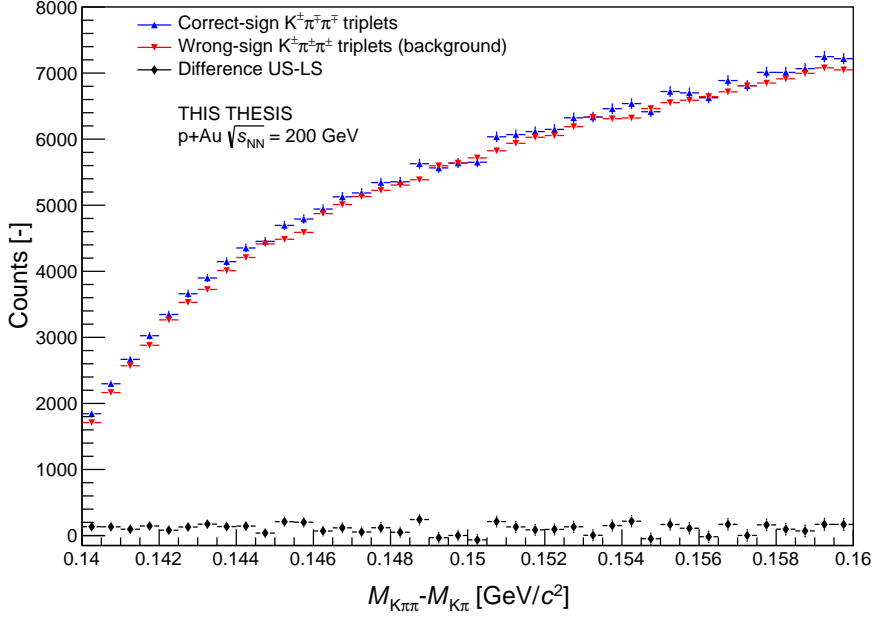


Figure 5.21: The $M_{K^{\mp}\pi^{\pm}\pi^{\pm}} - M_{K^{\mp}\pi^{\pm}}$ spectrum with combinatorial background estimated by wrong-sign method and the subtracted wrong-sign background and correct-sign signal for all D^* candidate p_T bins in the p+Au collisions at $\sqrt{s_{NN}} = 200$ GeV.

combinations and only two correct-sign combinations. From the obtained mass of D^* meson candidate was subtracted the mass of D^0 meson daughter particle and these results were plotted. The correct-sign and wrong-sign combinations were scaled and subtracted and the results can be seen in Figs. 5.21-5.24 in multiple D^* candidate p_T bins.

As can be seen from the figures, there is not visible any peak in the expected area. The expected signal from [3] can be seen in Fig. 5.25.

Since all the above-mentioned attempts to receive the D^0 signal failed, it is possible that the background is simply too large in p+Au collisions and these methods are not sophisticated enough to reach any raw yield.

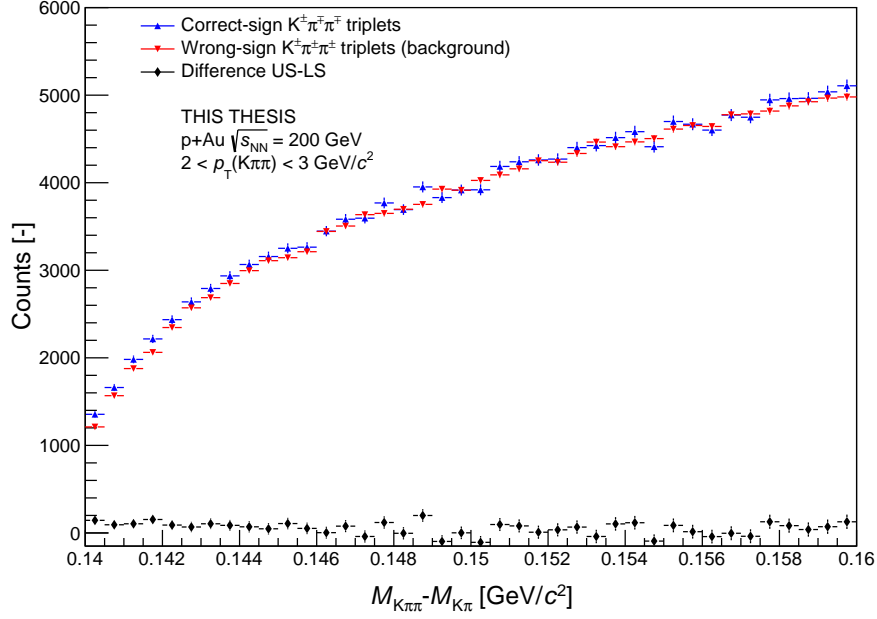


Figure 5.22: The $M_{K^\mp\pi^\pm\pi^\pm} - M_{K^\mp\pi^\pm}$ spectrum with combinatorial background estimated by wrong-sign method and the subtracted wrong-sign background and correct-sign signal for D^* candidate $2 < p_T < 3$ GeV/ c bin in the p+Au collisions at $\sqrt{s_{NN}} = 200$ GeV.

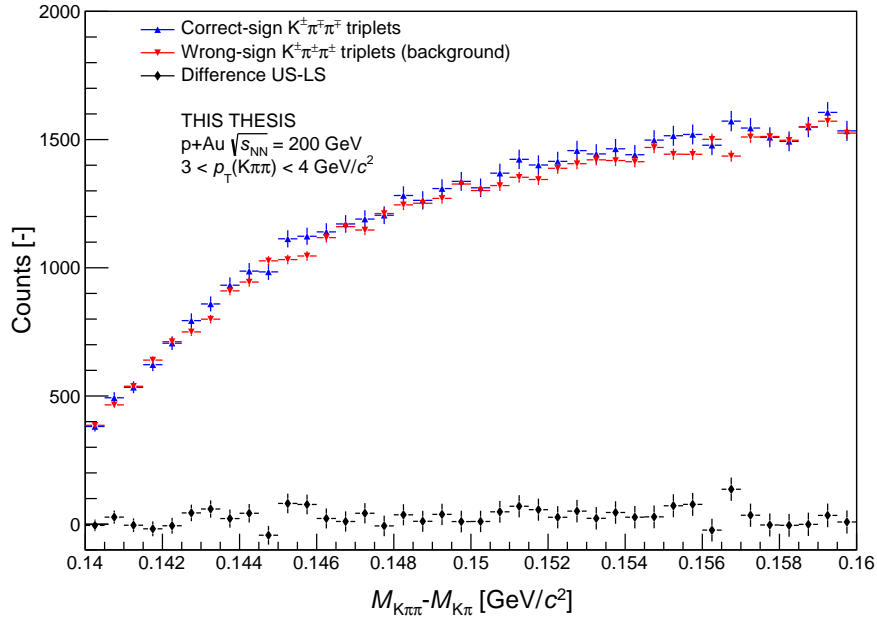


Figure 5.23: The $M_{K^\mp\pi^\pm\pi^\pm} - M_{K^\mp\pi^\pm}$ spectrum with combinatorial background estimated by wrong-sign method and the subtracted wrong-sign background and correct-sign signal for D^* candidate $3 < p_T < 4$ GeV/ c bin in the p+Au collisions at $\sqrt{s_{NN}} = 200$ GeV.

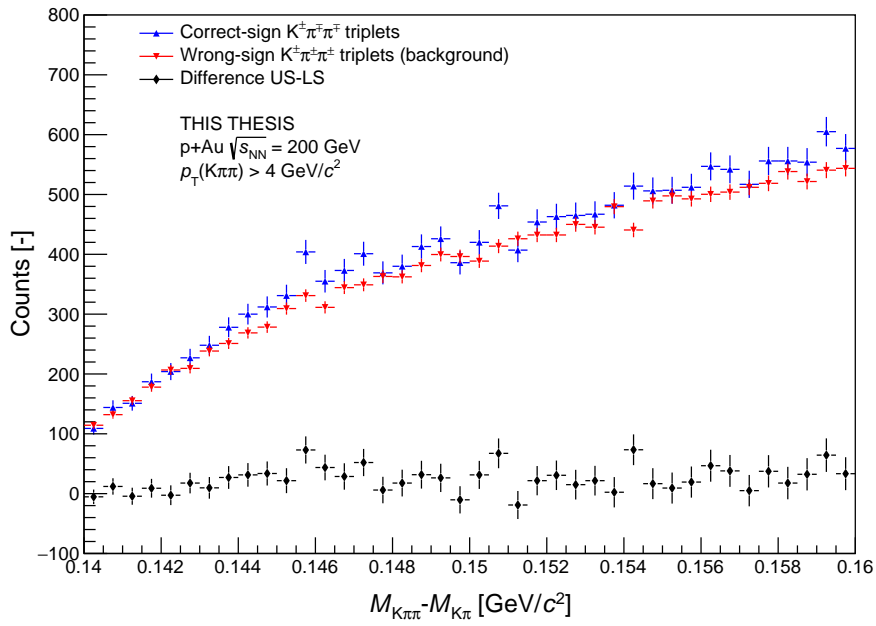


Figure 5.24: The $M_{K^\mp\pi^\pm\pi^\pm} - M_{K^\mp\pi^\pm}$ spectrum with combinatorial background estimated by wrong-sign method and the subtracted wrong-sign background and correct-sign signal for D^* candidate $p_T > 4$ GeV/ c bin in the p+Au collisions at $\sqrt{s_{NN}} = 200$ GeV.

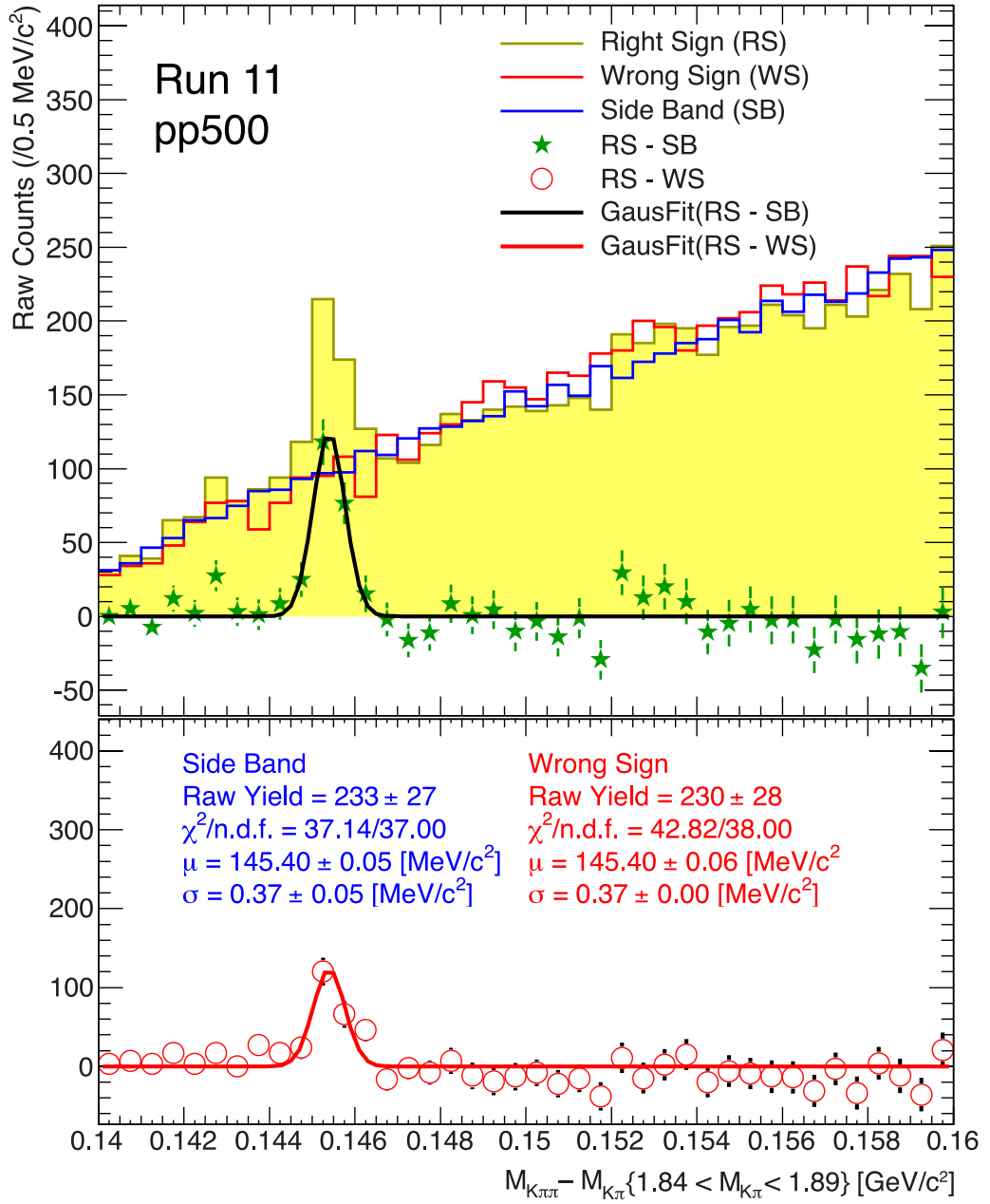


Figure 5.25: Upper panel: $M_{K^{\mp}\pi^{\pm}\pi^{\pm}} - M_{K^{\mp}\pi^{\pm}}$ spectrum with background reconstructed by Side-band and Wrong-sign techniques. Lower panel: $M_{K^{\mp}\pi^{\pm}\pi^{\pm}} - M_{K^{\mp}\pi^{\pm}}$ spectrum after subtraction of Wrong-sign background and the gaussian fit. Taken from Ref. [3].

5.2 Analysis of p+p Collisions

5.2.1 Dataset and Event Selection

This section uses same steps as were used in the p+Au analysis with small deviations.

Data for this analysis were taken in the p+p collisions in year 2017 by STAR detector at energy $\sqrt{s} = 510$ GeV. Total number of collisions was $2.8 \cdot 10^9$.

In 2017, the HFT was not present at STAR anymore so once again it cannot be used to reconstruct D mesons. The input for the analysis were the PicoDst files.

The used trigger is the minimum bias trigger. The total of $1.1 \cdot 10^9$ of events passed this trigger.

The selection cut $|V_{z[\text{VPD}]} - V_{z[\text{TPC}]}|$, where $V_{z[\text{VPD}]}$ is the z-position of the vertex calculated using Eq. (2.4) from the VPD detector and $V_{z[\text{TPC}]}$ is the z-position measured by TPC, was not used the same way as for the case of p+Au collisions because the VPD does not have sufficient efficiency in the collisions of protons. Instead of 6 cm was used cut 100 cm.

If event is to be accepted it has to pass the following criteria

- pass the minimum bias trigger
- $|V_{z[\text{TPC}]}| < 30$ cm

Histogram of the event statistics is shown in Fig. 5.26.

5.2.2 Particle Identification

Same track quality cuts were used to improve track selection for the further analysis as in the case of p+Au collisions and are listed below:

- number of TPC hits > 20
- $\frac{\text{number of TPC hits}}{\text{maximal possible number of TPC hits}} > 0.52$
- $p_T > 0.15$ GeV/c
- global DCA < 2 cm
- $|\eta| < 1$

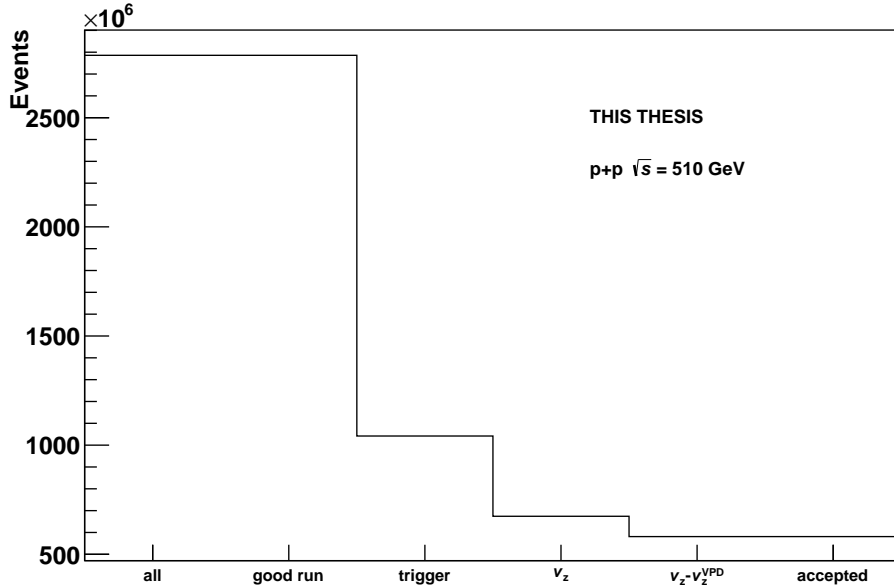


Figure 5.26: Number of events that passed individual event selection criteria.

where number of TPC hits denotes the number of spatial hit points used for the reconstruction of a track, $\frac{\text{number of TPC hits}}{\text{maximal possible number of TPC hits}}$ is used to prevent tracks which split into two tracks, global DCA is the distance of the closest approach of a track to primary vertex, the minimum transverse momentum p_T and pseudorapidity η are set for the track to be able to reach TOF.

Also in this case was used the hybrid-TOF to increase possible signal because with strict TOF matching the statistics is too low.

The $n\sigma$ and $1/\beta$ cuts used the same as in the case of p+Au collision with the similar iterative process. The TPC $n\sigma$ cut was $n\sigma_\pi < 3$ for pions and $n\sigma_K < 2$ for kaons and the TOF $1/\beta < 0.03$ for both pions and kaons.

The $1/\beta$ momentum dependent PID cuts were fitted and calculated also for this dataset with the same approach as in the previous section. Fits can be seen in Fig. 5.27 and Fig. 5.28. These points were obtained from a configuration with a requirement for a strict TOF matching for both kaons and pions. The values of parameters for the functions for sigmas and means, respectively are

$$f_{\text{res}} = 1.0551 + \frac{0.0985232}{(p + 0.183495)^{2.87264}}, f_{\text{pos}} = 0.0457193 + \frac{0.0123594}{(p + 0.447614)^{10.0479}}. \quad (5.7)$$

The candidates which were supposed to pass this stage of analysis had to fall within the band ranged by functions

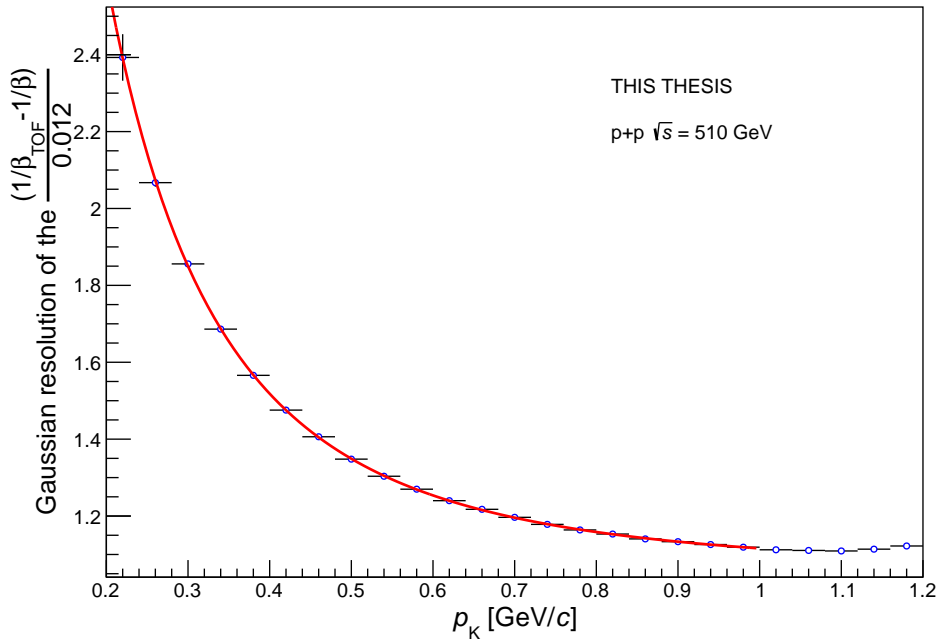


Figure 5.27: Points represent sigmas of gaussian fits of the slices of $\Delta 1/\beta$ distribution and are fitted by a power law function (5.1).

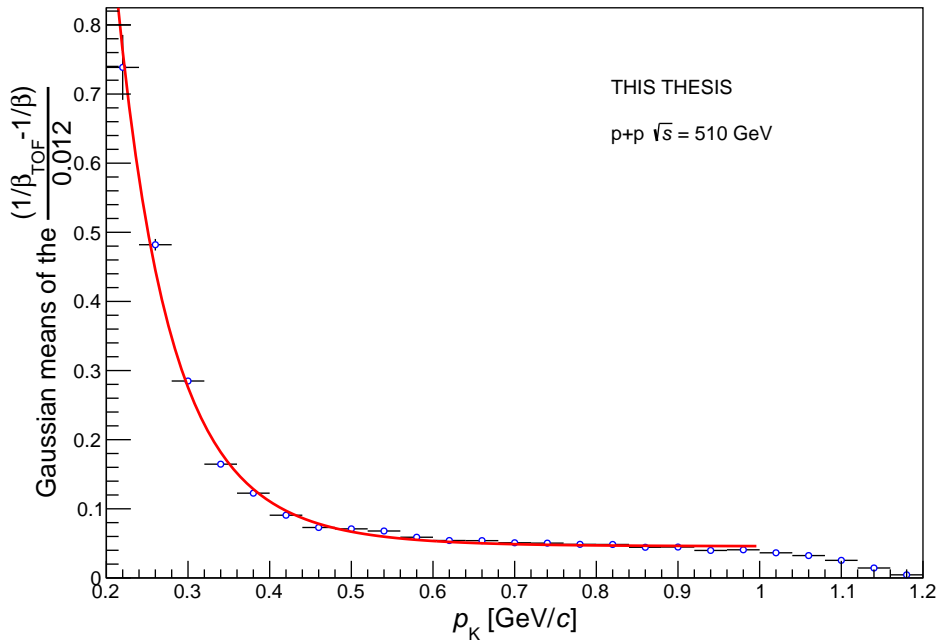


Figure 5.28: Points represent means of gaussian fits of the slices of $\Delta 1/\beta$ distribution and are fitted by a power law function (5.1).

$$(3 \cdot f_{\text{res}} + f_{\text{pos}}) > \frac{\Delta 1/\beta}{0.012} > (-2 \cdot f_{\text{res}} + f_{\text{pos}}) \quad (5.8)$$

Similar cuts were used for the $1/\beta$ of pions. In the momentum $p < 1.5$ GeV/ c were used functions

$$(6 - \frac{8}{3} \cdot p) > \frac{\Delta 1/\beta}{0.012} > (-6 + \frac{8}{3} \cdot p), \quad (5.9)$$

and for $p > 1.5$ GeV/ c was used

$$2 > \frac{\Delta 1/\beta}{0.012} > -2. \quad (5.10)$$

A summary of all the cuts used for the reconstruction and comparison with the cuts used for the p+Au analysis are in Tab. 5.1.

For the reconstruction of D^* meson was also used different implementation of so called hybrid TOF taking advantage of another fast detector BEMC. However adding another detector brings another systematical uncertainty into account but adding BEMC is necessary to remove pile-up events.

These cuts were taken from [3] and are separated into groups according to the momentum of the track. Different detectors are effective in separating kaons and pions at different momentum.

- $p_{\text{T}} < 1.3$ GeV/ c : For low momentum TOF provides clear separation of kaons and pions. Kaons were defined as tracks that passed condition 5.8 and pions as those fulfilling for $p < 1.5$ GeV/ c condition 5.9 and for $p > 1.5$ GeV/ c condition 5.10. If tracks were matched only in the BEMC, those were counted as pions upon passing $-3 < n\sigma_{\pi}^{\text{d}E/\text{d}x} < 3$.
- $1.3 < p_{\text{T}} < 2.07$ GeV/ c : If track was matched in TOF, TOF was used for particle identification, kaons were defined as tracks that pass the condition 5.8 and pions as those fulfilling $|n\sigma_{\pi}^{1/\beta}| < 3$. If track was matched in BEMC and not in TOF, kaons were accepted for $|n\sigma_{\text{K}}^{\text{d}E/\text{d}x}| < 2$ and pions for $|n\sigma_{\pi}^{\text{d}E/\text{d}x}| < 3$.
- $p_{\text{T}} > 2.07$ GeV/ c : TPC provides good separation of pions and kaons at this momentum. If the track had matching in any of the fast detectors (TOF or BEMC) then kaons were accepted for $|n\sigma_{\text{K}}^{\text{d}E/\text{d}x}| < 2$ and pions for $|n\sigma_{\pi}^{\text{d}E/\text{d}x}| < 3$.

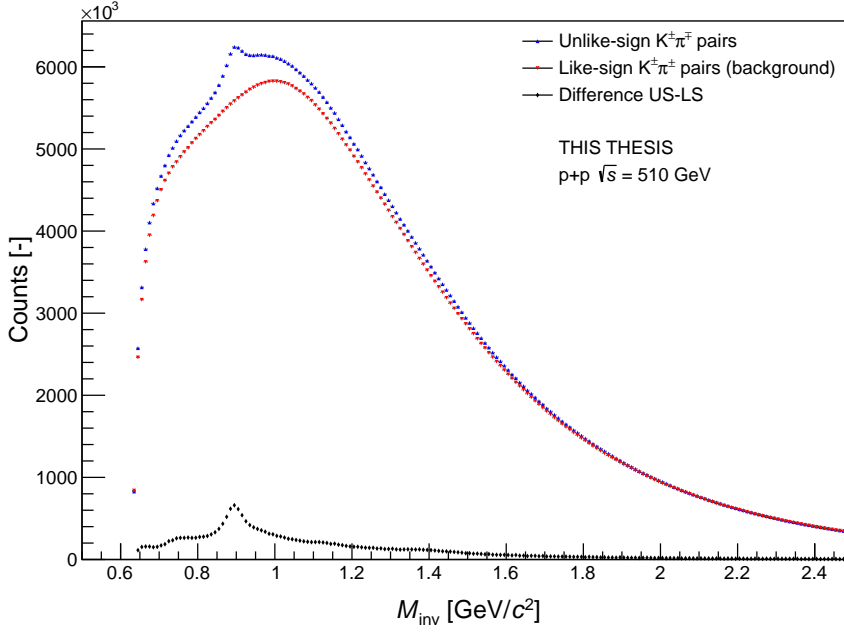


Figure 5.29: Invariant mass distribution of opposite charge kaon and pion pairs ($K\pi$) with the combinatorial background estimated by like-sign method and the difference of unlike-sign and like-sign distributions for all p_T bins in the p+p collisions at $\sqrt{s} = 510$ GeV.

5.2.3 D^0 Invariant Mass Spectra

Like-Sign Method

The kaons and pions of same charge were combined to obtain background and of opposite charge to obtain signal candidates with exactly the same approach as in the case of p+Au analysis. Multiple configurations of selecting pions and kaon were used. The results shown in the following Figs. 5.29-5.33 are with an additional requirement for pions to be matched in TOF.

Even for this configuration for p+p collisions there is not any peak around the expected D^0 mass in any of the p_T bins. However the $K^{*0}(892)$ peak is clear in all the bins. In the Figs. 5.34-5.34 are zooms into the narrow windows where the expected peaks should be for the same p_T bins as the previous figures.

None of the shown histograms has any significant hint of peak in the expected D^0 mass area. The results for other sets of cuts and configurations have shown similar results and are not shown in this thesis.

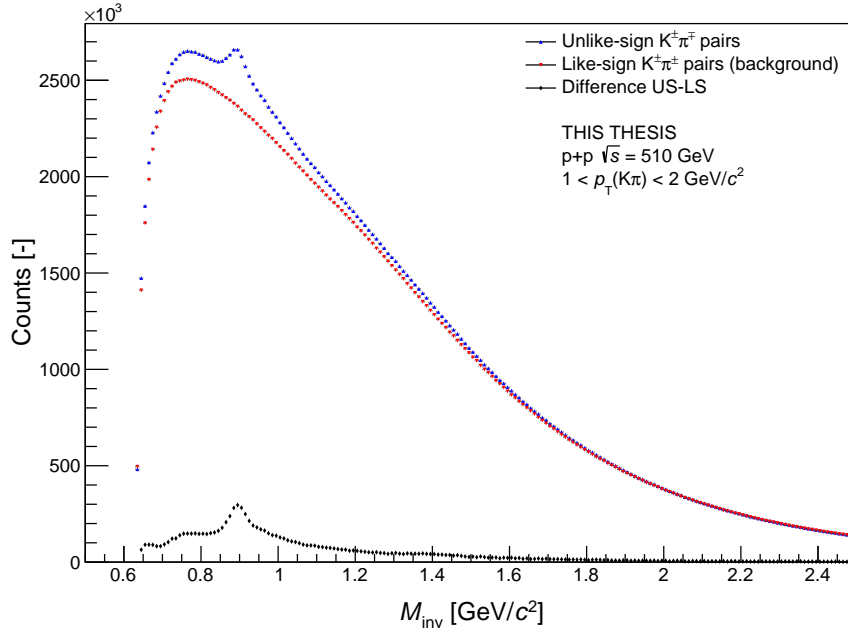


Figure 5.30: Invariant mass distribution of opposite charge kaon and pion pairs ($K\pi$) with the combinatorial background estimated by like-sign method and the difference of unlike-sign and like-sign distributions for $1 < p_T < 2$ GeV/ c bin in the p+p collisions at $\sqrt{s} = 510$ GeV.

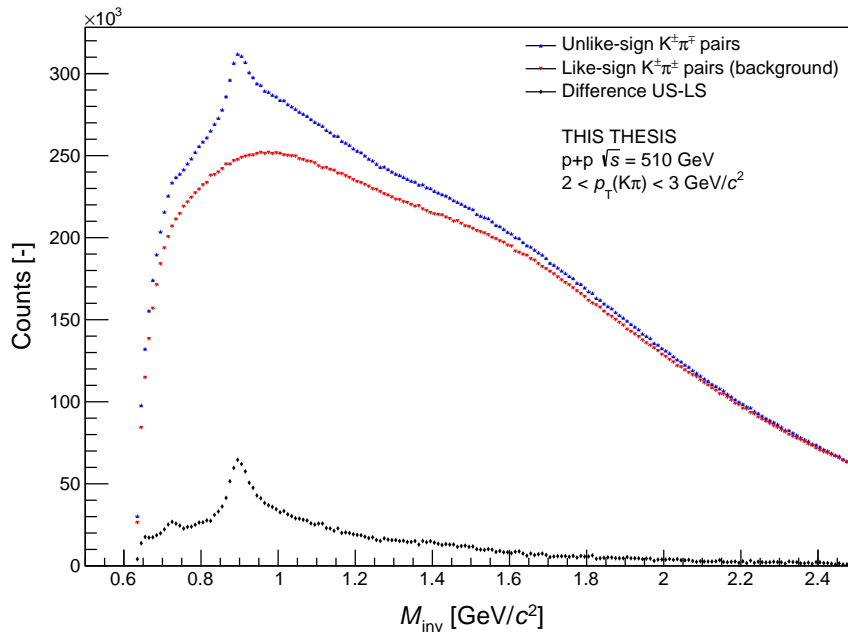


Figure 5.31: Invariant mass distribution of opposite charge kaon and pion pairs ($K\pi$) with the combinatorial background estimated by like-sign method and the difference of unlike-sign and like-sign distributions for $2 < p_T < 3$ GeV/ c bin in the p+p collisions at $\sqrt{s} = 510$ GeV.

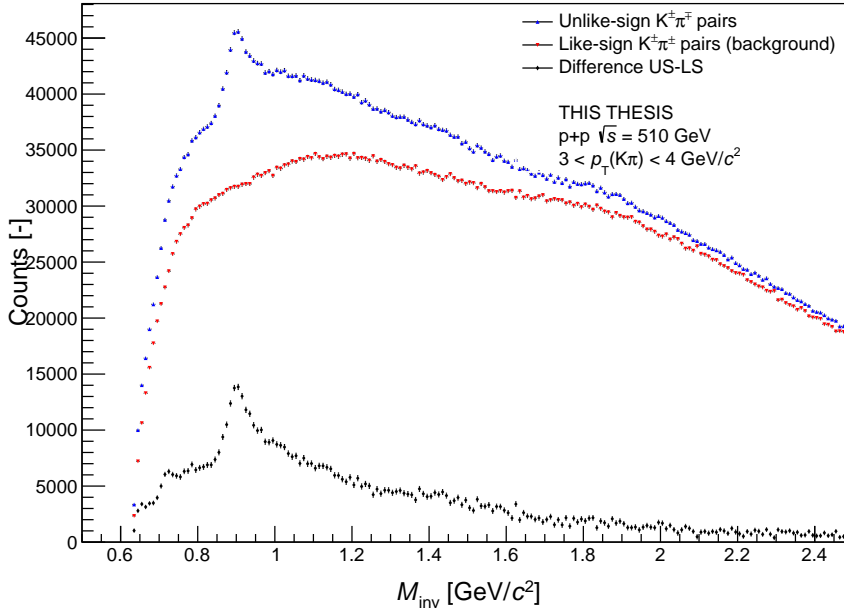


Figure 5.32: Invariant mass distribution of opposite charge kaon and pion pairs ($K\pi$) with the combinatorial background estimated by like-sign method and the difference of unlike-sign and like-sign distributions for $3 < p_T < 4$ GeV/ c bin in the p+p collisions at $\sqrt{s} = 510$ GeV

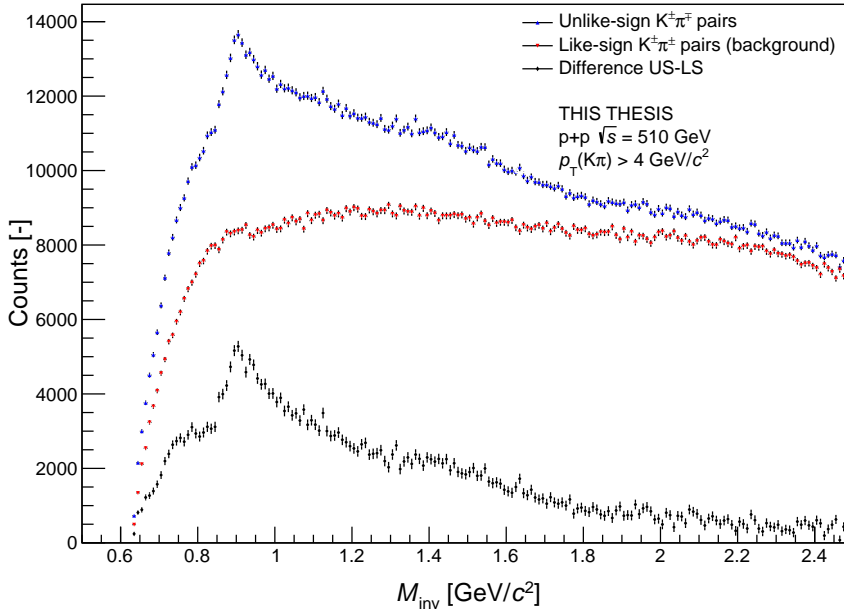


Figure 5.33: Invariant mass distribution of opposite charge kaon and pion pairs ($K\pi$) with the combinatorial background estimated by like-sign method and the difference of unlike-sign and like-sign distributions for $p_T > 4$ GeV/ c bin in the p+p collisions at $\sqrt{s} = 510$ GeV.

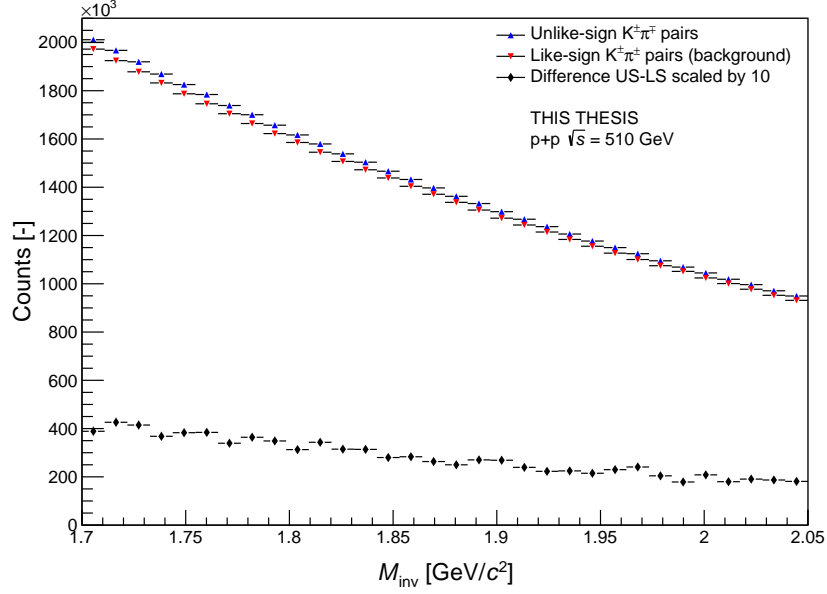


Figure 5.34: Invariant mass distribution of opposite charge kaon and pion pairs ($K\pi$) with the combinatorial background estimated by like-sign method and the difference of unlike-sign and like-sign distributions (multiplied by 10 for visibility) for all p_T bins in the window around expected D^0 peak in the p+p collisions at $\sqrt{s} = 510$ GeV.

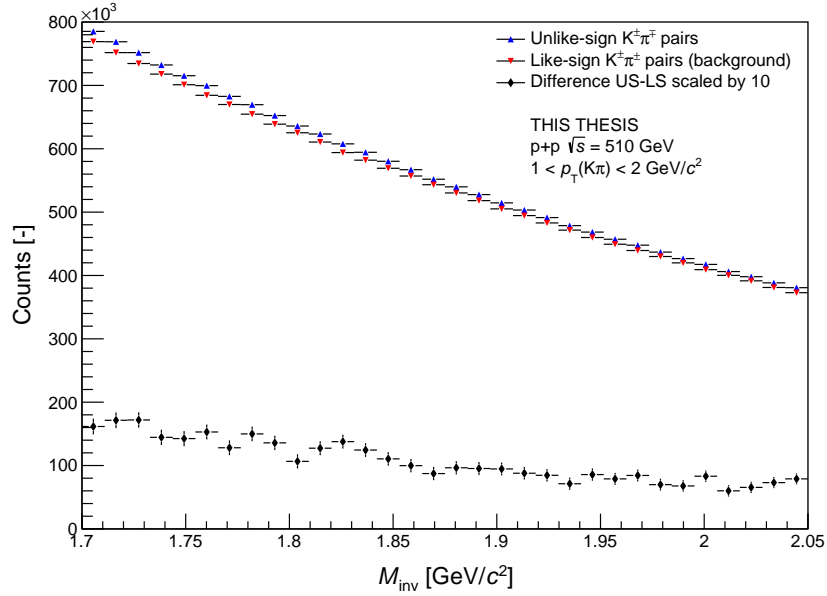


Figure 5.35: Invariant mass distribution of opposite charge kaon and pion pairs ($K\pi$) with the combinatorial background estimated by like-sign method and the difference of unlike-sign and like-sign distributions (multiplied by 10 for visibility) for $1 < p_T < 2$ GeV/c bin in the window around expected D^0 peak in the p+p collisions at $\sqrt{s} = 510$ GeV.

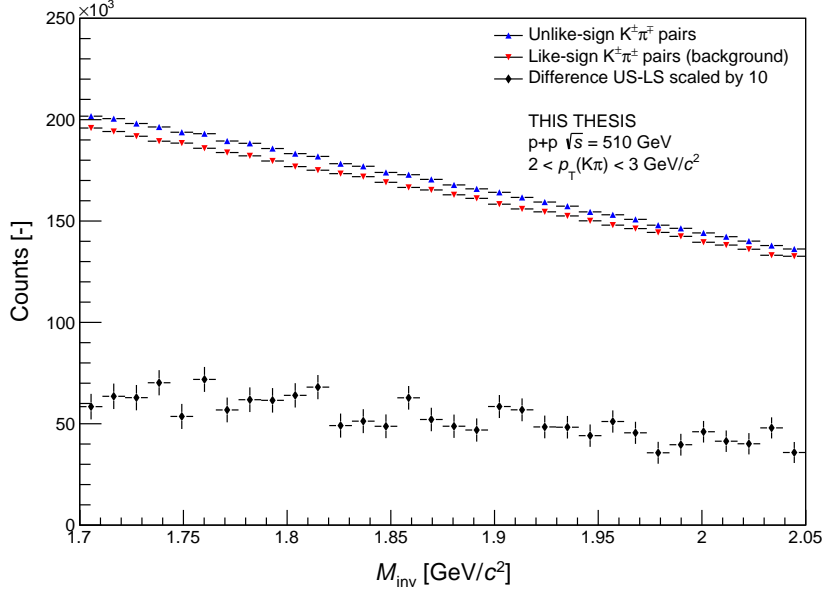


Figure 5.36: Invariant mass distribution of opposite charge kaon and pion pairs ($K\pi$) with the combinatorial background estimated by like-sign method and the difference of unlike-sign and like-sign distributions (multiplied by 10 for visibility) for $2 < p_T < 3 \text{ GeV}/c$ bin in the window around expected D^0 peak in the p+p collisions at $\sqrt{s} = 510 \text{ GeV}$.

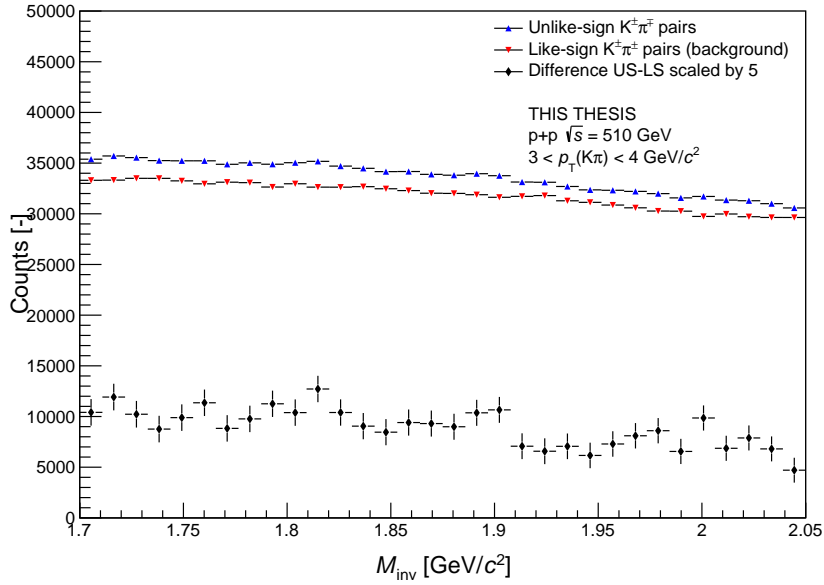


Figure 5.37: Invariant mass distribution of opposite charge kaon and pion pairs ($K\pi$) with the combinatorial background estimated by like-sign method and the difference of unlike-sign and like-sign distributions (multiplied by 10 for visibility) for $3 < p_T < 4 \text{ GeV}/c$ bin in the window around expected D^0 peak in the p+p collisions at $\sqrt{s} = 510 \text{ GeV}$.

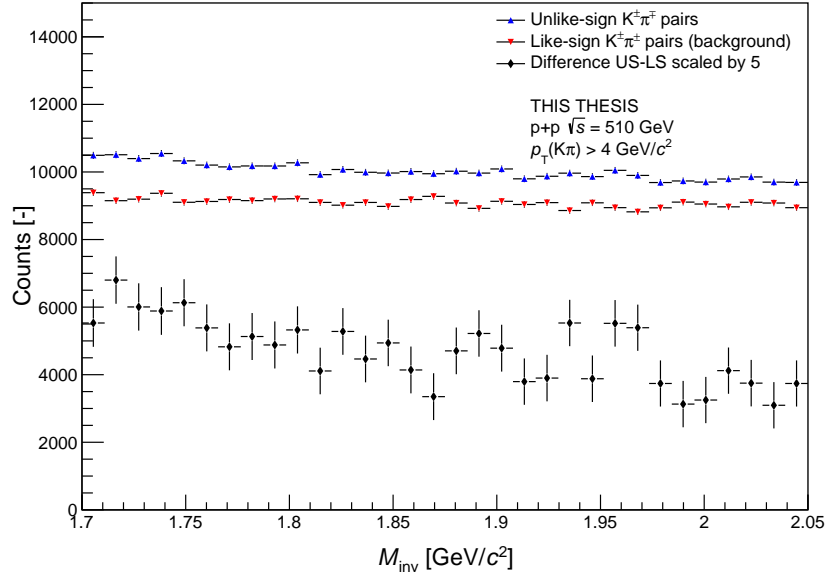


Figure 5.38: Invariant mass distribution of opposite charge kaon and pion pairs ($K\pi$) with the combinatorial background estimated by like-sign method and the difference of unlike-sign and like-sign distributions (multiplied by 5 for visibility) for $p_T > 4$ GeV/c bin in the window around expected D^0 peak in the p+p collisions at $\sqrt{s} = 510$ GeV.

Side-Band Method

Approach in this section follows the procedure used in the section 5.1.3. As an input served the unlike-sign signal distributions shown in the previous section. The third order polynomial served again as a best description of the data and the fit is shown in Fig. 5.39. Subtraction of the unlike-sign distribution and the shown fitted function is in Fig. 5.40. However the result does not show any hint of peak in the expected area of D^0 mass.

Event-Mixing Method

To describe background with another method, so called Event-Mixing method has been used. This approach expands simple Like-sign method. The LS pairs can all have the same bias, so the event-mixing combines pairs from 10 last events and not just one. Each kaon is combined with all the pions (after PID cuts are applied) from the last ten events. The pions are required to have opposite charge of the kaon. This approach reduces the statistical error as can be seen in the further figures. This background distribution needs to be scaled to unlike-sign distribution so it could be subtracted. Comparisons of like-sign and event-mixing are in Figs. 5.41 and 5.42.

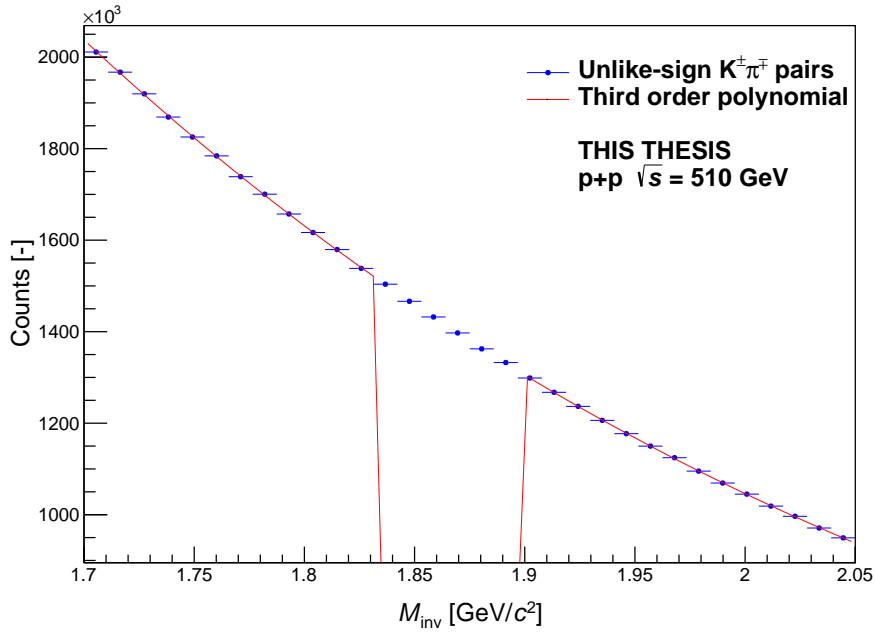


Figure 5.39: Third order polynomial fit of the unlike-sign pairs in the shown area.

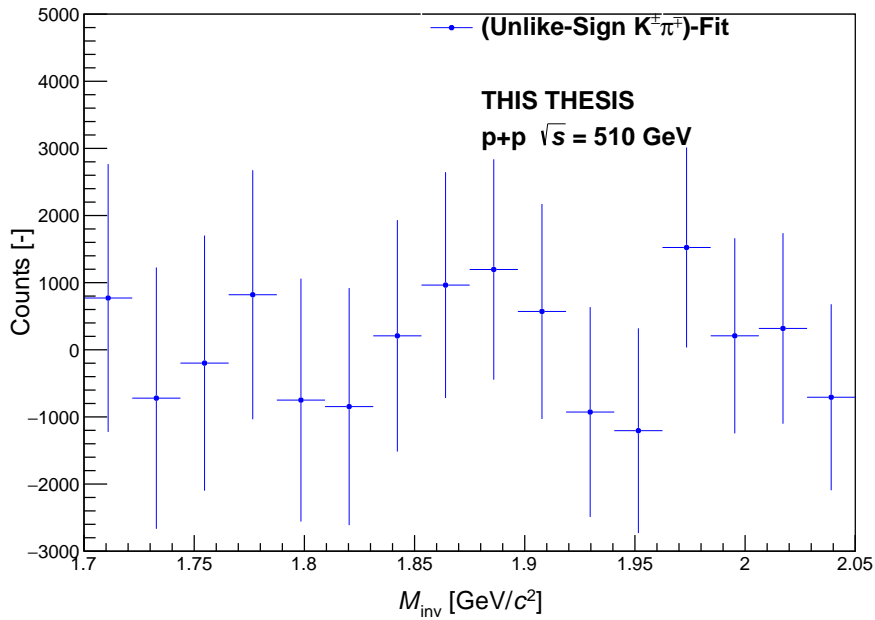


Figure 5.40: Unlike-sign spectrum ($k\pi$ pairs) of the invariant mass with subtracted polynomial fit of the background obtained from the side-band method for all p_T bins in the $p+p$ collisions at $\sqrt{s} = 510$ GeV.

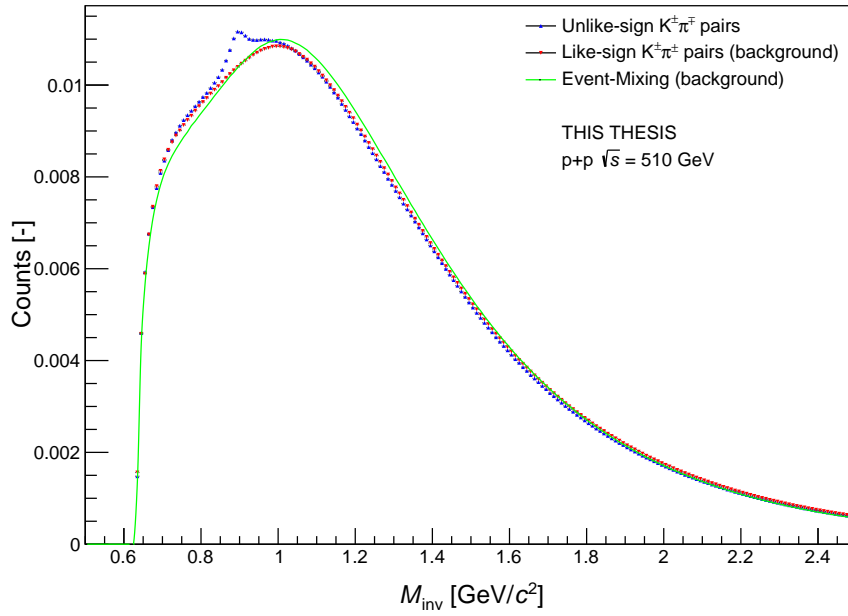


Figure 5.41: Comparison of like-sign background (red triangles), event-mixing background (green line) and unlike-sign (blue triangles) distributions for all p_T bins in the p+p collisions at $\sqrt{s} = 510$ GeV.

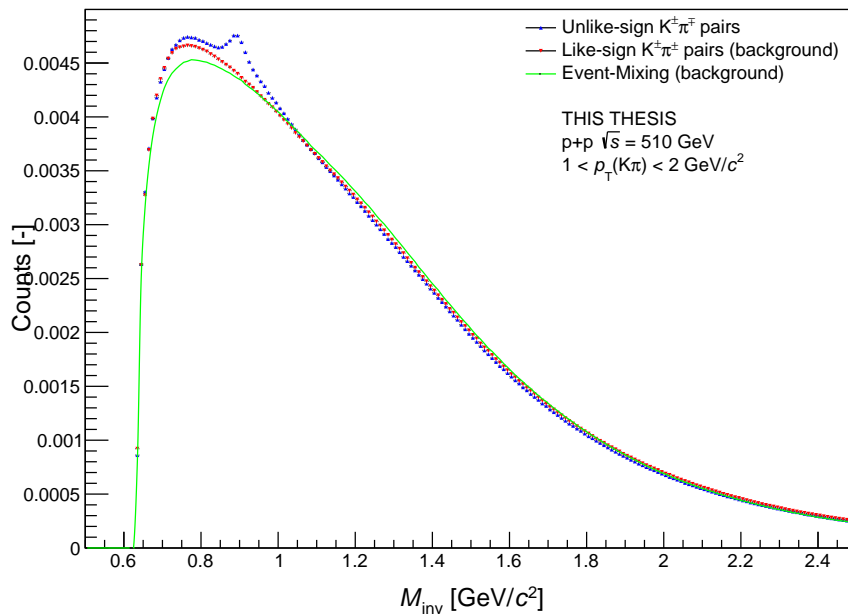


Figure 5.42: Comparison of like-sign background (red triangles), event-mixing background (green line) and unlike-sign (blue triangles) distributions for $1 < p_T < 2$ GeV/c bin in the p+p collisions at $\sqrt{s} = 510$ GeV.

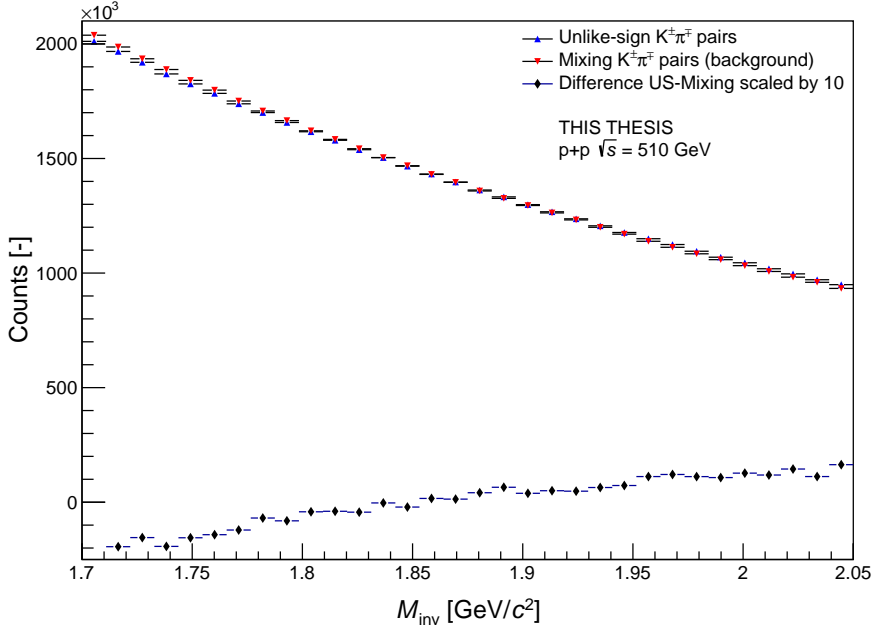


Figure 5.43: Unlike-sign (signal) distribution (blue triangles) and scaled background estimated by event mixing method (red triangles) and its subtraction scaled by 10 (black diamonds) for all p_T bins in the p+p collisions at $\sqrt{s} = 510$ GeV.

Results from the zoomed view are in Figs. 5.43-5.47. The event-mixing distributions have been scaled to unlike-sign (signal) and subtracted. However the event-mixing method does not show any peak in any of the p_T bins and probably needs to be further tuned. However the statistical errors are lower than for the case of Like-sign method.

5.2.4 D^* Invariant Mass Spectra

D^* Analysis without BEMC

This section shows results of the same approach as the one used for p+Au collisions. The D^0 daughter particles were chosen from the unlike-sign method described in the previous section with the requirement for strict pion matching. The $\cos(\theta^*) < 0.8$ cut has also been used.

The $M_{K^\mp\pi^\pm\pi^\pm} - M_{K^\mp\pi^\pm}$ distributions for various p_T bins are in Figs. 5.48-5.51.

These results however do not show any significant sign of peak in any of the D^* p_T bin.

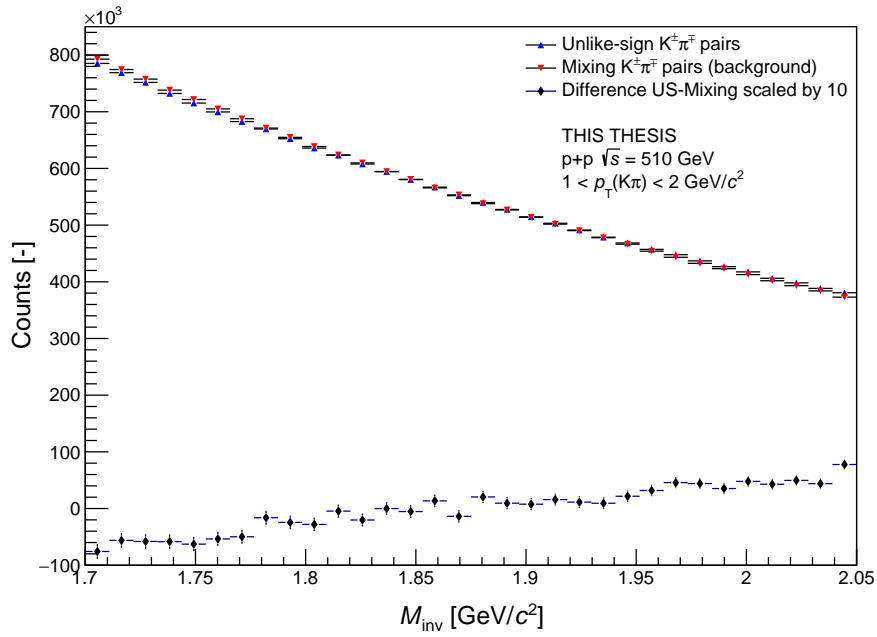


Figure 5.44: Unlike-sign (signal) distribution (blue triangles) and scaled background estimated by event mixing method (red triangles) and its subtraction scaled by 10 (black diamonds) for $1 < p_T < 2$ bin in the p+p collisions at $\sqrt{s} = 510$ GeV.

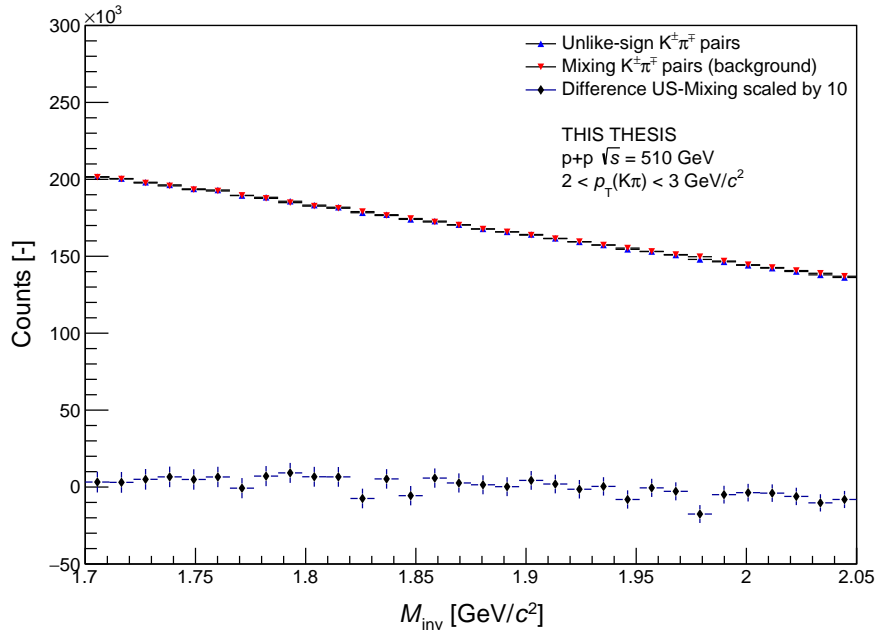


Figure 5.45: Unlike-sign (signal) distribution (blue triangles) and scaled background estimated by event mixing method (red triangles) and its subtraction scaled by 10 (black diamonds) for $2 < p_T < 3$ bin in the p+p collisions at $\sqrt{s} = 510$ GeV.

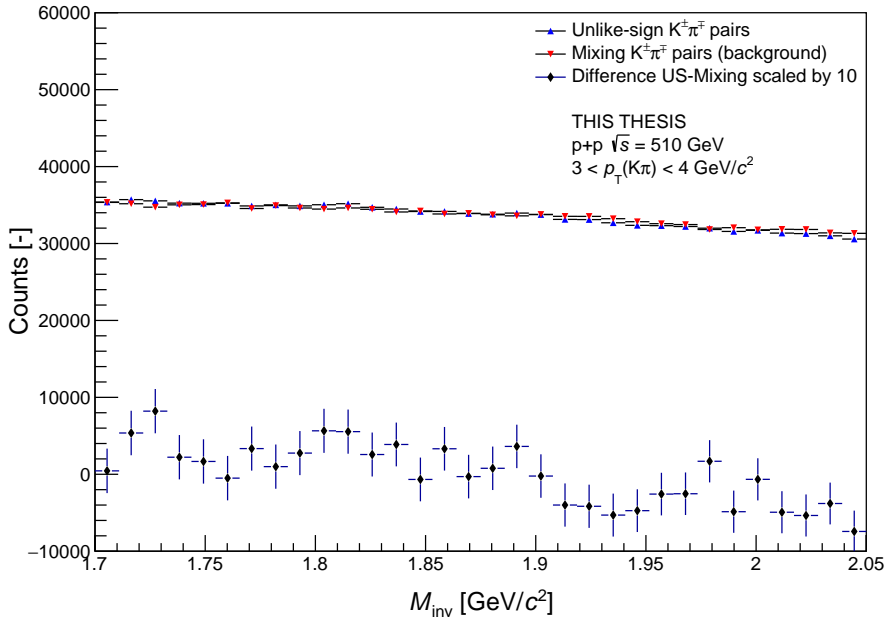


Figure 5.46: Unlike-sign (signal) distribution (blue triangles) and scaled background estimated by event mixing method (red triangles) and its subtraction scaled by 10 (black diamonds) for $3 < p_T < 4$ bin in the p+p collisions at $\sqrt{s} = 510$ GeV.

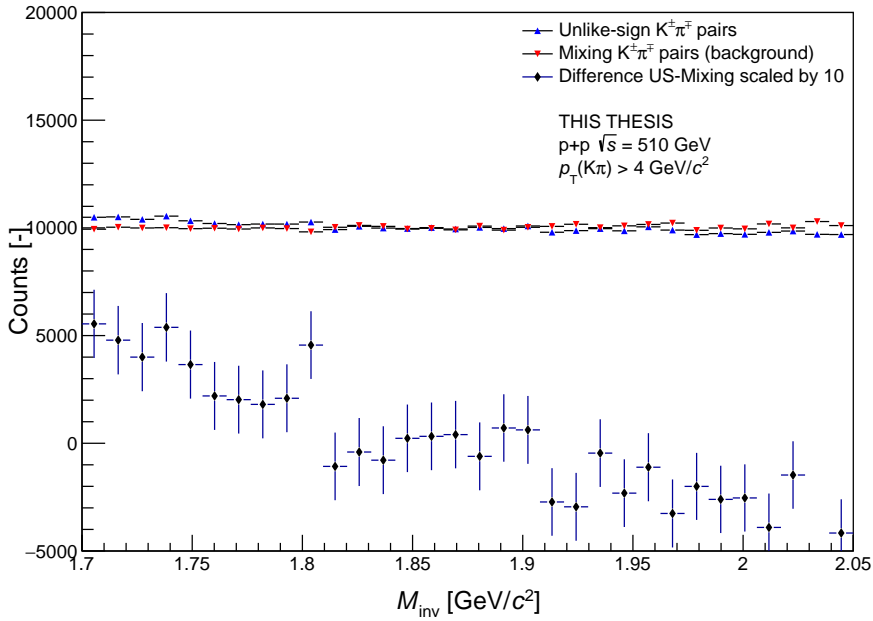


Figure 5.47: Unlike-sign (signal) distribution (blue triangles) and scaled background estimated by event mixing method (red triangles) and its subtraction scaled by 10 (black diamonds) for $p_T > 4$ bin in the p+p collisions at $\sqrt{s} = 510$ GeV.

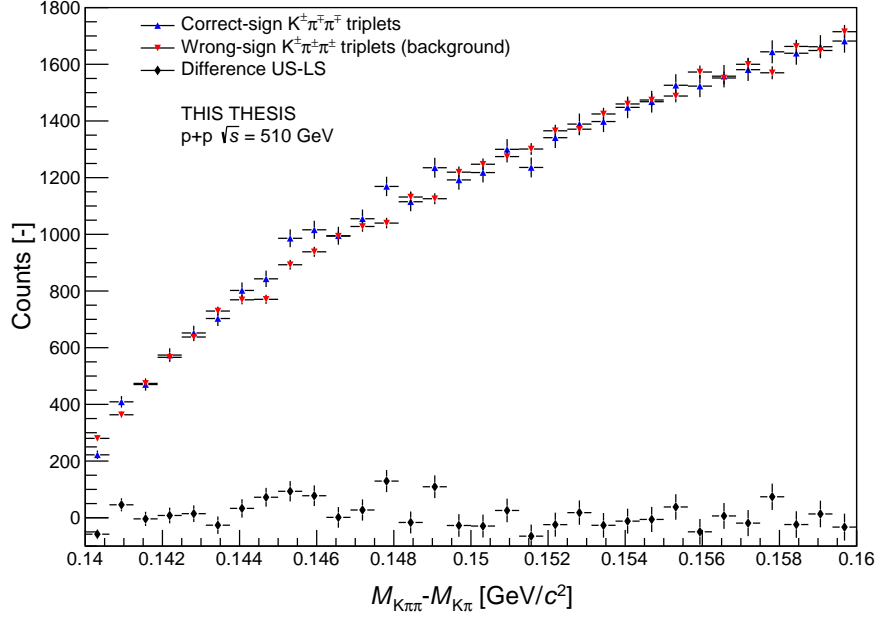


Figure 5.48: The $M_{K^{\mp}\pi^{\pm}\pi^{\pm}} - M_{K^{\mp}\pi^{\pm}}$ spectrum with combinatorial background estimated by wrong-sign method and the subtracted wrong-sign background and correct-sign signal for all D^* candidate p_T bins in the p+p collisions at $\sqrt{s} = 510$ GeV.

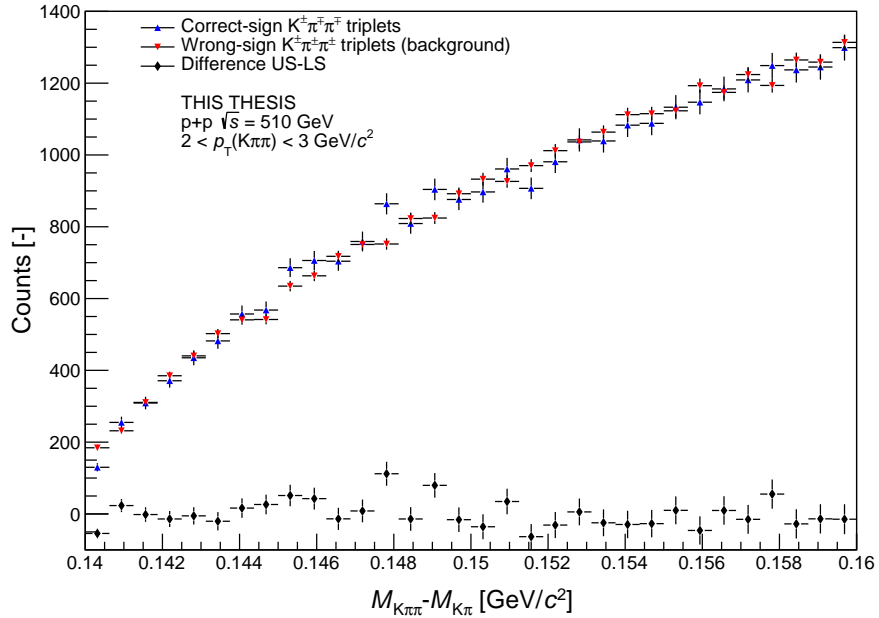


Figure 5.49: The $M_{K^{\mp}\pi^{\pm}\pi^{\pm}} - M_{K^{\mp}\pi^{\pm}}$ spectrum with combinatorial background estimated by wrong-sign method and the subtracted wrong-sign background and correct-sign signal for D^* candidate $2 < p_T < 3$ GeV/ c bin in the p+p collisions at $\sqrt{s} = 510$ GeV.

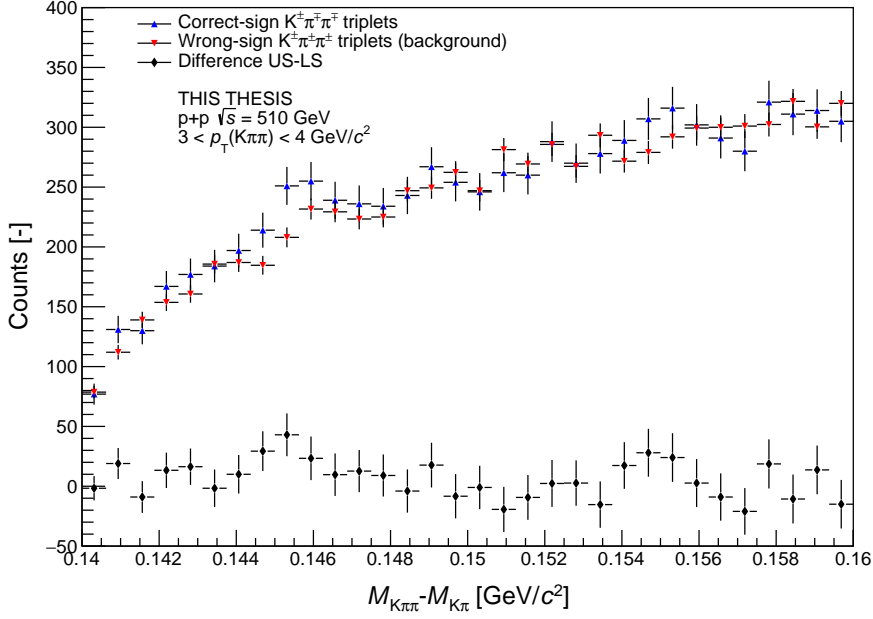


Figure 5.50: The $M_{K^{\mp}\pi^{\pm}\pi^{\pm}} - M_{K^{\mp}\pi^{\pm}}$ spectrum with combinatorial background estimated by wrong-sign method and the subtracted wrong-sign background and correct-sign signal for D^* candidate $3 < p_T < 4$ GeV/ c bin in the p+p collisions at $\sqrt{s} = 510$ GeV.

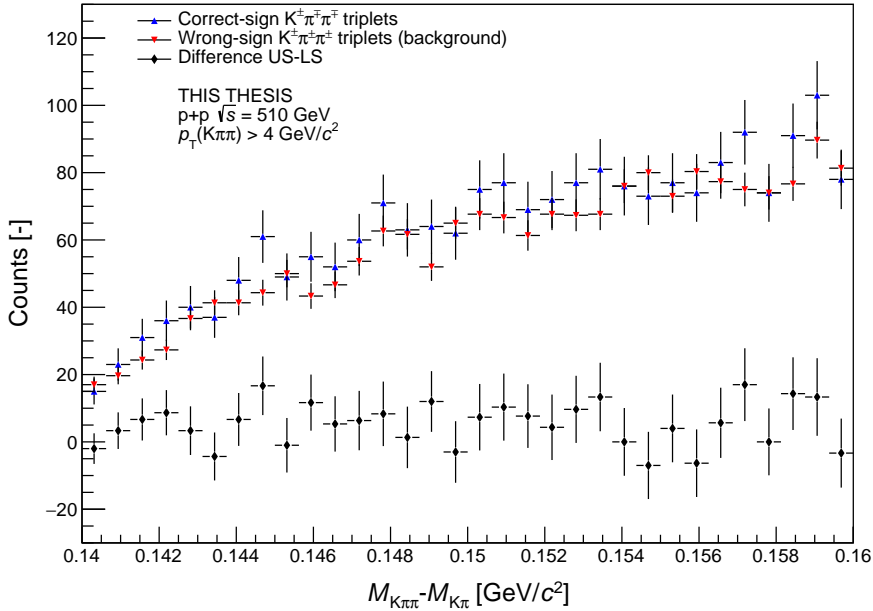


Figure 5.51: The $M_{K^{\mp}\pi^{\pm}\pi^{\pm}} - M_{K^{\mp}\pi^{\pm}}$ spectrum with combinatorial background estimated by wrong-sign method and the subtracted wrong-sign background and correct-sign signal for D^* candidate $p_T > 4$ GeV/ c bin in the p+p collisions at $\sqrt{s} = 510$ GeV.

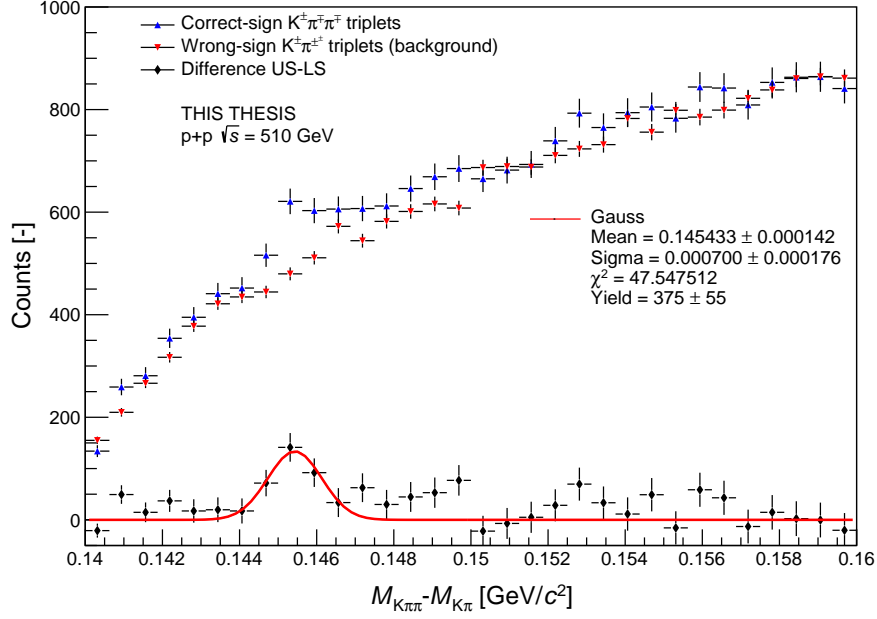


Figure 5.52: The $M_{K^{\mp}\pi^{\pm}\pi^{\pm}} - M_{K^{\mp}\pi^{\pm}}$ spectrum with combinatorial background estimated by wrong-sign method and the subtracted wrong-sign background and correct-sign signal for all D^* candidate p_T bins in the p+p collisions at $\sqrt{s} = 510$ GeV fitted by gaussian function.

D^* Analysis with BEMC

For this section the procedure mentioned at the end of section 5.2.2 has been used. The results for various D^* p_T bins are shown in Figs. 5.52-5.55. In all bins, there is a visible hint of peak around the expected value. This peak is fitted by a gaussian in Figs. 5.52 and 5.53 where the results for all p_T and $2 < p_T < 3$ GeV/ c bin, respectively are shown. In other two bins the peak would be too insignificant. The fits look reasonable, however the data tend to fluctuate for higher $M_{K^{\mp}\pi^{\pm}\pi^{\pm}} - M_{K^{\mp}\pi^{\pm}}$ which has impact at the goodness of the fit. The fluctuations are increasing in higher p_T bins where the number of candidates is much lower. The invariant yield from p+p collisions at $\sqrt{s} = 510$ GeV [3] for all p_T is (230 ± 28) . The dataset in 2011 had approximately 4 times smaller statistics than in 2017 so the expected yield should be at least four times larger, because the luminosity also increased since 2017. However result from this analysis for D^* raw yield is (375 ± 55) , which is only about 1.5 times larger than 2011 result. Furthermore data from this analysis need to be corrected for the effects of the detectors. This points to the conclusion that the separation of candidates needs to be improved and the pile-up problem needs to be solved.

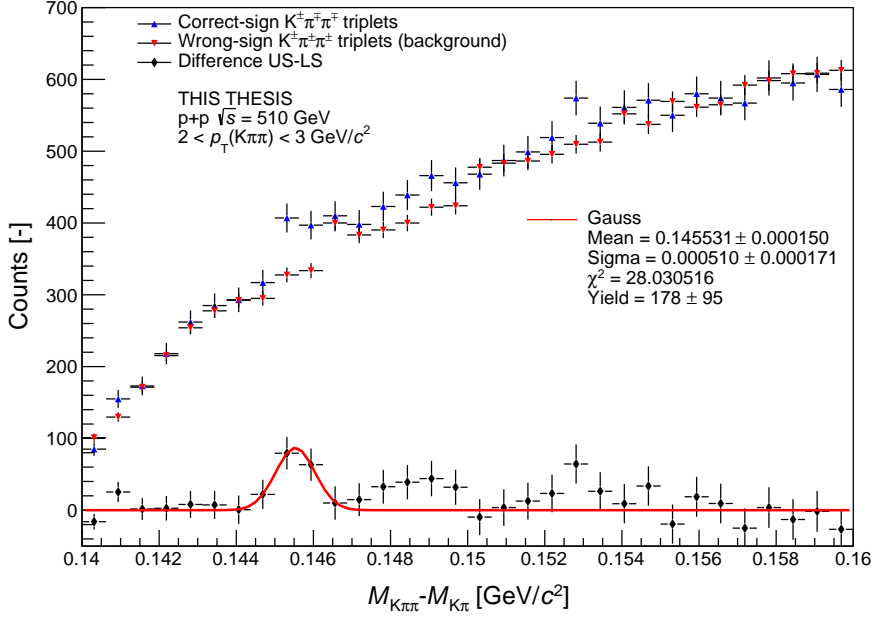


Figure 5.53: The $M_{K^{\mp}\pi^{\pm}\pi^{\pm}} - M_{K^{\mp}\pi^{\pm}}$ spectrum with combinatorial background estimated by wrong-sign method and the subtracted wrong-sign background and correct-sign signal for D^* candidate $2 < p_T < 3$ GeV/ c bin in the p+p collisions at $\sqrt{s} = 510$ GeV.

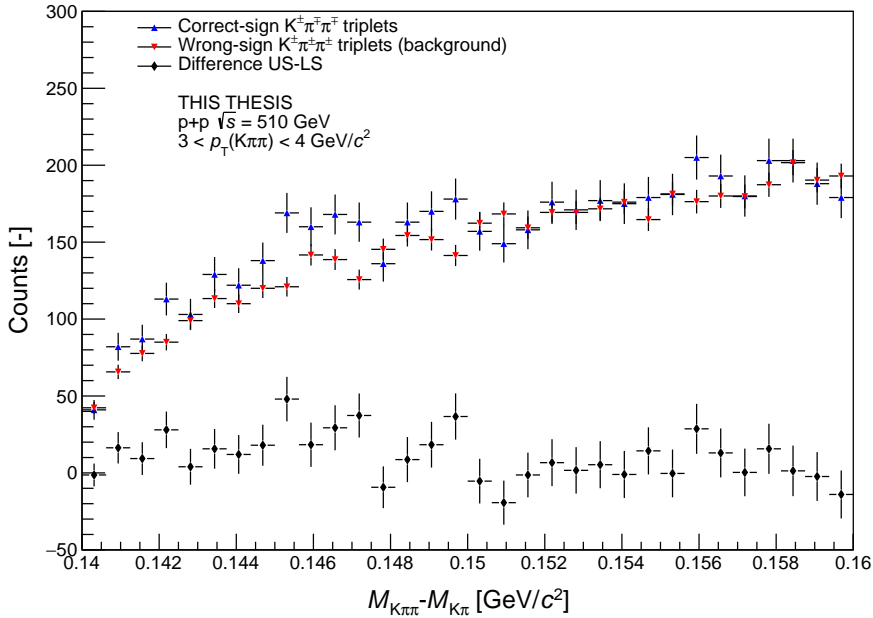


Figure 5.54: The $M_{K^{\mp}\pi^{\pm}\pi^{\pm}} - M_{K^{\mp}\pi^{\pm}}$ spectrum with combinatorial background estimated by wrong-sign method and the subtracted wrong-sign background and correct-sign signal for D^* candidate $3 < p_T < 4$ GeV/ c bin in the p+p collisions at $\sqrt{s} = 510$ GeV.

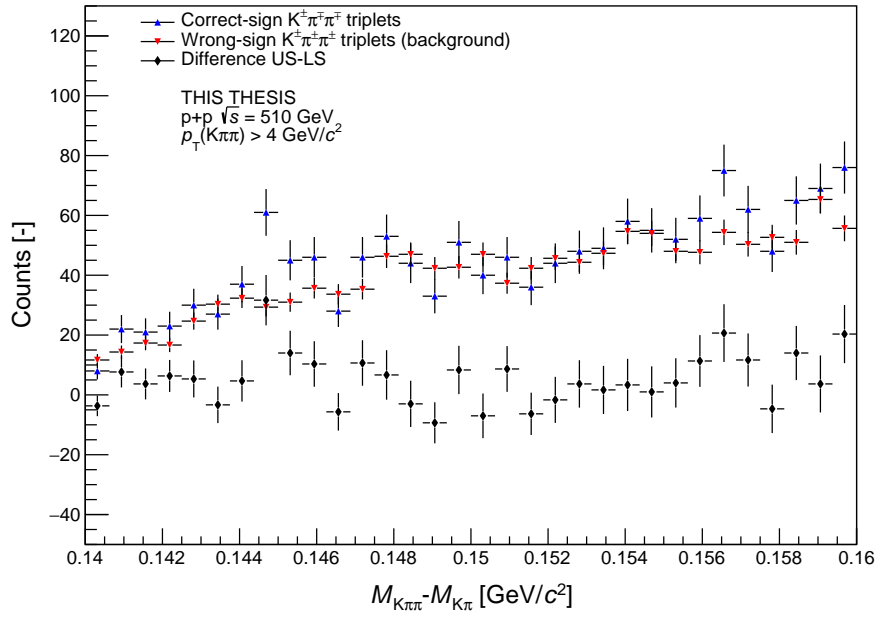


Figure 5.55: The $M_{K^{\mp}\pi^{\pm}\pi^{\pm}} - M_{K^{\mp}\pi^{\pm}}$ spectrum with combinatorial background estimated by wrong-sign method and the subtracted wrong-sign background and correct-sign signal for D^* candidate $p_T > 4$ GeV/ c bin in the p+p collisions at $\sqrt{s} = 510$ GeV.

Summary and Discussion

D mesons such as D^0 are lightest hadrons containing heavy charm quarks. Heavy quarks are useful probes of heavy-ion collisions since they originate in the hard partonic scattering before the formation of the Quark-Gluon Plasma. To describe the heavy-ion collisions and the QGP, it is necessary to understand the small systems. Those are collisions of protons and asymmetric collisions (p+Au, p+Pb..) where the effects caused by a presence of a nucleus in a collision (so called Cold Nuclear Matter effects) are tested.

The first chapter provides an introduction to the physics of particle collisions done at LHC and RHIC. The Standard Model and Quantum Chromodynamics are briefly introduced together with the variables and phenomena used to study heavy-ion collisions and also different collision systems. The focus is put into the signature measurement of properties present in the heavy-ion collisions which help to prove the presence of the QGP. Those are nuclear modification factor, jet quenching, quarkonia suppression, baryon to meson ratio and hydrodynamic flow.

The second chapter describes the experimental setup used for the analysis presented in this thesis. The Relativistic Heavy Ion Collider located at the Brookhaven National Laboratory is the second largest particle collider in the world and only one able to collide polarized beams of protons. The Solenoidal Tracker at RHIC is a large multipurpose experiment present at RHIC since 2000. Its subdetectors are described in the second chapter with a focus to those important for this analysis (TPC, TOF, VPD...). RHIC will conclude its program in 2025 and after that will be replaced by a device called Electron-Ion Collider where electrons and heavy-ions/protons will be collided. It is expected that this collider might begin its data-taking phase after 2030 and is introduced in the last section of the chapter.

The third chapter explains so called Cold Nuclear Matter effects. Those are effects caused by a presence of a nucleus in the collision and are measured in the asymmetric collisions at LHC and RHIC. Multiple effects might contribute, such as Cronin effect, or modification of parton distribution function of free nucleon with respect to that bound in a nucleus. In the second part are shown selected results from

the asymmetric collisions done at ALICE and PHENIX such as nuclear modification factors or hydrodynamic flow measured in the small systems at RHIC.

The next chapter summarizes properties of heavy-charm quarks in the collisions. The first part explains general properties and the well-understood production in the collisions of protons. The second half shows selected results measured at ALICE and STAR detectors. Focus is put into charm mesons and results of their measurement such as nuclear modification factor, hydrodynamic flow or baryon to meson ratios.

The last chapter shows analysis of D^0 and D^* meson in two datasets - p+Au collisions measured at STAR in 2015 at $\sqrt{s_{NN}} = 200$ GeV and p+p collisions measured at STAR in 2017 at $\sqrt{s} = 510$ GeV. The approach is similar in both the datasets with small differences. The methods used for the analysis of both datasets were tested in previous analyses [2], [3]. Typical analysis of D mesons from STAR takes advantage of using the HFT detector which was not available for either of the datasets so other methods (not usually used in HFT analyses) were applied to get clean samples of pions and kaons.

Two methods were used to describe the background in p+Au collisions - Like-Sign and Side-Band, and three for the description of background in p+p collisions - Like-Sign, Side-Band and Event-Mixing. Except for the section with BEMC the methods are not sufficient to obtain significant signal, however are working since the structure at low M_{inv} looks as was expected - the $K^{*0}(892)$ peak is clearly visible.

STAR has previously measured D^0 mesons in the small systems without the HFT detector, such as in Ref. [3]. However the data are from the years 2010 and 2011 and the luminosity was lower compared to 2017 and the statistics of the dataset was about 4 times smaller than in 2017. Larger luminosity leads to the production of more particles and thus to higher background and the separation of signal of signal and background is more difficult even though same approach has been used for the analysis. The p+Au collisions have more binary collisions than the collisions of protons which is again origin of larger background which makes the separation more difficult.

The most successful part of this thesis is the measurement of D^* meson with the use of BEMC detector, where the peaks of invariant mass were sufficient to extract raw yield. The expected yield should be approximately 4 times larger than in the 2011 measurement [3], however the result (375 ± 55) is only about 1.5 times larger. Furthermore data from this analysis need to be corrected for the effects of the detectors. This points to the problem with pile-up which would need to be solved in the next steps. The data could be possibly further tuned with the use of different trigger or by implementing additional requirements for the particles matched in the

BEMC.

The next step for all the parts of the analysis is to remove effects of the pile-up which was beyond the scope of this thesis. Another possible step would be implementation of machine learning techniques such as a Toolkit for Multivariate Analysis (TMVA) implemented in ROOT. The machine learning was not used in the analysis yet because there were not observed any peaks in the spectra to be improved by TMVA so instead another method for the description of background (Event-Mixing) was implemented.

Bibliography

- [1] Satz, H., Sarkar, S., & Sinha, B. (Eds.). (2010). The physics of the quark-gluon plasma. *Lect.Notes Phys.*, (785), 1-369. <https://doi.org/10.1007/978-3-642-02286-9>
- [2] Kramárik, L. for the STAR collaboration, L. (2020). Reconstruction of D^0 meson in d+Au collisions at $\sqrt{s_{NN}} = 200$ GeV by the STAR experiment. *Physica Scripta*, 95(7). <https://doi.org/10.1088/1402-4896/ab9034>
- [3] Tlustý, D. (2014). *A Study of Open Charm Production in p+p Collisions at STAR* [Ph.D. thesis]. České vysoké učení technické v Praze.
- [4] J. J. Thomson on "Cathode Rays". (1948). *Nature*, 162(4107), 98-98. <https://doi.org/10.1038/162098a0>
- [5] Rutherford, E. (1911). LXXIX. The scattering of α and β particles by matter and the structure of the atom. *The London, Edinburgh, and Dublin Philosophical Magazine and Journal of Science*, 21(125), 669-688. <https://doi.org/10.1080/14786440508637080>
- [6] Chadwick, J. (1932). Possible Existence of a Neutron. *Nature*, 129(3252), 312-312. <https://doi.org/10.1038/129312a0>
- [7] Bloom, E. D., Coward, D. H., DeStaebler, H., Drees, J., Miller, G., Mo, L. W., Taylor, R. E., Breidenbach, M., Friedman, J. I., Hartmann, G. C., & Kendall, H. W. (1969). High-Energy Inelastic e-p Scattering at 6° and 10° . *Physical Review Letters*, 23(16), 930-934. <https://doi.org/10.1103/PhysRevLett.23.930>
- [8] Breidenbach, M., Friedman, J. I., Kendall, H. W., Bloom, E. D., Coward, D. H., DeStaebler, H., Drees, J., Mo, L. W., & Taylor, R. E. (1969). Observed Behavior of Highly Inelastic Electron-Proton Scattering. *Physical Review Letters*, 23(16), 935-939. <https://doi.org/10.1103/PhysRevLett.23.935>
- [9] Aubert, J. J., Becker, U., Biggs, P. J., Burger, J., Chen, M., Everhart, G., Goldhagen, P., Leong, J., McCorrison, T., Rhoades, T. G., Rohde,

- M., Ting, S. C. C., Wu, S. L., & Lee, Y. Y. (1974). Experimental Observation of a Heavy Particle J. *Physical Review Letters*, *33*(23), 1404-1406. <https://doi.org/10.1103/PhysRevLett.33.1404>
- [10] [SPEAR Collaboration] Augustin, J. -E., et al. (1974). Discovery of a Narrow Resonance in e^+e^- Annihilation. *Physical Review Letters*, *33*(23), 1406-1408. <https://doi.org/10.1103/PhysRevLett.33.1406>
- [11] *The Nobel Prize*. Retrieved December 24, 2022, from <https://www.nobelprize.org/>
- [12] [E288 Collaboration] Herb, S. W., Hom, D. C., Lederman, L. M., Sens, J. C., Snyder, H. D., Yoh, J. K., Appel, J. A., Brown, B. C., Brown, C. N., Innes, W. R., Ueno, K., Yamanouchi, T., Ito, A. S., Jöstlein, H., Kaplan, D. M., & Kephart, R. D. (1977). Observation of a Dimuon Resonance at 9.5 GeV in 400-GeV Proton-Nucleus Collisions. *Physical Review Letters*, *39*(5), 252-255. <https://doi.org/10.1103/PhysRevLett.39.252>
- [13] [D0 Collaboration] Abachi, S., et al. (1995). Search for High Mass Top Quark Production in $p\bar{p}$ Collisions at $\sqrt{s} = 1.8$ TeV. *Physical Review Letters*, *74*(13), 2422-2426. <https://doi.org/10.1103/PhysRevLett.74.2422>
- [14] Anderson, C. D., & Neddermeyer, S. H. (1936). Cloud Chamber Observations of Cosmic Rays at 4300 Meters Elevation and Near Sea-Level. *Physical Review*, *50*(4), 263-271. <https://doi.org/10.1103/PhysRev.50.263>
- [15] Anderson, C. D. (1932). The Apparent Existence of Easily Deflectable Positives. *Science*, *76*(1967), 238-239. <https://doi.org/10.1126/science.76.1967.238>
- [16] Cowan, C. L., Reines, F., Harrison, F. B., Kruse, H. W., & McGuire, A. D. (1956). Detection of the Free Neutrino: a Confirmation. *Science*, *124*(3212), 103-104. <https://doi.org/10.1126/science.124.3212.103>
- [17] Bacino, W., Ferguson, T., Nodulman, L., Slater, W., Ticho, H. K., Diamant-Berger, A., Faessler, M., Hall, A., Irwin, G., Kirkby, J., Merritt, F., Wojcicki, S., Burns, R., Condon, P., Cowell, P., & Kirz, J. (1978). Measurement of the Threshold Behavior of $\tau^+\tau^-$ Production in e^+e^- Annihilation. *Physical Review Letters*, *41*(1), 13-15. <https://doi.org/10.1103/PhysRevLett.41.13>
- [18] [UA1 Collaboration] Arnison, G., et al. (1983). Experimental observation of isolated large transverse energy electrons with associated missing energy at $\sqrt{s} = 540$ GeV. *Physics Letters B*, *122*(1), 103-116. [https://doi.org/10.1016/0370-2693\(83\)91177-2](https://doi.org/10.1016/0370-2693(83)91177-2)

- [19] [UA2 Collaboration] Banner, M., et al. (1983). Observation of single isolated electrons of high transverse momentum in events with missing transverse energy at the CERN $p\bar{p}$ collider. *Physics Letters B*, *122*(5-6), 476-485. [https://doi.org/10.1016/0370-2693\(83\)91605-2](https://doi.org/10.1016/0370-2693(83)91605-2)
- [20] [UA1 Collaboration] Arnison, G., et al. (1983). Experimental observation of lepton pairs of invariant mass around 95 GeV/ c^2 at the CERN SPS collider. *Physics Letters B*, *126*(5), 398-410. [https://doi.org/10.1016/0370-2693\(83\)90188-0](https://doi.org/10.1016/0370-2693(83)90188-0)
- [21] [UA2 Collaboration] Bagnaia, P., et al. (1983). Evidence for $Z^0 \rightarrow e^+e^-$ at the CERN $p\bar{p}$ collider. *Physics Letters B*, *129*(1-2), 130-140. [https://doi.org/10.1016/0370-2693\(83\)90744-X](https://doi.org/10.1016/0370-2693(83)90744-X)
- [22] Ellis, J., Gaillard, M. K., & Ross, G. G. (1976). Search for gluons in e^+e^- annihilation. *Nuclear Physics B*, *111*(2), 253-271. [https://doi.org/10.1016/0550-3213\(76\)90542-3](https://doi.org/10.1016/0550-3213(76)90542-3)
- [23] [ATLAS Collaboration] Aad, G., et al. (2012). Observation of a new particle in the search for the Standard Model Higgs boson with the ATLAS detector at the LHC. *Physics Letters B*, *716*(1). <https://doi.org/10.1016/j.physletb.2012.08.020>
- [24] [CMS Collaboration] Chatrchyan, S., et al. (2012). Observation of a new boson at a mass of 125 GeV with the CMS experiment at the LHC. *Physics Letters B*, *716*(1). <https://doi.org/10.1016/j.physletb.2012.08.021>
- [25] Higgs, P. W. (1964). Broken Symmetries and the Masses of Gauge Bosons. *Physical Review Letters*, *13*(16), 508-509. <https://doi.org/10.1103/PhysRevLett.13.508>
- [26] Englert, F., & Brout, R. (1964). Broken Symmetry and the Mass of Gauge Vector Mesons. *Physical Review Letters*, *13*(9), 321-323. <https://doi.org/10.1103/PhysRevLett.13.321>
- [27] Guralnik, G. S., Hagen, C. R., & Kibble, T. W. B. (1964). Global Conservation Laws and Massless Particles. *Physical Review Letters*, *13*(20), 585-587. <https://doi.org/10.1103/PhysRevLett.13.585>
- [28] [KATRIN Collaboration] Aker, M., et al. (2022). Direct neutrino-mass measurement with sub-electronvolt sensitivity. *Nature Physics*, *18*(2), 160-166. <https://doi.org/10.1038/s41567-021-01463-1>

- [29] [Particle Data Group] Workman, R. L., et al. (2022). Review of Particle Physics. *Progress of Theoretical and Experimental Physics*, 2022(8). <https://doi.org/10.1093/ptep/ptac097>
- [30] [Super-KAMIOKANDE Collaboration] Kajita, T., et al. (2016). Establishing atmospheric neutrino oscillations with Super-Kamiokande. *Nuclear Physics B*, 908, 14-29. <https://doi.org/10.1016/j.nuclphysb.2016.04.017>
- [31] *File:Standard Model of Elementary Particles Anti.svg*. Wikipedia: the free encyclopedia. Retrieved February 7, 2022, from https://en.wikipedia.org/wiki/File:Standard_Model_of_Elementary_Particles_Anti.svg
- [32] Kumar, L., & Keane, D. (2015). Experimental studies of the quantum chromodynamics phase diagram at the STAR experiment. *Pramana*, 84(5), 773-786. <https://doi.org/10.1007/s12043-015-0969-9>
- [33] Tlustý, D. (2018). The RHIC Beam Energy Scan Phase II: Physics and Upgrades, *arXiv:1810.04767 [nucl-ex]*.
- [34] Sanches, S. M., Fogaça, D. A., & Navarra, F. S. (2015). The time evolution of the quark gluon plasma in the early Universe. *Journal of Physics: Conference Series*, 630. <https://doi.org/10.1088/1742-6596/630/1/012028>
- [35] Blaizot, J. P., & Iancu, E. (Eds.). (2002). *QCD Perspectives on Hot and Dense Matter*. Springer.
- [36] Florkowski, W. (2010). *Phenomenology of Ultra-Relativistic Heavy-Ion Collisions*. World Scientific.
- [37] Shi, S. (2010). *Event anisotropy v_2 at STAR* [Ph. D. thesis]. Hua-Zhong Normal U.
- [38] Snellings, R. (2011). Elliptic flow: a brief review. *New Journal of Physics*, 13(5). <https://doi.org/10.1088/1367-2630/13/5/055008>
- [39] Aggarwal, M. M. et al. (2002). Transverse mass distributions of neutral pions from ^{208}Pb -induced reactions at 158 $\cdot A$ GeV. *The European Physical Journal C*, 23(2), 225-236. <https://doi.org/10.1007/s100520100886>
- [40] d'Enterria, D. (2004). Indications of suppressed high p_T hadron production in nucleus-nucleus collisions at CERN-SPS. *Physics Letters B*, 596(1), 32-43. <https://doi.org/https://doi.org/10.1016/j.physletb.2004.06.071>

- [41] [PHENIX Collaboration] Adare, A., et al. (2008). Suppression pattern of neutral pions at high transverse momentum in Au+Au collisions at $\sqrt{s_{\text{NN}}} = 200$ GeV and constraints on medium transport coefficients. *Physical Review Letters*, *101*(23). <https://doi.org/10.1103/PhysRevLett.101.232301>
- [42] [STAR Collaboration] Adams, J., et al. (2003). Transverse-momentum and collision-energy dependence of high- p_{T} hadron suppression in Au+Au collisions at ultrarelativistic energies. *Physical Review Letters*, *91*(17). <https://doi.org/10.1103/PhysRevLett.91.172302>
- [43] [ALICE Collaboration] Aamodt, K., et al. (2011). Suppression of charged particle production at large transverse momentum in central Pb-Pb collisions at $\sqrt{s_{\text{NN}}} = 2.76$ TeV. *Physics Letters B*, *696*(1-2), 30-39. <https://doi.org/10.1016/j.physletb.2010.12.020>
- [44] [CMS Collaboration] Chatrchyan, S., et al. (2012). Study of high- p_{T} charged particle suppression in PbPb compared to pp collisions at $\sqrt{s_{\text{NN}}} = 2.76$ TeV. *The European Physical Journal C*, *72*(3), 1-22. <https://doi.org/10.1140/epjc/s10052-012-1945-x>
- [45] Dainese, A., Loizides, C., & Paic, G. (2005). Leading-particle suppression in high energy nucleus-nucleus collisions. *The European Physical Journal C*, *38*(4), 461-474. <https://doi.org/10.1140/epjc/s2004-02077-x>
- [46] Vitev, I., & Gyulassy, M. (2002). High- p_{T} Tomography of d+Au and Au+Au at SPS, RHIC, and LHC. *Physical Review Letters*, *89*(25). <https://doi.org/10.1103/PhysRevLett.89.252301>
- [47] Vitev, I. (2004). Jet tomography. *Journal of Physics G: Nuclear and Particle Physics*, *30*(8), S791-S800. <https://doi.org/10.1088/0954-3899/30/8/019>
- [48] Salgado, C. A., & Wiedemann, U. A. (2003). Calculating quenching weights. *Physical Review D*, *68*(1). <https://doi.org/10.1103/PhysRevD.68.014008>
- [49] Armesto, N., Dainese, A., Salgado, C. A., & Wiedemann, U. A. (2005). Testing the color charge and mass dependence of parton energy loss with heavy-to-light ratios at BNL RHIC and CERN LHC. *Physical Review D*, *71*(5). <https://doi.org/10.1103/PhysRevD.71.054027>
- [50] Renk, T., Holopainen, H., Paatelainen, R., & Eskola, K. J. (2011). Systematics of the charged-hadron P_{T} spectrum and the nuclear suppression factor in heavy-ion collisions from $\sqrt{s_{\text{NN}}} = 200$ GeV to $\sqrt{s_{\text{NN}}} = 2.76$ TeV. *Physical Review C*, *84*(1). <https://doi.org/10.1103/PhysRevC.84.014906>

- [51] [ALICE Collaboration] Acharya, S., et al. (2018). Transverse momentum spectra and nuclear modification factors of charged particles in pp, p-Pb and Pb-Pb collisions at the LHC. *Journal of High Energy Physics*, 2018(11). [https://doi.org/10.1007/JHEP11\(2018\)013](https://doi.org/10.1007/JHEP11(2018)013)
- [52] [STAR Collaboration] Adamczyk, L., et al. (2018). Beam Energy Dependence of Jet-Quenching Effects in Au+Au Collisions at $\sqrt{s_{\text{NN}}} = 7.7, 11.5, 14.5, 19.6, 27, 39, \text{ and } 62.4$ GeV. *Physical Review Letters*, 121(3). <https://doi.org/10.1103/PhysRevLett.121.032301>
- [53] [STAR Collaboration] Adams, J., et al. (2003). Evidence from d+Au measurements for final state suppression of high p_{T} hadrons in Au+Au collisions at RHIC. *Physical Review Letters*, 91(7). <https://doi.org/10.1103/PhysRevLett.91.072304>
- [54] [ATLAS Collaboration] Aaboud, M., et al. (2019). Measurement of the nuclear modification factor for inclusive jets in Pb+Pb collisions at $\sqrt{s_{\text{NN}}} = 5.02$ TeV with the ATLAS detector. *Physics Letters B*, 790, 108-128. <https://doi.org/10.1016/j.physletb.2018.10.076>
- [55] [CMS Collaboration] Chatrchyan, S., et al. (2012). Observation of Sequential Υ Suppression in PbPb Collisions. *Physical Review Letters*, 109(22). <https://doi.org/10.1103/PhysRevLett.109.222301>
- [56] [ALICE Collaboration] Adam, J., et al. (2016). Differential studies of inclusive J/ψ and $\psi(2S)$ production at forward rapidity in Pb-Pb collisions at $\sqrt{s_{\text{NN}}} = 2.76$ TeV. *Journal of High Energy Physics*, 2016(5). [https://doi.org/10.1007/JHEP05\(2016\)179](https://doi.org/10.1007/JHEP05(2016)179)
- [57] [ALICE Collaboration] Adam, J., et al. (2017). J/ψ suppression at forward rapidity in Pb-Pb collisions at $\sqrt{s_{\text{NN}}} = 5.02$ TeV. *Physics Letters B*, 766. <https://doi.org/10.1016/j.physletb.2016.12.064>
- [58] [PHENIX Collaboration] Adare, A., et al. (2011). J/ψ suppression at forward rapidity in Au+Au collisions at $\sqrt{s_{\text{NN}}} = 200$ GeV. *Physical Review C*, 84(5). <https://doi.org/10.1103/PhysRevC.84.054912>
- [59] Scomparin, E. (2017). Quarkonium production in A-A and p-A collisions. *Nuclear Physics A*, 967, 208-215. <https://doi.org/10.1016/j.nuclphysa.2017.05.072>
- [60] [STAR Collaboration] Adams, J., et al. (2005). Pion, kaon, proton and anti-proton transverse momentum distributions from p+p and

- d+Au collisions at $\sqrt{s_{\text{NN}}} = 200$ GeV. *Physics Letters B*, 616(1-2).
<https://doi.org/10.1016/j.physletb.2005.04.041>
- [61] [STAR Collaboration] Adams, J., et al. (2006). Identified hadron spectra at large transverse momentum in p p and d Au collisions at $s_{\text{NN}} = 200$ GeV. *Physics Letters B*, 637(3), 161-169.
<https://doi.org/10.1016/j.physletb.2006.04.032>
- [62] [DELPHI Collaboration] Abreu, P. et al. (1998). π^\pm , K^\pm , p and \bar{p} production in $Z^0 \rightarrow q\bar{q}$, $Z^0 \rightarrow b\bar{b}$, $Z^0 \rightarrow u\bar{u}$, $d\bar{d}$, $s\bar{s}$. *The European Physical Journal C*, 5(4), 585-620. <https://doi.org/10.1007/s100529800989>
- [63] Hwa, R. C., & Yang, C. B. (2004). Recombination of shower partons at high p_T in heavy-ion collisions. *Physical Review C*, 70(2).
<https://doi.org/10.1103/PhysRevC.70.024905>
- [64] Fries, R. J., Müller, B., Nonaka, C., & Bass, S. A. (2003). Hadron production in heavy ion collisions: Fragmentation and recombination from a dense parton phase. *Physical Review C*, 68(4).
<https://doi.org/10.1103/PhysRevC.68.044902>
- [65] [STAR Collaboration] Abelev, B. I., et al. (2006). Identified Baryon and Meson Distributions at Large Transverse Momenta from Au+Au Collisions at $\sqrt{s_{\text{NN}}} = 200$ GeV. *Physical Review Letters*, 97(15).
<https://doi.org/10.1103/PhysRevLett.97.152301>
- [66] Stefaniak, M., & Zbroszczyk, H. (2017). Examination of the heavy-ion collisions using EPOS model in the frame of BES program at RHIC. *EPJ Web Conf.*, (164). <https://doi.org/https://doi.org/10.1051/epjconf/201716407013>
- [67] [ALICE Collaboration] Acharya, S., et al. (2018). Anisotropic flow of identified particles in Pb-Pb collisions at $\sqrt{s_{\text{NN}}} = 5.02$ TeV. *Journal of High Energy Physics*, 2018(9). [https://doi.org/10.1007/JHEP09\(2018\)006](https://doi.org/10.1007/JHEP09(2018)006)
- [68] [CMS Collaboration] Khachatryan, V., et al. (2017). Evidence for collectivity in pp collisions at the LHC. *Physics Letters B*, 765.
<https://doi.org/10.1016/j.physletb.2016.12.009>
- [69] Weller, R. D., & Romatschke, P. (2017). One fluid to rule them all: Viscous hydrodynamic description of event-by-event central p+p, p+Pb and Pb+Pb collisions at $\sqrt{s} = 5.02$ TeV. *Physics Letters B*, 774, 351-356.
<https://doi.org/10.1016/j.physletb.2017.09.077>

- [70] *Brookhaven National Laboratory*. About Brookhaven. Retrieved December 20, 2022, from <https://www.bnl.gov/about/history/>
- [71] Yi, L. (2014). *Study Quark Gluon Plasma by Particle Correlations in Heavy Ion Collisions* [Ph.D. thesis]. Purdue University.
- [72] Hahn, H., et al. (2003). The RHIC design overview. *Nuclear Instruments and Methods in Physics Research Section A: Accelerators, Spectrometers, Detectors and Associated Equipment*, 499(2-3), 245-263. [https://doi.org/10.1016/S0168-9002\(02\)01938-1](https://doi.org/10.1016/S0168-9002(02)01938-1)
- [73] *CERN - Facts and figures about the LHC*. Retrieved May 14, 2020, from <https://home.cern/resources/faqs/facts-and-figures-about-lhc>
- [74] Weng, W., & Lee, Y. Y. (1988). Design and construction status of the AGS booster accelerator, *BNL - 41030*.
- [75] Alessi, J., et al. (2005). Electron Beam Ion Source Pre-injector Project (EBIS) Conceptual Design Report. <https://doi.org/10.2172/15020507>
- [76] *The STAR experiment*. Retrieved May 14, 2020, from <https://www.star.bnl.gov/>
- [77] Tannenbaum, M. J. (2019). Latest Results from RHIC Progress on Determining $\hat{q}L$ in RHI Collisions Using Di-Hadron Correlations. *Universe*, 5(6). <https://doi.org/10.3390/universe5060140>
- [78] [STAR Collaboration] Anderson, M., et al. (2003). The STAR time projection chamber: a unique tool for studying high multiplicity events at RHIC. *Nuclear Instruments and Methods in Physics Research Section A: Accelerators, Spectrometers, Detectors and Associated Equipment*, 499(2-3), 659-678. [https://doi.org/10.1016/S0168-9002\(02\)01964-2](https://doi.org/10.1016/S0168-9002(02)01964-2)
- [79] [STAR Collaboration] Adam, J., et al. (2019). Centrality and transverse momentum dependence of D^0 -meson production at mid-rapidity in Au+Au collisions at $\sqrt{s_{NN}} = 200$ GeV. *Physical Review C*, 99(3). <https://doi.org/10.1103/PhysRevC.99.034908>
- [80] Hu, D., Sauter, D., Wang, X., Sun, Y., Deppner, I., Herrmann, N., Simon, C., Weidenkaff, P., Brandt, J., Zhou, J., Shao, M., Li, C., Chen, H., Tang, Z., Zhang, Y., Lavrik, E., & Zeng, H. (2019). MRPC3b mass production for CBM-TOF and eTOF at STAR. *Journal of Instrumentation*, 14(06), C06013-C06013. <https://doi.org/10.1088/1748-0221/14/06/C06013>

- [81] Judd, E. G., Bland, L. C., Crawford, H. J., Engelage, J., Landgraf, J. M., Llope, W. J., Nelson, J. M., Ng, M., Ogawa, A., Perkins, C., Visser, G., & Xu, Z. (2018). The evolution of the STAR Trigger System. *Nuclear Instruments and Methods in Physics Research Section A: Accelerators, Spectrometers, Detectors and Associated Equipment*, 902, 228-237. <https://doi.org/10.1016/j.nima.2018.03.070>
- [82] Adamczyk, L., et al. (2017). Measurement of D^0 Azimuthal Anisotropy at Midrapidity in Au+Au Collisions at $\sqrt{s_{NN}} = 200$ GeV. *Physical Review Letters*, 118(21). <https://doi.org/10.1103/PhysRevLett.118.212301>
- [83] Brandenburg, J. (2021). STAR Forward Rapidity Upgrade. *Proceedings of 10th International Conference on Hard and Electromagnetic Probes of High-Energy Nuclear Collisions - PoS(HardProbes2020)*, 179-. <https://doi.org/10.22323/1.387.0179>
- [84] Accardi, A., et al. (2016). Electron-Ion Collider: The next QCD frontier. *The European Physical Journal A*, 52(9). <https://doi.org/10.1140/epja/i2016-16268-9>
- [85] Abdul Khalek, R., et al. (2022). Snowmass 2021 White Paper: Electron Ion Collider for High Energy Physics. *ArXiv*. <https://doi.org/10.48550/arXiv.2203.13199>
- [86] Eskola, K. J., Paukkunen, H., & Salgado, C. A. (2009). EPS09 - A new generation of NLO and LO nuclear parton distribution functions. *Journal of High Energy Physics*, 2009(04), 065-065. <https://doi.org/10.1088/1126-6708/2009/04/065>
- [87] Andronic, A., et al. (2016). Heavy-flavour and quarkonium production in the LHC era: from proton-proton to heavy-ion collisions. *The European Physical Journal C*, 76(3). <https://doi.org/10.1140/epjc/s10052-015-3819-5>
- [88] Fritzsche, H. (1977). Producing heavy quark flavors in hadronic collisions - A test of quantum chromodynamics. *Physics Letters B*, 67(2), 217-221. [https://doi.org/10.1016/0370-2693\(77\)90108-3](https://doi.org/10.1016/0370-2693(77)90108-3)
- [89] Vogt, R. (2014). Predictions for p+Pb collisions at $\sqrt{s_{NN}} = 5$ TeV: Expectations vs. data. *Nuclear Physics A*, 932, 494-499. <https://doi.org/10.1016/j.nuclphysa.2014.07.004>
- [90] Marquet, C. (2013). Open questions in QCD at high parton density. *Nuclear Physics A*, 904-905, 294c-301c. <https://doi.org/10.1016/j.nuclphysa.2013.01.07>

- [91] Fujii, H., & Watanabe, K. (2013). Heavy quark pair production in high energy pA collisions: Open heavy flavors. *Nuclear Physics A*, *920*, 78-93. <https://doi.org/10.1016/j.nuclphysa.2013.10.006>
- [92] Fujii, H., & Watanabe, K. (2013). Heavy quark pair production in high-energy pA collisions: Quarkonium. *Nuclear Physics A*, *915*, 1-23. <https://doi.org/10.1016/j.nuclphysa.2013.06.011>
- [93] Kopeliovich, B. Z., Potashnikova, I. K., Pirner, H. J., & Schmidt, I. (2011). Heavy quarkonium production: Nontrivial transition from pA to AA collisions: Kopeliovich, B. Z. and Potashnikova, I. K. and Pirner, H. J. and Schmidt, Iván. *Phys. Rev. C*, *83*(1). <https://doi.org/10.1103/PhysRevC.83.014912>
- [94] Kopeliovich, B. Z., Potashnikova, I. K., & Schmidt, I. (2011). Nuclear suppression of: From RHIC to the LHC. *Nuclear Physics A*, *864*(1), 203-212. <https://doi.org/10.1016/j.nuclphysa.2011.06.024>
- [95] Vitev, I., Goldman, T., Johnson, M. B., & Qiu, J. W. (2006). Open charm tomography of cold nuclear matter. *Physical Review D*, *74*(5). <https://doi.org/10.1103/PhysRevD.74.054010>
- [96] Vitev, I. (2007). Non-Abelian energy loss in cold nuclear matter. *Physical Review C*, *75*(6). <https://doi.org/10.1103/PhysRevC.75.064906>
- [97] Arleo, F., Peigné, S., & Sami, T. (2011). Revisiting scaling properties of medium-induced gluon radiation. *Physical Review D*, *83*(11). <https://doi.org/10.1103/PhysRevD.83.114036>
- [98] Arleo, F., & Peigné, S. (2013). Heavy-quarkonium suppression in p-A collisions from parton energy loss in cold QCD matter. *Journal of High Energy Physics*, *2013*(3). [https://doi.org/10.1007/JHEP03\(2013\)122](https://doi.org/10.1007/JHEP03(2013)122)
- [99] Arleo, F., Kolevatov, R., Peigné, S., & Rostamova, M. (2013). Centrality and p dependence of J/ψ suppression in proton-nucleus collisions from parton energy loss. *Journal of High Energy Physics*, *2013*(5). [https://doi.org/10.1007/JHEP05\(2013\)155](https://doi.org/10.1007/JHEP05(2013)155)
- [100] Arleo, F., Kolevatov, R., & Peigné, S. (2016). Coherent medium-induced gluon radiation in hard forward 1 1 partonic processes. *Physical Review D*, *93*(1). <https://doi.org/10.1103/PhysRevD.93.014006>
- [101] Peigné, S., & Kolevatov, R. (2014). On the process-dependence of coherent medium-induced gluon radiation. *ArXiv*. <https://doi.org/10.48550/arXiv.1405.4241>

- [102] Sharma, R., & Vitev, I. (2013). High transverse momentum quarkonium production and dissociation in heavy ion collisions. *Physical Review C*, 87(4). <https://doi.org/10.1103/PhysRevC.87.044905>
- [103] [ALICE Collaboration] Acharya, S., et al. (2019). Measurement of prompt D^0 , D^+ , D^{*+} , and D_s^+ production in p+Pb collisions at $\sqrt{s_{NN}} = 5.02$ TeV. *Journal of High Energy Physics*, 2019(12). [https://doi.org/10.1007/JHEP12\(2019\)092](https://doi.org/10.1007/JHEP12(2019)092)
- [104] Pumplin, J., Stump, D. R., Huston, J., Lai, H. -L., Nadolsky, P., & Tung, W. -K. (2002). New Generation of Parton Distributions with Uncertainties from Global QCD Analysis. *Journal of High Energy Physics*, 2002(07), 012-012. <https://doi.org/10.1088/1126-6708/2002/07/012>
- [105] Eskola, K. J., Paakkinen, P., Paukkunen, H., & Salgado, C. A. (2017). EPPS16: nuclear parton distributions with LHC data. *The European Physical Journal C*, 77(3). <https://doi.org/10.1140/epjc/s10052-017-4725-9>
- [106] Sharma, R., Vitev, I., & Zhang, B. -W. (2009). Light-cone wave function approach to open heavy flavor dynamics in QCD matter. *Physical Review C*, 80(5). <https://doi.org/10.1103/PhysRevC.80.054902>
- [107] Kang, Z. -B., Vitev, I., Wang, E., Xing, H., & Zhang, C. (2015). Multiple scattering effects on heavy meson production in p+A collisions at backward rapidity. *Physics Letters B*, 740, 23-29. <https://doi.org/10.1016/j.physletb.2014.11.024>
- [108] Xu, Y., Cao, S., Nahrgang, M., Ke, W., Qin, G. -Y., Auvinen, J., & Bass, S. A. (2016). Heavy-flavor dynamics in relativistic p-Pb collisions at $\sqrt{s_{NN}} = 5.02$ TeV. *Nuclear and Particle Physics Proceedings*, 276-278, 225-228. <https://doi.org/10.1016/j.nuclphysbps.2016.05.050>
- [109] Beraudo, A., De Pace, A., Monteno, M., Nardi, M., & Prino, F. (2016). Heavy-flavour production in high-energy d-Au and p-Pb collisions. *Journal of High Energy Physics*, 2016(3). [https://doi.org/10.1007/JHEP03\(2016\)123](https://doi.org/10.1007/JHEP03(2016)123)
- [110] [PHENIX Collaboration] Aidala, C., et al. (2019). Creation of quark-gluon plasma droplets with three distinct geometries. *Nature Physics*, 15(3), 214-220. <https://doi.org/10.1038/s41567-018-0360-0>
- [111] Habich, M., Nagle, J. L., & Romatschke, P. (2015). Particle spectra and HBT radii for simulated central nuclear collisions of C+C, Al+Al, Cu+Cu, Au+Au, and Pb+Pb from $\sqrt{s} = 62.4 - 2760$ GeV. *The European Physical Journal C*, 75(1). <https://doi.org/10.1140/epjc/s10052-014-3206-7>

- [112] Shen, C., Paquet, J. -F., Denicol, G. S., Jeon, S., & Gale, C. (2017). Collectivity and electromagnetic radiation in small systems. *Physical Review C*, *95*(1). <https://doi.org/10.1103/PhysRevC.95.014906>
- [113] Mace, M., Skokov, V. V., Tribedy, P., & Venugopalan, R. (2018). Hierarchy of Azimuthal Anisotropy Harmonics in Collisions of Small Systems from the Color Glass Condensate. *Physical Review Letters*, *121*(5). <https://doi.org/10.1103/PhysRevLett.121.052301>
- [114] Mace, M., Skokov, V. V., Tribedy, P., & Venugopalan, R. (2019). Erratum: Hierarchy of Azimuthal Anisotropy Harmonics in Collisions of Small Systems from the Color Glass Condensate. *Physical Review Letters*, *121*(5). <https://doi.org/10.1103/PhysRevLett.121.052301>
- [115] Goldhaber, G., Pierre, F. M., Abrams, G. S., Alam, M. S., Boyarski, A. M., Breidenbach, M., Carithers, W. C., Chinowsky, W., Cooper, S. C., DeVoe, R. G., Dorfan, J. M., Feldman, G. J., Friedberg, C. E., Fryberger, D., Hanson, G., Jaros, J., Johnson, A. D., Kadyk, J. A., Larsen, R. R., et al. (1976). Observation in e^+e^- Annihilation of a Narrow State at $1865 \text{ MeV}/c^2$ Decaying to $K\pi$ and $K\pi\pi\pi$. *Physical Review Letters*, *37*(5), 255-259. <https://doi.org/10.1103/PhysRevLett.37.255>
- [116] Peruzzi, I., Piccolo, M., Feldman, G. J., Nguyen, H. K., Wiss, J. E., Abrams, G. S., Alam, M. S., Boyarski, A. M., Breidenbach, M., Carithers, W. C., Chinowsky, W., DeVoe, R. G., Dorfan, J. M., Fischer, G. E., Friedberg, C. E., Fryberger, D., Goldhaber, G., Hanson, G., Jaros, J. A., et al. (1976). Observation of a Narrow Charged State at $1876 \text{ MeV}/c^2$ Decaying to an Exotic Combination of $K\pi\pi$. *Physical Review Letters*, *37*(10), 569-571. <https://doi.org/10.1103/PhysRevLett.37.569>
- [117] Bothmann, E., Singh Chahal, G., Höche, S., Krause, J., Krauss, F., Kuttimalai, S., Liebschner, S., Napoletano, D., Schönherr, M., Schulz, H., Schumann, S., & Siebert, F. (2019). Event generation with Sherpa 2.2. *SciPost Physics*, *7*(3). <https://doi.org/10.21468/SciPostPhys.7.3.034>
- [118] Sjöstrand, T., Ask, S., Christiansen, J. R., Corke, R., Desai, N., Ilten, P., Mrenna, S., Prestel, S., Rasmussen, C. O., & Skands, P. Z. (2015). An introduction to PYTHIA 8.2. *Computer Physics Communications*, *191*, 159-177. <https://doi.org/10.1016/j.cpc.2015.01.024>
- [119] [ALICE Collaboration] Acharya, S., et al. (2022). Direct observation of the dead-cone effect in quantum chromodynamics. *Nature*, *605*(7910). <https://doi.org/10.1038/s41586-022-04572-w>

- [120] Dokshitzer, Y. L., Leder, G. D., Moretti, S., & Webber, B. R. (1997). Better jet clustering algorithms. *Journal of High Energy Physics*, 1997(08), 001-001. <https://doi.org/10.1088/1126-6708/1997/08/001>
- [121] [ALICE Collaboration] Abelev, B., et al. (2012). Measurement of charm production at central rapidity in proton-proton collisions at $\sqrt{s} = 7$ TeV. *Journal of High Energy Physics*, 2012(1). [https://doi.org/10.1007/JHEP01\(2012\)128](https://doi.org/10.1007/JHEP01(2012)128)
- [122] Cacciari, M., Greco, M., & Nason, P. (1998). The p_T spectrum in heavy-flavour hadroproduction. *Journal of High Energy Physics*, 1998(05), 007-007. <https://doi.org/10.1088/1126-6708/1998/05/007>
- [123] Cacciari, M., Frixione, S., & Nason, P. (2001). The p_T spectrum in heavy-flavour photoproduction. *Journal of High Energy Physics*, 2001(03), 006-006. <https://doi.org/10.1088/1126-6708/2001/03/006>
- [124] Cacciari, M., Frixione, S., Houdeau, N., Mangano, M. L., Nason, P., & Ridolfi, G. (2012). Theoretical predictions for charm and bottom production at the LHC. *Journal of High Energy Physics*, 2012(10). [https://doi.org/10.1007/JHEP10\(2012\)137](https://doi.org/10.1007/JHEP10(2012)137)
- [125] Kniehl, B. A., Kramer, G., Schienbein, I., & Spiesberger, H. (2006). Reconciling Open-Charm Production at the Fermilab Tevatron with QCD. *Physical Review Letters*, 96(1). <https://doi.org/10.1103/PhysRevLett.96.012001>
- [126] Kniehl, B. A., Kramer, G., Schienbein, I., & Spiesberger, H. (2012). Inclusive charmed-meson production at the CERN LHC. *The European Physical Journal C*, 72(7). <https://doi.org/10.1140/epjc/s10052-012-2082-2>
- [127] [ATLAS Collaboration] Aad, G., et al. (2016). Measurement of $D^{*\pm}$, D^\pm and D_s^\pm meson production cross sections in pp collisions at $\sqrt{s} = 7$ TeV with the ATLAS detector. *Nuclear Physics B*, 907. <https://doi.org/10.1016/j.nuclphysb.2016.04.032>
- [128] Kniehl, B. A., Kramer, G., Schienbein, I., & Spiesberger, H. (2005). Inclusive $D^{*\pm}$ production in $p\bar{p}$ collisions with massive charm quarks. *Physical Review D*, 71(1). <https://doi.org/10.1103/PhysRevD.71.014018>
- [129] Kniehl, B. A., Kramer, G., Schienbein, I., & Spiesberger, H. (2009). Open charm hadroproduction and the charm content of the proton. *Physical Review D*, 79(9). <https://doi.org/10.1103/PhysRevD.79.094009>

- [130] Cacciari, M., & Nason, P. (2003). Charm cross sections for the Tevatron Run II. *Journal of High Energy Physics*, 2003(09), 006-006. <https://doi.org/10.1088/1126-6708/2003/09/006>
- [131] Cacciari, M., Frixione, S., Mangano, M. L., Nason, P., & Ridolfi, G. (2004). QCD analysis of first b cross section data at 1.96 TeV. *Journal of High Energy Physics*, 2004(07), 033-033. <https://doi.org/10.1088/1126-6708/2004/07/033>
- [132] Frixione, S., & Webber, B. R. (2002). Matching NLO QCD computations and parton shower simulations. *Journal of High Energy Physics*, 2002(06), 029-029. <https://doi.org/10.1088/1126-6708/2002/06/029>
- [133] Frixione, S., Nason, P., & Webber, B. R. (2003). Matching NLO QCD and parton showers in heavy flavour production. *Journal of High Energy Physics*, 2003(08), 007-007. <https://doi.org/10.1088/1126-6708/2003/08/007>
- [134] Nason, P. (2004). A New Method for Combining NLO QCD with Shower Monte Carlo Algorithms. *Journal of High Energy Physics*, 2004(11), 040-040. <https://doi.org/10.1088/1126-6708/2004/11/040>
- [135] Frixione, S., Ridolfi, G., & Nason, P. (2007). A positive-weight next-to-leading-order Monte Carlo for heavy flavour hadroproduction. *Journal of High Energy Physics*, 2007(09), 126-126. <https://doi.org/10.1088/1126-6708/2007/09/126>
- [136] [STAR Collaboration] Adamczyk, L., et al. (2012). Measurements of D^0 and D^* production in p+p collisions at $\sqrt{s} = 200$ GeV. *Physical Review D*, 86(7). <https://doi.org/10.1103/PhysRevD.86.072013>
- [137] Cacciari, M., Nason, P., & Vogt, R. (2005). QCD Predictions for Charm and Bottom Quark Production at RHIC. *Physical Review Letters*, 95(12). <https://doi.org/10.1103/PhysRevLett.95.122001>
- [138] [ALICE Collaboration] Acharya, S., et al. (2021). Λ_c^+ production in pp and in p-Pb collisions at $\sqrt{s_{NN}} = 5.02$ TeV. *Physical Review C*, 104(5). <https://doi.org/10.1103/PhysRevC.104.054905>
- [139] Skands, P., Carrazza, S., & Rojo, J. (2014). Tuning PYTHIA 8.1: the Monash 2013 tune. *The European Physical Journal C*, 74(8). <https://doi.org/10.1140/epjc/s10052-014-3024-y>
- [140] Christiansen, J. R., & Skands, P. Z. (2015). String formation beyond leading colour. *Journal of High Energy Physics*, 2015(8). [https://doi.org/10.1007/JHEP08\(2015\)003](https://doi.org/10.1007/JHEP08(2015)003)

- [141] [ALICE Collaboration] Acharya, S., et al. (2022). Observation of a multiplicity dependence in the p_T -differential charm baryon-to-meson ratios in proton-proton collisions at $\sqrt{s} = 13$ TeV. *Physics Letters B*, 829. <https://doi.org/10.1016/j.physletb.2022.137065>
- [142] [STAR Collaboration] Abelev, B. I., et al. (2007). Energy dependence of π^\pm , p and \bar{p} transverse momentum spectra for Au + Au collisions at $\sqrt{s_{NN}} = 62.4$ and 200 GeV. *Physics Letters B*, 655(3-4), 104-113. <https://doi.org/10.1016/j.physletb.2007.06.035>
- [143] [ALICE Collaboration] Abelev, B., et al. (2013). Centrality dependence of charged particle production at large transverse momentum in Pb-Pb collisions at $\sqrt{s_{NN}} = 2.76$ TeV. *Physics Letters B*, 720(1-3). <https://doi.org/10.1016/j.physletb.2013.01.051>
- [144] [ALICE Collaboration] Adam, J., et al. (2016). Transverse momentum dependence of D-meson production in Pb-Pb collisions at $\sqrt{s_{NN}} = 2.76$ TeV. *Journal of High Energy Physics*, 2016(3). [https://doi.org/10.1007/JHEP03\(2016\)081](https://doi.org/10.1007/JHEP03(2016)081)
- [145] [STAR Collaboration] Adamczyk, L., et al. (2014). Observation of D^0 Meson Nuclear Modifications in Au + Au Collisions at $\sqrt{s_{NN}} = 200$ GeV. *Physical Review Letters*, 113(14). <https://doi.org/10.1103/PhysRevLett.113.142301>
- [146] [STAR Collaboration] Adamczyk, L., et al. (2018). Erratum: Observation of D^0 Meson Nuclear Modifications in Au+Au Collisions at $\sqrt{s_{NN}} = 200$ GeV. *Physical Review Letters*, 121(22). <https://doi.org/10.1103/PhysRevLett.121.229901>
- [147] Vaněk, J. (2022). *Measurement of open-charm mesons in heavy-ion collisions by the STAR experiment* [Ph.D. thesis]. České vysoké učení technické v Praze.
- [148] [ALICE Collaboration] Acharya, S., et al. (2018). Measurement of D^0 , D^+ , D^{*+} and D_s^+ production in Pb-Pb collisions at $\sqrt{s_{NN}} = 5.02$ TeV. *Journal of High Energy Physics*, 2018(10). [https://doi.org/10.1007/JHEP10\(2018\)174](https://doi.org/10.1007/JHEP10(2018)174)
- [149] [STAR Collaboration] Adam, J., et al. (2021). Observation of D_s^\pm/D^0 enhancement in Au+Au collisions at $\sqrt{s_{NN}} = 200$ GeV. *Physical Review Letters*, 127(9). <https://doi.org/10.1103/PhysRevLett.127.092301>
- [150] [STAR Collaboration] Adam, J., et al. (2020). First Measurement of Λ_c Baryon Production in Au+Au Collisions at $\sqrt{s_{NN}} = 200$ GeV. *Physical Review Letters*, 124(17). <https://doi.org/10.1103/PhysRevLett.124.172301>
- [151] [STAR Collaboration] Abelev, B. I., et al. (2008). Centrality dependence of charged hadron and strange hadron elliptic flow from

- $\sqrt{s_{\text{NN}}} = 200$ GeV Au+Au collisions. *Physical Review C*, 77(5).
<https://doi.org/10.1103/PhysRevC.77.054901>
- [152] Bierlich, C., & Christiansen, J. R. (2015). Effects of color reconnection on hadron flavor observables. *Physical Review D*, 92(9).
<https://doi.org/10.1103/PhysRevD.92.094010>
- [153] [STAR Collaboration] Agakishiev, G., et al. (2012). Strangeness Enhancement in Cu-Cu and Au-Au Collisions at $\sqrt{s_{\text{NN}}} = 200$ GeV. *Physical Review Letters*, 108(7). <https://doi.org/10.1103/PhysRevLett.108.072301>
- [154] Oh, Y., Ko, C. M., Lee, S. H., & Yasui, S. (2009). Ratios of heavy baryons to heavy mesons in relativistic nucleus-nucleus collisions. *Physical Review C*, 79(4). <https://doi.org/10.1103/PhysRevC.79.044905>
- [155] Cho, S., Sun, K. -J., Ko, C. M., Lee, S. H., & Oh, Y. (2020). Charmed hadron production in an improved quark coalescence model. *Physical Review C*, 101(2). <https://doi.org/10.1103/PhysRevC.101.024909>
- [156] Plumari, S., Minissale, V., Das, S. K., Coci, G., & Greco, V. (2018). Charmed hadrons from coalescence plus fragmentation in relativistic nucleus-nucleus collisions at RHIC and LHC. *The European Physical Journal C*, 78(4). <https://doi.org/10.1140/epjc/s10052-018-5828-7>
- [157] Zhao, J., Shi, S., Xu, N., & Zhuang, P. (2018). Sequential Coalescence with Charm Conservation in High Energy Nuclear Collisions. *ArXiv*. <https://doi.org/10.48550/arXiv.1805.10858>
- [158] He, M., & Rapp, R. (2020). Hadronization and Charm-Hadron Ratios in Heavy-Ion Collisions. *Physical Review Letters*, 124(4). <https://doi.org/10.1103/PhysRevLett.124.042301>
- [159] Cao, S., Sun, K. -J., Li, S. -Q., Liu, S. Y. F., Xing, W. -J., Qin, G. -Y., & Ko, C. M. (2020). Charmed hadron chemistry in relativistic heavy-ion collisions. *Physics Letters B*, 807. <https://doi.org/10.1016/j.physletb.2020.135561>
- [160] [ALICE Collaboration] Acharya, S., et al. (2018). Λ_c^+ production in pp collisions at $\sqrt{s} = 7$ TeV and in p-Pb collisions at $\sqrt{s_{\text{NN}}}=5.02$ TeV. *Journal of High Energy Physics*, 2018(4). [https://doi.org/10.1007/JHEP04\(2018\)108](https://doi.org/10.1007/JHEP04(2018)108)
- [161] [LHCb Collaboration] Aaij, R., et al. (2019). Prompt Λ_c^+ production in pPb collisions at $\sqrt{s_{\text{NN}}} = 5.02$ TeV. *Journal of High Energy Physics*, 2019(2). [https://doi.org/10.1007/JHEP02\(2019\)102](https://doi.org/10.1007/JHEP02(2019)102)

- [162] [STAR Collaboration] Adam, J., et al. (2019). First Observation of the Directed Flow of D^0 and \bar{D}^0 in Au+Au Collisions at $\sqrt{s_{NN}} = 200$ GeV. *Physical Review Letters*, 123(16). <https://doi.org/10.1103/PhysRevLett.123.162301>
- [163] [STAR Collaboration] Adamczyk, L., et al. (2018). Beam-Energy Dependence of Directed Flow of Λ , $\bar{\Lambda}$, K^\pm , K_S^0 , and ϕ in Au+Au Collisions. *Physical Review Letters*, 120(6). <https://doi.org/10.1103/PhysRevLett.120.062301>
- [164] Chatterjee, S., & Bożek, P. (2019). Interplay of drag by hot matter and electromagnetic force on the directed flow of heavy quarks. *Physics Letters B*, 798. <https://doi.org/10.1016/j.physletb.2019.134955>
- [165] Das, S. K., Plumari, S., Chatterjee, S., Alam, J., Scardina, F., & Greco, V. (2017). Directed flow of charm quarks as a witness of the initial strong magnetic field in ultra-relativistic heavy ion collisions. *Physics Letters B*, 768, 260-264. <https://doi.org/10.1016/j.physletb.2017.02.046>
- [166] Nasim, M., & Singha, S. (2018). Directed flow of open charm in Au+Au collisions at $\sqrt{s_{NN}} = 200$ GeV using a quark coalescence model. *Physical Review C*, 97(6). <https://doi.org/10.1103/PhysRevC.97.064917>
- [167] [CMS Collaboration] Sirunyan, A. M., et al. (2018). Nuclear modification factor of D^0 mesons in PbPb collisions at $\sqrt{s_{NN}} = 5.02$ TeV. *Physics Letters B*, 782. <https://doi.org/10.1016/j.physletb.2018.05.074>
- [168] Djordjevic, M., & Djordjevic, M. (2015). Predictions of heavy-flavor suppression at 5.1 TeV Pb+Pb collisions at the CERN Large Hadron Collider. *Physical Review C*, 92(2). <https://doi.org/10.1103/PhysRevC.92.024918>
- [169] He, M., Fries, R. J., & Rapp, R. (2014). Heavy flavor at the large hadron collider in a strong coupling approach. *Physics Letters B*, 735, 445-450. <https://doi.org/10.1016/j.physletb.2014.05.050>
- [170] Song, T., Berrehrh, H., Cabrera, D., Cassing, W., & Bratkovskaya, E. (2016). Charm production in Pb+Pb collisions at energies available at the CERN Large Hadron Collider. *Physical Review C*, 93(3). <https://doi.org/10.1103/PhysRevC.93.034906>
- [171] Beraudo, A., De Pace, A., Monteno, M., Nardi, M., & Prino, F. (2015). Heavy flavors in heavy-ion collisions: quenching, flow and correlations. *The European Physical Journal C*, 75(3). <https://doi.org/10.1140/epjc/s10052-015-3336-6>
- [172] Nahrgang, M., Aichelin, J., Gossiaux, P. B., & Werner, K. (2014). Influence of hadronic bound states above T c on heavy-quark observables in Pb Pb

- collisions at the CERN Large Hadron Collider. *Physical Review C*, 89(1). <https://doi.org/10.1103/PhysRevC.89.014905>
- [173] Cao, S., Luo, T., Qin, G. -Y., & Wang, X. -N. (2018). Heavy and light flavor jet quenching at RHIC and LHC energies. *Physics Letters B*, 777, 255-259. <https://doi.org/10.1016/j.physletb.2017.12.023>
- [174] Uphoff, J., Fochler, O., Xu, Z., & Greiner, C. (2015). Elastic and radiative heavy quark interactions in ultra-relativistic heavy-ion collisions. *Journal of Physics G: Nuclear and Particle Physics*, 42(11). <https://doi.org/10.1088/0954-3899/42/11/115106>
- [175] [ALICE Collaboration] Acharya, S., et al. (2019). Λ_c^+ production in Pb-Pb collisions at $\sqrt{s_{NN}} = 5.02$ TeV. *Physics Letters B*, 793, 212-223. <https://doi.org/10.1016/j.physletb.2019.04.046>
- [176] Li, H. -hong, Shao, F. -lan, Song, J., & Wang, R. -qin. (2018). Production of single-charm hadrons by the quark-combination mechanism in p-Pb collisions at $\sqrt{s_{NN}} = 5.02$ TeV. *Physical Review C*, 97(6). <https://doi.org/10.1103/PhysRevC.97.064915>
- [177] Song, J., Li, H. -hong, & Shao, F. -lan. (2018). New feature of low p_T charm quark hadronization in pp collisions at $\sqrt{s} = 7$ TeV. *The European Physical Journal C*, 78(4). <https://doi.org/10.1140/epjc/s10052-018-5817-x>
- [178] [ALICE Collaboration] Acharya, S., et al. (2018). D-Meson Azimuthal Anisotropy in Midcentral Pb-Pb Collisions at $\sqrt{s_{NN}} = 5.02$ TeV. *Physical Review Letters*, 120(10). <https://doi.org/10.1103/PhysRevLett.120.102301>